Development of 2-Dimensional Photonic Crystal Sensors and Pure Protein Organogel Sensing and Biocatalytic Materials

by

Natasha Lynn Smith

B.S. West Virginia University, 2009

Submitted to the Graduate Faculty of the

Dietrich School of Arts and Sciences in partial fulfillment

of the requirements for the degree of

Doctor of Philosophy

University of Pittsburgh

2019

UNIVERSITY OF PITTSBURGH

DIETRICH SCHOOL OF ARTS AND SCIENCES

This dissertation was presented

by

Natasha Lynn Smith

It was defended on

August 12, 2019

and approved by

Dr. Sean Garrett-Roe, Associate Professor, Department of Chemistry, University of Pittsburgh

Dr. Seth Horne, Associate Professor, Department of Chemistry, University of Pittsburgh

Dr. Sachin Velankar, Associate Professor, Mechanical Engineering and Material Science, University of Pittsburgh

Dissertation Director: Dr. Sanford A. Asher, Distinguished Professor of Chemistry, Department of Chemistry, University of Pittsburgh

Development of 2-Dimensional Photonic Crystal Sensors and Pure Protein Organogel Sensing and Biocatalytic Materials

Natasha L. Smith, PhD

University of Pittsburgh, 2019

We developed responsive hydrogels, organogels, and ionogels for chemical sensing and catalysis applications. Gels have two components, polymer networks and solvent mobile phases. Hydrogels contain an aqueous mobile phase; organogels an organic solvent; and ionogels an ionic liquid. Different solvent types were required to target different applications, e.g. gas sensing requires solvents that resist evaporation.

Colorimetric chemical sensors utilize our 2-Dimensional Photonic Crystals (2DPC) technology. 2DPC are arrays of self-assembled polystyrene nanoparticles that have close-packed, hexagonal crystal structures. 2DPC diffract wavelengths of light into discrete angles according to the 2D Bragg equation. Diffraction depends on 2DPC particle spacing and ordering. 2DPC—embedded into gels that were designed such that analytes actuate polymer volume phase transitions (VPT)—change particle spacing with the VPT, shifting diffraction angles. VPT occur when analytes cause Gibbs free energy changes, ΔG.

2DPC surfactant sensors utilized poly(N-isopropylacrylamide) (PNIPAAm) hydrogels. PNIPAAm hydrogels swell when the hydrophobic tail of ionic surfactants binds to the PNIPAAm isopropyl group. A Donnan potential created by bound charges induces ΔG_{Ionic}, causing swelling that red shifts the diffraction.

2DPC gas sensors for humidity and ammonia utilized poly(hydroxyethyl methacrylate)-based polymers in the ionic liquid ethylguanidine perchlorate (EGP). Ionogels are suitable gas

sensors—ionic liquids have negligible vapor pressures, delivering mobile phases that don't evaporate. ΔG_{Mixing} occurs when EGP absorbs water vapor, causing ionogel shrinking that blue shifts the diffraction. Ammonia sensors incorporated acrylic acid into the polymer. Ammonia absorbed by EGP deprotonated the carboxyl groups, causing swelling that red shifts the diffraction.

Responsive pure protein organogels were fabricated from protein hydrogels by exchanging water with ethylene glycol. 2DPC albumin organogels swell when the proteins bind ligands, enabling water insoluble analyte detection that utilizes protein selectivity. Organophosphorus Hydrolase organogels catalyze hydrolysis of organophosphate nerve agents ~160 times faster than their monomers in organic solvent.

Organic solvents typically denature proteins. Crosslinked organogel proteins mostly retain their native protein reactivity because the proteins are immobilized—i.e. stabilized—during hydrogel polymerization. Protein polymer phase separation that accompanies the solvent exchange irreversibly changes the polymer morphology, however the proteins retain their secondary structure and solvation shell waters in pure ethylene glycol.

Table of Contents

List of Tables

List of Figures

List of Equations

Preface

Acknowledgements

There is that saying “if you like what you do, you will never work a day in your life,” but this leaves out the importance of those around you that make the work you like to do enjoyable. I have been immensely privileged to have many talented and compassionate people around me that made my graduate school experience rewarding and fun.

I must begin by thanking my research advisor, Dr. Sanford Asher. Working for Dr. Asher was one of the most enjoyable and fulfilling experiences of my life. I was given the opportunity to grow as a leader and independent research scientist—sharpening my critical thinking skills and learning to develop new research ideas. I am forever grateful to Dr. Asher for giving me the freedom to explore my creativity in research as well as my emergence as an artist, for challenging me and teaching me to push the boundaries of what I think is possible, and for the example he set as a compassionate and effective leader. I could write many pages explaining my appreciation for Dr. Asher and the impact he has had on my life, but in the interest of brevity I shall just conclude by saying, I will truly miss working for him.

I have had the pleasure of working with some amazing people in the Asher group. I want to thank all the past and present group members for their friendship and for fostering a collaborative environment full of intellectually stimulating discussions that helped my research progress. I want to thank my collaborator Andrew Coukouma for writing the MATLAB script that analyzed particle ordering which was critical towards our 2D photonic crystal diffraction work, for all his assistance in the lab, and for the spirited debates that lead to important

revelations. I thank Ryan Jakubek for his contributions to the protein polymer work, including but not limited to collecting UVRR spectra for our protein hydrogel and organogel work and deep discussions on the interpretation of those results, and Dr. Ivan Palleras for his friendship and advice on navigating the stormy sea that is the months leading up to a PhD defense. I quickly moved up the learning curve when I first joined the group due to training from Dr. Alexander Tikhonov, who taught me the mysteries of photonic crystal diffraction and Dr. Jiantao Zhang who trained me on methods for fabricating photonic crystals and responsive hydrogels. Finally, I want to acknowledge Dr. David Punihaole for helping me acclimate to the group and setting an example for what a great researcher should be, Dr. Kyle Hufziger for consistently being one to help talk through difficult problems, and Elizabeth Dahlburg for her continuous friendship, support, and level-headed advice.

I am grateful for all the advice and assistance given by Sharon Mansfield. Thank you for all you have done and for all you continue to do to ensure the group runs smoothly. Also thank you for being the best Pittcon roommate, all the great conversations, laughs, and overall just helping make graduate school an enjoyable experience.

I would also like to thank the members of my committee, Dr. Sean Garrett-Roe, Dr. Sachin Velankar, and Dr. Seth Horne, for their time and helpful influence during the preparation of my dissertation. I appreciate your patience and the encouragement you provided during these last few weeks.

Our collaboration with Chris Fretham and Hanseung Lee at the University of Minnesota Characterization Facility to obtain Cryo-SEM images of our BSA hydrogels and organogels was critical in understanding our pure protein hydrogels and organogels. I am grateful for their time and assistance as well as allowing our group to book a whole week of time on the Cryo-SEM

instrument, not once but twice. I appreciate their help in obtaining the high resolution images seen in Chapter 6 and for sharing their deep knowledge of the Cryo-EM procedures.

I would be remiss if I did not acknowledge my supremely supportive friends, both in Pittsburgh and at home in West Virginia. They have dealt with me in joy and in stress, and continue to love and support me, for that I am grateful. I want to acknowledge Jeffrey Morris in particular, who allowed me to occupy his extra room whenever I needed to stay in Pittsburgh for the last 8 months. Having a comfortable place to stay when I couldn't drive back to WV made finishing this dissertation significantly less painful. Thank you for cooking me dinner, getting me coffee when I was working late in the evening, and being my rock.

Last, but certainly not least, I am thankful for my incredibly supportive and patient parents David and Dee Smith. They initiated my journey towards a scientific career by encouraging my creativity and curiosity from a young age, exposing me to science through fun at-home experiments, and teaching me the value of education and persistence. I am grateful for their hard work and sacrifice which allowed me to attend a private high school, go to college, and continue my education in graduate school to become the first person in my family to attain an advanced degree. I would not have been able to accomplish this without their support and encouragement.

Abbreviations and Nomenclature

2DPC- 2-Dimensional Photonic Crystal; consisting of an ordered array of polystyrene nano- or microparticles.

2DPC Sensor- 2DPC embedded within a responsive hydrogel, organogel, or ionogel network that undergoes volume changes in response to chemical stimuli, resulting in a colorimetric or optical response.

Hydrogel- A crosslinked polymer network containing an aqueous mobile phase

Organogel- A crosslinked polymer network containing an organic solvent mobile phase

Ionogel- A crosslinked polymer network containing an ionic liquid mobile phase

VPT- Volume Phase Transition; volume change of a hydrogel network, where the volume of solvent mobile phase within the polymer network changes due to a change in the free energy. For hydrogel swelling mobile phase partitions into the polymer network, whereas the mobile phase is expelled from the polymer work during hydrogel shrinking.

PNIPAAm- poly(N-isopropyl acrylamide)

PHEMA- poly(hydroxyethyl methacrylate)

EGP- Ethylguanidine perchlorate; a novel ionic liquid discovered in our group by Zhenmin Hong. This ionic liquid is used as the mobile phase of the ionogels described in Chapter 4. **BSA**- Bovine Serum Albumin; blood transport protein known to bind numerous hydrophobic ligands

OPH- Organophosphorus Hydrolase; enzyme that catalyzes the hydrolysis of organophosphates

EG- ethylene glycol; low vapor pressure organic solvent used as the mobile phase for the protein organogel sensors and catalyst in Chapter 5 and 6.

1.0 Introduction

1.1 Scope of Introduction

Chapter 1 provides an overview the research goals and briefly introduces the topics necessary to understand the design and development 2-Dimensional Photonic Crystal (2DPC) sensors. The motivations for developing novel materials that sense and decontaminate hazardous chemicals will be presented. This section also provides background on the use of organophosphate nerve agents, current sensing and decontamination technologies, and current projects aimed at developing novel functional materials. A discussion on the development of two-dimensional (2D) photonic crystals follows. In that section, the 2DPC diffraction that serves as the basis of the sensor's optical response is presented. This section concludes with a discussion on the hydrogel and hydrogel-like materials that actuate this optical response. Flory polymer theory is introduced in relation to the design of stimuli responsive hydrogels. These theories serve as the basis for the development of chemical sensing hydrogels, organogels and ionogels discussed in subsequent chapters. Finally, an overview of the research presented in this dissertation is provided.

1.2 Motivations

Research on novel chemical sensing materials potentially enables the development of new sensing devices that can revolutionize personal healthcare, industrial/environmental safety,

and military preparedness. For example, the development of home blood glucose monitors revolutionized medical care for patients with diabetes mellitus. Careful control of blood glucose levels enabled by at-home glucose monitoring devices drastically increases the long-term health of patients and increased life expectancy.[2] These improved outcomes also decrease overall medical costs associated with emergency intervention. Early iterations of these important medical devices in the 1980s relied on research preformed over a decade earlier at the Ames corporation that developed a colorimetric paper-based sensor for quantifying blood glucose levels.[3-4]

The ideal chemical sensing device has a low limit of detection, large sensing dynamic range, and is selective, insensitive to environmental variations, inexpensive, portable, and easy to use. Thus, chemical sensors employing photonic crystals (PC)[5-8] are ideal candidates for these applications as they produce optical responses that could be easily be integrated into easy to use, portable devices that utilize inexpensive electronics. Most commonly hydrogels are used in the photonic crystal sensors to actuate the chemical response.[9-13] Responsive hydrogels are well-studied volume responsive materials however their applications in sensing gas phase analytes is limited by evaporation of the aqueous mobile phase.

The utilization of hydrogel materials was required in the fabrication 3DPC. 3DPC sensors were fabricated by self-assembling the charged colloids that form the 3DPC in the monomer solution. This self-assembly is highly sensitive to changes in solvent such as the ionic strength.[6, 14-15] The development of 2DPC sensors expanded the type of monomer solutions that could be used to create the chemical sensing material. The 2DPC is self-assembled and adhered to glass slides prior to responsive material polymerization such that a high ionic strength monomer solution does not disrupt the 2DPC ordering that gives rise to bright diffraction of light.

In this context, the motivations behind the research presented in this dissertation was to (1) advance the understanding of 2DPC fabrication and diffraction enabling more efficient integration of these materials into future devices and (2) develop air-stable 2DPC sensing materials that expand our current photonic crystal sensing capabilities to gas phase analytes and materials that can be utilized in ambient conditions.

The final goal of the research grant that funded this was to develop of air-stable sensing materials that can be utilized for detecting highly toxic compounds such as organophosphate (OP) nerve agents. Equally as important as developing materials to sense these chemical threats, is developing materials that decontaminate those hazardous compounds. Decontamination can be accomplished by absorbing the chemical into a material or by catalyzing reactions that break the chemical threat molecule into less toxic products.[16] Materials that catalyze the hydrolysis of OP compounds are the most desirable, because absorbent materials can leach the toxins into the environment after use. For this objective, we also developed enzyme-based materials that catalyze the decontamination of OP compounds. These enzymatic materials have significant increases in the enzymatic activity under harsh conditions such as in denaturing organic solvents compared to the monomeric enzyme.

1.3 Organophosphate Nerve Agent Background

This research was working towards the development of sensing materials that target OP nerve agents. Additionally, we developed catalytic pure protein organogels that decontaminate these toxic substances. Below, we provide a background on the uses of OP as chemical weapons and pesticides, followed by a discussion of current OP sensing and decontamination methods.

World War I initiated the first large-scale utilization of hazardous chemicals as weapons of mass destruction such as chlorine and phosgene gases.[17] Organophosphates (OP) are a class of toxic compounds that were developed as chemical warfare agents during World War II (Figure 1.1). OP were initially utilized as insecticides prior to the war. G-series OP nerve agents Sarin, Soman, and Tabun were some of the first nerve agents, developed by German scientists at I.G Farben industries from 1934-1944.[18] After WWII, many countries including the United States, the United Kingdom, USSR, and China continued funding research to create various other OP chemical warfare agents, including V-series OP nerve agents with significantly increased toxicity. VX was the most potent nerve agent developed, where a lethal dose is just 0.3 mg (inhalation)-5 mg (dermal) per person.[17] Post WWII research also led to the development of numerous OP pesticides like chlorpyrifos. OP pesticides were the most widely used pest control substances globally until recent years. Many western countries have begun banning OP pesticides, however they are still heavily used in developing countries.

Numerous countries began stockpiling OP nerve agents after WWII, most commonly Sarin. However, OP nerve agents were not used as chemical warfare agents during WWII. The first use of OP nerve agents as chemical weapons did not occur until the 1980s during the Iraq-Iran War.[18] The Iraqi military used Sarin and Tabun against the Iranian military killing an estimated 100,000 people. The Iraqi military also used Tabun on a Kurdish town during this conflict, killing as estimated 5000-8000 civilians in a matter of 3 days. In the 1990s, terrorists began using OP nerve agents as chemical weapons. The Aum Shinrikyo Cult released Sarin at several locations in Japan, killing 8 people and poisoning 600 more. The next year, Sarin was released inside Tokyo subway trains, poisoning over 5000 people and causing 11 fatalities.

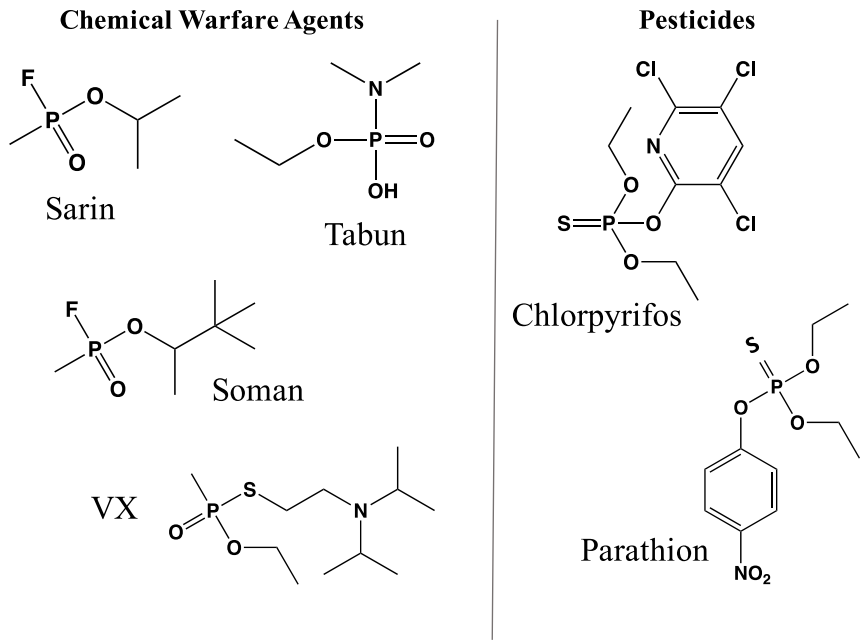

Figure 1.1 - Chemical structures of various organophosphates used as chemical weapons and pesticides.

Chemical weapons including OP nerve agents are still in use despite the Chemical Weapons Convention ban, signed by 165 countries, on the production, stockpiling and use of chemical weapons and their precursors that took effect in 1997. Syria, a signatory of the ban, has been accused in recent years of using chemical weapons, most recently on April 4, 2017.[19] This suspected sarin gas attack injured nearly 300 people and killed at least 83 people including 28 children. Just in the past two years, VX nerve agent was used in the assassination of Kim Jong Un's brother Kim Jong Nam at a Malaysian airport[20], and Sergei Skripal and daughter Yulia were poisoned with Novichok, a Russian military grade nerve agent.[21]

1.3.1 Organophosphate Sensing and Decontamination

OP pose a serious threat to human safety and ecological health. Fast reliable OP sensing and decontamination solutions are needed to protect military and medical personnel from

potential exposure, to neutralize OP stockpiles, and to detect and decontaminate OP residues after chemical weapon attacks. For example, OP poisoning of emergency responders can occur due to cross contamination from the victims.[19] Additionally, the evidence for claimed OP chemical weapon attacks, like those in Syria, rely on witness reports and photographic evidence instead of chemical analysis to substantiate the accusation.[22] Reliable methods to detect a chemical weapons attack would accelerate international response and provide knowledge to emergency responders or military entering the area. The following paragraphs provide an overview of current OP sensing and decontamination techniques and highlight the need for new OP selective materials for the development of wearable sensors and functional protective fabrics.

Numerous lab based techniques can be used for the selective detection of OP, including Mass Spectrometry, FTIR, NMR, and capillary electrophoresis.[23-26] These techniques often have extremely low limits of detection and can differentiate between different OP chemical structures; however, transitioning these instruments into inexpensive portable devices that can be used by untrained personnel has proven difficult. A few commercialized portable sensing devices exist, for example, FLIR Systems Inc., developed a portable GC-MS. This portable GC-MS is accurate, has low limits of detection, and can detect a large variety of explosives, chemical threats, and narcotics. The portable GC-MS instrument has 5-15 minute response times and weighs 36 lbs, such that it is appropriate for transportation in a vehicle but is too heavy to be carried for extended periods of time through rough terrain. The sensor's response time is suitable for targeted testing of a few samples or surfaces but is not sufficient for gathering real-time data of affected areas on a large scale. Furthermore, none of these instrumental sensing techniques are appropriate for applications like a wearable sensor or a protective responsive fabric.

Colorimetric testing kits have been developed for OP sensing, for example the company Aquapheonix developed a colorimetric reagent to detect OP in water samples. These kits can easily be used for testing water samples and produce visually detectable color changes, but this sensing motif is not suitable for detecting OP gases or residues on a surface as it relies on the addition of the reagent to water samples. Colorimetric and Fluorescent Sprays have been developed to test for OP residues on surfaces, like FLIR's Agentase C2 spray. These sprays have very fast response times and are marketed for detecting OP residues on surfaces after an attack. However, the colorimetric or fluorescent response relies on the presence of water, which has a high vapor pressure. Thus, this sensing motif could not easily be integrated into wearable devices that need to sense the presence of OP for long periods of time while the user works in an area of potential OP contact.

To create a wearable sensor, the sensing motif must be integrated into a small device that has a simple sensor readout. In that context, the development of novel materials is necessary. In the past, Asher et al. developed 3DPC OP sensors with extremely low limits of detection by attaching proteins to hydrogel polymers.[9-10] The 3DPC sensor response relies on a pH change in the water mobile phase due to enzyme hydrolysis of OP. These aqueous- based sensing motifs limit many real-world applications that commonly occur in hot and dry environments because the water mobile phase evaporates. Numerous other OP sensing materials or platforms suitable for integration into wearable sensors have been developed, however these also require the presence of water. These include electrochemical sensors[27], enzymes containing carbon-based sensing materials[23, 28-29], fluorescent sensing materials[30], gold nanoparticle-based sensors[31], and potentiometric sensing of enzyme hydrolysis.[32]

Methods to decontaminate OP nerve agents are needed to neutralize chemical weapon stockpiles as well as to treat surfaces and the people exposed after a chemical weapons attack. Neutralization of OP stockpiles is required under the Chemical Weapons Convention ban and reduce the risk of these threat agents falling into the hands of terrorist groups. Decontamination of OP reduces the risk of post-attack exposure and cross-contamination. It also reduces the impact of a chemical weapons attack on the surrounding environment and wildlife.

Many of the readily available methods are rudimentary, in that they are caustic and many decontamination solutions do not detoxify the molecules.[16] The ideal decontamination solutions will catalyze the degradation of the OP molecule, thus removing the immediate threat. Ideal solutions must be applicable for use in OP stockpiles, on all surfaces as well as being safe for use on skin and should have fast reactions times. Additionally, the ideal decontamination agent should be ready for immediate use and not require preparation in the field to maximize its usefulness and effectiveness.

OP contamination on unreactive robust surfaces such as concrete can be treated with hypochlorite solutions or sodium hydroxide solutions.[16] These readily available decontamination solutions are very caustic, therefore they are not applicable for all surfaces where the surface integrity or electronics might be damaged by the solution. Diethylenetriamine solutions can also decontaminate OP[16], however it can cause corneal damage and respiratory issues. This solution should not be used in large quantities because leeching into the soil and groundwater would impact local populations and wildlife.

BX-24, and DF-200 are commercially available decontamination options used my US forces for materials or surfaces that are less caustic than the previous decontamination solutions, however these are still not suitable for personal decontamination on the skin.[16] These

decontamination solutions also require preparation in the field, increasing the risk of error and insufficient OP detoxification.[16]

Personal decontamination treatments often used by military forces and emergency responders are absorbent materials like Fuller's earth.[16] Absorbing the chemical agent prevents absorption through the skin but does not decrease the OP toxicity. Fuller's earth is an aluminum silicate power that does not neutralize the toxic molecule. Furthermore, it can create contaminated dust particles that pose risk. M291 SDK is another personal decontamination solution able to hydrolyze the OP, however, it has very low efficacy for some of the most toxic OP agents like VX and Soman.[16] Reactive Skin Decontamination lotion (RSDL) is an improved skin decontamination formulation that has higher hydrolysis rates against commonly used nerve agents than M291 SDK. RSDL is able to neutralize OP on the skin in less than 3 minutes. None of these personal decontamination solutions are compatible with the eyes or open wounds, complicating their real-world applications.

Enzymes generally catalyze OP hydrolysis more efficiently than synthetic or inorganic catalysts. This has led to extensive research to develop novel solutions that utilize OP degrading enzymes.[16, 33-36] The utilization of enzymes also imparts an innate biocompatibility, enabling use of the product on skin with open wounds and expands their potential uses as prophylactics and therapeutics.[35] The cost of recombinant protein production has decreased over the last decade, potentially making the development of enzymatic decontamination solutions economically feasible as costs continue to decrease. However, enzyme stability continues to be a limiting factor. To be an effective decontamination solution, enzymes must be stabilized to increase the shelf-life of the product. The enzymes must be formulated into solutions that operates efficiently in hot, dry environments for long time periods. Additionally, OP stockpiles typically contain

high concentrations of OP in an organic solvent. Thus, stabilization of the enzyme for efficient catalysis in organic solvents is also necessary.

There is obviously still a need for novel OP specific sensing and decontamination materials. The US Department of Defense is funding research programs through the Defense Threat Reduction Agency (DTRA) to develop novel responsive sensing and decontamination materials that can be utilized in fabric based or wearable applications. The research in this dissertation was funded by DTRA as a basic research grant to work towards this goal.

1.4 2-Dimensional Photonic Crystal Chemical Sensors

The Asher group pioneered research developing photonic crystal-based colorimetric sensing materials.[5-6, 8] Sensing motifs that utilize both 3-Dimensional[6] and 2-Dimensional[8] Photonic Crystals (3DPC and 2DPC) have been developed. These photonic crystal sensors couple the photonic crystal visible light diffraction to polymer volume phase transitions (VPT). The inclusion of photonic crystals in stimuli responsive polymeric films effectively enables the use of the polymer VPT phenomenon in sensing motifs. Physical measurements of the soft materials that exhibit VPT are difficult, whereas the intense photonic crystal diffraction is easily measured or visually observed.[1, 6-7, 37]

The 3DPC and 2DPC sensing motifs are similar in that they both produce colorimetric responses due to shifts in visible light diffracted from nanostructured materials.[10-11, 38-41] As shown in Figure 1.2, volume changes in the responsive material cause 2DPC particle spacing changes, which shift the wavelengths of light diffracted at a particular angle.[7-8] Colorimetric 3DPC and 2DPC sensors have been developed for numerous analytes, including pH,[40, 42]

ethanol,[40] proteins,[13] organophosphates,[9-10] glucose[11, 43] and several others.[38-39, 44-46] The diffraction wavelengths are highly sensitive to the particle spacing[7, 14, 47], thus photonic crystal chemical sensors can detect small changes in volume caused by an analyte. The development of 2DPC chemical sensors are the focus of the research in this dissertation and the primary subject of this introduction.

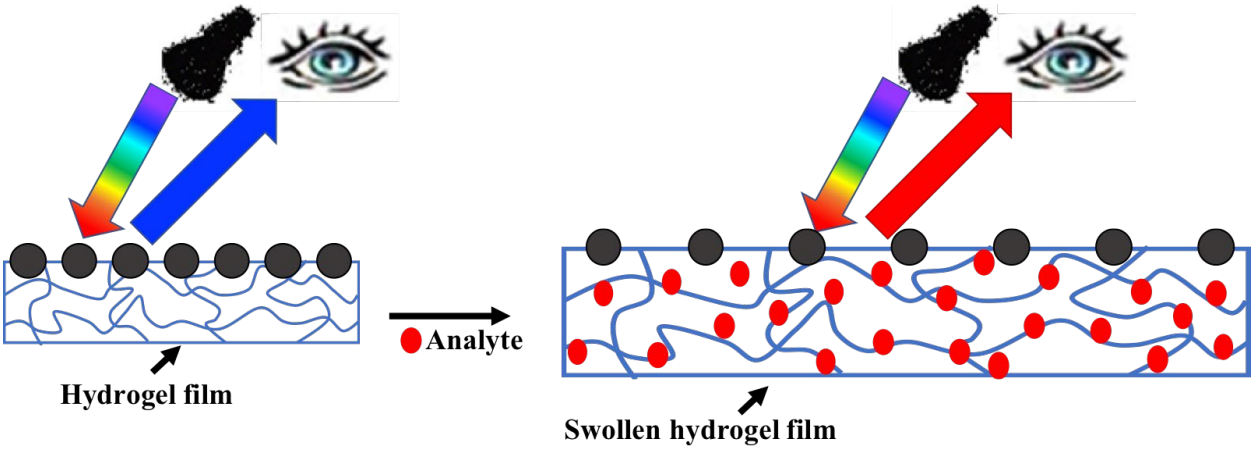

Figure 1.2 – The 2DPC Sensing Motif. Polymer volume phase transitions alter the 2DPC particle spacing, causing shifts in the wavelengths of diffracted light.

2DPC are fabricated through the self-assembly of charged colloidal particles into close packed hexagonal array monolayers. These 2DPC can be fabricated by self-assembly of particles on a mercury surface[8, 48] or by self-assembly at the air-water interface.[1, 49] The self-assembly of 2DPC is covered in detail in Chapter 2. The 2DPC are then embedded in volume responsive materials by polymerizing monomer solutions on top of the 2DPC to form the 2DPC polymer films, as shown in Figure 1.3.[1, 48-49]. 2DPC self-assembled at the air-water interface must be transferred to solid substrates such as glass slides and dried before their inclusion into the polymers.[44] Monomer solutions can be directly added to 2DPC that are self-assembled on

mercury surfaces because mercury has an extremely large surface tension that supports the weight of the particle array, monomer solution, and glass slide that is placed on top.[41]

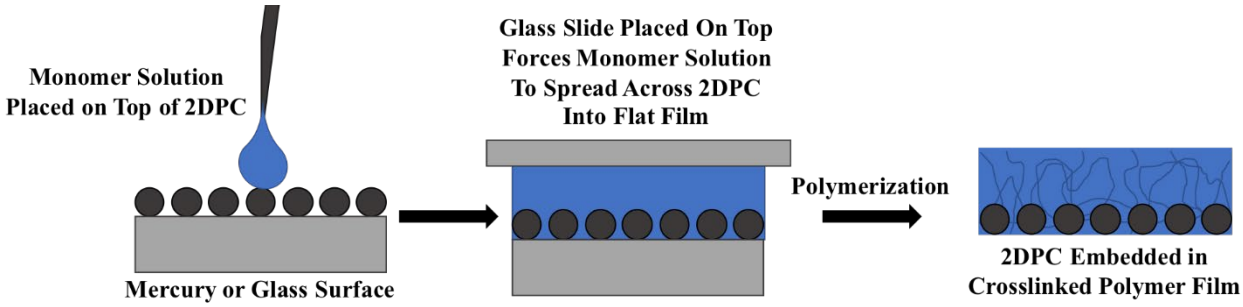

Figure 1.3 – Fabrication of 2DPC Sensors. Monomer solutions are placed on top of 2DPC that are either self-assembled on mercury surfaces or self-assembled at the air-water interface and transferred to glass slides. A second glass slide placed on top of the monomer solution forces the solution to spread over the 2DPC. Polymerization of the monomer solution produces a crosslinked polymer film with the embedded 2DPC.

2DPC sensor fabrication can utilize ionic monomer solutions because the 2DPC is already self-assembled and dried prior to introduction of the monomer solutions.[46] 3DPC sensor fabrication relies on the self-assembly of charged colloidal particles in the monomer solutions. Monomer solutions used to fabricate 3DPC sensors cannot contain ionic species because the 3DPC self-assembly is highly sensitive to ionic impurities.[6, 14, 50] Thus, the development of 2DPC sensors expanded the types of polymers that could be utilized in the fabrication of our colorimetric chemical sensors by enabling the use of ionic monomer solutions. 2DPC sensors have been fabricated using solutions containing acrylic acid and ionic liquids[46], as well as proteins in buffered solutions.[42-43, 51]

The photonic crystal provides the optical response in our 2DPC sensors, whereas the volume response polymeric material enables selective analyte detection. These volume responsive materials consist of a crosslinked polymer network that serves as the stationary phase

and a liquid mobile phase. Hydrogels that contain aqueous mobile phases are most commonly used as the responsive material,[52-53] however, organogels[54-55] and ionogels,[56-57] which utilize organic solvent and ionic liquid mobile phases, also exhibit the VPT phenomenon.

The hydrogel volume is sensitive to changes in its environment.[52, 58-59] By including specific molecular recognition groups on the polymer network, selective sensing materials are created that undergo VPT in response to a specific analyte.[9-10, 12-13, 39, 42] Molecular recognition groups that have high binding affinities enable ultra-low limits of detection. For example, 3DPC Acetylcholinesterase-acrylamide hydrogels detected fM concentrations of OP because the protein has a high binding affinity for OP.[10]

Each subsequent chapter contains details on the self-assembly of 2DPC and the fabrication of 2DPC sensors. Below we briefly introduce the 2DPC diffraction of visible light. Chapter 2 provides a more in-depth description of this 2DPC diffraction and the 2DPC self-assembly at the air-water interface. The design of volume responsive materials that undergo VPT in response to analytes are introduced in terms of Flory Polymer Theory. This section focuses on volume responsive hydrogels, however, the principles discussed for designing such materials also apply to organogels and ionogels. Chapters 3-6 discusses the development of 2DPC chemical sensors that utilize these responsive hydrogels, organogels, and ionogels.

1.5 2-Dimensional Photonic Crystal Diffraction

2DPC are periodic materials that control the propagation of light.[7, 47] Here, 2DPC are fabricated by self-assembly of charged polystyrene (PS) particles into close packed hexagonal array monolayers, as shown in the SEM image in Figure 1.4A. The hexagonal PS particle array

creates a periodic variation in the refractive index (Figure 1.4B), because the PS particle refractive index (n=1.59) is larger than that of the surrounding medium such as air (n=1) or water (n=1.33). The diffraction efficiency depends on the contrast between the particle refractive index and the refractive index surrounding the 2DPC.[6] When the refractive index contrast is large, light efficiently diffracts, whereas low refractive index contrast leads to weak diffraction.

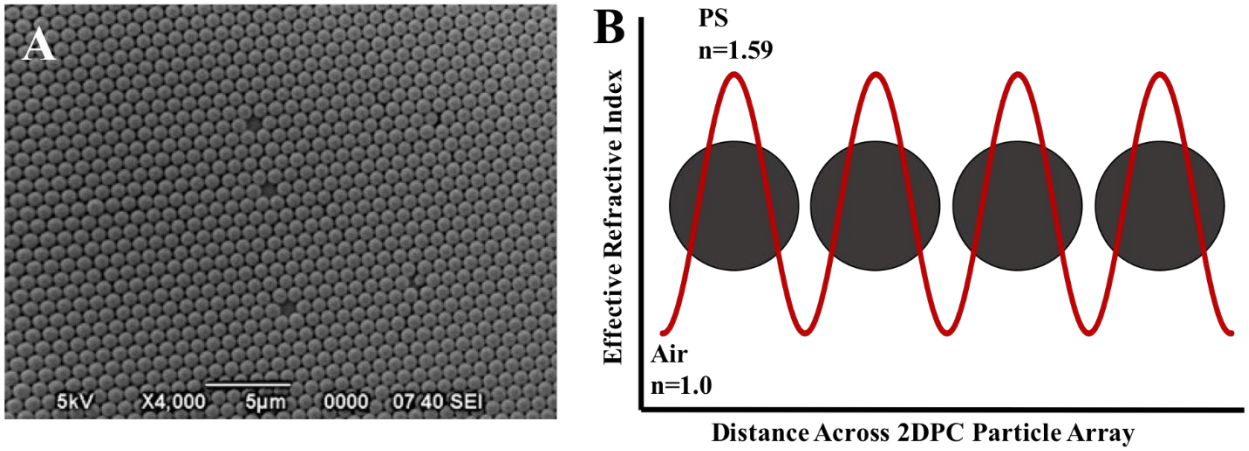

Figure 1.4 – (A) SEM of 2DPC close packed hexagonal array of 915 nm polystyrene particles. (B) Refractive index modulation caused by refractive index contrast between PS particles and air.

When the wavelengths of incident light are on the same order as the particle diameter, Mie scattering of the incident light occurs. Mie scattering from each individual particle in the periodic array causes interference of the scattered waves.[1] Constructive interference of the scattered waves from the periodic particle array results in Bragg diffraction.[47] 3DPC diffraction results in a narrow band of wavelengths diffracting at the Bragg angles, such that a single color is observed, as shown in Figure 1.5A.

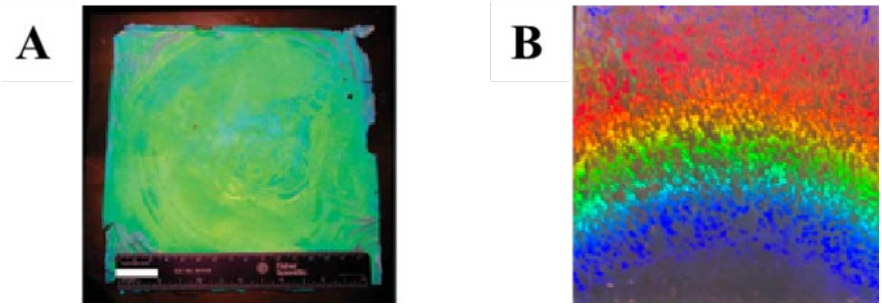

Figure 1.5 – (A) Photograph of 3DPC diffraction, when the angle of incident and diffracted light is normal to the 3DPC surface. (B) Photograph of the 2DPC diffraction showing the diffraction of forward scattered light.

In contrast, the 2DPC diffracts a broad band of wavelengths simultaneously into different angles, producing the rainbow pattern shown in Figure 1.5B. This is because many wavelengths meet the conditions for constructive interference. The general conditions for constructive interference that results in diffraction are illustrated in Figure 1.6A, for an arbitrary particle array spacing, d, diffracting an incident plane wave of monochromatic light. The plane wave strikes the particle array at an incident angle, α. Light scattering from particles on the left side of the image in Figure 1.6A must travel farther by a distance x_A than light scattering from the particles on the right. This creates a phase shift in the incident and scattered light waves having shifts equal to the distances, x_A and x_B. Constructive interference occurs when the sum of the phase shifts from incident and scattered light are equal to the wavelength, $x_A + x_B = \lambda$. The light diffracts at the angle β, fulfilling the condition, $x_B = \lambda - x_A$. Thus, a broad band of wavelengths can meet this condition by diffracting into wavelength dependent diffraction angles, β_λ.

The 2DPC hexagonal crystal lattice with particle spacing, a, is defined by the reciprocal lattice vectors, $\vec{G}$, shown in Figure 1.6B. Diffraction is an elastic scattering event; the magnitude of incident and diffracted light wavevectors are equal for a specific wavelength, $\left|\overrightarrow{k_{in}}\right| = \left|\overrightarrow{k_{sc}}\right| = \left|\vec{k}\right|$. The projections of the incident and diffracted light wavevectors onto $\vec{G}$ in the 2DPC plane,

$\overrightarrow{k_{in}^{\backslash\backslash\backslash}}$ and $\overrightarrow{k_{sc}^{\backslash\backslash\backslash}}$, are used to derive the Kinematic theory 2D diffraction condition (Equation 1.1).[6] These projections are dependent on the angle of the incident wave vector, as shown in Figure 1.6C, such that is both the $\left|\overrightarrow{k_{in}^{\backslash\backslash\backslash}}\right|$ and $\left|\overrightarrow{k_{sc}^{\backslash\backslash\backslash}}\right| < |\vec{k}|$. Projecting these wavevectors into the 2DPC plane also leads to the condition, $\left|\overrightarrow{k_{in}^{\backslash\backslash\backslash}}\right| \neq \left|\overrightarrow{k_{sc}^{\backslash\backslash\backslash}}\right|$, except when the angle of incident and diffracted light are equal.

Equation 1.1 $\boldsymbol{\overrightarrow{k_{sc}^{\backslash\backslash\backslash}} = \overrightarrow{k_{in}^{\backslash\backslash\backslash}} + \vec{G}}$

The Kinematic theory 2D diffraction condition, Equation 1.1, is depicted in Figure 1.6D. For $\overrightarrow{k_{in}^{\backslash\backslash\backslash}} = \overrightarrow{OP}$ incident on a lattice with reciprocal vectors $\vec{G} = \overrightarrow{PG}$, the scattered wavevector $\overrightarrow{k_{sc}^{\backslash\backslash\backslash}}$, must originate from point O and end at point G, $\overrightarrow{OG}$ to meet the conditions of Equation 1.1.[6] As shown in Figure 1.6E, the projections, $\overrightarrow{k_{in}^{\backslash\backslash\backslash}}$ and $\overrightarrow{k_{sc}^{\backslash\backslash\backslash}}$ are parallel to $\vec{G}$, thus $\left|\overrightarrow{k_{in}^{\backslash\backslash\backslash}}\right| + \left|\overrightarrow{k_{sc}^{\backslash\backslash\backslash}}\right| = |\vec{G}|$, yielding the general 2D Bragg diffraction, Equation 1.2. The magnitude of the light wavevector, $|\vec{k}| = 2\pi/\lambda$ is wavelength dependent, so a broad range of λ fulfill the diffraction conditions. The 2DPC hexagonal crystal particle spacing, a is included in the magnitude of the reciprocal lattice vector $|\vec{G}| = \frac{4\pi}{\sqrt{3}a}$, yielding the 2D diffraction equation for our 2DPC hexagonal particle arrays, Equation 1.3.

Equation 1.2 $\boldsymbol{|\vec{G}| = |\vec{k}| \sin\alpha + |\vec{k}| \sin\beta}$

Equation 1.3 $\boldsymbol{\lambda = \frac{\sqrt{3}a}{2}(\sin\alpha + \sin\beta)}$

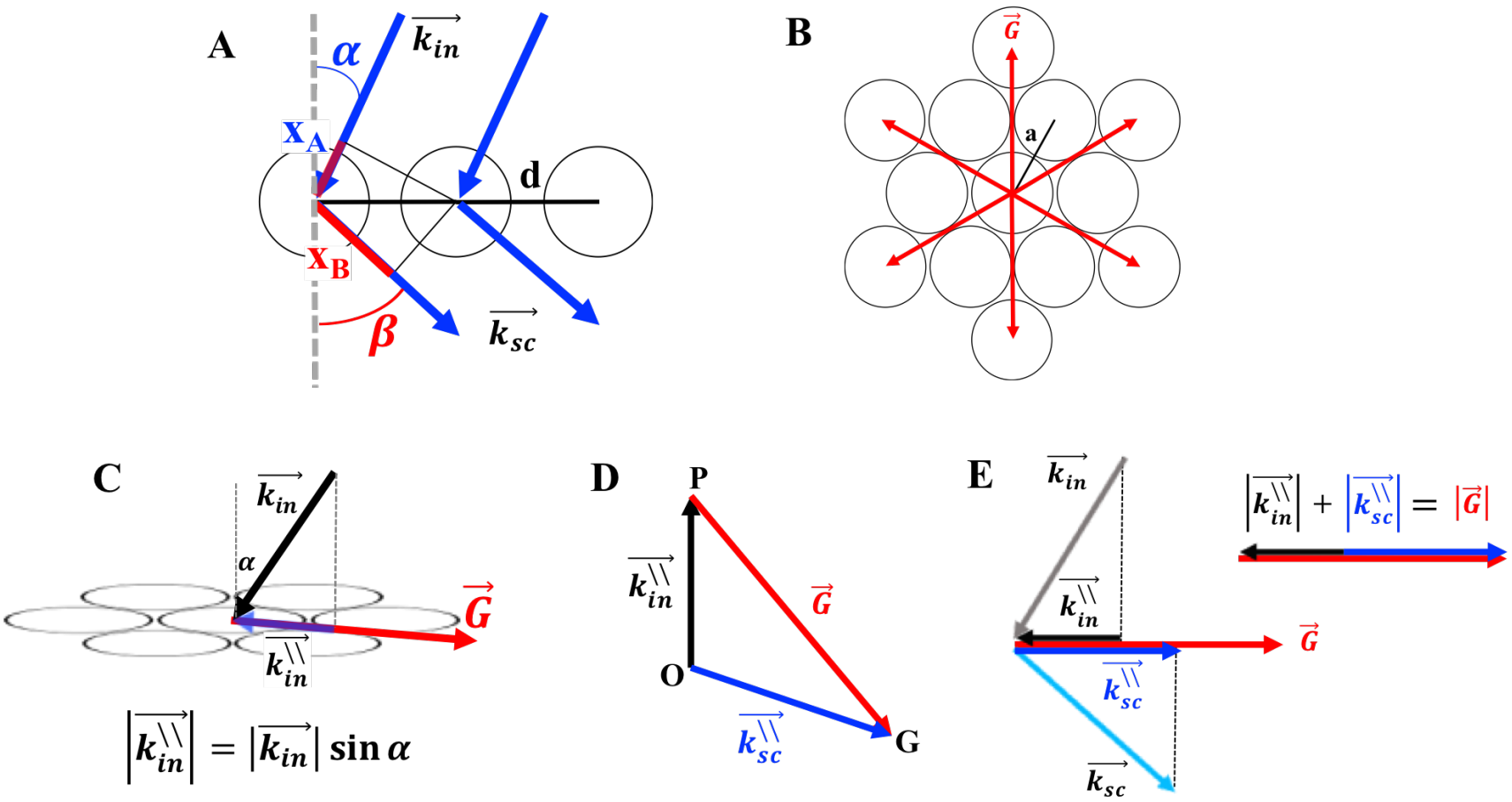

Figure 1.6 – (A) Schematic showing the conditions for constructive interference of an incident plane wave on a particle array with spacing, d. The angle of incident light is α and the angle of diffracted light is β. (B) The reciprocal lattice vectors of the 2DPC hexagonal crystal structure with particle spacing, a. (C) The projection of the incident wavevector with incident angle α onto the reciprocal lattice vector. (D) The Kinematic theory 2D diffraction condition illustrated. (E) The parallel projections of incident and diffracted light vectors onto the reciprocal lattice vector.

White light incident on the 2DPC diffracts most of the light in the forward scattered direction into its wavelength dependent diffraction angles, β_λ, as shown in Figure 1.7A. Roughly 90% of the incident light is diffracted in the forward direction.[7,47] In the 3DPC, the wavelengths of light predominantly back diffract and are easily measured on a spectrometer using a fiber optic probe in the Littrow configuration, where the angle of incident and back diffracted light are equal. Due to this dominant forward scattering, the wavelengths diffracted from the 2DPC are not as easy to measure using a spectrometer and fiber optic probe. However, placing the 2DPC on a mirror reflects the forward scattered light diffraction into the back diffracted direction. Higher diffraction efficiencies in the back scattered direction can be observed when the 2DPC is placed on a mirror surface.[7] As shown in Figure 1.7B, the wavelength of light back diffracted from two 2DPC sensors on a mirror surface shifts when the incident and diffraction angle are equal, producing an observed color change when the particle spacings are different. This result in a colorimetric response similar to that measured for the 3DPC sensors.

Since light is predominantly forward scattered in the 2DPC, we also developed methods to monitor the 2DPC sensor response using the Debye ring.[1, 13] The Debye ring appears on a screen below the 2DPC when the incident light is normal to the hexagonal array plane. The diameter of the Debye ring is proportional to the 2DPC particle spacing. Chapter 2 provides a detailed description of the Debye ring diffraction from 2DPC.

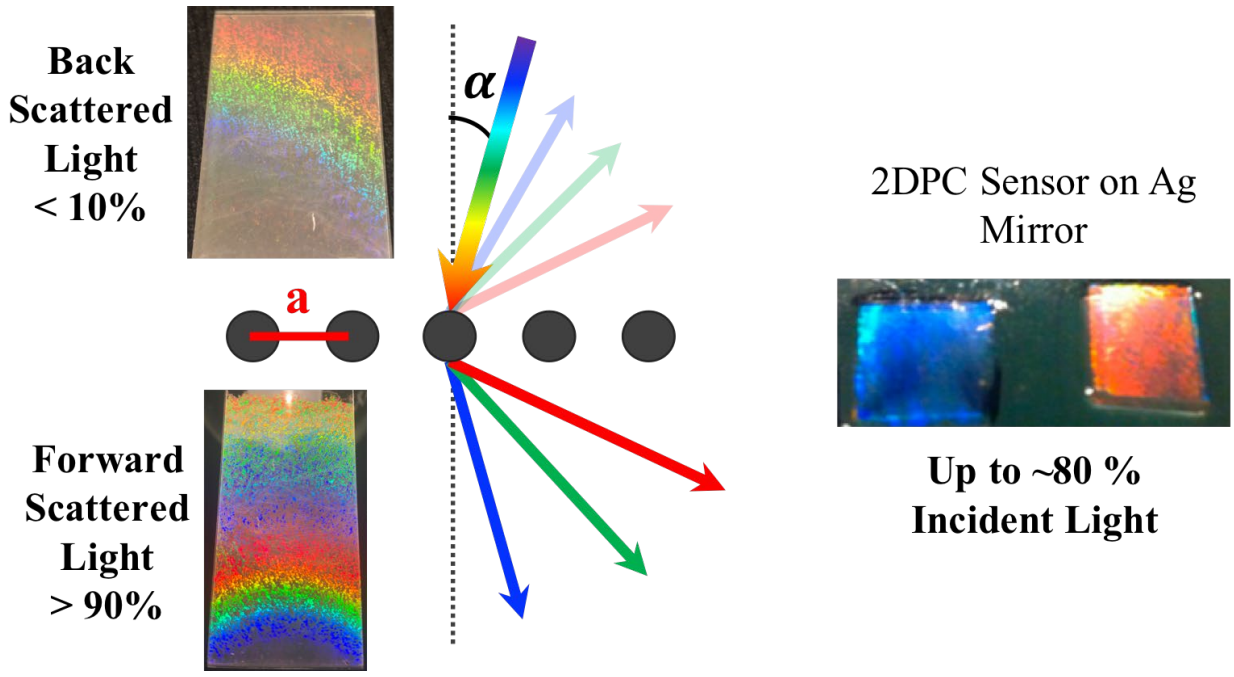

Figure 1.7 – The 2DPC forward scattered diffracted light accounts for ~90% of the incident light, whereas the back scattered diffracted light accounts for ~10% of the incident light. Placing the 2DPC on a mirror reflects the intense forward scattered light into the direction of the back scattered diffraction angle. ~80% of the incident light is observed for the 2DPC on a mirrored surface.

1.6 Chemically Stimulated Polymer Volume Phase Transitions

The 2DPC sensing mechanism relies on the polymer VPT to actuate the optical response. The abrupt volume change in response to an analyte alters the 2DPC particle spacing causing shifts in the diffracted light.[8, 44] These volume responsive materials consist of a stationary phase made of a 3-dimensional crosslinked polymer network and a liquid mobile phase that solvates the polymer network. Hydrogels are defined as polymer networks dispersed in aqueous mobile phases; whereas the organogels contain organic solvent mobile phases and ionogels contain ionic liquid mobile phases. For simplicity, this section will discuss the hydrogel VPT. Hydrogel VPT

are the most well-studied stimuli responsive, volume changing materials that have been utilized in numerous applications, including drug delivery, tissue engineering, microfluidic valves, and chemical and biosensing.[60-62] It is important to keep in mind that the principles discussed for designing stimuli responsive hydrogels also apply to the organogels and ionogels.

The hydrogel volume is sensitive to its environment such that small changes in the chemical environment can induce large VPT. For example, poly(acrylamide) hydrogels undergo relatively large VPT in response to small changes in solution pH and ionic strength.[63] Thermoresponsive PNIPAAm hydrogels exhibit some of the largest known VPT in response to temperature fluctuations near its Lower Critical Solution Temperature (LCST).[64]

Hydrogel VPT are driven by osmotic pressures according to Flory polymer theory.[65] These osmotic pressures, Π generate mass transfer of the mobile phase, either partitioning solvent into the polymer network causing swelling, or expelling solvent causing shrinking. The osmotic pressure is elicited by changes in the Gibbs free energy of the system, ΔG_{Total}.[12, 66] A ΔG_{Total} generates a volume change until the new equilibrium volume is obtain where the osmotic pressure equals zero (Equation 1.4).

$$\textbf{Equation 1.4} \quad \Pi = \frac{\partial G_{Total}}{\partial V} = 0$$

The total Gibbs free energy change contains contributions from changes in the free energy of mixing, ΔG_{Mix}, the elastic free energy, $\Delta G_{Elastic}$, and the ionic free energy, ΔG_{Ion}. At equilibrium, the polymer-mobile phase interactions arising from these three contributions are balanced (Equation 1.5). Thus, changes to the polymer network or to the mobile phase environment that disrupt this delicate balance of interactions cause ΔG_{Total}, generating osmotic pressures that actuate the hydrogel VPT.

$$\textbf{Equation 1.5} \quad \Delta G_{Total} = \Delta G_{Mix} + \Delta G_{Elastic} + \Delta G_{Ion} = 0$$

Creating the 2DPC chemical sensors require careful design of the responsive hydrogel, organogel, and ionogel polymer networks so that selective chemical reactions with molecular recognition groups induce changes in at least one of these free energy contributions. Below we discuss the individual free energy contributions in more detail.

1.6.1 Free Energy of Mixing

The free energy of mixing contribution is determined by the solubility of the polymer network in the mobile phase. It has both enthalpic, ΔH and entropic contributions, ΔS.[62] The enthalpic contributions arise from the molecular interactions between the polymer and mobile phase. This can contribute to hydrogel swelling ($\Delta H < 0$) or hydrogel shrinking ($\Delta H > 0$) depending on the chemical composition of the polymer and mobile phase.[67] There are also entropic contributions that favor polymer-mobile phase mixing ($\Delta S > 0$), stemming from an increase in possible polymer chain conformations that can be sampled in the liquid mobile phase. There are also entropic contributions that resist this swelling ($\Delta S < 0$), arising from stretching of the polymer chains during hydrogel swelling that reduce the number of possible chain conformations.[67]

This description illustrations the complexity of the free energy of mixing that contribute to ΔG_{Total}. However, the intricate influences of entropic and enthalpic polymer-solvent interactions in ΔG_{Mix} are contained within the measurable Flory-Huggins interaction parameter, χ. χ essentially describes the solubility of the polymer and solvent. Simply put, swelling is favored when $\Delta G_{Mix} < 0$ and the enthalpic contributions from polymer solvent interactions are favorable, whereas shrinking is favored when $\Delta G_{Mix} > 0$ and the enthalpic contributions from polymer-solvent interactions are unfavorable.[65, 68]

1.6.2 Elastic Free Energy

The elastic free energy arises from crosslinking in the polymer network.[65, 67] The $\Delta G_{Elastic}$ contributions arise from changes in the polymer chain conformations that occur during hydrogel volume changes.[12] The polymer chain conformations are assumed to configure into the statistically most probable state when the polymer network is crosslinked during polymerization. Volume changes that change the polymer chain conformations cause configurations that are not in that ideal state.

Thus, the elastic free energy acts as the restoring force, resisting both swelling and shrinking that changes the polymer chain conformations. The strength of this restoring force is determined by the crosslink density. Hydrogels with low crosslink densities have larger VPT compared to hydrogels with high crosslink densities.

1.6.3 Ionic Free Energy

Changes in the ionic free energy, ΔG_{Ion}, occur when a charge is bound to the polymer network.[69] A Donnan potential is created when a polymer is ionized. The Donnan potential is created from a difference in the concentration of ions in the bulk mobile phase surrounding the hydrogel film and the concentration of ions bound to the polymer network in the hydrogel film. When a charge binds to the polymer, its counterions are also effectively bound inside the polymer network. Polymer ionization results in hydrogel swelling because the liquid mobile phase must partition into the polymer network to alleviate the chemical potential, $\mu_{Ion,}$ created by the concentration difference across the hydrogel and bulk mobile phase interface.

High ionic strength of the mobile phase attenuates the ΔG_{Ion} induced by the charge binding event.[11, 70] In a solution with a large concentration of ions, the addition of charged groups (and its counterions) to the polymer network generates a smaller change in the ionic concentration difference between inside and outside the hydrogel. Thus, the VPT that arises from charged analytes binding to the polymer is smaller in buffered solutions compared to the VPT in pure water.

1.7 Overview of Research Program

Chapters 2-6 contain published or soon-to-be published work involving 2DPC diffraction, the development of 2DPC chemical sensors and novel responsive pure protein organogel sensors and catalysis. Responsive hydrogels, organogels, and ionogels were developed that utilize aqueous, organic solvent, and ionic liquid mobile phases, respectively. This enabled unique/novel applications of our photonic crystal technology. The development of air-stable sensing materials, i.e. ionogels and organogels is emphasized.

In Chapter 2, a detailed description of the 2DPC fabrication via self-assembly and the Debye ring diffraction from ordered and disordered 2DPC is provided. It is much simpler to monitor the analyte response of 2DPC sensors using the Debye ring diffraction diameter compared to measuring the diffracted wavelengths at a specific angle using a spectrometer. We demonstrate here that the Debye ring diffraction can also be used as a non-destructive and quantitative measure of the 2DPC particle ordering. Using these results, we investigate the self-assembly of charged colloidal particles at the air-water interface using the needle tip flow

method. We establish that fabricating 2DPC using the needle tip flow method produces close packed hexagonal arrays on the water surface.

In Chapter 3, 2DPC poly(N-isopropylacrylamide) (PNIPAAm) based hydrogel sensors for ionic surfactants are presented. 2DPC PNIPAAm hydrogels are fabricated by polymerizing the hydrogel on top of a 2DPC array that was self-assembled on a mercury surface. These chapter demonstrate the colorimetric response of the 2DPC diffraction-based sensing motif by measuring the wavelengths of diffracted visible light as opposed to measuring the Debye ring diameter. The 2DPC PNIPAAm hydrogel swells as the concentration of surfactant in solution increases, redshifting the diffracted wavelengths due to increases in the 2DPC particle spacing. The hydrogel swells when ionic surfactants bind to the PNIPAAm hydrogel network because the bound charges create a Donnan potential, changing the ionic free energy of the system. The hydrophobic tails of anionic and cationic surfactants bind to the isopropyl groups of PNIPAAm via hydrophobic interactions, attaching the charged surfactant head group to the hydrogel network. The addition of more hydrophobic co-monomers increases the hydrophobic interactions that bind the surfactants to the polymer. Thus, p(NIPAAm-co-t-butyl acrylate) hydrogels exhibit larger surfactant induced swelling responses compared to PNIPAAm hydrogels.

Chapter 4 discusses the development of air-stable 2DPC poly(hydroxyethyl methacrylate) PHEMA ionogel sensors. Ionogels are polymer networks that contain an ionic liquid mobile phase as opposed to hydrogels, which contain aqueous mobile phases. A novel ionic liquid, ethylguanidine perchlorate (EGP) that has a negligible vapor pressure was utilized as the mobile phase to produce materials that are not limited by evaporation of the mobile phase. The 2DPC PHEMA ionogel sensors demonstrate proof-of-concept gas sensing. This expands on the 2DPC

hydrogel sensing technology because water evaporation severely limits the hydrogel gas sensing capabilities. We discovered EGP was also able to act as a co-solvent during PHEMA polymerization, replacing traditional glycol co-solvents that are used to prevent polymerization induced phase separation in PHEMA hydrogels. The particle spacing of 2DPC pHEMA ionogels decreases in response to increasing humidity. Absorption of water by the hydroscopic ionic liquid induces changes in the free energy of mixing. Ionogel ammonia gas sensors were fabricated by including the co-monomer, acrylic acid. Ammonia absorbed by EGP deprotonates the acrylic acid carboxyl groups, causing the 2DPC ionogel to swell.

Chapter 5 and 6 discuss the development of revolutionary responsive pure protein organogels. In Chapter 5, we describe the fabrication of responsive pure protein organogels and demonstrate their utilization as sensors and catalysts. The responsive pure protein organogels are fabricated from pure protein hydrogels using a stepwise solvent exchange that replaces the aqueous mobile phase with low vapor pressure organic solvent. We used ethylene glycol (EG) mobile phases to create materials that are more resistant to mobile phase evaporation compared to hydrogels. The proteins in the organogels are immobilized which stabilizes the protein structure such that the proteins retain much of the native protein reactivities in the EG e.g. ligand binding affinity and enzyme activity. We fabricated pure Bovine Serum Albumin (BSA) 2DPC organogel sensors that undergo VPT in response to protein-ligand binding. This is the first report of a pure protein organogel material that exhibits chemically actuated Volume Phase Transitions (VPT). Organophosphorus Hydrolase (OPH) organogels were also fabricated to demonstrate catalysis in these novel materials. These OPH organogels catalyze organophosphates at much higher rates compared to the uncrosslinked OPH monomers, which are deactivated in organic solvent.

We discovered that this water to EG exchange causes an irreversible VPT in the gel. Exchanging the EG mobile phase back to pure water does not cause measurable changes to the protein organogel volume. The irreversibility of the VPT creates sensors which would be insensitive to humidity. The mechanisms by which the EG exchange transforms protein hydrogels into protein organogels is explored in Chapter 6. Using UV Resonance Raman and IR spectroscopy, Cryo-SEM, and titration of the carboxyl containing amino acids on the protein surface, we were able to characterize changes to the BSA secondary structure and BSA polymer morphology that accompany the irreversible VPT. Using these results, we conclude the phase separation of the protein polymer from EG drives the large VPT shrinking and that additional crosslinks between protein polymer chains in the collapsed state result in the irreversible behavior.

1.8 References

1. Nathan, D.M.; Genuth, S; Lachin, J.; Cleary, P.; Crofford, O.; Davis, M.; Rand, L.; Siebert, C. The Effect of Intensive Treatment of Diabetes on the Development and Progression of Long-Term Complications in Insulin-Dependent Diabetes Mellitus. *New England Journal of Medicine.* **1993**, 329, 977-986.

2. Rock, J. A.; Gerende, L. J. Dextrostix Method for Determination of Blood Glucose Levels: A Statistical Evaluation. *JAMA.* **1966**, 198, 231-236.

3. Scherstén, B. Clinical Evaluation of a Rapid Enzyme Strip Method (Dextrostix) for Blood Glucose Estimation. *Acta Medica Scandinavica*. **1965**, 178, 583-590.

4. Holtz, J. H.; Asher, S. A., Polymerized colloidal crystal hydrogel films as intelligent chemical sensing materials. *Nature* **1997**, 389, 829.

5. Asher, S. A.; Holtz, J.; Liu, L.; Wu, Z., Self-Assembly Motif for Creating Submicron Periodic Materials. Polymerized Crystalline Colloidal Arrays. *Journal of the American Chemical Society*. **1994**, 116, 4997-4998.

6. Alexander Tikhonov, N. K., Jian-Tao Zhang, Luling Wang, Sanford A. Asher, Relectivity Enhanced Two-Dimensional Dielectric Particle Array Monoloayer Diffraction. *Journal of Nanophotonics.* **2012,** 6, 063509-1-063509-9.

7. Zhang, J.-T.; Wang, L.; Luo, J.; Tikhonov, A.; Kornienko, N.; Asher, S. A., 2-D Array Photonic Crystal Sensing Motif. *Journal of the American Chemical Society*. **2011**, 133, 9152-9155.

8. Walker, J.; Kimble, K.; Asher, S., Photonic crystal sensor for organophosphate nerve agents utilizing the organophosphorus hydrolase enzyme. *Anal. Bioanal. Chem*. **2007**, 389, 2115-2124.

9. Walker, J. P.; Asher, S. A., Acetylcholinesterase-Based Organophosphate Nerve Agent Sensing Photonic Crystal. *Analytical Chemistry*. **2005**, 77, 1596-1600.

10. Alexeev, V. L.; Das, S.; Finegold, D. N.; Asher, S. A., Photonic Crystal Glucose-Sensing Material for Noninvasive Monitoring of Glucose in Tear Fluid. *Clinical Chemistry*. **2004**, 50, 2353.

11. Goponenko, A. V.; Asher, S. A., Modeling of Stimulated Hydrogel Volume Changes in Photonic Crystal Pb2+ Sensing Materials. *Journal of the American Chemical Society*. **2005**, 127, 10753-10759.

12. Zhang, J.-T.; Chao, X.; Liu, X.; Asher, S. A., Two-dimensional array Debye ring diffraction protein recognition sensing. *Chemical Communications*. **2013**, 49, 6337-6339.

13. Hufziger, K. T.; Bykov, S. V.; Asher, S. A., Raman Hyperspectral Imaging Spectrometer Utilizing Crystalline Colloidal Array Photonic Crystal Diffraction. *Appl. Spectrosc.* **2014**, 68, 1219-1223.

14. Holtz, J. H.; Asher, S. A., Polymerized colloidal crystal hydrogel films as intelligent chemical sensing materials. *Nature* **1997**, 389, 829-832.

15. Jacquet, P.; Daudé, D.; Bzdrenga, J.; Masson, P.; Elias, M.; Chabrière, E., Current and emerging strategies for organophosphate decontamination: special focus on hyperstable enzymes. *Environmental Science and Pollution Research*. **2016**, 23, 8200-8218.

16. Szinicz, L., History of chemical and biological warfare agents. *Toxicology*. **2005**, 214, 167-181.

17. Shadnia, K. S. a. S., History of the Use and Epidemiology of Organophosphorus Poisoning. *In Basic and Clinical Toxicology of Organophosphorus Compounds*; Abdollahi, M. B.-M. a. M., Ed. Springer: London, 2014.

18. Brooks, J.; Erickson, T. B.; Kayden, S.; Ruiz, R.; Wilkinson, S.; Burkle, F. M., Responding to chemical weapons violations in Syria: legal, health, and humanitarian recommendations. *Conflict and Health*. **2018**, 12, 12.

19. Chai, P. R.; Boyer, E. W.; Al-Nahhas, H.; Erickson, T. B., Toxic chemical weapons of assassination and warfare: nerve agents VX and sarin. *Toxicology Communications*. **2017**, 1, 21-23.

20. Chai, P. R.; Hayes, B. D.; Erickson, T. B.; Boyer, E. W., Novichok agents: a historical, current, and toxicological perspective. *Toxicology Communications*. **2018**, 2, 45-48.

21. Kostov, S. M. a. N., French Publish Report Asserting Assad Used Chemical Weapons in Attack. *The Wall Street Journal*. April 2018.

22. Lee, J. H.; Park, J. Y.; Min, K.; Cha, H. J.; Choi, S. S.; Yoo, Y. J., A novel organophosphorus hydrolase-based biosensor using mesoporous carbons and carbon black for the detection of organophosphate nerve agents. *Biosensors and Bioelectronics*. **2010**, 25, 1566-1570.

23. Thompson, C. M.; Prins, J. M.; George, K. M., Mass spectrometric analyses of organophosphate insecticide oxon protein adducts. *Environmental health perspectives*. **2010**, 118, 11-19.

24. Pyschik, M.; Winter, M.; Nowak, S., Capillary Electrophoresis as Analysis Technique for Battery Electrolytes: (i) Monitoring Stability of Anions in Ionic Liquids and (ii) Determination of Organophosphate-Based Decomposition Products in LiPF6-Based Lithium Ion Battery Electrolytes. *Separations*. **2017**, 4, 26.

25. Kumar, V.; Upadhay, N.; Wasit, A.B.; Singh, S.; Kaur, P. Spectroscopic Methods for the Detection of Organophosphate Pesticides, A Preview. *Current World Environment*. 8, 313-318.

26. Beshay, M.; Cordero, S. R.; Mukamal, H.; Ruiz, D.; Lieberman, R. A., Recent advances toward a fiber optic sensor for nerve agent. *SPIE*. **2008**, 6954.

27. Liu, G.; Lin, Y., Electrochemical Sensor for Organophosphate Pesticides and Nerve Agents Using Zirconia Nanoparticles as Selective Sorbents. *Analytical Chemistry* **2005**, 77, 5894-5901.

28. Li, H.; Yan, X.; Lu, G.; Su, X., Carbon dot-based bioplatform for dual colorimetric and fluorometric sensing of organophosphate pesticides. *Sensors and Actuators B: Chemical*. **2018**, 260, 563-570.

29. Liu, N.; Cai, X.; Lei, Y.; Zhang, Q.; Chan-Park, M. B.; Li, C.; Chen, W.; Mulchandani, A., Single-Walled Carbon Nanotube Based Real-Time Organophosphate Detector. *Electroanalysis*. **2007**, 19, 616-619.

30. Obare, S. O.; De, C.; Guo, W.; Haywood, T. L.; Samuels, T. A.; Adams, C. P.; Masika, N. O.; Murray, D. H.; Anderson, G. A.; Campbell, K.; Fletcher, K. Fluorescent chemosensors for toxic organophosphorus pesticides: a review. *Sensors*. **2010**, 10, 7018-7043.

31. Li, X.; Cui, H.; Zeng, Z., A Simple Colorimetric and Fluorescent Sensor to Detect Organophosphate Pesticides Based on Adenosine Triphosphate-Modified Gold Nanoparticles. *Sensors.* **2018**, 18, 4302.

32. Mulchandani, A.; Mulchandani, P.; Chauhan, S.; Kaneva, I.; Chen, W., A Potentiometric Microbial Biosensor for Direct Determination of Organophosphate Nerve Agents. *Electroanalysis.* **1998**, 10, 733-737.

33. Lu, H. D.; Wheeldon, I. R.; Banta, S., Catalytic biomaterials: engineering organophosphate hydrolase to form self-assembling enzymatic hydrogels. *Protein Engineering, Design and Selection.* **2010**, 23, 559-566.

34. Blatchford, P. A.; Scott, C.; French, N.; Rehm, B. H. A., Immobilization of organophosphohydrolase OpdA from Agrobacterium radiobacter by overproduction at the surface of polyester inclusions inside engineered Escherichia coli. *Biotechnology and Bioengineering.* **2012**, 109, 1101-1108.

35. Novikov, B. N.; Grimsley, J. K.; Kern, R. J.; Wild, J. R.; Wales, M. E., Improved pharmacokinetics and immunogenicity profile of organophosphorus hydrolase by chemical modification with polyethylene glycol. *Journal of Controlled Release.* **2010**, 146, 318-325.

36. Dennis, P. B.; Walker, A. Y.; Dickerson, M. B.; Kaplan, D. L.; Naik, R. R., Stabilization of Organophosphorus Hydrolase by Entrapment in Silk Fibroin: Formation of a Robust Enzymatic Material Suitable for Surface Coatings. *Biomacromolecules.* **2012**, 13, 2037-2045.

37. Flaugh, P. L.; O'Donnell, S. E.; Asher, S. A., Development of a New Optical Wavelength Rejection Filter: Demonstration of Its Utility in Raman Spectroscopy. *Applied Spectroscopy.* **1984**, 38, 847-850.

38. Smith, N. L.; Coukouma, A.; Dubnik, S.; Asher, S. A., Debye ring diffraction elucidation of 2D photonic crystal self-assembly and ordering at the air-water interface. *Physical Chemistry Chemical Physics.* **2017**, 19, 31813-31822.

39. Zhang, J-T.; Smith, N.L.; Asher, S.A. Two Dimensional Photonic Crystal Surfactant Detection. *Analytical Chemistry.* **2012**, 84, 6416-6420.

40. Sharma, A. C.; Jana, T.; Kesavamoorthy, R.; Shi, L.; Virji, M. A.; Finegold, D. N.; Asher, S. A., A General Photonic Crystal Sensing Motif: Creatinine in Bodily Fluids. *Journal of the American Chemical Society.* **2004**, 126, 2971-2977.

41. Xu, X.; Goponenko, A. V.; Asher, S. A., Polymerized PolyHEMA Photonic Crystals: pH and Ethanol Sensor Materials. *Journal of the American Chemical Society.* **2008**, 130, 3113-3119.

42. Zhang, J.-T.; Smith, N.; Asher, S. A., Two-Dimensional Photonic Crystal Surfactant Detection. *Analytical Chemistry.* **2012**, 84, 6416-6420.

43. Cai, Z.; Zhang, J.-T.; Xue, F.; Hong, Z.; Punihaole, D.; Asher, S. A., 2D Photonic Crystal Protein Hydrogel Coulometer for Sensing Serum Albumin Ligand Binding. *Analytical Chemistry.* **2014**, 86, 4840-4847.

44. Cai, Z.; Luck, L. A.; Punihaole, D.; Madura, J. D.; Asher, S. A., Photonic crystal protein hydrogel sensor materials enabled by conformationally induced volume phase transition. *Chemical Science.* **2016**, 7, 4557-4562.

45. Cai, Z.; Smith, N. L.; Zhang, J.-T.; Asher, S. A., Two-Dimensional Photonic Crystal Chemical and Biomolecular Sensors. *Analytical Chemistry.* **2015**, 87, 5013-5025.

46. Kamenjicki, M.; Lednev, I. K.; Asher, S. A., Photoresponsive Azobenzene Photonic Crystals. *The Journal of Physical Chemistry B.* **2004**, 108, 12637-12639.

47. Smith, N. L.; Hong, Z.; Asher, S. A., Responsive ionic liquid-polymer 2D photonic crystal gas sensors. *Analyst.* **2014**, 139, 6379-6386.

48. Freymann, G. v.; Koch, W.; Meisel, D. C.; Wegener, M.; Diem, M.; Garcia-Martin, A.; Pereira, S.; Busch, K.; Schilling, J.; Wehrspohn, R. B.; Gösele, U., Diffraction properties of two-dimensional photonic crystals. *Applied Physics Letters.* **2003**, 83, 614-616.

49. Zhang, J.-T.; Wang, L.; Chao, X.; Asher, S. A., Periodicity-Controlled Two-Dimensional Crystalline Colloidal Arrays. *Langmuir.* **2011**, 27, 15230-15235.

50. Zhang, J.-T.; Wang, L.; Lamont, D. N.; Velankar, S. S.; Asher, S. A., Fabrication of Large-Area Two-Dimensional Colloidal Crystals. *Angewandte Chemie International Edition.* **2012**, 51, 6117-6120.

51. Manoharan, V. N., Colloidal matter: Packing, geometry, and entropy. *Science.* **2015**, 349, 1253751.

52. Zhongyu, C.; H., K. D.; David, P.; Zhenmin, H.; S., V. S.; Xinyu, L.; A., A. S., A Photonic Crystal Protein Hydrogel Sensor for Candida albicans. *Angewandte Chemie.* **2015**, 127, 13228-13232.

53. Richter, A.; Howitz, S.; Kuckling, D.; Arndt, K.-F., Influence of volume phase transition phenomena on the behavior of hydrogel-based valves. *Sensors and Actuators B: Chemical.* **2004**, 99, 451-458.

54. Fu, J., Tough responsive hydrogels and applications as smart devices. *Journal of Polymer Science Part B: Polymer Physics.* **2018**, 56, 1279-1280.

55. Mukhopadhyay, P.; Iwashita, Y.; Shirakawa, M.; Kawano, S.-i.; Fujita, N.; Shinkai, S., Spontaneous Colorimetric Sensing of the Positional Isomers of Dihydroxynaphthalene in a 1D Organogel Matrix. *Angewandte Chemie.* **2006**, 118, 1622-1625.

56. N.L. Smith, A. E. C., D.C. Wison, B. Ho, V.P. Gray, and S.A. Asher, Revolutionary Pure Protein Organogel Sensors and Biocatalytic Materials. *Applied Materials and Interfaces* **2019**, In Review.

57. Benito-Lopez, F.; Byrne, R.; Raduta, A. M.; Vrana, N. E.; McGuinness, G.; Diamond, D., Ionogel-based light-actuated valves for controlling liquid flow in micro-fluidic manifolds. *Lab on a Chip.* **2010**, 10, 195-201.

58. Gallagher, S.; Kavanagh, A.; Ziolkowski, B.; Florea, L.; MacFarlane, D. R.; Fraser, K.; Diamond, D., Ionic liquid modulation of swelling and LCST behavior of N-isopropylacrylamide polymer gels. *Physical Chemistry Chemical Physics.* **2014**, 16, 3610-3616.

59. Shigemitsu, H.; Hamachi, I., Design Strategies of Stimuli-Responsive Supramolecular Hydrogels Relying on Structural Analyses and Cell-Mimicking Approaches. *Accounts of Chemical Research.* **2017**, 50, 740-750.

60. Hirotsu, S.; Hirokawa, Y.; Tanaka, T., Volume-phase transitions of ionized N-isopropylacrylamide gels. *The Journal of Chemical Physics.* **1987**, 87, 1392-1395.

61. Hu, J.; Meng, H.; Li, G.; Ibekwe, S. I., A review of stimuli-responsive polymers for smart textile applications. *Smart Materials and Structures.* **2012**, 21, 053001.

62. Mano, J. F., Stimuli-Responsive Polymeric Systems for Biomedical Applications. *Advanced Engineering Materials.* **2008**, 10, 515-527.

63. White, E. M.; Yatvin, J.; Grubbs III, J. B.; Bilbrey, J. A.; Locklin, J., Advances in smart materials: Stimuli-responsive hydrogel thin films. *Journal of Polymer Science Part B: Polymer Physics.* **2013**, 51, 1084-1099.

64. Lee, K.; Asher, S. A., Photonic Crystal Chemical Sensors: pH and Ionic Strength. *Journal of the American Chemical Society.* **2000**, 122, 9534-9537.

65. Wu, C., A comparison between the `coil-to-globule' transition of linear chains and the "volume phase transition" of spherical microgels. Dedicated to the 80th birthday of Professor Renyuan Qian. *Polymer.* **1998**, 39, 4609-4619.

66. Flory, P. J., *Principles of Polymer Chemistry*. Cornell University Press: 1953.

67. Wu, S.; Li, H.; Chen, J. P.; Lam, K. Y., Modeling Investigation of Hydrogel Volume Transition. *Macromolecular Theory and Simulations.* **2004**, 13, 13-29.

68. Sperling, L., Introduction to Polymer Science. Molecular Weights and Sizes. The Crystalline State. *Introduction to Physical Polymer Science.* **1992**, 14-108.

69. Wang, R.; Wang, Z.-G., Theory of Polymer Chains in Poor Solvent: Single-Chain Structure, Solution Thermodynamics, and Θ Point. *Macromolecules.* **2014**, 47, 4094-4102.

70. Tanaka, T.; Fillmore, D.; Sun, S.-T.; Nishio, I.; Swislow, G.; Shah, A., Phase Transitions in Ionic Gels. *Physical Review Letters.* **1980**, 45, 1636-1639.

71. Ward Muscatello, M. M.; Stunja, L. E.; Asher, S. A., Polymerized Crystalline Colloidal Array Sensing of High Glucose Concentrations. *Analytical Chemistry.* **2009**, 81, 4978-4986.

2.0 Debye Ring Diffraction Elucidation of 2D Photonic Crystal Self-Assembly and Ordering at the Air-Water Interface

This chapter was previously published in the journal Physical Chemistry Chemical Physics as Smith, N. L.; Coukouma, A.; Dubnik, S.; Asher, S. A., *Physical Chemistry Chemical Physics* 2017, *19* (47), 31813-31822, and is reprinted with permission.

Author Contributions: N.L.S. collected 2DPC SEM images. N.L.S. fabricated samples, collected data, and analyzed data with assistance from A.E.C. The MATLAB program that calculated the 2D pair correlation function from SEM images of the 2DPC was written and run by A.E.C. The manuscript was prepared by N.L.S with assistance from S.A.A.

We fabricate 2D Photonic Crystals (2DPC) by spreading a dispersion of charged colloidal particles (diameters= 409, 570, and 915 nm) onto the surface of electrolyte solutions using a needle tip flow method. When the interparticle electrostatic interaction potential is large, particles self-assemble into highly ordered hexagonal close packed (hcp) monolayers. Ordered 2DPC efficiently forward diffract monochromatic light to produce a Debye ring on a screen parallel to the 2DPC. The diameter of the Debye ring is inversely proportional to the 2DPC particle spacing, while the Debye ring brightness and thickness depends on the 2DPC ordering. The Debye ring thickness increases as the 2DPC order decreases. The Debye ring ordering measurements of 2DPC attached to glass slides track measurements of the 2D pair correlation function order parameter calculated from SEM micrographs. The Debye ring method was used to investigate the 2DPC particle spacing, and ordering at the air-solution interface of NaCl

solutions, and for 2DPC arrays attached to glass slides. Surprisingly, the 2DPC ordering does not monotonically decrease as the salt concentration increases. This is because of chloride ion adsorption onto the anionic particle surfaces. This adsorption increases the particle surface charge and compensates for the decreased Debye length of the electric double layer when the NaCl concentration is below a critical value.

2.1 Introduction

2-Dimensional photonic crystals (2DPC) are two dimensional dielectric periodic materials that control the propagation of light.[71] 2DPC are commonly fabricated using colloidal nano- or mesoparticles with a significant dielectric constant difference from that of the surrounding media. When the particle diameter is on the same order as the wavelengths of light, the individual particles will Mie scatter the incident light. For a colloidal crystal like the a 2DPC, visible light is scattered from a periodic array of particles, causing interference of the scattered waves.[72-73] Constructive interference of the scattered waves from the periodic lattice results in Bragg diffraction, which is analogous to x-ray diffraction from ordered atomic and molecular crystal structures.[74-75] For 2D Bragg diffraction, white light is scattered by particles in a periodic monolayer such that each wavelength is diffracted at a particular angle.[7] The forward diffracted light through a 2DPC film diffracts as a rainbow. The Mie scattering cross sections are large. Thus, these 2DPC diffract nearly all incident light into the Debye ring.

These periodic, optical materials have numerous applications such as sensing[8, 44, 76], waveguiding[77-79], superhydrophobic and antifogging coatings.[80-82] Further, these periodic materials are useful for fabricating SERS substrates[83], for Localized Surface Plasmon Resonance

Spectroscopy substrates[84], and for particle lithography[85-87]. There is intense interest in the development of methods to fabricate large area, highly ordered 2DPC.[85, 88]

Nanoparticle 2D array self-assembly is the most commonly used technique to fabricate 2DPC. Alternatively, AFM nano-lithographic techniques offer a high level of precision for fabricating 2DPC structures with few defects.[89] Unfortunately, lithography is slow and limited to fabricating small areas. Self-assembly has the advantage of being less expensive than lithography; it can fabricate much larger areas in less time. Many methods have been developed to self-assemble nanoparticles into hexagonal close packed (hcp) ordered arrays, including the needle tip flow (NTF) method (which has recently been called micro-propulsive injection)[49, 77], spin coating[90], the Langmuir-Blodgett technique[85, 91-92], wet coating[93], floating[94-95], and evaporation induced self assembly[96-97].

Each of the self-assembly methods constrain interparticle interactions such that a hexagonal close packed structure is the minimum free energy.[98] The interactions that determine particle ordering differ between the different self-assembly techniques. For example, solvent-substrate and particle-substrate interactions that impact ordering in evaporation induced self-assembly methods[83, 99] do not significantly impact ordering for particles self-assembled at the air-water interface. The interparticle interactions are optimized for each different method to improve particle ordering to obtain large hcp crystal domains. Alternatively, post self-assembly methods to improve 2DPC order have also been investigated. Shinotsuka *et al*[85] utilized ultrasonic annealing, or repeated compression cycles after self-assembly at the air-water interface to increase the 2DPC order through Oswald ripening of the colloidal crystal domains.

In this work, we investigated the self-assembly of charged colloidal particles at the air-water interface using the needle tip flow method.[49, 100] Our objective was to control the 2DPC

ordering by decreasing the electrostatic repulsions between particles by the addition of NaCl to the water subphase. We monitored the 2DPC particle spacing and ordering by using Debye ring diffraction of visible light.

2.2 Experimental

2.2.1 Materials

Sodium 4-Vinylbenzenesulfonate, Ammonium Persulfate, 2,2`-Azobis(2-Methylpropionitrile), 1-Propanol, and 2-Hydroxyethyl Methacrylate were acquired from Sigma Aldrich (≥90% purity) and used as received. Styrene was acquired from Sigma Aldrich and purified by column chromatography. Methanol (>99.8%) and Sodium Chloride (>99.5%) were acquired from Fischer Scientific and used as received.

2.2.2 Polymerization and Characterization of Monodisperse Negatively Charged Polystyrene Nanoparticles

Negatively charged PS nanoparticles with diameters of 915 nm were synthesized by dispersion polymerization using a procedure described by Zhang et al.[101] Negatively charged polystyrene nanoparticles with diameters of 570 nm and 409 nm were synthesized by emulsifier free emulsion polymerization using a procedure described by Reese et al.[102]

The weight percent of each PS particle dispersion was calculated by dividing the weight of dried particles by the original weight of the dispersion. The average particle diameter was

determined by measuring the diameter of >150 particles in SEM micrographs using the National Institute of Health program, ImageJ. SEM micrographs of 2DPC were obtained using a JEOL 6390LV Scanning Electron Microscope.

PS water dispersions were cleaned by centrifuging the particles into a pellet (10,000 RPM for 10 min) then redispersing them in nanopure water at least three times before use. The final volume of water added to the PS particle pellet was adjusted so that the final concentration is 15 wt% PS particles in water. The zeta-potentials of the PS particles in nanopure water, or in 0.001, 0.01, 0.1 or 1 M NaCl solutions were measured on a Brookhaven Zeta-PALS instrument.

2.2.3 2DPC Fabrication Using Needle Tip Flow Method

We fabricated the 2DPC by self-assembling charged colloidal nanoparticles on a water surface using our Needle Tip Flow (NTF) method[49] as shown in Figure 2.1. The 15 wt% PS nanoparticle aqueous dispersion is mixed with propanol to lower the particle dispersion surface tension. The NTF flow method utilizes the Marangoni effect, which drives the PS particles to spread on the water surface due to surface tension gradients. The Marangoni flow guides the particles towards areas with higher surface tension, this directs particles towards the dish outer edge. Therefore, particles radially spread outwards from the needle tip to the edge of the water surface as shown in Figure 2.1, part 3. The video provided in Appendix A demonstrates that the particles initially spread to cover the outer water surface at the edge of the dish.

A 21-gauge needle is attached to a 1 mL plastic syringe containing ~0.6 mL of a 3:1 PS particle dispersion: propanol mixture. A 9 cm diameter, 6 cm deep glass crystallization dish is filled with nanopure water, or aqueous salt solutions containing 0.001, 0.01, 0.1 or 1 M NaCl. The vertically oriented needle pierces the water surface such that half of the needle tip beveled

orifice bisects the water meniscus. The particle dispersion flow rate is controlled by the pressure applied to the 1 mL syringe plunger. The particle dispersion that is layered on the water surface spreads onto the water surface until the surface becomes completely covered with particles. Once the water surface is filled with the particle monolayer, the particle dispersion will begin to disperse into the bulk water instead of spreading on the surface. The circular boundary of the self-assembled 2DPC along the outer edge of the water surface is easily observed as shown in Figure 2.1, part 3. The visually evident 2DPC boundary is monitored during particle deposition to determine the point when the water surface is filled with particles. The particle dispersion flowing onto the water surface is then stopped.

Optical microscopy was used to obtain images of a 2DPC made from 915 nm particles at the air-water interface. A Leica TCS SP5 confocal laser scanning microscope with a Leica HCX-PL APO 40x/0.85 objective was used to collect images in transmission mode, and the scan rate was 100 Hz.

The 2DPC is lifted from the water surface with a glass microscope slide (Figure 2.1, part 4). The slide is vertically inserted into the water. The plane of the slide is then rotated to be parallel with the water surface while the slide lifts the self-assembled 2DPC from the water surface. The slide is placed on a flat surface and allowed to dry at room temperature. After drying, the 2DPC adheres to the microscope slide surface. 2DPC were fabricated using 409, 570, and 915nm diameter PS particles. The particles were self-assembled on nanopure water surfaces, and on aqueous salt solutions containing 0.001, 0.01, 0.1, and 1M NaCl. Ten replicate samples were fabricated for each set of particles and salt solutions.

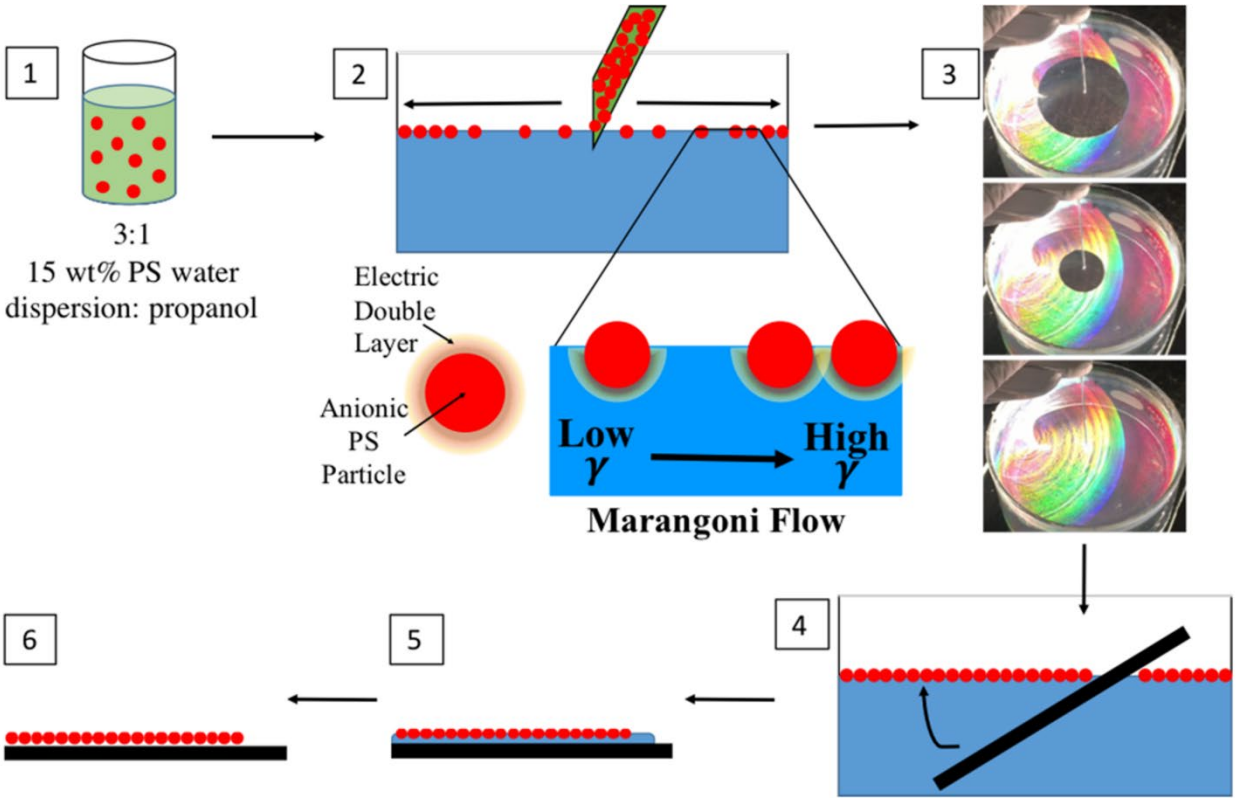

Figure 2.1 - Schematic of needle tip flow 2DPC fabrication at the air-water interface. 1) Addition of propanol lowers the surface tension of the particle dispersion. 2) The dispersion is spread on the water surface through a needle tip at a constant rate. The surface tension gradient forces the particles to the outer edge of the water surface. 3) Appendix A contains a link to a video showing 2DPC self-assembly on the water surface. The boundary between the self-assembled 2DPC and the particle-free pure water surface is visually evident. The radius of this boundary decreases as more particles are spread onto the surface. 4) The 2DPC is lifted from the water surface by a microscope slide. 5) The wet slide with the lifted 2DPC is dried at room temperature. 6) After the water evaporation, the particles on the slide surface adhere to the microscope slide.

2.2.4 2DPC Debye Ring Diffraction Measurements

The ordered 2DPC efficiently forward diffract light. In the case of a perfectly ordered 2DPC monochromatic light will be diffracted onto a screen parallel to the 2DPC monolayer as a hexagonal array of spots. These six spots correspond to the six reciprocal lattice vectors of the 2D close packed hexagonal particle array.

If the self-assembled 2DPC consists of small crystallites that are rotationally disordered, the diffraction of normal incident monochromatic light will form a continuous ring, called the Debye ring, shown in Figure 2.2B. We measured the Debye ring diameter to calculate the 2DPC particle spacing. We can utilize the Debye ring thickness to monitor the 2DPC order, provided that the width of the Debye ring is limited by disorder and not by the laser beam spot size.

For example, Figure 2.2A shows the diffraction geometry used for measuring the Debye ring with a 406 nm violet laser diode (Thor Labs, 2.2 mm diameter spot size). The normally incident monochromatic light is forward diffracted at an angle, θ onto a screen parallel to the 2DPC plane. The diameter of the Debye ring projected onto the screen depends on both the 2DPC particle spacing, a and the distance, h between the 2DPC and the screen.

The Debye rings were measured at five different locations on each 2DPC attached to the glass slide. The difference between the outer and inner Debye ring diameters are the widths of the Debye rings. The average of the inner and outer diameters, d, gives us the Debye ring diffraction angle,θ (Equation 2.1), and the particle spacing, a (Equation 2.2)[13, 76].

$$\textbf{Equation 2.1} \quad \theta = tan^{-1}\frac{d}{2h}$$

$$\textbf{Equation 2.2} \quad sin\theta = \frac{2\lambda}{\sqrt{3}a}$$

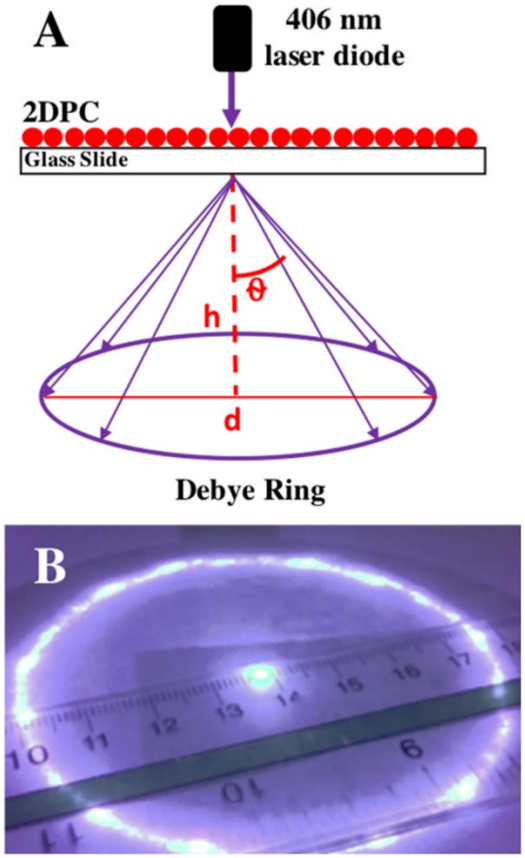

Figure 2.2 - (A) Illustration showing the angles of diffraction for 406 nm light travelling through water, θ_w, and air, θ_a. The distance the light travels in each medium, h_w and h_a determines the final Debye ring diameter. (B) Photograph of the Debye ring.

The Debye ring diffraction was also measured for a 915 nm 2DPC on the water surface. The measurements were repeated at least three times for the 2DPC on a nanopure water surface, and on 0.01 M, and 0.1 M NaCl solutions. The Debye rings were also measured for the 2DPC on the surface of the microscope slide directly after the 2DPC was lifted off the water surface.

As shown in Figure 2.3 the diffraction of the 2DPC lying on the water surface is shifted due to refraction of the light by the air-water interfaces. The Debye ring diameter of a 2DPC on the water surface will be smaller than that from an identical 2DPC on a glass slide.

The diffraction angle in air, θ_a can be calculated from Debye ring diffraction measurements of a 2DPC on a water surface using Equation 2.3, which details the impact of Snell's Law, $\theta_w=\sin^{-1}((n_a \sin\theta_a)/n_w)$. The thickness and refractive index of water and air layers are h_w, n_w, and h_a, n_a respectively.

Equation 2.3 $$\frac{d}{2} = h_w \tan\left(\sin^{-1}\left((n_a \sin\theta_a)/n_w\right)\right) + h_a \tan\theta_a$$

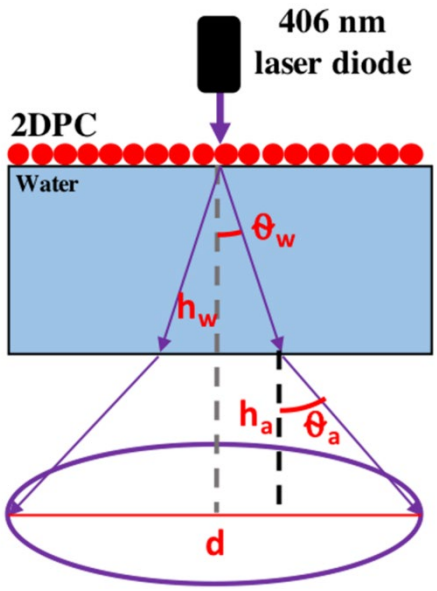

Figure 2.3 - Cartoon showing the angles of diffraction for 406 nm light travelling through water, θ_w, and air, θ_a. The distance the light travels in each medium, h_w and h_a determines the final Debye ring diameter.

2.2.5 2DPC Ordering Analysis

We examined the ordering of three 2DPC samples for each set of experimental conditions. We sputter coated the 2DPC on glass slides with gold for 90 sec (30 mA current) using a PELCO SC-7 sputter coater. The gold coated 2DPC were imaged using a scanning electron microscope (JEOL 6390LV SEM). Five SEM micrographs were collected from

different areas of each 2DPC sample. Representative SEM images for each particle diameter and salt concentration are provided in Appendix A. These 2DPC images were used to calculate the 2D pair correlation function, g(r) (Equation 2.4).[49, 103-104] The pair correlation function calculates the number of particles (dn) within the area (da) of a ring having an inner diameter (r) and outer diameter (r+dr). g(r) was calculated for shell radii ranging from 0 to 14, where dr was $0.016R_0$. R_o is the particle radius.

Equation 2.4 $$g(r) = \frac{1}{\langle p \rangle} \frac{dn(r,r+dr)}{da(r,r+dr)}$$

A detailed description of our 2DPC ordering analysis and the MATLAB code written to calculate the 2D pair correlation function can be found in Appendix A. Briefly, the MATLAB circle finding algorithm, imfindcircles, was used to find the centers of the particles in each SEM micrograph. This function creates a matrix of the particle positions from which the pair correlation function can be calculated. A discrete Fast Fourier Transform (FFT) was then calculated for the function g(r)-1. The dimensionless order parameter (κ/κ_o) is calculated as the ratio of the FWHM of the FFT peak for a fabricated 2DPC, κ and the FWHM of the FFT peak for a perfect array, κ_o.[49] The average order parameter was calculated using data from at least 15 SEM micrographs for each experimental condition.

2.3 Results and Discussion

2.3.1 Needle Tip Flow Nanoparticle Self-Assembly at the Air-Water Interface

The Needle Tip Flow (NTF) method for self-assembling charged nanoparticles at the air-water interface produces highly ordered 2DPC, with large crystalline domains (~100 μm^2).[23, 34] The 2DPC can be fabricated on large area water surfaces (730 cm^2 for a single needle tip) in ~2 min using the NTF method (Figure 2.1). Gao et al[10] fabricated very large area (~1m^2) 2DPC using a micro-propulsive injection method, which is analogous to our NTF method. They were able to quickly fabricate very large areas of 2DPC at the air-water interface because the particle dispersion was spread on the water surface at multiple injection points using syringe pumps.

The NTF flow method, described in previous papers[10, 23, 34, 40, 41] utilizes Marangoni flow that spreads the PS particle dispersion on the water surface. The Marangoni flow results from surface tension gradients that generate surface fluid motion such that lower surface tension liquid regions are pulled towards regions of high surface tension. The 15 wt% PS nanoparticle aqueous dispersion contains propanol to lower its surface tension. The resulting Marangoni flow spreads the particle dispersion radially outwards from the needle tip to the edge of the water surface (Figure 2.1, part 3). As shown by the video in Appendix A the particles spread as a monolayer onto the surface until the entire water surface is covered.

The ordering of the self-assembled 2DPC depends on the rate of spreading and upon the detailed balance between attractive and repulsive particle interactions in the 2DPC film. Adding NaCl to the water subphase should decrease the electrostatic repulsions between these negatively charged particles.

This can be clearly shown by qualitatively viewing the 2DPC ordering in SEM micrographs as shown in Figure 2.4 1a-1c. 2DPC fabricated on higher concentration salt solutions are clearly less ordered. We can quantitatively determine the 2DPC order by calculating the 2D pair correlation function, g(r), from these SEM micrographs.

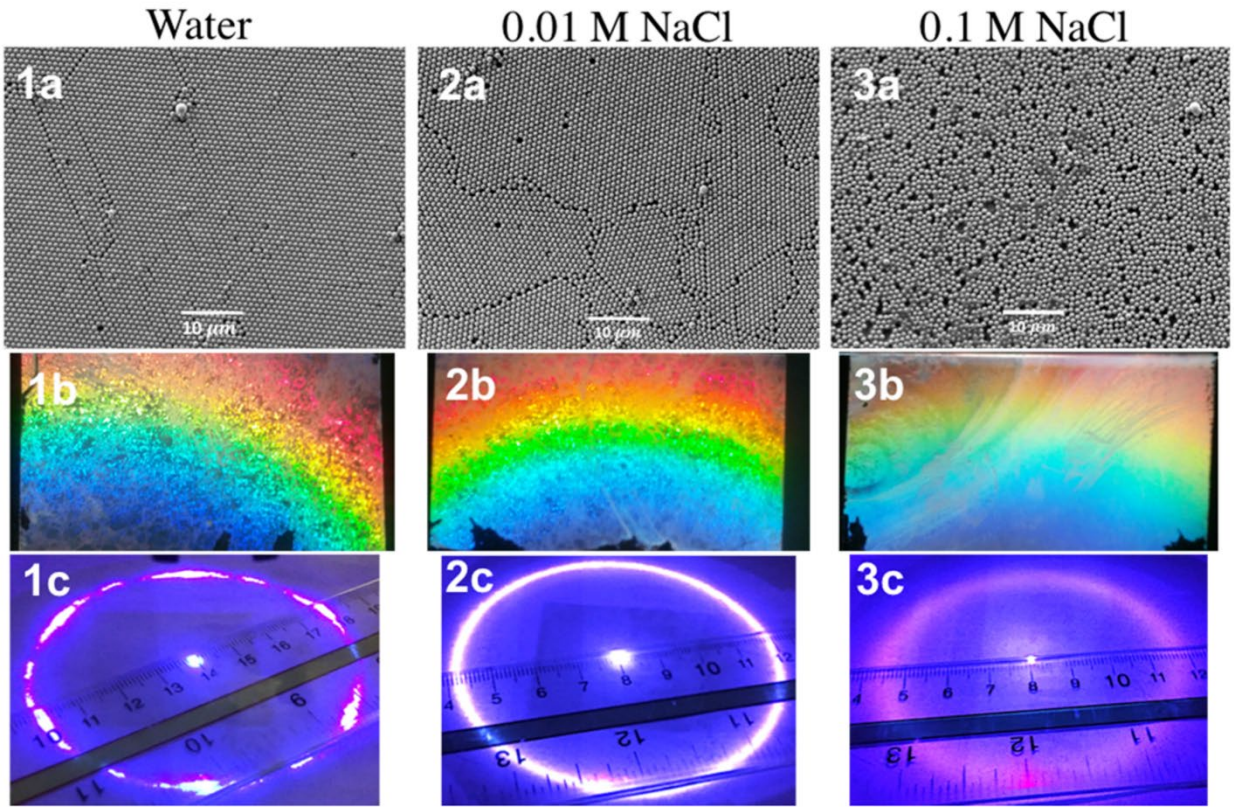

Figure 2.4 -SEM micrographs (1a - 3a) of 2DPC of 915 nm PS particles prepared on solutions of increasing salt concentrations (pure water, 0.01 M NaCl and 0.1 M NaCl). (1b - 3b) Photographs of polychromatic light diffraction of 2DPC prepared on solutions of increasing salt concentrations. The diffraction polychromatic dispersion becomes more diffuse and less intense at larger salt concentrations. (1c - 3c) Photographs of Debye ring diffraction of normally incident 405 nm monochromatic light at increasing salt concentrations. Debye ring diffraction photograph of the 2DPC at 0.1 M NaCl was edited with regards to brightness/contrast and color balance so that the Debye ring could be easily be observed. This diffuse Debye ring is very hard to photograph due to the weak diffraction intensity.

Alternatively, we can quantitatively determine the 2DPC ordering without perturbing the sample by monitoring the Debye ring diffraction. Samples probed using the Debye ring diffraction method can be used in future experiments, unlike samples that are sputtered with gold prior to SEM.

2.3.2 Estimating 2DPC Order from Debye Ring Measurements

Most of the light incident on the 2DPC is diffracted into the Debye ring.[42] Unlike for the case of 3D Bragg diffraction, 2DPC planes forward diffract polychromatic light such that each wavelength diffracts at a discrete angle, θ as shown in Figure 2.4 1b-3b according to the 2D Bragg diffraction condition (Equation 2.5) for a 2DPC particle array with spacing, a.

$$\textbf{Equation 2.5} \quad \boldsymbol{\lambda = \frac{\sqrt{3}a}{2}(sin\,\alpha + sin\,\theta)}$$

For normally incident monochromatic light to the 2DPC plane, as shown in Figure 2.2, sinα = 0, and Equation 2.5 becomes Equation 2.2. Thus, the light is forward diffracted at an angle, θ that depends on the particle spacing, a, of the 2DPC array and the detailed 2DPC particle ordering. If a single 2DPC domain is irradiated, six spots are diffracted onto the screen (Figure 2.4 1c). These six spots correspond to the six reciprocal lattice vectors of the 2D hcp particle array. The fabricated 2DPC studied here often show a distribution of randomly oriented 2D crystallites. Simultaneous irradiation of numerous crystalline 2DPC domains give rise to diffraction of a continuous Debye ring (Figure 2.4 2c-3c). The diameter of the Debye ring, determined by the diffraction angle θ, is inversely proportional to the 2DPC particle spacing, a.

Figure 2.4 illustrates the impact of 2DPC disorder on the diffraction. The decreasing 2DPC ordering of the particle array self-assembled on water, 0.01 M NaCl, and 0.1 M NaCl is

evident in the SEM micrographs in Figure 2.4 a1-a3. As the 2DPC order decreases, the forward diffracted white light intensity decreases (Figure 2.4 1b-3b), while the Debye ring thickness increases (Figure 2.4 1c-3c). The Debye ring width (w), can be used to monitor the 2DPC order and particle spacing on the glass slides, as well as, at the air-water interface, without perturbing the 2DPC.

The disordered 2DPC Debye rings will be broader than Debye rings from highly ordered 2DPC. The disordered 2DPC Debye ring broadening results from variations of particle spacing within the probed areas as shown in Figure 2.5. We are assuming the broadening contribution from the finite crystallite size is negligible compared to the laser beam spot size.

The hexagonal close packed (hcp) crystal shows the smallest plane spacing possible. This plane spacing will diffract light into the maximum diffraction angle for this particle diameter. The Debye ring width of a perfectly ordered close packed 2DPC is only limited by the incident laser spot size. Less ordered crystals will diffract light into smaller diffraction angles. The sum of these contributions broadens the Debye ring. The outer Debye ring diameter does not change because it is fixed at the minimum particle spacing of the 2DPC lattice. In contrast the Debye ring inner diameter will shrink with increasing disorder as the average particle spacing increases. In general, the standard deviations of the Debye ring measurements increase as the 2DPC disorder increases, because the particle spacing is more heterogeneous.

The Debye ring width and calculated particle spacing change of the 2DPC adhered to glass slides are shown in Figure 2.6 and Figure 2.7, respectively for 570 nm and 915 nm diameter particle arrays fabricated on water and on NaCl solutions. The particle spacings were calculated using Equation 2.1 and Equation 2.2. The average of the inner and outer Debye ring diameter was used to calculate the average particle spacing.

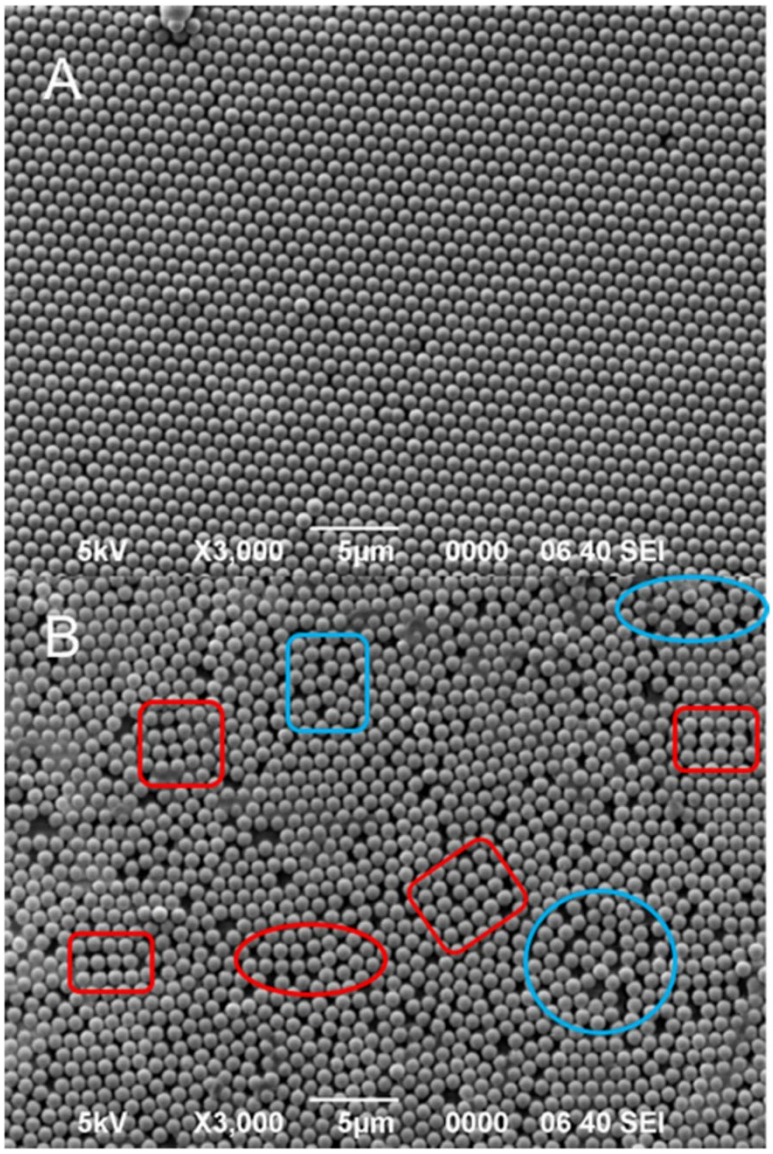

Figure 2.5 - SEM images of 915 nm particle 2DPC (A) self-assembled on pure water and (B) on 0.1 M NaCl. (A) shows a well ordered 2DPC where the particle spacings show little variation. (B) shows a highly disordered 2DPC. The areas outlined in red are where the particle arrays assembled into a square lattice instead of a hexagonal lattice. Areas highlighted in blue show regions that are randomly oriented with little crystalline order.

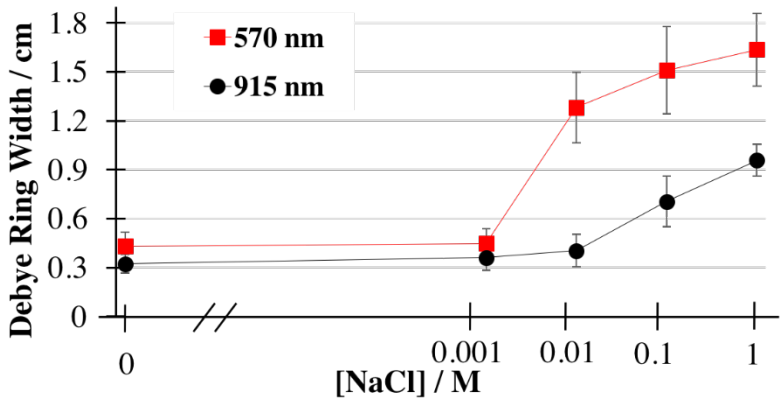

Figure 2.6 - Dependence of Debye ring widths of 570 nm and 915 nm 2DPC as a function of the NaCl concentration.

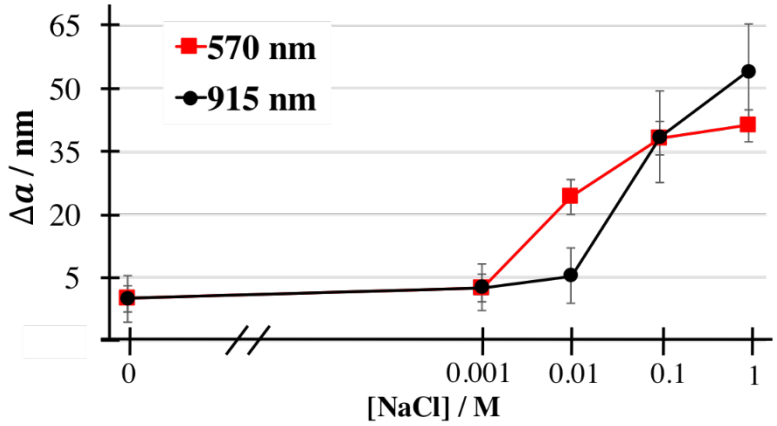

Figure 2.7 - Particle spacing change, $\Delta a = a_{[NaCl]} - a_{water}$, for 570 and 915 nm 2DPC as a function of NaCl concentration. Particle Spacing is calculated from the Debye ring diameter measurements.

The average salt induced particle spacing change is the difference between the particle spacing of the 2DPC fabricated on a salt solution and the particle spacing of the 2DPC fabricated on pure water, $\Delta a = a_{[NaCl]} - a_{water}$. The increasing particle spacing change results from the decreased inner diameter of the Debye ring.

We expect the Debye ring width to monotonically increase with NaCl concentration. The 2DPC ordering is determined by the balance of attractive and repulsive interactions between particles at the air-water interface.[21] The addition of salt to the water subphase should monotonically decease the electrostatic repulsions between particles. This leads to "faster" assembly of particle arrays because the probability of particle adhesion between colliding particles increases, leading to disordered particle aggregates that can serve as nucleation sites for crystal growth. The formation of randomly ordered particle clusters prevent 2D array annealing, where particles repel each other and arrange into a structure that minimizes the total energy of the system.

In contrast, our results indicate the 2DPC order is relatively unaffected by low concentrations of salt in the water subphase. The Debye ring width that is indicative of the 2DPC order, at low NaCl concentrations does not significantly differ from that of 2DPC fabricated in pure water. We find that there is a critical salt concentration, C* of NaCl required to induce significant disorder. This critical salt concentration depends on the particle diameter, C*≈ 0.01 M NaCl for the 570 nm diameter particle 2DPC, while C*≈ 0.1 M NaCl for the 915 nm particle 2DPC.

We examined the salt concentration dependence of the order parameter, κ/κ_o from our measured 2D pair correlation function, g(r) (Equation 2.4) from SEM micrographs of the same samples used for our salt concentration Debye ring width measurements. We also studied 409

nm diameter particles to examine the dependence of the 2DPC ordering on the particle diameter. The salt concentration dependence on the order parameter, κ/κ_o of the fabricated 2DPC, determined from the FFT of (g(r)-1), is shown in Figure 2.8. The threshold for disorder occurs when κ/κ_o >1.5.

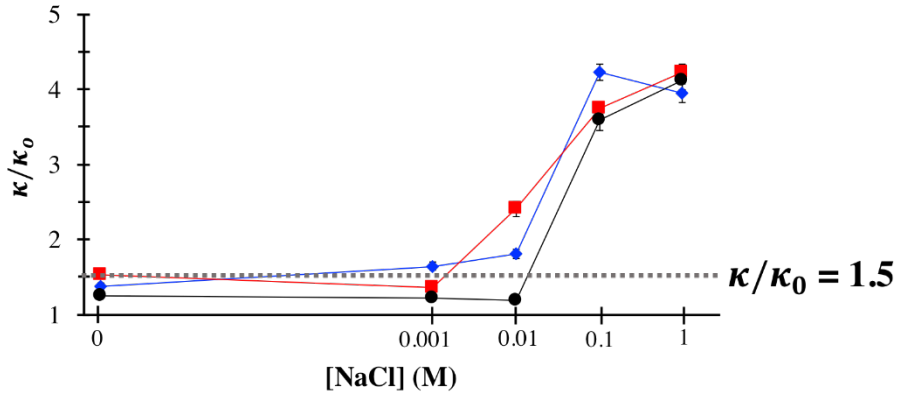

Figure 2.8 - Dependence of the 2DPC order parameter, κ/κ_o on salt concentration for 409, 570 and 915 nm particle diameters. The horizontal line indicates κ/κ_o= 1.5, above which disorder is present. Error bars indicate 95% confidence intervals.

The 2DPC order estimated from measurements of Debye ring width appears consistent with the detection of disorder from κ/κ_o calculated from SEM micrographs. The order parameter results confirm that 2DPC order does not significantly decrease until the salt concentration exceeds the critical salt concentration. Analogous to the Debye ring width results, C* increases with an increasing particle diameter. The salt concentration at which κ/κ_o>1.5 is 0.001 M NaCl for 409 nm diameter particles, 0.01 M for 570 nm particles, and 0.1 M NaCl for 915 nm particles. This dependence of the 2DPC ordering on the particle diameter and salt concentration is discussed below.

These results clearly indicate that the Debye ring width can be used to monitor the 2DPC order. This Debye ring width dependence is important because it enables non-destructive 2DPC order determinations of fragile systems such as the 2DPC at the air-water (or oil-water) interface.

2.3.3 2DPC Ordering and Particle Spacing at the Air-Water Interface

Three decades ago, Pieranski[43] showed that charged colloidal particles trapped at the air-water interface would self-assemble into ordered particle monolayers. Since then numerous additional methods were developed to fabricate close packed and non-close packed ordered particle monolayers, and to transfer them onto solid substrates.[3, 21, 44, 45] Each new method developed tuned the interparticle interactions to optimize the array ordering. Often, the ordering was monitored by determining the pair correlation function of images collected using Electron Microscopy[23, 45, 46] or AFM[3]. Any conclusions drawn from these SEM images must account for 2DPC disorder and particle spacing changes induced by transfer of the 2DPC from the air-water interface to the substrate and the impact of drying.

Optical microscopy has been used to investigate the particle array ordering at the air-water interface.[31, 43, 47] Confocal laser scanning microscopy is a powerful tool to investigate interfacial particle ordering, but the experiments require expensive optics and objectives. Confocal microscopy measurements are also complicated by motion of the air-water interface. In contrast, the Debye ring diffraction measurements allow us to easily probe the 2DPC ordering and particle spacing at the air-water interface using a laser pointer and a ruler or calliper.

The 2DPC particle spacing at the air-water interface is calculated from the Debye ring diameter using Equation 2.2 and Equation 2.3. We also compared the spacings of the 2DPC transferred from these interfaces to wet and dry microscope slides. The post-transfer

measurements were taken prior to evaporation of the thin water film on the microscope slide surface, where the particles are still trapped at this air-water interface. The Debye ring was also measured after slide water evaporation, where the 2DPC adheres to the slide. Figure 2.9 shows the salt concentration dependence for the Debye ring width of the 915 nm diameter 2DPC at the air-water interface of pure water, 0.01 M NaCl, and 0.1 M NaCl. The calculated particle spacings of these 2DPC samples are shown in Figure 2.10.

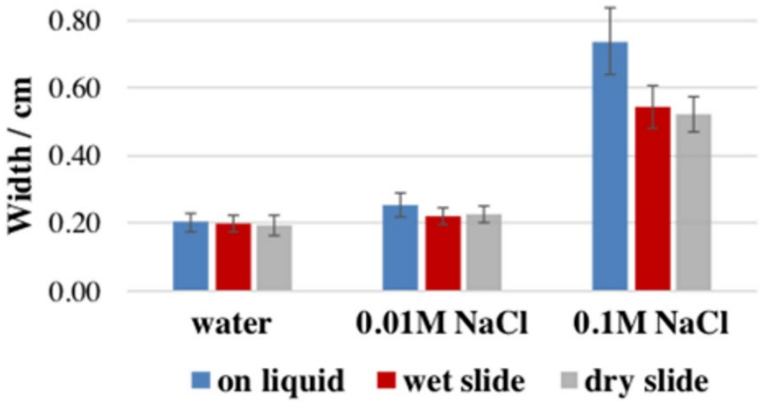

Figure 2.9 - Debye ring width, w of 915 nm diameter particle 2DPC at different stages of fabrication. 2DPC were fabricated by self-assembly of 915 nm PS particles on pure water, 0.01 M NaCl and 0.1 M NaCl. Error bars represent one std. dev.

With the exception of the 0.1 M NaCl samples, the Debye ring widths are the same for the 2DPC at the air-water interface, on the wet slide, and when dried on the slide, indicating that the 2DPC transfer to the slide, and drying has little impact on the array ordering. The Debye ring width of the 2DPC at the air-water interface of the 0.1 M NaCl samples may be slightly larger than the Debye ring width after transfer to the slide.

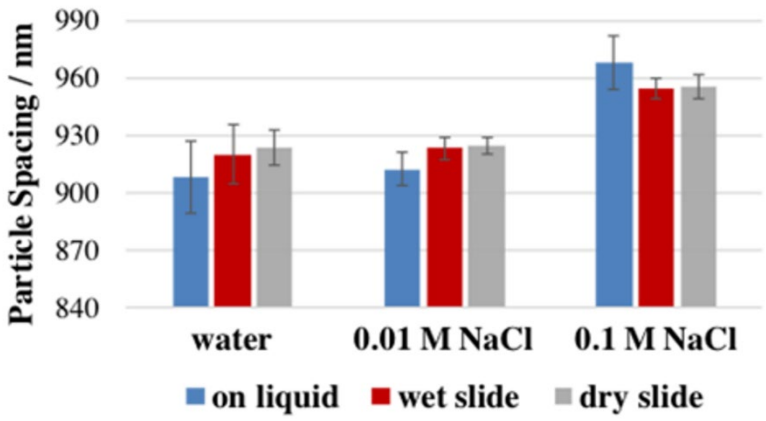

Figure 2.10 - Dependence of 2DPC particle spacings for 915 nm diameter particle 2DPC at different stages of fabrication. The Debye ring was measured for a 2DPC at the air-water interface of the crystallization dish (on liquid), at the air-water interface after the 2DPC and a thin water layer are transferred to a slide (wet slide), and after the 2DPC is dried on the slide (dry slide). 2DPC were fabricated by self-assembly of 915 nm PS particles on pure water, and in the presence of 0.01M NaCl and 0.1M NaCl. Error bars represent one standard deviation.

At 0.1 M NaCl concentrations, the particles spread from the needle tip increasingly disperse into the bulk water, increasing the turbidity of the water subphase. This turbidity partially obscures the diffuse Debye ring and makes it more difficult to measure its width. However, it is clear that the Debye ring widths of the 0.1 M NaCl samples are at least 2X greater than the widths of the 2DPC samples fabricated at lower salt concentrations.

The 2DPC particle spacing, a does not significantly change upon 2DPC transfer to the slide and the subsequent 2DPC drying. The 2DPC particle spacing at the air-water interface is very close to that found for the 2DPC on the wet and dried glass slides; these calculated particle spacings are roughly equal to the particle diameter when the 2DPC is well ordered. Thus, the NTF method produces self-assembled, highly ordered, hexagonal close packed (hcp) particle array monolayers at the air-water interface. These results are confirmed by confocal microscope

imaging of the 915 nm 2DPC at the air-water interface, shown in Figure 2.11. These results are significant because it shows that highly ordered close-packed 2DPC can be straight-forwardly fabricated at the air-water interface and transferred to substrates without disrupting 2DPC ordering or particle spacing.

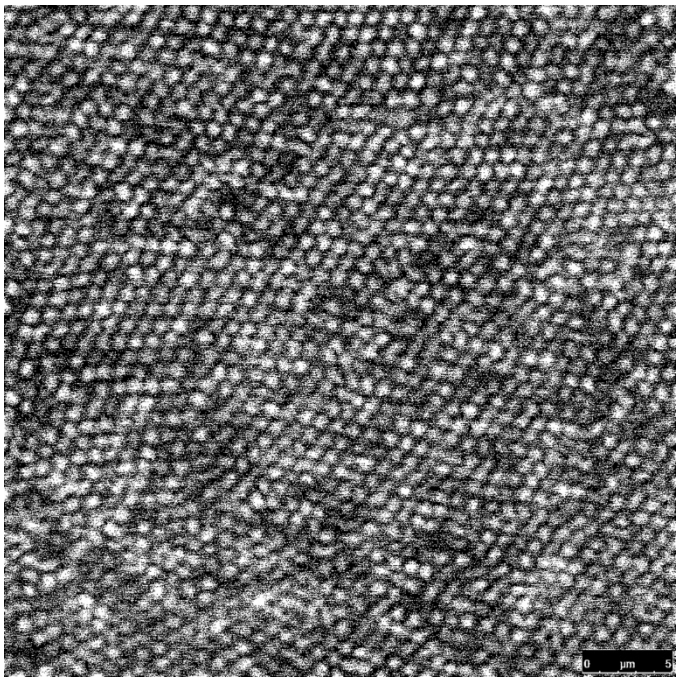

Figure 2.11 - Confocal microscope image of 915 nm particles at the air-water interface fabricated using the NTF method. The levels, thresholds, and sharpness in the image were edited using GIMP software so that the particles are clearly visible.

It was recently proposed for the analogous micro-propulsive injection method[10] and other methods[21, 48] that capillary attractive interactions between particles during water evaporation play a significant role in formation of the close packed structure. We believe we have shown that for the NTF method immersion capillary forces described by Kralchevsky and Nagayama[48] do not play a significant role in the formation of the close packed structure. The close packed particle array structure is present at the interface.

In a Langmuir-Blodgett trough, close packed hexagonal arrays are formed by compressing the monolayer to the close packed particle spacing after the particles are spread on the water surface.[49] This requires large amounts of sample and instrumentation that controls barrier movement and monitors the surface pressure. The NTF method is an improvement on the commonly used Langmuir-Blodgett method because it is faster, eliminates expensive instrumentation, avoids compression of the monolayer, and uses less sample.

2.3.4 Electrostatic Interactions of Charged Particles at the Air-Water Interface

The electrostatic interactions of charged colloidal particles at the air-water interface are different than the interactions of charged colloidal particles dispersed in solution. Interfacial particles are partially exposed to water so that only the charged groups on the water exposed particle surface can dissociate.[50, 51] The asymmetric ion cloud of the particle creates a dipole moment normal to the air-water interface.[19, 52] Thus, the electrostatic repulsive interaction potential, ψ_{ES} (Equation 2.6) of charged interfacial particles has contributions from the screened-Coulomb repulsions (first term of Equation 2.6) and dipole-dipole repulsions (second term of Equation 2.6).[53, 54] The term s is the distance between particle surfaces, q is the particle charge, $\mathcal{L}_D$ is the Debye screening length, and ε is the average of the air and water dielectric constants.

$$\textbf{Equation 2.6} \quad \psi_{ES} = \frac{2q^2e^2}{s\varepsilon(\varepsilon^2-1)} exp^{-s/\mathcal{L}_D} + 2\left(\frac{q\mathcal{L}_D}{\varepsilon}\right)^2 s^{-3}$$

The screened-Coulomb repulsions decay rapidly with distance away from the particle. This short-range interaction dominates ψ_{ES} when the separation between particles is small. The dipole-dipole repulsions are long range interactions that dominate the potential when distances between particles are large.[53] These long-range repulsive forces have been experimentally

observed,[43, 55] theoretically derived,[53] and modeled[56] for charged particles at the air-water or air-oil interface. If the particles are not constrained to a small finite surface area, the dipole-dipole repulsions will create hexagonal particle arrays with spacings larger than the particle diameter.[55]

The electrostatic interaction potential between particles decreases exponentially with distance between particles. The decay rate of the electrostatic interactions increases at higher salt concentrations. The particle surface charges electrostatically interact with ions in solution creating the electric double layer in the electrolyte solution surrounding the particle. Increasing the ion concentration in solution more effectively screens the electrostatic repulsive forces between the ionic interfacial particles and their electric double layers. The electric double layer thickness is roughly given by the Debye length, Equation 2.7, for a 1:1 electrolyte.[57-59] The double layer thickness decreases with increasing salt concentration.

$$\textbf{Equation 2.7} \quad \mathcal{L}_D(nm) = \left((2000e^2 N_A[NaCl])/(\varepsilon_o \varepsilon_w kT)\right)^{1/2}$$

The Debye length of charged particles in electrolyte solutions decreases monotonically with increasing salt concentration. $\mathcal{L}_D$ is 966 nm for particles in pure water (assuming an ion concentration of 10^{-7} M), 9.7 nm in 0.001 M NaCl, 3.1 nm in 0.01 M NaCl, 0.97 nm in 0.1 M NaCl, and 0.31 nm in 1 M NaCl. Accordingly, it is expected that the electrostatic repulsive interaction potential will monotonically decrease as salt concentration increases, which should have negative consequences on 2DPC ordering. Despite the seemingly straight forward relationship between salt concentration and the Debye screening length, both the Debye ring measurements and order parameter calculations show that 2DPC close packed self-assembly and ordering is not impeded by low salt concentrations using the NTF method. In contrast, at NaCl concentrations exceeding 0.01 M NaCl there is a dramatically increased disorder, indicating there is a mechanism counter-balancing the decrease in ψ_{ES} caused by decreasing $\mathcal{L}_D$.

2.3.5 Mechanism of Self-Assembly for Close Packed Particle Arrays at the Air-Water Interface

The charged particles dispersed in a water/propanol mixture flow onto the air-water interface from the needle tip due to the large surface tension gradient between the particle dispersion and the water surface.[23, 34, 60] The interfacial particles are transported via Marangoni flow across the water surface towards interfacial areas with the highest surface tension. Marangoni flow induces the in-plane packing of the particles against the walls of the circular crystallization dish. The particles fill the water surface moving inward from the walls of the dish. This packing force thrusts the particles together so that particles order into a close packed hexagonal array.

The packing force is counter-balanced by the strong electrostatic repulsions that prevent interparticle adhesion and aggregation of random clusters. The electrostatic repulsive interactions between highly charged particles on a pure water surface are larger than the combined attractive Van der Waals interactions and the packing force. The interparticle surface spacings of 2DPC fabricated by the NTF method are small, therefore the screened-Coulomb repulsions are the dominant electrostatic force driving self-assembly of ordered 2DPC.

The particle mobility gained from the strong electrostatic repulsions give the individual particles time to anneal. Here the term anneal is used to describe the process where individual particles are capable of jiggling around each other on the crowded air-water interface to form the ordered hexagonal 2D particle array with a minimum energy structure.

At low and modest salt concentrations, the particles do not contact one another. The separated particles have a thin water layer between them which lubricates the particle annealing process, to form 2D colloidal crystals. At higher salt concentrations, the electrostatic repulsive

interactions are weak and particles approach one another more closely. This increases the probability of interparticle adhesion caused by Van der Waals forces where they collapse into their primary minimum, or they suffer polymer entanglements that could also lead to particle sticking. This stabilizes disorder by slowing or preventing annealing. Disordered 2D arrays form with increased average interparticle spacing and larger Debye ring widths (Figure 2.6 and Figure 2.7). This disorder stems from the aggregation of randomly ordered particle clusters.

The unexpected behaviour of the 2DPC ordering as the ionic strength increases appears to result from adsorption of Cl^- onto the polystyrene particles as is independently shown by the salt concentration dependence of the Zeta potential, ξ shown in Figure 2.12. Chloride anions have been previously shown to adsorb to anionic polystyrene surfaces, increasing the electrophoretic mobility of the particles up to a critical salt concentration.[61, 62] Increasing the salt concentration further, decreases the electrophoretic mobility due to the collapse of the electric double layer in the high ionic strength solution.

The increase in ξ (more negative) for anionic polystyrene colloids at low concentrations of NaCl salt results from chloride adsorption.[61, 62] ξ reaches a minimum at a NaCl concentration that is consistent with the critical salt concentration, C* determined from the ordering results. At larger salt concentrations, ξ decreases sharply (less negative) due to compression of the diffuse electric double layer and counter-ion screening. The critical salt concentration, C* at which this transition occurs is dependent on particle diameter. Again, we find the same C* for a certain particle diameter in the Zeta-potential data as in the Debye ring diffraction and order parameter results.

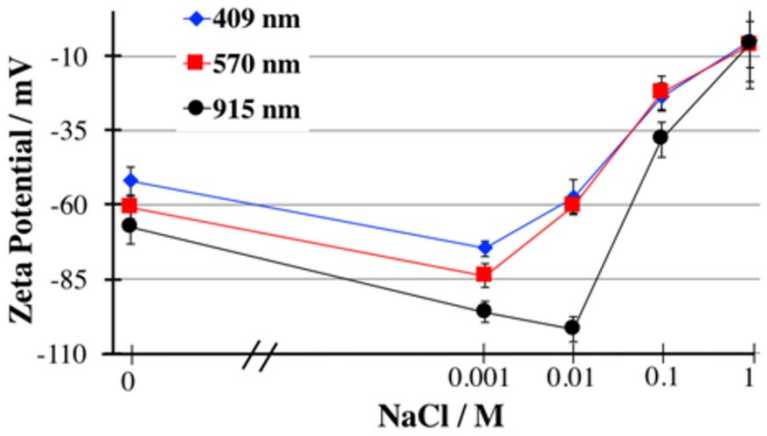

Figure 2.12 - Zeta-potentials (mV) for 409, 570, and 915 nm diameter anionic polystyrene particles in solutions as a function of NaCl concentration. Error bars indicate one standard deviation.

The similarity between the zeta potential, Debye ring measurement, and calculated order parameter results suggests adsorption of Chloride ions onto the polystyrene surface increases the particle anionic surface charge significantly and counteracts the decreasing $\mathcal{L}_D$. Chloride ions adsorbed to the polystyrene surface act as potential determining ions to increase interparticle electrostatic repulsions; this results in better annealing and therefore better ordering of the self-assembled 2DPC.

2.4 Conclusions

We have shown that utilization of Debye ring measurements is a viable method for monitoring 2DPC ordering for colloidal particle arrays having diameters roughly the size of the wavelengths of visible light. This method could be extended to larger or smaller particles by utilizing Infrared or UV light and a detector. The Debye ring thickness is a reliable indicator of

2DPC order because 2DPC disorder creates larger average particle spacings that decrease the Debye ring inner diameter. Conclusions on 2DPC ordering drawn from Debye ring measurements are consistent with the order parameter found by analysing SEM micrographs of the 2DPC.

Using the Debye ring method, we show the NTF method for self-assembly of 2DPC produces highly ordered hexagonal close packed (hcp) monolayers of colloidal particles (diameters= 409, 570, and 915 nm). While investigating the relationship between 2DPC ordering and Debye ring diffraction, we discovered that disorder in the 2DPC does not monotonically increase as salt concentration increases. This behaviour is attributed to chloride anion adsorption to the particle surface. The behaviour of the Zeta potential of particles in salt solutions is analogous to the 2DPC ordering results for 2DPC fabricated on salt solutions. This leads to the conclusion that chloride adsorption increases the particle surface charge which compensates for the decreasing Debye length at low or moderate salt concentrations.

2.5 References

1. Prather, D. W.; Sharkawy, A.; Shi, S.; Murakowski, J.; Schneider, G., *Photonic Crystals, Theory, Applications and Fabrication*. Wiley Publishing: 2009; p 405.

2. Rybin, M. V.; Khanikaev, A. B.; Inoue, M.; Samusev, K. B.; Steel, M. J.; Yushin, G.; Limonov, M. F., Fano Resonance between Mie and Bragg Scattering in Photonic Crystals. *Physical Review Letters.* **2009,** *103*, 023901.

3. van Duffel, B.; Ras, R. H. A.; De Schryver, F. C.; Schoonheydt, R. A., Langmuir-Blodgett deposition and optical diffraction of two-dimensional opal. *Journal of Materials Chemistry.* **2001,** *11*, 3333-3336.

4. Chapman, H. N.; Fromme, P.; Barty, A.; White, T. A.; Kirian, R. A.; Aquila, A.; Hunter, M. S.; Schulz, J.; DePonte, D. P.; Weierstall, U.; Doak, R. B.; Maia, F. R. N. C.; Martin, A. V.; Schlichting, I.; Lomb, L.; Coppola, N.; Shoeman, R. L.; Epp, S. W.; Hartmann, R.;

Rolles, D.; Rudenko, A.; Foucar, L.; Kimmel, N.; Weidenspointner, G.; Holl, P.; Liang, M.; Barthelmess, M.; Caleman, C.; Boutet, S.; Bogan, M. J.; Krzywinski, J.; Bostedt, C.; Bajt, S.; Gumprecht, L.; Rudek, B.; Erk, B.; Schmidt, C.; Hömke, A.; Reich, C.; Pietschner, D.; Strüder, L.; Hauser, G.; Gorke, H.; Ullrich, J.; Herrmann, S.; Schaller, G.; Schopper, F.; Soltau, H.; Kühnel, K.-U.; Messerschmidt, M.; Bozek, J. D.; Hau-Riege, S. P.; Frank, M.; Hampton, C. Y.; Sierra, R. G.; Starodub, D.; Williams, G. J.; Hajdu, J.; Timneanu, N.; Seibert, M. M.; Andreasson, J.; Rocker, A.; Jönsson, O.; Svenda, M.; Stern, S.; Nass, K.; Andritschke, R.; Schröter, C.-D.; Krasniqi, F.; Bott, M.; Schmidt, K. E.; Wang, X.; Grotjohann, I.; Holton, J. M.; Barends, T. R. M.; Neutze, R.; Marchesini, S.; Fromme, R.; Schorb, S.; Rupp, D.; Adolph, M.; Gorkhover, T.; Andersson, I.; Hirsemann, H.; Potdevin, G.; Graafsma, H.; Nilsson, B.; Spence, J. C. H., Femtosecond X-ray protein nanocrystallography. *Nature.* **2011,** *470*, 73-77.

5. Elser, V.; Henley, C. L., Crystal and quasicrystal structures in Al-Mn-Si alloys. *Physical Review Letters.* **1985,** *55*, 2883-2886.

6. Alexander Tikhonov, N. K., Jian-Tao Zhang, Luling Wang, Sanford A. Asher, Relectivity Enhanced Two-Dimensional Dielectric Particle Array Monoloayer Diffraction. *Journal of Nanophotonics.* **2012,** *6*, 063509-1-063509-9.

7. Smith, N. L.; Hong, Z.; Asher, S. A., Responsive ionic liquid-polymer 2D photonic crystal gas sensors. *Analyst.* **2014,** *139*, 6379-6386.

8. Zhang, J.-T.; Wang, L.; Luo, J.; Tikhonov, A.; Kornienko, N.; Asher, S. A., 2-D Array Photonic Crystal Sensing Motif. *Journal of the American Chemical Society.* **2011,** *133*, 9152-9155.

9. Cai, Z.; Smith, N. L.; Zhang, J.-T.; Asher, S. A., Two-Dimensional Photonic Crystal Chemical and Biomolecular Sensors. *Analytical Chemistry.* **2015,** *87*, 5013-5025.

10. Gao, P.; He, J.; Zhou, S.; Yang, X.; Li, S.; Sheng, J.; Wang, D.; Yu, T.; Ye, J.; Cui, Y., Large-Area Nanosphere Self-Assembly by a Micro-Propulsive Injection Method for High Throughput Periodic Surface Nanotexturing. *Nano Letters.* **2015,** *15*, 4591-4598.

11. Branham, M. S.; Hsu, W.-C.; Yerci, S.; Loomis, J.; Boriskina, S. V.; Hoard, B. R.; Han, S. E.; Chen, G., 15.7% Efficient 10-μm-Thick Crystalline Silicon Solar Cells Using Periodic Nanostructures. *Advanced Materials.* **2015,** *27*, 2182-2188.

12. Karg, M.; König, T. A. F.; Retsch, M.; Stelling, C.; Reichstein, P. M.; Honold, T.; Thelakkat, M.; Fery, A., Colloidal self-assembly concepts for light management in photovoltaics. *Materials Today.* **2015,** *18*, 185-205.

13. Utech, S.; Bley, K.; Aizenberg, J.; Vogel, N., Tailoring re-entrant geometry in inverse colloidal monolayers to control surface wettability. *Journal of Materials Chemistry A.* **2016,** *4* (18), 6853-6859.

14. Bravo, J.; Zhai, L.; Wu, Z.; Cohen, R. E.; Rubner, M. F., Transparent Superhydrophobic Films Based on Silica Nanoparticles. *Langmuir.* **2007,** *23*, 7293-7298.

15. Li, Y.; Zhang, J.; Zhu, S.; Dong, H.; Jia, F.; Wang, Z.; Sun, Z.; Zhang, L.; Li, Y.; Li, H.; Xu, W.; Yang, B., Biomimetic Surfaces for High-Performance Optics. *Advanced Materials.* **2009,** *21*, 4731-4734.

16. Malinsky, M. D.; Kelly, K. L.; Schatz, G. C.; Van Duyne, R. P., Chain Length Dependence and Sensing Capabilities of the Localized Surface Plasmon Resonance of Silver Nanoparticles Chemically Modified with Alkanethiol Self-Assembled Monolayers. *Journal of the American Chemical Society.* **2001,** *123*, 1471-1482.

17. Das, A.; Zhao, J.; Schatz, G. C.; Sligar, S. G.; Van Duyne, R. P., Screening of Type I and II Drug Binding to Human Cytochrome P450-3A4 in Nanodiscs by Localized Surface Plasmon Resonance Spectroscopy. *Analytical Chemistry.* **2009,** *81*, 3754-3759.

18. Shinotsuka, K.; Kajita, Y.; Hongo, K.; Hatta, Y., Crystal Perfection of Particle Monolayer at the Air–Water Interface. *Langmuir.* **2015,** *31*, 11452-11457.

19. Vogel, N.; Weiss, C. K.; Landfester, K., From soft to hard: the generation of functional and complex colloidal monolayers for nanolithography. *Soft Matter.* **2012,** *8*, 4044-4061.

20. Zhang, J.; Li, Y.; Zhang, X.; Yang, B., Colloidal Self-Assembly Meets Nanofabrication: From Two-Dimensional Colloidal Crystals to Nanostructure Arrays. *Advanced Materials.* **2010,** *22*, 4249-4269.

21. Lotito, V.; Zambelli, T., Approaches to self-assembly of colloidal monolayers: A guide for nanotechnologists. *Advances in Colloid and Interface Science*. **2017**, 246, 217-274.

22. Xie, X. N.; Chung, H. J.; Sow, C. H.; Wee, A. T. S., Nanoscale materials patterning and engineering by atomic force microscopy nanolithography. *Materials Science and Engineering: R: Reports.* **2006,** *54*, 1-48.

23. Zhang, J.-T.; Wang, L.; Lamont, D. N.; Velankar, S. S.; Asher, S. A., Fabrication of Large-Area Two-Dimensional Colloidal Crystals. *Angewandte Chemie International Edition.* **2012,** *51*, 6117-6120.

24. Ogi, T.; Modesto-Lopez, L. B.; Iskandar, F.; Okuyama, K., Fabrication of a large area monolayer of silica particles on a sapphire substrate by a spin coating method. *Colloids and Surfaces A: Physicochemical and Engineering Aspects.* **2007,** *297*, 71-78.

25. Truzzolillo, D.; Sharaf, H.; Jonas, U.; Loppinet, B.; Vlassopoulos, D., Tuning the Structure and Rheology of Polystyrene Particles at the Air–Water Interface by Varying the pH. *Langmuir.* **2016,** *32*, 6956-6966.

26. Kim, J. Y.; Kwon, S. J.; Chang, J.-B.; Ross, C. A.; Hatton, T. A.; Stellacci, F., Two-Dimensional Nanoparticle Supracrystals: A Model System for Two-Dimensional Melting. *Nano Letters.* **2016,** *16*, 1352-1358.

27. Hu, M.; Chujo, S.; Nishikawa, H.; Yamaguchi, Y.; Okubo, T., Spontaneous formation of large-area monolayers of well-ordered nanoparticles via a wet-coating process. *Journal of Nanoparticle Research.* **2004,** *6*, 479-487.

28. Ho, C.-C.; Chen, P.-Y.; Lin, K.-H.; Juan, W.-T.; Lee, W.-L., Fabrication of Monolayer of Polymer/Nanospheres Hybrid at a Water-Air Interface. *ACS Applied Materials & Interfaces.* **2011,** *3*, 204-208.

29. Retsch, M.; Zhou, Z.; Rivera, S.; Kappl, M.; Zhao, X. S.; Jonas, U.; Li, Q., Fabrication of Large-Area, Transferable Colloidal Monolayers Utilizing Self-Assembly at the Air/Water Interface. *Macromolecular Chemistry and Physics.* **2009,** *210*, 230-241.

30. Okubo, T.; Chujo, S.; Maenosono, S.; Yamaguchi, Y., Microstructure of Silica Particle Monolayer Films Formed by Capillary immersion Force. *Journal of Nanoparticle Research.* **2003,** *5*, 111-117.

31. Rödner, S. C.; Wedin, P.; Bergström, L., Effect of Electrolyte and Evaporation Rate on the Structural Features of Dried Silica Monolayer Films. *Langmuir.* **2002,** *18*, 9327-9333.

32. Grzelczak, M.; Vermant, J.; Furst, E. M.; Liz-Marzán, L. M., Directed Self-Assembly of Nanoparticles. *ACS Nano.* **2010,** *4*, 3591-3605.

33. Minh, N. V.; Hue, N. T.; Lien, N. T. H.; Hoang, C. M., Close-packed monolayer self-assembly of silica nanospheres assisted by infrared irradiation. *Electronic Materials Letters.* **2017**, 14, 64-69.

34. Zhang, J.-T.; Wang, L.; Chao, X.; Velankar, S. S.; Asher, S. A., Vertical spreading of two-dimensional crystalline colloidal arrays. *Journal of Materials Chemistry C.* **2013,** 38, 6099-6102.

35. Zhang, F.; Cao, L.; Yang, W., Preparation of Monodisperse and Anion-Charged Polystyrene Microspheres Stabilized with Polymerizable Sodium Styrene Sulfonate by Dispersion Polymerization. *Macromol. Chem. Phys.* **2010,** *211*, 744-751.

36. Reese, C. E.; Asher, S. A., Emulsifier-Free Emulsion Polymerization Produces Highly Charged, Monodisperse Particles for Near Infrared Photonic Crystals. *Journal of Colloid and Interface Science.* **2002,** *248*, 41-46.

37. Zhang, J.-T.; Chao, X.; Liu, X.; Asher, S. A., Two-dimensional array Debye ring diffraction protein recognition sensing. *Chemical Communications.* **2013,** *49*, 6337-6339.

38. Bohn, J. J.; Ben-Moshe, M.; Tikhonov, A.; Qu, D.; Lamont, D. N.; Asher, S. A., Charge stabilized crystalline colloidal arrays as templates for fabrication of non-close-packed inverted photonic crystals. *J. Colloid Interface Sci.* **2010,** *344*, 298-307.

39. Rengarajan, R.; Mittleman, D.; Rich, C.; Colvin, V., Effect of disorder on the optical properties of colloidal crystals. *Physical Review E.* **2005,** *71*, 016615.

40. Zhang, J.-T.; Chao, X.; Asher, S. A., Asymmetric Free-Standing 2-D Photonic Crystal Films and Their Janus Particles. *Journal of the American Chemical Society.* **2013,** *135*, 11397-11401.

41. Xue, F.; Asher, S. A.; Meng, Z.; Wang, F.; Lu, W.; Xue, M.; Qi, F., Two-dimensional colloidal crystal heterostructures. *RSC Advances.* **2015,** *5*, 18939-18944.

42. Weitenberg, C.; Schauß, P.; Fukuhara, T.; Cheneau, M.; Endres, M.; Bloch, I.; Kuhr, S., Coherent Light Scattering from a Two-Dimensional Mott Insulator. *Physical Review Letters.* **2011,** *106*, 215301.

43. Pieranski, P., Two-Dimensional Interfacial Colloidal Crystals. *Physical Review Letters.* **1980,** *45*, 569-572.

44. Schmudde, M.; Grunewald, C.; Goroncy, C.; Noufele, C. N.; Stein, B.; Risse, T.; Graf, C., Controlling the Interaction and Non-Close-Packed Arrangement of Nanoparticles on Large Areas. *ACS Nano.* **2016,** *10*, 3525-3535.

45. Lotito, V.; Zambelli, T., Self-Assembly of Single-Sized and Binary Colloidal Particles at Air/Water Interface by Surface Confinement and Water Discharge. *Langmuir.* **2016,** *32*, 9582-9590.

46. Reincke, F.; Kegel, W. K.; Zhang, H.; Nolte, M.; Wang, D.; Vanmaekelbergh, D.; Mohwald, H., Understanding the self-assembly of charged nanoparticles at the water/oil interface. *Physical Chemistry Chemical Physics.* **2006,** *8*, 3828-3835.

47. Yoshida, H.; Ito, K.; Ise, N., Colloidal crystal growth. *Journal of the Chemical Society, Faraday Transactions.* **1991,** *87*, 371-378.

48. Kralchevsky, P. A.; Nagayama, K., Capillary forces between colloidal particles. *Langmuir.* **1994,** *10*, 23-36.

49. Bardosova, M.; Pemble, M. E.; Povey, I. M.; Tredgold, R. H., The Langmuir-Blodgett Approach to Making Colloidal Photonic Crystals from Silica Spheres. *Advanced Materials.* **2010,** *22*, 3104-3124.

50. Paunov, V. N., Novel Method for Determining the Three-Phase Contact Angle of Colloid Particles Adsorbed at Air−Water and Oil−Water Interfaces. *Langmuir.* **2003,** *19*, 7970-7976.

51. Aveyard, R.; Clint, J. H.; Nees, D.; Paunov, V. N., Compression and Structure of Monolayers of Charged Latex Particles at Air/Water and Octane/Water Interfaces. *Langmuir.* **2000,** *16*, 1969-1979.

52. Bossa, G. V.; Bohinc, K.; Brown, M. A.; May, S., Dipole Moment of a Charged Particle Trapped at the Air–Water Interface. *The Journal of Physical Chemistry B.* **2016,** *120*, 6278-6285.

53. Hurd, A. J., The electrostatic interaction between interfacial colloidal particles. *Journal of Physics A: Mathematical and General.* **1985,** *18*, L1055.

54. Wu, S.; Nikolov, A.; Wasan, D., Role of Collective Interactions in Self-Assembly of Charged Particles at Liquid Interfaces. *The Canadian Journal of Chemical Engineering.* **2007,** *85*, 562-569.

55. Nikolaides, M. G.; Bausch, A. R.; Hsu, M. F.; Dinsmore, A. D.; Brenner, M. P.; Gay, C.; Weitz, D. A., Electric-field-induced capillary attraction between like-charged particles at liquid interfaces. *Nature.* **2002,** *420*, 299-301.

56. Girotto, M.; dos Santos, A. P.; Levin, Y., Interaction of Charged Colloidal Particles at the Air–Water Interface. *The Journal of Physical Chemistry B.* **2016,** *120*, 5817-5822.

57. Okubo, T., Extraordinary behavior in the structural properties of colloidal macroions in deionized suspension and the importance of the Debye screening length. *Accounts of Chemical Research.* **1988,** *21*, 281-286.

58. Hunter, R. J., *Zeta Potential in Colloid Science*. Academic Press Inc: New York, New York, 1981; p 386.

59. Hiemenz, P. C., *Principles of Colloid and Surface Chemistry*. 2nd ed.; Marcel Dekker, Inc: New York, New York, 1986.

60. Dong, L.; Johnson, D., Surface Tension of Charge-Stabilized Colloidal Suspensions at the Water−Air Interface. *Langmuir.* **2003,** *19*, 10205-10209.

61. Elimelech, M.; O'Melia, C. R., Effect of electrolyte type on the electrophoretic mobility of polystyrene latex colloids. *Colloids and Surfaces.* **1990,** *44*, 165-178.

62. Ma, C. M.; Micale, F. J.; El-Aasser, M. S.; Vanderhoff, J. W., The Relationship Between the Electrophoretic Mobility and the A dsorption of Ions on Polystyrene Latex. In Emulsion Polymers and Emulsion Polymerization, *Journal of the American Chemical Society.* **1981**, *165*, 251-262.

3.0 Two-Dimensional Photonic Crystal Surfactant Detection

This chapter was previously published in the journal Analytical Chemistry as Zhang, J.-T.; Smith, N.; Asher, S. A., *Analytical Chemistry* 2012, *84* (15), 6416-6420, and is reprinted with permission.

Author Contributions: N.L.S fabricated 2DPC hydrogels and collected data. N.L.S. assisted J.T.Z. with data analysis. The manuscript was prepared by J.T.Z. with assistance from N.L.S. and S.A.A.

We developed a novel two-dimensional (2-D) crystalline colloidal array photonic crystal sensing material for the visual detection of amphiphilic molecules in water. A close packed polystyrene 2-D array monolayer was embedded in a poly(N-isopropylacrylamide) (PNIPAAm)-based hydrogel film. These 2-D photonic crystals placed on a mirror show intense diffraction that enables them to be used for visual determination of analytes. Binding of surfactant molecules attaches ions to the sensor that swells the PNIPAAm-based hydrogel. The resulting increase in particle spacing red shifts the 2-D diffracted light. Incorporation of more hydrophobic monomers increases the sensitivity to surfactants.

3.1 Introduction

Amphiphilic surfactants are organic compounds that contain both hydrophobic groups and hydrophilic groups. Surfactants are widely used as emulsifiers, detergents, and in cosmetics, industrial cleaners, etc.[1] These applications result in release of these compounds into the environment, which impacts the environment and human health.[1,2] Therefore, there is significant interest in developing efficient detection methods for surfactants. Existing methods for determining the concentrations of surfactants in solution include titration, spectroscopy, and chromatography.[3-9] High-performance liquid chromatography (HPLC) is the preferred approach for surfactant analysis.[4-6] HPLC is somewhat expensive and requires highly trained personnel. Mass spectroscopy (MS),[7] evaporative light scattering detection (ELSD)[8] and charged aerosol detection (CAD)[9] can also be used to detect surfactants. These methods involve time-consuming sample preparation and expensive instruments. There is a need to develop economical methods that require little sample preparation and utilize inexpensive methodologies.

In the work here, we report on a new approach for the visual detection of surfactants. We utilize poly(N-isopropylacrylamide) (PNIPAAm) hydrogels as a substrate for surfactant molecule binding. PNIPAAm, which in water is a temperature sensitive polymer with a lower critical solution temperature (LCST) at 32ºC, has side hydrophobic isopropyl group chains attached to hydrophilic amide groups.[10-12] The PNIPAAm materials have been widely investigated and utilized for drug release carriers, separations, photonic crystals, etc.[13-19]

Our two-dimensional (2-D) sensor, schematically shown in Figure 3.1, consists of a PNIPAAm-based hydrogel film attached to a 2-D crystalline colloidal array (CCA) monolayer of 490 nm polystyrene (PS) particles. The 2-D PS array hydrogel when placed on a mirror strongly Bragg back-diffracts light of wavelengths that depend on the 2-D array spacings.[20,21] Surfactants

in water solution are known to bind to PNIPAAm hydrogels through hydrophobic interactions, giving rise to ionic hydrogels.[22, 23] These bound ions result in a Donnan potential that causes the hydrogel to swell. This increases the 2-D array spacing, causing a red shift in the diffracted wavelength that increases with the amount of surfactant bound.

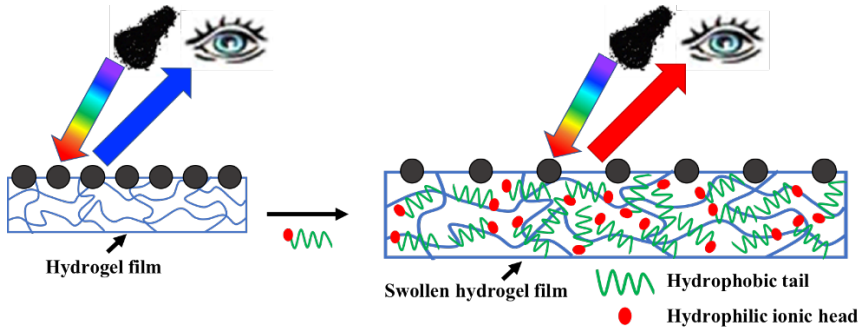

Figure 3.1 - Schematic illustration of 2-D photonic crystal sensor formed by polymerization of a PNIPAAm hydrogel network onto a 2-D array of 490 nm PS particles on a liquid Hg surface. The PNIPAAm hydrogel swells upon binding of surfactant molecules. The 2-D particle spacing increases upon swelling of the PNIPAAm hydrogel, red shifting the diffracted wavelength.

3.2 Experimental

3.2.1 Materials

N-isopropylacrylamide (NIPAAm) was purchased from Sigma-Aldrich and was purified by recrystallization in hexane. *N*,*N'*-methylenebisacrylamide (MBAAm), hydroxyethyl acrylate (HEA), tert-butyl acrylate (tBA) 2-hydroxy-1-[4-(2-hydroxy-ethoxy)-phenyl]-2-methyl-1-propanone (Irgacure 2959), sodium dodecyl sulfate (SDS), sodium dodecylbenzene sulfonate (SDBS), cetyl trimethyl ammonium bromide (CTAB), and mercury (Hg) were purchased from

Sigma-Aldrich and were used as received. Sodium C14-16 Olefin sulfonate (SOS) was obtained from Stepan Company (IL). The structures of SDS, SDBS and SOS are shown in Figure 3.2. Polystyrene (PS) particles with a diameter of 490 nm were synthesized according to references.[24]

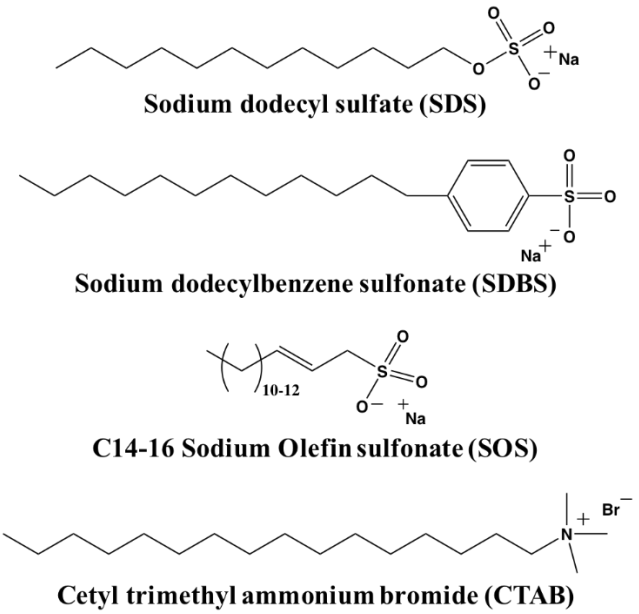

Figure 3.2 - Chemical structures ofsurfactants, SDS, SDBS, SOS, and CTAB.

3.2.2 2D Array Sensor Preparation

The PS particle dispersion (15 wt %) and propanol were mixed at a ratio of 3:1 (in volume). A close packed 2-D PS array was fabricated on a Hg surface through the self-assembly of colloidal PS particles during spreading of the particle dispersion.[20, 25] A 1 mL reaction mixture consisting of NIPAAm (10 wt%) and MBAAm (0.2 wt%) in Nanopure water was mixed with 20 µL Irgacure 2959 (in DMSO, 33 % (w:v)). This polymerization solution was layered onto the 2D array monolayer on the Hg surface. A glass slide (60 mm × 24 mm × 0.12 mm) was placed onto the reaction solution. The polymerization was initiated by UV light (UVGL-55 Handheld UV

Lamp, UVP. CA). The resulting 2-D array PNIPAAm-based hydrogel film was lifted from the Hg surface, peeled from the glass slide and rinsed with large amounts of water. The hydrogel film was equilibrated in water for at least 24 hrs, during which the water was frequently replaced. The thickness of the swollen hydrogel sensor is between 500-600 μm.

The PNIPAAm gel was made more hydrophobic by incorporating HEA or tBA monomer. Different amounts of HEA and tBA (5 vol% in DMSO) were added to the NIPAAm reaction solutions and the reaction mixtures were cooled in an ice bath before polymerization. Ice was also packed around the petri dish containing the 2-D array on Hg to prevent phase separation during polymerization. This is critical because the hydrophobic monomers decrease the hydrogel LCST. Polymerization at higher temperatures results in phase separated, white, opaque hydrogels. The chilled reaction solution was layered onto the chilled 2-D array monolayer and polymerized.

3.2.3 Diffraction Measurements

Diffraction of the 2-D PCCA was monitored by using an Ocean Optics USB2000-UV-VIS Spectrometer, a LS-1 Tungsten Halogen Light Source and an R-series Fiber Optic Reflection Probe. The diffraction measurements were carried out in a Littrow configuration with a 28^{o} measurement angle between the probe and the normal to the 2-D array. Surfactants were dissolved in Nanopure water (18.2 MΩ). The surfactant concentrations ranged from 0 to 20 mM. The hydrogel sensors were immersed in 20 mL surfactant solutions. After equilibration at room temperature, the 2-D array PNIPAAm-based hydrogel sensors in surfactant solutions were taken out and placed on front surface silver mirrors (Thor Labs, VA) for the diffraction measurements. The measurement was carried out at room temperature.

3.3 Results and Discussion

In a Littrow configuration, the 2-D array Bragg diffraction condition is: $m\lambda = 3^{1/2} d \sin\theta$, where m is the diffraction order, λ is the wavelength of the diffracted light, d is the nearest neighboring particle spacing, and θ is the angle between the incident light and the normal to the 2-D array. For a fixed incidence angle θ, the diffracted wavelength, λ, is proportional to the 2-D particle spacing, d.

Surfactant binding to the PNIPAAm hydrogel results in attachment of negative charges to the hydrogel. This bound hydrogel charge and its counterions give rise to a Donnan potential that increases the hydrogel osmotic pressure, resulting in a hydrogel volume increase and an increase in the spacing of the 2-D particles, d, that red shifts the diffraction.

Anionic surfactants account for 50% of the surfactant used in Europe and 60% in US.[1, 26] We examined the response of our sensors to three anionic surfactants, SDS, SDBS and SOS. When the sensing hydrogel is placed in the surfactant solution, the surfactant molecules diffuse into the hydrogel network. Strong binding takes place through the hydrophobic interactions between the PNIPAAm and the surfactant hydrophobic tails.[27, 28] As a result, the volume of the hydrogel sensor increases with surfactant binding, and the diffraction red shifts.

Figure 3.3a shows the dependence of the 2-D array PNIPAAm-based hydrogel sensor diffraction spectra on the SDS concentration in aqueous solutions. In pure water the 2-D array PNIPAAm-based hydrogel sensor diffracts at 470 nm. The diffracted wavelength red shifts to 500 nm in 1 mM SDS. Increasing the concentration to 5 mM further shifts the diffraction to 622 nm. Figure 3.3b shows the dependence of the 2-D diffraction wavelength and color on the SDS concentration.

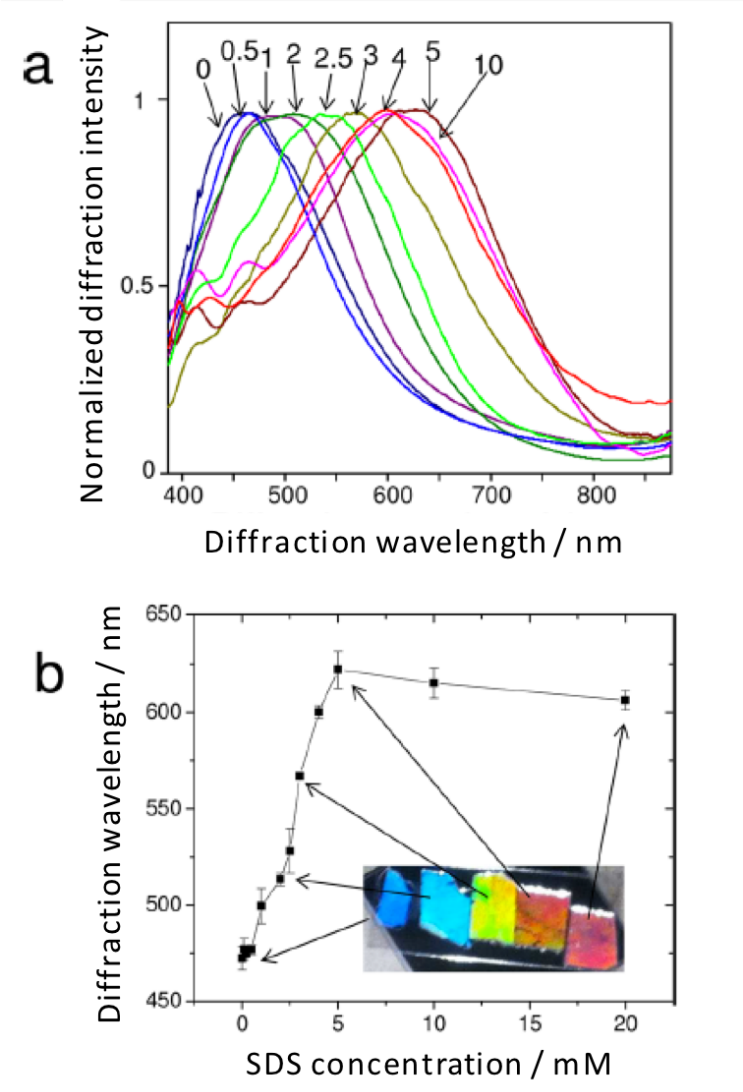

Figure 3.3 - (a) Normalized and smoothed diffraction spectra of 2-D PNIPAAm sensors at different concentrations of aqueous SDS solutions. The spectra were measured with 40 ms accumulations. The measurement angle between the probe and the normal to the 2-D array is 28º. (b) Diffraction wavelength versus SDS concentration. The inset shows photographs taken close to the Littrow configuration at an angle of 28º between the source and the camera to the 2-D array normal.

The critical aggregation concentration (CAC) of a surfactant to a polymer is the concentration where the surfactant forms polymer-bound micelles. The CAC is lower than the solution critical micelle concentration (CMC). The SDS CAC is reported to be ~0.79 mM for PNIPAAm hydrogels.[28] At low SDS concentrations (≤ 0.5 mM) there is little binding of SDS to PNIPAAm and the hydrogel volume does not change and the diffraction wavelength of the 2-D array remains similar to that in pure water (Figure 3.3). However, at SDS concentrations above the CAC, surfactant binding to the hydrogel attaches charged surfactants that induce a Donnan potential that swells the hydrogel.[29] For example, the diffraction wavelength shifts to 500 nm for 1 mM SDS solution. The inset in Figure 3.3b illustrates the visually evident color changes of the surfactant sensor at the different SDS concentrations.

Figure 3.4 shows the concentration dependence of the diffraction wavelength shift of the 2-D sensor for SDS, SDBS and SOS surfactants of different hydrocarbon lengths. With increasing surfactant concentrations, the amount of bound surfactant to the hydrogel increases, which causes the hydrogel to swell and the diffraction to shift to longer wavelengths. However, at high concentrations (>5 mM), the surfactant molecules form free micelles that increase the solution ionic strength which decreases the hydrogel swelling[29] and the 2-D particle spacing, causing the diffraction to blue shift.

Figure 3.4 shows that the 2-D hydrogel sensor is most sensitive to SDBS. Moreover, for surfactant concentrations below 5 mM, the diffraction red shifts most for surfactants of largest hydrocarbon chain length (SDBS (18C)> SOS (14-16C)> SDS (12C)). For example, at 1 mM surfactant concentrations, the SDBS, SOS and SDS wavelength red shifts are 174 nm, 105 nm and 30 nm, respectively. This is because the surfactant hydrophobic binding affinity increases with increasing surfactant chain length. Our results are consistent with hydroxyethyl cellulose

hydrogel swelling observed in surfactant solutions, where longer surfactant alkyl lengths show increased swelling.[29, 30]

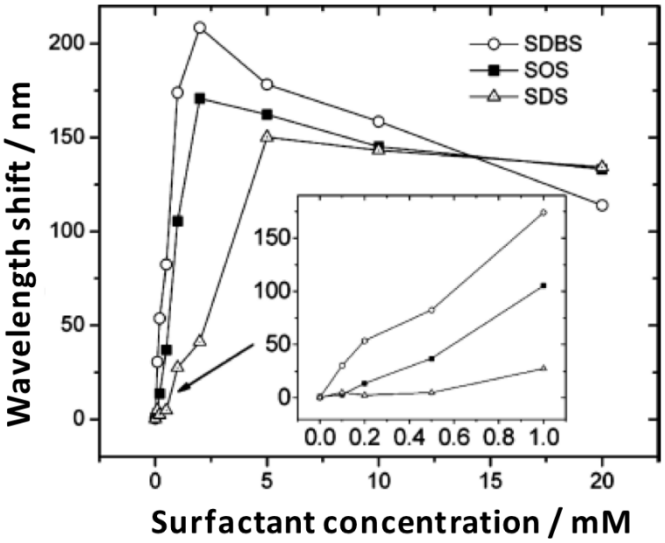

Figure 3.4 - Dependence of the diffraction red shift on the concentrations of surfactants SDS, SDBS, and SOS. The inset expands the low concentration regime. The spectra were measured with 40 ms accumulations.

Our 2-D hydrogel sensors also sense cationic surfactants. Figure 3.5a shows the diffraction spectra of 2-D PNIPAAm sensors at different CTAB concentrations, while Figure 3.5b shows the concentration dependence of the diffraction shift of the 2-D sensor for cationic CTAB. The diffraction wavelength shifts about 70 nm when increasing the CTAB concentration from 0 to 5 mM due to the binding of CTAB to the PNIPAAm hydrogel.[31] At higher concentrations (10 and 20 mM), the diffraction blue shifts because the surfactant binding reaches saturation. Note that the peak shift of the 2-D sensors in the cationic CTAB solution is less than for anionic surfactants. This is possibly due to the smaller hydrophilicity of the CTAB trimethyl ammonium ionic head groups. Our results agree with the previously reported swelling of PNIPAAm hydrogel in CTAB.[32]

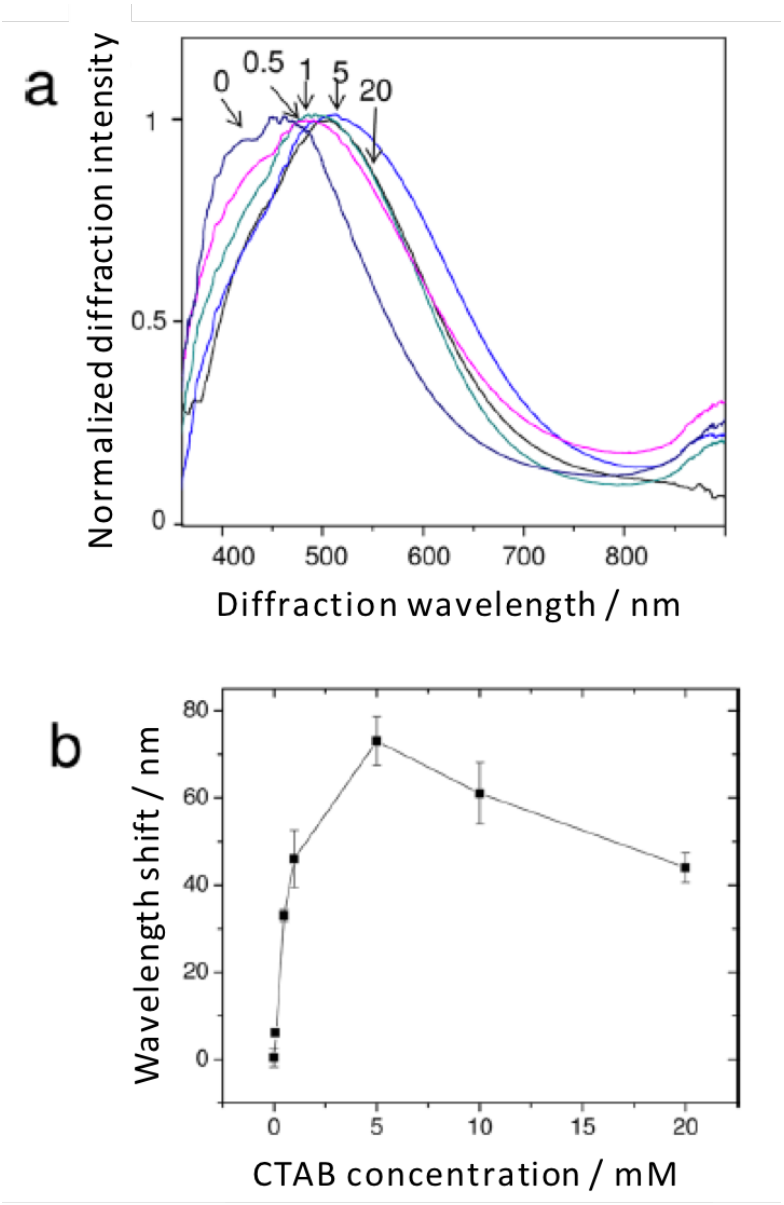

Figure 3.5 - (a) Normalized and smoothed diffraction spectra of 2-D PNIPAAm sensors at different concentrations of aqueous CTAB solutions. The measurement angle between the probe and the normal to the 2-D array is 28º. (b) The diffraction red shift versus the concentrations of CTAB.

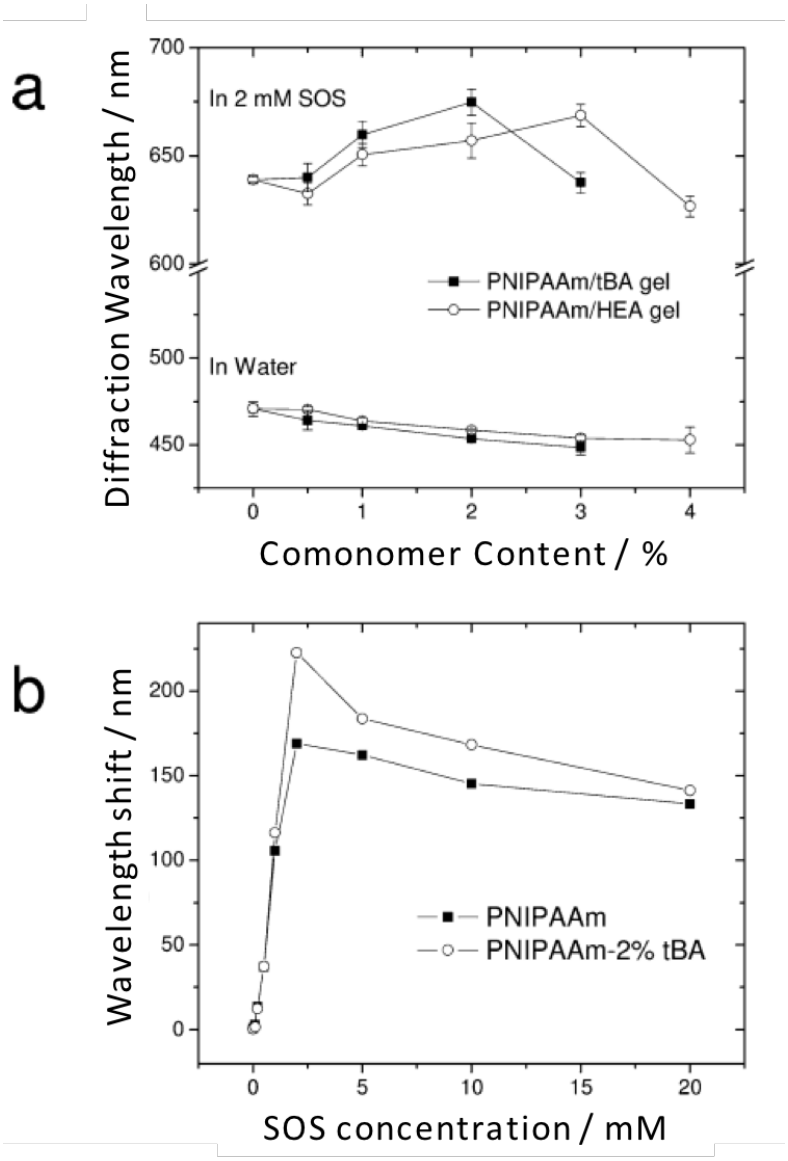

Figure 3.6 - (a) The impact of HEA and tBA content on the 2-D PNIPAAm-based hydrogel diffracted wavelength in 2 mM SOS solution. (b) SOS concentration dependence of the diffraction wavelength shift of PNIPAAm and PNIPAAm/tBA (2%)-based hydrogel sensors.

Copolymerization of hydrophobic monomers into the NIPAAm hydrogels increases the sensor sensitivity to surfactant. We copolymerized hydrophobic HEA and tBA into the PNIPAAm hydrogels to increase their hydrophobicity. Figure 3.6a shows the dependence of the diffraction wavelength on the HEA and tBA content. The diffraction of the 2-D hydrogels in water blue shifts with increasing hydrophobic monomer content, because the hydrogel free energy of mixing with water decreases.

In 2 mM SOS, the diffraction red shifts and then blue shifts as the content of hydrophobic monomers increases. For example, the 2-D array PNIPAAm/HEA hydrogel sensor diffracts at 632 nm, 650 nm 657 nm and 669 nm at 0.5%, 1%, 2% and 3% HEA content, respectively. However, an increase in the HEA content to 4% causes a diffraction blue shift to 627 nm (Figure 3.6a) because the increased amount of comonomer, HEA, increases the hydrophobicity of the hydrogel. Binding of SOS does not overcome this large increase in hydrophobic interactions. Therefore, at 4% HEA and 3% tBA content, the hydrogel swelling in 2 mM SOS is decreased and the diffraction is blue shifted.

The 2-D PNIPAAm/tBA hydrogel sensor shows a similar behavior. These hydrophobically modified 2-D PNIPAAm sensors likely binds more surfactant, causing higher swelling and red shifts.[23] For the tBA modified PNIPAAm-based hydrogel sensor, the diffraction maximum occurs at lower copolymer content than for HEA because tBA is more hydrophobic than HEA.

Figure 3.6b shows the concentration dependence of the diffraction wavelength shift of pure PNIPAAm and PNIPAA 2-D sensors containing 2% tBA in SOS. With increasing SOS concentrations, the hydrogels swell, which red shifts the diffraction to longer wavelengths. At high concentrations, the diffraction blue shifts due to the formation of free micelles that decrease

the swelling of the hydrogel. The diffraction shift of PNIPAA/tBA hydrogel-based sensor is larger than that of the PNIPAAm-based hydrogel sensors because copolymerization of tBA increases the binding of SOS to PNIPAA/tBA hydrogels. Therefore, we can conclude that the sensor sensitivity which is defined as the diffraction shift divided by the surfactant concentration is increased by the incorporation of hydrophobic monomers.

3.4 Conclusions

We developed a photonic crystal sensing material that can be used to visually determine the concentrations of anionic and cationic surfactants such as SDS, SOS, SDBS and CTAB in water. The sensor material consists of 2-D PS particle arrays on a PNIPAAm-based hydrogel. Binding of ionic surfactant molecules to PNIPAAm polymer chains attaches ions that induce a Donnan potential that swells the hydrogel and increases the 2-D particle spacing, red shifting the diffracted light. Incorporating hydrophobic monomers into the hydrogel increases the sensor sensitivity.

Our 2-D photonic crystal sensing materials can detect ~0.1 mM concentrations of surfactants. The detected concentration range covers the surfactant concentrations present in municipal sewer discharges (20-70 mg/L)[33, 34] and in industrial wastewater (300 mg/L).[35]

3.5 References

1. Huber, L.; Nitschke, L. *Handbook of Applied Surface and Colloid Chemistry*; Edited by Holmberg, K.; John Wiley & Sons, Ltd, **2001**; pp 509–536.

2. Beltrán-Heredia, J.; Sánchez-Martín, J.; Solera-Hernández, C., Anionic Surfactants Removal by Natural Coagulant/Flocculant Products. *Industrial & Engineering Chemistry Research* **2009,** *48*, 5085-5092.

3. Stodghill, S. P.; Smith, A. E.; O'Haver, J. H., Thermodynamics of Micellization and Adsorption of Three Alkyltrimethylammonium Bromides Using Isothermal Titration Calorimetry. *Langmuir* **2004,** *20*, 11387-11392.

4. Haefliger, O. P., Universal Two-Dimensional HPLC Technique for the Chemical Analysis of Complex Surfactant Mixtures. *Analytical Chemistry* **2003,** *75*, 371-378.

5. Radke, M.; Behrends, T.; Förster, J.; Herrmann, R., Analysis of Cationic Surfactants by Microbore High-Performance Liquid Chromatography−Electrospray Mass Spectrometry. *Analytical Chemistry* **1999,** *71*, 5362-5366.

6. Levine, L. H.; Garland, J. L.; Johnson, J. V., HPLC/ESI-Quadrupole Ion Trap Mass Spectrometry for Characterization and Direct Quantification of Amphoteric and Nonionic Surfactants in Aqueous Samples. *Analytical Chemistry* **2002,** *74*, 2064-2071.

7. Norton, D.; Shamsi, S. A., Capillary Electrochromatography−Mass Spectrometry of Nonionic Surfactants. *Analytical Chemistry* **2007,** *79*, 9459-9470.

8. Im, S. H.; Jeong, Y. H.; Ryoo, J. J., Simultaneous analysis of anionic, amphoteric, nonionic and cationic surfactant mixtures in shampoo and hair conditioner by RP-HPLC/ELSD and LC/MS. *Analytica Chimica Acta* **2008,** *619*, 129-136.

9. Stojanovic, A.; Lämmerhofer, M.; Kogelnig, D.; Schiesel, S.; Sturm, M.; Galanski, M.; Krachler, R.; Keppler, B. K.; Lindner, W., Analysis of quaternary ammonium and phosphonium ionic liquids by reversed-phase high-performance liquid chromatography with charged aerosol detection and unified calibration. *Journal of Chromatography A* **2008,** *1209*, 179-187.

10. Heskins, M.; Guillet, J. E., Solution Properties of Poly(N-isopropylacrylamide). *Journal of Macromolecular Science: Part A - Chemistry* **1968,** *2*, 1441-1455.

11. Otake, K.; Inomata, H.; Konno, M.; Saito, S., Thermal analysis of the volume phase transition with N-isopropylacrylamide gels. *Macromolecules* **1990,** *23*, 283-289.

12. Miyamae, T.; Akiyama, H.; Yoshida, M.; Tamaoki, N., Characterization of Poly(N-isopropylacrylamide)-Grafted Interfaces with Sum-Frequency Generation Spectroscopy. *Macromolecules* **2007,** *40*, 4601-4606.

13. Zhang, J.-T.; Huang, S.-W.; Zhuo, R.-X., A novel sol–gel strategy to prepare temperature-sensitive hydrogel for encapsulation of protein. *Colloid and Polymer Science* **2005,** *284*, 209-213.

14. Zhang, J.-T.; Keller, T. F.; Bhat, R.; Garipcan, B.; Jandt, K. D., A novel two-level microstructured poly(N-isopropylacrylamide) hydrogel for controlled release. *Acta Biomaterialia* **2010,** *6*, 3890-3898.

15. Kobayashi, J.; Kikuchi, A.; Sakai, K.; Okano, T., Cross-Linked Thermoresponsive Anionic Polymer-Grafted Surfaces To Separate Bioactive Basic Peptides. *Analytical Chemistry* **2003,** *75*, 3244-3249.

16. Reese, C. E.; Mikhonin, A. V.; Kamenjicki, M.; Tikhonov, A.; Asher, S. A., Nanogel Nanosecond Photonic Crystal Optical Switching. *Journal of the American Chemical Society* **2004,** *126*, 1493-1496.

17. Weissman, J. M.; Sunkara, H. B.; Tse, A. S.; Asher, S. A., Thermally Switchable Periodicities and Diffraction from Mesoscopically Ordered Materials. *Science* **1996,** *274*, 959.

18. Ahmed, Z.; Gooding, E. A.; Pimenov, K. V.; Wang, L.; Asher, S. A., UV resonance Raman determination of molecular mechanism of poly(N-isopropylacrylamide) volume phase transition. *J Phys Chem B* **2009,** *113*, 4248-4256.

19. Tang, S.; Hu, Z.; Zhou, B.; Cheng, Z.; Wu, J.; Marquez, M., Melting Kinetics of Thermally Responsive Microgel Crystals. *Macromolecules* **2007,** *40*, 9544-9548.

20. Zhang, J.-T.; Wang, L.; Luo, J.; Tikhonov, A.; Kornienko, N.; Asher, S. A., 2-D Array Photonic Crystal Sensing Motif. *Journal of the American Chemical Society* **2011,** *133*, 9152-9155.

21. Alexander Tikhonov, N. K., Jian-Tao Zhang, Luling Wang, Sanford A. Asher, Relectivity Enhanced Two-Dimensional Dielectric Particle Array Monoloayer Diffraction. *Journal of Nanophotonics* **2012,** *6*, 063509-1-063509-9.

22. Kokufuta, E.; Zhang, Y. Q.; Tanaka, T.; Mamada, A., Effects of surfactants on the phase transition of poly(N-isopropylacrylamide) gel. *Macromolecules* **1993,** *26*, 1053-1059.

23. Xue, W.; Hamley, I. W., Thermoreversible swelling behaviour of hydrogels based on N-isopropylacrylamide with a hydrophobic comonomer. *Polymer* **2002,** *43*, 3069-3077.

24. Reese, C. E.; Asher, S. A., Emulsifier-Free Emulsion Polymerization Produces Highly Charged, Monodisperse Particles for Near Infrared Photonic Crystals. *Journal of Colloid and Interface Science* **2002,** *248*, 41-46.

25. Zhang, J.-T.; Wang, L.; Chao, X.; Asher, S. A., Periodicity-Controlled Two-Dimensional Crystalline Colloidal Arrays. *Langmuir* **2011,** *27*, 15230-15235.

26. Schmitt, T. M. *Analysis of Surfactants*, 2nd ed.; Marcel Dekker: New York, 2001; pp 1-57.

26. Kokufuta, E.; Nakaizumi, S.; Ito, S.; Tanaka, T., Uptake of sodium dodecylbenzenesulfonate by poly(N-isopropylacrylamide) gel and effect of surfactant uptake on the volume-phase transition. *Macromolecules* **1995,** *28*, 1704-1708.

27. Schild, H. G.; Tirrell, D. A., Interaction of poly(N-isopropylacrylamide) with sodium n-alkyl sulfates in aqueous solution. *Langmuir* **1991,** *7*, 665-671.

28. Sjöström, J.; Piculell, L., Simple Gel Swelling Experiments Distinguish between Associating and Nonassociating Polymer−Surfactant Pairs. *Langmuir* **2001,** *17*, 3836-3843.

29. Rosen, O. S., J.; Piculell, L., Responsive Polymer Gels Based on Hydrophobically Modified Cellulose Ethers and Their Interactions with Ionic Surfactants. *Langmuir* **1998,** *14*, 5795-5801.

30. Lynch, I.; Sjöström, J.; Piculell, L., Hydrophobicity and Counterion Effects on the Binding of Ionic Surfactants to Uncharged Polymeric Hydrogels. *J. Phys. Chem. B* **2005,** *109*, 4252-4257.

31. Chauhan, G. S.; Chauhan, S., Synthesis, characterization, and swelling studies of pH- and thermosensitive hydrogels for specialty applications. *Journal of Applied Polymer Science* **2008,** *109*, 47-55.

32. Han, Z.; Zhang, F.; Lin, D.; Xing, B., Clay Minerals Affect the Stability of Surfactant-Facilitated Carbon Nanotube Suspensions. *Environmental Science & Technology* **2008,** *42*, 6869-6875.

33. Matthijs, E.; Holt, M. S.; Kiewiet, A.; Rijs, G. B. J., Environmental monitoring for linear alkylbenzene sulfonate, alcohol ethoxylate, alcohol ethoxy sulfate, alcohol sulfate, and soap. *Environmental Toxicology and Chemistry* **1999,** *18*, 2634-2644.

34. Wagener, S.; Schink, B., Anaerobic degradation of nonionic and anionic surfactants in enrichment cultures and fixed-bed reactors. *Water Research* **1987,** *21*, 615-622.

4.0 Responsive Ionic Liquid-Polymer 2D Photonic Crystal Gas Sensors

This chapter was previously published in the journal Analyst as Smith, N.L.; Hong, Z.; Asher, S.A., *Analyst* 2014, *139* (24), 6379-6386, and is reprinted with permission.

Author Contributions: N.L.S. fabricated samples, collected data, and analyzed data. Z.H. discovered the ionic liquid used in this study. The manuscript was prepared by N.L.S with assistance from S.A.A.

We developed novel air-stable 2D polymerized photonic crystal (2DPC) sensing materials for visual detection of gas phase analytes such as water and ammonia by utilizing a new ionic liquid, ethylguanidine perchlorate (EGP) as the mobile phase. Because of the negligible ionic liquid vapor pressure these 2DPC sensors are indefinitely air stable and, therefore, can be used to sense atmospheric analytes. 2D arrays of ~640 nm polystyrene nanospheres were attached to the surface of crosslinked poly(hydroxyethyl methacrylate) (pHEMA)-based polymer networks dispersed in EGP. The wavelength of the bright 2D photonic crystal diffraction depends sensitively on the 2D array particle spacing. The volume phase transition response of the EGP-pHEMA system to water vapor or gaseous ammonia changes the 2DPC particle spacing, enabling the visual determination of the analyte concentration. Water absorbed by EGP increases the Flory-Huggins interaction parameter, which shrinks the polymer network and causes a blue shift in the diffracted light. Ammonia absorbed by the EGP deprotonates the pHEMA-co-Acrylic Acid carboxyl groups, swelling the polymer which red shifts the diffracted light.

4.1 Introduction

There is an ever increasing demand for simple, selective and inexpensive methods for determining the presence of chemical species in the environment. In response, we previously developed 3D and 2D Polymerized Photonic Crystal Sensors that can determine the concentrations of specific analytes in aqueous solutions.[1-6] We designed 3D Polymerized Photonic Crystal Sensors (3DPC) for a variety of analytes such as glucose, for example, where two boronic acid side chains bind a glucose molecule, creating crosslinks that shrink the gel.

Recently we developed a 2D Polymerized Photonic Crystal Sensor (2DPC) that consists of a monolayer array of polystyrene nanospheres (450-650nm diameter) attached to a crosslinked polymer network containing an aqueous mobile phase. These sensing materials are inexpensive and can be used for visual detection of analyte concentrations because the visible light diffracted sensitively depends on the particle spacing of the attached 2D photonic crystal array.

The polymer network is designed to undergo a volume phase transition (VPT) in response to the analyte, which in turn alters the particle spacing of the attached 2D array. For example, we recently fabricated a 2DPC sensor for surfactant detection by attaching a 2D photonic crystal array onto a poly(N-isopropylacrylamide) (pNIPAAm) hydrogel.[1] The polymer hydrogel undergoes a VPT[7]; swelling when the ionic surfactant binds to the hydrogel therefore changing the 2D array particle spacing. This particle spacing change shifts the wavelengths of light diffracted from the 2D array.

The current hydrogel 2DPC and 3DPC cannot be easily used to sense analytes in the vapor phase because the mainly aqueous mobile phase has a high vapor pressure. In the work here, we demonstrate the development of an air-stable 2DPC that utilizes an ionic liquid as the mobile phase; ionic liquids generally have negligible vapor pressures. We show that these ionic

liquid 2DPC (IL2DPC) can be used to measure gas phase analytes such as the water and ammonia vapor in air.

These IL2DPC consist of 2D photonic crystals attached to responsive polymer networks that are in contact with an ionic liquid mobile phase. Ionic liquid-polymer composite materials are fabricated by polymerizing the monomers within ionic liquids or by exchanging a solvent with an ionic liquid after polymerization.[8-11] These IL2DPC are stable in air due to the ionic liquid's negligible vapor pressure.[12] Previous work utilizing polymers dispersed in ionic liquid media include that of Furumi et al[10] who fabricated an air-stable 3D colloidal crystal gel film that was used as a laser gain medium by exchanging the aqueous medium of the 3D polymerized crystalline colloidal array (PCCA) with the ionic liquid 1-allyl-3-butylimidazolium bromide. Kanai et al[11] also fabricated a 3D PCCA by exchanging the aqueous media with an ionic liquid. They demonstrated the occurrence of the polymer VPT in response to changes in the free energy of mixing by utilizing ionic liquids with different solubility parameters.

Polymer-ionic liquid systems can display VPT, where the mechanisms of response are similar to those of hydrogels. A photoinduced VPT was observed for an azobenzene-containing polymer-ionic liquid composite[13], similar to what we previously demonstrated in hydrogels.[14, 15] These systems contained azobenzene derivatives that reversibly switched between cis- and trans-conformations when irradiated with visible or UV light. This switching results in changes in the polymer solubility parameters, causing a VPT between these two states. In addition, an ionic liquid-polymer material using benzospiropyran switching was recently fabricated for use as a light switching microfluidic valve.[16] The microfluidic valve opens when the polymer is irradiated with light. This photosensitive spiropyran ionic liquid-polymer is similar to the light responsive 3DPC hydrogel switching material we previously pioneered.[17]

The utilization of polymerizable cations in an ionic liquid allow for the fabrication of poly(ionic liquid) materials. A poly(ionic liquid) 3DPC was fabricated by photo-copolymerization of the ionic liquid, 1-(2-acryloyloxyhexyl)-3-methylimidazolium bromide with methylmethacrylate around a 3D close packed array of monodisperse SiO2 particles.[18] An inverse opal is formed by etching away the SiO2 particles. The polymer swells upon water absorption presumably because the ionic liquid molecules become hydrated forming free anions and immobilized cations. This polymer responds to saturated ethanol vapors if the ionic liquid anions are exchanged with SDS anions. The ionic liquid containing SDS anions is more hydrophobic, which causes the poly(ionic liquid) to preferentially absorb ethanol. Ionic liquids have been called 'designer solvents' because their properties can be tuned by varying the cation/anion pair.

The IL2DPC humidity sensor described in this paper consists of a pHEMA 2DPC swollen in the ionic liquid, ethylguanidine perchlorate (EGP). EGP is an excellent solvent for pHEMA; it causes the polymer to swell to more than four times its volume in pure water. The free energy of mixing between EGP and pHEMA becomes less favorable as hygroscopic EGP absorbs water from humid environments; this causes the swollen pHEMA to shrink; blue shifting the diffracted wavelengths.

There are a number of different methods for measuring humidity. The most accurate current methods include chilled mirror dew point hygrometers, capacitive and resistive humidity sensors, thermal conductivity humidity sensors and gravimetric hygrometers. These methods are very sensitive, for example the chilled mirror dew point hygrometer has an accuracy of 1.2 % relative humidity (RH). All of the aforementioned hygrometers require some power source.

Here we report a humidity sensor that does not require a power source, and instead changes color in response to humidity.

We also fabricated an IL2DPC ammonia gas sensor that consists of a crosslinked pHEMA-co-acrylic acid polymer 2DPC. Acrylic acid carboxyls ionize in the presence of ammonia, resulting in a more favorable free energy of mixing between the polymer and EGP. This causes the IL2DPC to swell in the presence of ammonia and red shift the light diffracted.

Many industries such as fertilizer manufacturers and power plants require storage of large amounts of pressurized anhydrous ammonia on site. Current fire and building codes require that engine rooms and refrigerated spaces have ammonia detectors. Exposure to ammonia irritates the eyes, respiratory system, and skin at concentrations as low as 30 ppm. Ammonia causes necrosis of the skin and long-term damage to the eyes and respiratory system occur at higher concentrations (>200 ppm).[19] Ammonia can also become explosive at very high concentrations.[20]

Current ammonia sensors include metal oxide sensors and conducting polymer detectors which have about 1 ppm detection limits and different optical or spectroscopic methods that are able to detect as low as 1 ppb for absorption spectroscopic methods.[21] The inexpensive IL2DPC sensors developed here can easily detect 3 ppm NH3 and do not require expensive electronics as it is monitored by the visual determination of color changes.

4.2 Experimental

4.2.1 Materials

Barium perchlorate (97% Sigma), 1-ethylguanidine sulfate (98% Sigma), N,N' methylene bisacrylamide (BIS) (98% Sigma), 2,2-diethoxyacetophenone (DEAP) (>95% Sigma), 1-propanol (≥99.5% Sigma), and ammonium hydroxide (28.0-30.0% Sigma) were used as received. Hydroxyethylmethacrylate (HEMA) (97% Sigma) and acrylic acid (AA) (98% Sigma) were distilled under reduced pressure and stored at 4°C. A Fischer Scientific Traceable Dew point/Wet bulb/Humidity and Thermometer and Dri-Rite was purchased from Fischer Scientific. The BW Honeywell GasAlert Extreme Ammonia 0-400 ppm Monitor and the calibration gas (50 ppm) were purchased from Honeywell. Stericup GP Filter Units (0.22 μm) were purchased from Millipore. The nanopure water was obtained from a Barnstead Infinity Nanopure water purifier.

4.2.2 Ionic Liquid, Ethylguanidine Perchlorate (EGP) Synthesis

100 ml of 0.4 M barium perchlorate in water was added to 100 ml of 0.4 M ethylguanidine sulfate in water with vigorous stirring. The barium sulfate precipitate was separated by centrifugation followed by vacuum filtration of the supernatant liquid using a stericup filter unit. Water was evaporated under reduced pressure at 60°C by using a Rotovap. The ionic liquid, ethylguanidine perchlorate (Figure 4.1) was further dehydrated by exposing it to a high vacuum pump for several days. It was then stored in a desiccator. Humidity inside the desiccator was 0.5% Relative Humidity (RH).

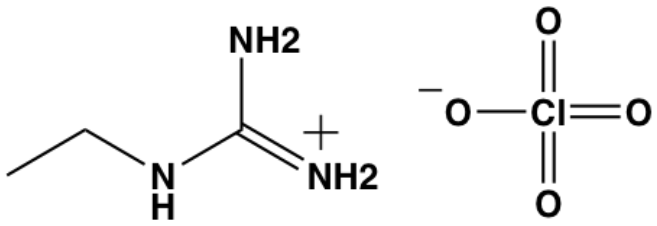

Figure 4.1 - Structure of ethylguanidine perchlorate ionic liquid.

4.2.3 Fabrication of IL2DPC Humidity Sensors

The polymerizable monomer solutions used to fabricate the IL2DPC humidity detectors contained 20 wt% HEMA, 1 wt% BIS as the crosslinker, and 30 wt% EGP (density = 1.4 g/mL) in water. 20 µL of a photoinitiator solution consisting of 30 wt% DEAP in DMSO was added per 1 mL of monomer solution. The co-solvent, EGP, functions in a way similar to that of propylene glycol, preventing pHEMA polymerization induced phase separation in order to produce transparent polymer films.[22]

The monomer solution was sandwiched between two glass slides with a spacer in between to produce 500 µm thick films. One of the slides had the 2D array on its surface. Fabrication of monodisperse polystyrene spheres as well as deposition of 2D arrays onto water and glass microscope slides were previously described.[4, 28]

The monomer solution was UV polymerized, by using 365 nm UV light from a 6-Watt Handheld UV Lamp (UVP UVGL-55 365nm) to catalyze the free radical polymerization. After UV light polymerization for 15 min, the polymer film with the 2D array attached to the surface was peeled from the slides and cut into pieces (~1 cm2). The IL2DPC pieces were washed with pure EGP several times to remove any unreacted monomers and water. IL2DPC were sealed in a vial with fresh EGP and stored in a desiccator until use.

4.2.4 Testing Humidity Sensor Response

4.2.4.1 Stagnant Air Response

IL2DPC sensor pieces (1 cm x 1 cm x 0.04cm) were placed in a small dish with 2 mL pure EGP. The particle spacing was measured before exposing the films to humid environments. Humidity was controlled inside a closed desiccator using the supersaturated salt solutions listed in Table 4.1. The relative humidity (RH) and temperature in the desiccators were monitored using the Fisher Scientific hygrometer. The pHEMA IL2DPC was exposed to each humidity for 48 hours before the particle spacing was measured, after which the supersaturated salt solution was exchanged to increase the humidity inside the chamber. We directly monitored the water concentration absorbed by EGP using near IR absorption measurements as described in Appendix B.

The particle spacings of the pHEMA IL2DPC samples in small dishes with 2 mL EGP were measured daily for 1 week. Samples were exposed to either 0.5% RH or 53% RH.

Table 4.1 - Salts used to make supersaturated solutions and their % relative humidies at 23 ºC

Salt	% Relative Humidity at 23 ºC
Lithium Chloride	11
Potassium Acetate	23
Magnesium Chloride	33
Magnesium Nitrate	53
Sodium Chloride	75
Potassium Chloride	84
Potassium Sulfate	97

4.2.4.2 Flowing Air Response

pHEMA IL2DPC pieces (5 mm x 5 mm x 0.4 mm) are placed on a glass cover slip, then placed in a desiccator to equilibrate to 0.5%RH. This desiccator is placed inside a glove box that contains a large dish of a supersaturated NaCl solution and three smalls fans to gently circulate the air surrounding the Debye Ring measurement apparatus. The humidity inside glove box is 70% RH. The samples on the cover slips are removed from the desiccator and the Debye ring is measured over the course of 5 hours.

4.2.4.3 Direct Water Addition

The particle spacings were measured for solutions with defined mole fractions of water in EGP after equilibrium is reached. The particle spacings were monitored while being cycled through increasing and decreasing concentrations of water in EGP. The particle spacings were also measured for samples over shorter time intervals. A pHEMA IL2DPC sample is placed in a vial with 500 µL of EGP and the Debye ring is measured through the vial. 85 µL of water (~0.5 mole fraction) is added and the vial is swirled until the two liquids mix completely. The Debye ring is then measured over the course of 5 hours. Then 250 µL of EGP is added to the solution to decrease the water concentration. Again, the Debye ring is measured over the course of 5 hours.

4.2.5 Fabrication of IL2DPC Ammonia Sensors

An IL2DPC containing carboxyl groups was fabricated for ammonia detection. A 500 µm thick pHEMA IL2DPC was fabricated in the same manner as described above by using a monomer solution containing 17 wt% HEMA, 1 wt% BIS, and 30 wt% EGP in water. After UV polymerization for 15 min, the polymer films with the imbedded 2D array were peeled from the

slides and swollen in a second monomer solution containing 15 wt% HEMA, 7 wt% AA, 1 wt% BIS and 50 wt% EGP in water. UV polymerization of the second monomer solution results in an interpenetrating network (IPN) of the pH sensitive polymer. The IPN-IL2DPC film was peeled from the glass slide and cut into pieces (1 cm x 1 cm x 0.04 cm). The IPN-IL2DPC films were then washed in pure EGP several times to remove unreacted monomers and water and then sealed in a vial with fresh EGP and stored in a desiccator until use.

4.2.6 Testing Ammonia Sensor Response

4.2.6.1 Stagnant NH_s Response

The IPN-IL2DPC pieces were placed in a small dish in contact with 2 mL of EGP in an air tight glass desiccator along with the GasAlert Extreme NH_3 sensor. A beaker with 40 ml of NH_4OH solution was utilized as the NH_3 source. The concentration of gas phase NH_3 was directly measured using the GasAlert Extreme NH_3 sensor. The IL2DPC were initially equilibrated to the humidity inside the desiccator for 48 hours prior to ammonia measurements; the beaker contained 40 mL of pure water. The NH_3 concentration was increased by increasing the NH_4OH concentration, using freshly made NH_4OH solutions. The particle spacings of the IPN-IL2DPC were measured after 24 hr exposure to the ammonia.

4.2.6.2 Flowing NH_3 Response

IPN-IL2DPC pieces are placed in a small dish with 250 μL of EGP and allowed to equilibrate inside the 60% RH glove box with three small fans that gently circulate the air. We very roughly adjusted the equilibrium NH_3 concentrations by mixing the air of a small reservoir

of high NH_3 concentration with air in a large reservoir. The Debye ring is measured over the course of 4 or 10 hours.

4.2.7 Monitoring Particle Spacings of IL2DPC Sensors

The magnitude of the VPT of the IL2DPC polymer as observed by the shift in the diffracted light wavelength due to changes in the particle spacing of the embedded 2D array depends upon the amount of analyte present.

When a laser pointer irradiates the 2D array at normal incident, the light is strongly forward diffracted. If the laser irradiated a single 2D array domain, six spots corresponding to the longest six reciprocal 2D array lattice vectors would be observed. In our case, the beam is diffracted by multiple randomly oriented crystal domains. The diffraction occurs in a Debye ring (Figure 4.2). The diameter of the Debye ring depends on the particle spacing of the IL2DPC.[25]

Our IL2DPC sample was placed on a microscope slide parallel to the bench top, 8.9 cm above the surface. A 532 nm laser pointer irradiated the sample at normal incident and the diameter of the Debye ring was measured below on a piece of paper. The diffraction angle, θ, was determined from the Debye ring radius as shown in Figure 4.2C (Equation 4.1). The particle spacing was calculated from the 2D Bragg diffraction condition (Equation 4.2).[25, 29, 30] This equation can be simplified for the normal incidence angle θ˚=0. The equation is therefore rearranged to solve for the lattice spacing, d (Equation 4.3).

$$\textbf{Equation 4.1} \quad \boldsymbol{\theta = tan^{-1}\frac{r}{h}}$$

$$\textbf{Equation 4.2} \quad \boldsymbol{\lambda = \frac{\sqrt{3}d}{2}(sin\,\theta^{\circ} + sin\,\theta)}$$

$$\textbf{Equation 4.3} \quad \boldsymbol{d = \frac{2\lambda}{\sqrt{3}\,sin\,\theta}}$$

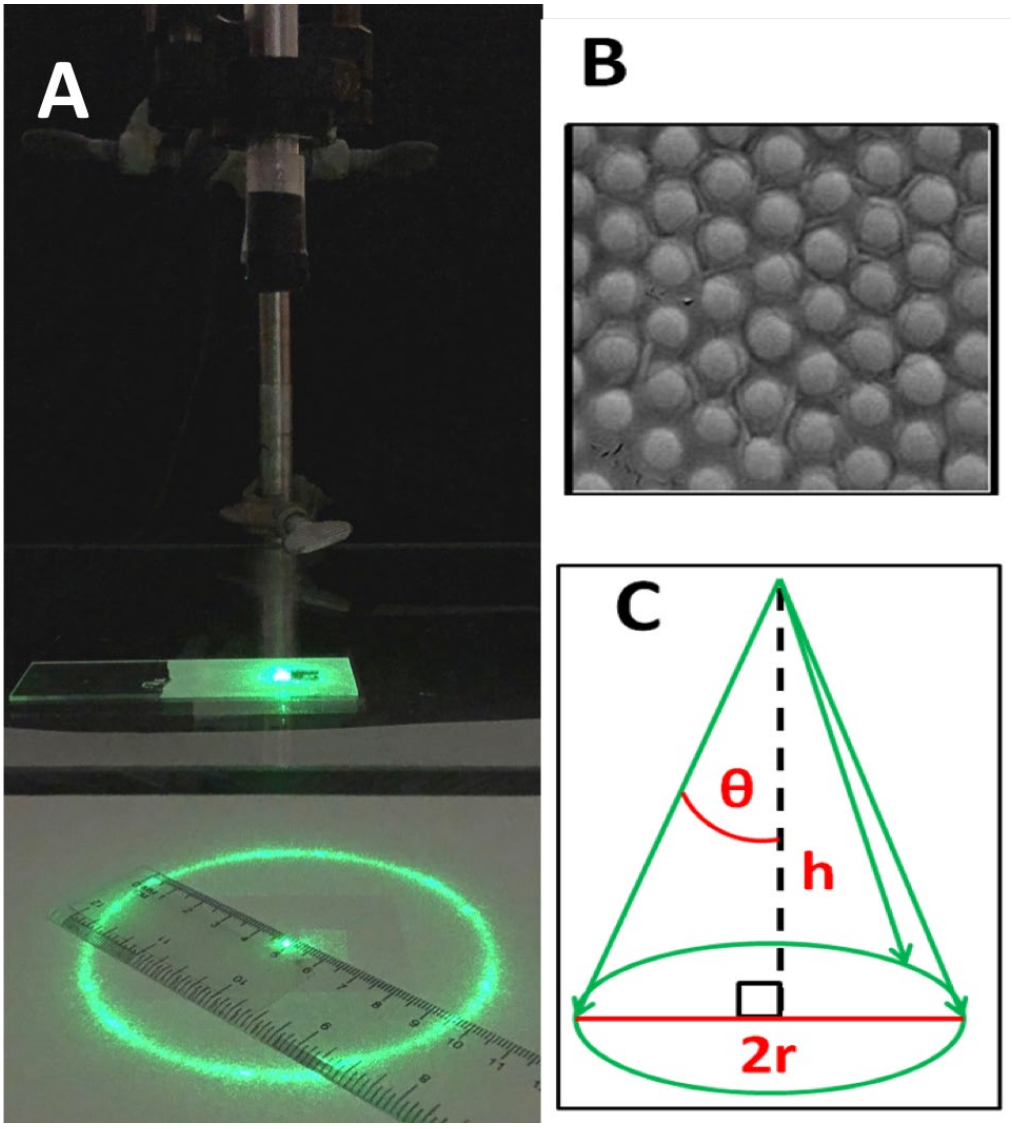

Figure 4.2 - Debye ring diffraction measurement. (A) The laser pointer beam (532 nm light) incident along the array normal is diffracted, producing a Debye ring. (B) Shows a SEM image of the 2D array 2DPC containing ~500 nm particles. (C) Illustrates the relationship between the diffraction angle, θ and the radius of the Debye ring, r.

4.3 Results and Discussion

4.3.1 IL2DPC Fabrication

To fabricate 2DPC to sense gas phase species we utilized the ionic liquid EGP as the mobile phase to solvate pHEMA. EGP is a compatible co-solvent that enables polymerization of transparent pHEMA films. Compatible polymer-solvent systems do not undergo phase separations and generally have a Flory-Huggins Interaction Parameter, χ below 0.5.[7, 22]

χ is a function of the difference between the solubility parameters of the polymer and solvent, δ_P and δ_S, (Equation 4.4).

$$\textbf{Equation 4.4} \quad \chi = \frac{V_m}{RT}(\delta_S - \delta_P)^2$$

where V_m is the solvent molar volume, T is the absolute temperature, and R the ideal gas constant.

Aqueous HEMA solutions undergo polymerization induced phase separations due to the large difference between the solubility parameters of pHEMA (δ=26.9 $MPa^{1/2}$) and water (δ=47.9 $MPa^{1/2}$).[22] Phase separation is undesirable because the resulting film turbidity that reduces the 2DPC light diffraction. Co-solvents can be used to alter δ_S, to minimize χ by minimizing the difference between δ_P and δ_S. For example, propylene glycol or ethylene glycol can be used as a co-solvent for aqueous HEMA solutions to produce transparent hydrogels.[22]

For our sensors we find that EGP lowers the interaction parameter below χ = 0.5, which produces transparent gels when EGP is used at 30 wt% (23 vol%) in a 20 wt% HEMA solution. The IL2DPC, polymerized using 23 vol % EGP, swells in pure EGP because the interaction

parameter between pHEMA and the solvent decreases with increasing EGP concentrations. The very large swelling indicates that their solubility parameters are very close.

4.3.2 Stability of IL2DPC in Air

IL2DPC are stable at room temperature in dry environments in contrast to hydrogel 2DPC and 3DPC that collapse when the water evaporates.[10, 23] Figure 4.3A shows the dependence of the particle spacing to exposure to stagnant 0.5% and 50% relative humidity environments. The particle spacing decreases as the initially dry EGP medium absorbs moisture and reaches equilibrium. The particle spacing then remains constant after equilibration. The IL2DPC particle spacing change is dependent on the relative humidity. The particle spacing change is 3 nm when the IL2DPC is exposed to the 0.5% RH while the IL2DPC particle spacing exposed to 50% RH decreases 8 nm.

4.3.3 IL2DPC Humidity Sensor

Flory Rehner solution theory models the polymer VPT as being induced by osmotic pressure within the system, Π_{Total} (Equation 4.5).[7, 24] The total osmotic pressure of a non-ionic polymer is the sum of the osmotic pressures generated by changes the free energy of mixing, ΔG_{mix} (Equation 4.6) and the elastic free energy, ΔG_{El} (Equation 4.7). The VPT relieves the osmotic pressure in the system so that the net osmotic pressure becomes zero at equilibrium.

At equilibrium the interaction parameter, χ can be related to the swelling ratio, $q= V/V_o$ (Equation 4.8).[7] Here V is the volume of the swollen polymer, V_o is the volume of the dried polymer gel, V_r is the volume of the relaxed polymer and n_{CL} is the number of crosslinks.

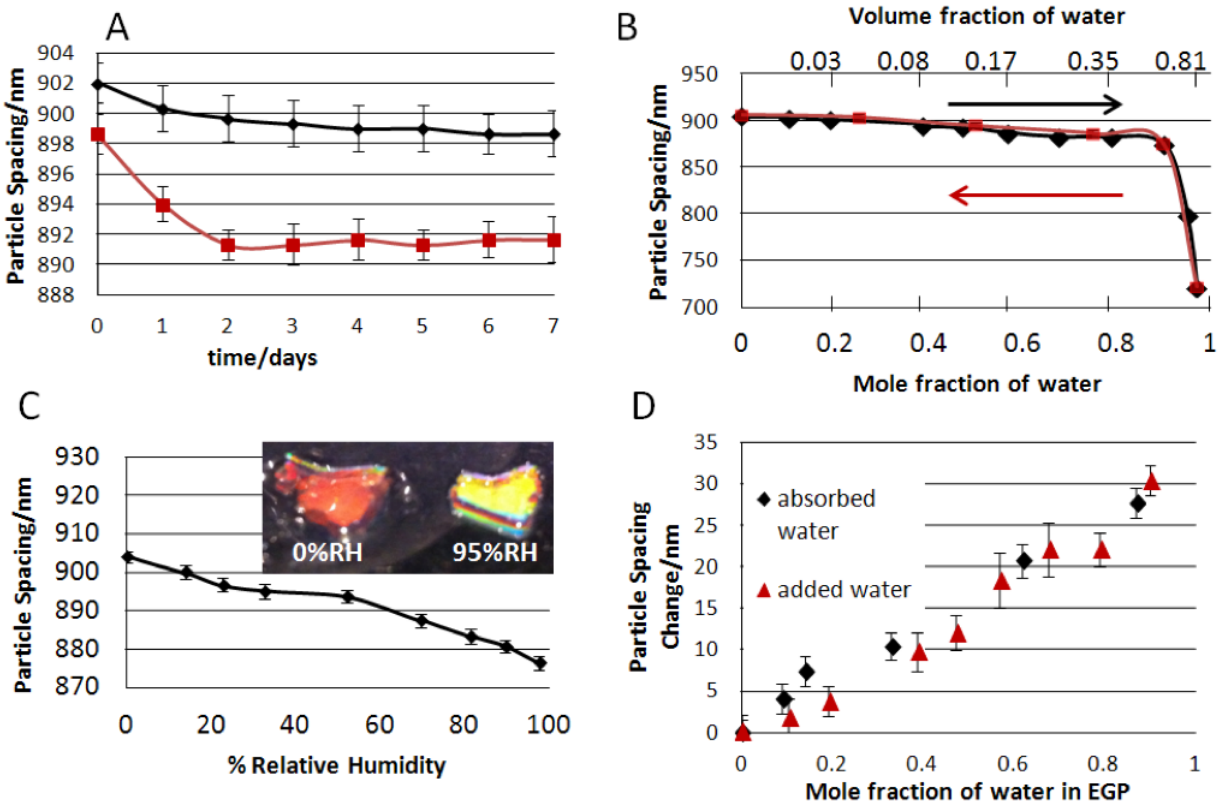

Figure 4.3 - (A) Stagnant Air time dependence of IL2DPC particle spacing exposed to 0.5 % RH (black) and 52% RH (red). (B) Particle spacing of pHEMA IL2DPC as a function of the mole fraction of water directly added to EGP. The black line shows particle spacing during increasing water concentrations, while red line shows particle spacings as water concentration decreases. The upper abscissa shows the volume fraction of water in EGP corresponding to 0.2, 0.4, 0.6, 0.8 and 0.97 water mole fractions. (C) Dependence of the particle spacing of pHEMA IL2DPC on water absorbed at different RH. The inset shows the diffraction colors of IL2DPC humidity sensors exposed to 0% RH(left) and 95% RH (right). The IL2DPC were placed on a mirror so that the forward diffracted light reflects back to the camera. (D) Particle spacing change for pHEMA IL2DPC as a function of the water mole fraction in EGP. Water was either directly added to EGP (red) or absorbed from air (black).

$$\textbf{Equation 4.5} \quad \frac{\partial \Delta G_{total}}{\partial V} = \Pi_{Total} = \Pi_{Mix} + \Pi_{El}$$

$$\textbf{Equation 4.6} \quad \Pi_{Mix} = -\frac{\partial \Delta G_{Mix}}{\partial V} = -\frac{RT}{V_m}\left[\ln\left(1 - \frac{V_o}{V}\right) + \frac{V_o}{V} + \chi\left(\frac{V_o}{V}\right)^2\right]$$

$$\textbf{Equation 4.7} \quad \Pi_{El} = -\frac{\partial \Delta G_{El}}{\partial V} = -\frac{RTn_{CL}}{V_r}\left[\left(\frac{V_r}{V}\right)^{1/3} - \frac{V_r}{2V}\right]$$

$$\textbf{Equation 4.8} \quad \chi = -\left[\frac{\ln\left(1-\frac{V_o}{V}\right)+\frac{V_o}{V}+\frac{n_{CL}}{V_r}\left[\left(\frac{V_r}{V}\right)^{1/3}-\frac{V_r}{2V}\right]}{\left(\frac{V_o}{V}\right)^2}\right]$$

We monitor the particle spacing changes, which disclose the swelling behavior that results from interaction parameter changes due to solvent composition changes. The addition of water to EGP increases the interaction parameter, shrinking the polymer as shown in Figure 4.3B. Unfavorable changes in the free energy of mixing between pHEMA and the solvent occur as the increasing water content increases the solvent solubility parameter (Equation 4.9). This process is fully reversible as shown in Figure 4.3B.

$$\textbf{Equation 4.9} \quad \delta_s = \sum_i \varphi_i \delta_i$$

4.3.3.1 Stagnant Air Response

The dependence of the particle spacings of pHEMA IL2DPC in EGP on the %RH is shown in Figure 4.3C. The particle spacing decreases as humidity increases as EGP absorbs more water at higher %RH. The mole fraction of water absorbed by EGP was directly measured using the near IR absorption overtones of water at 1420 nm and 1915 nm. The IR spectra used to generate the calibration curve and the IR spectra of EGP at different %RH are shown in Appendix B.

The mole fraction of water absorbed by EGP is less than expected for an ideal solution indicating that the activity of water in EGP is higher than in pure water. This is similar to the

increased water activity observed for many cholinium based ionic liquids.[114] Figure 4.3D shows similar particle spacing changes for our pHEMA IL2DPC when water was either directly added (red) versus being absorbed from the air (black).

4.3.3.2 Flowing Air Response

The data in Figure 4.3A was taken in stagnant air conditions where equilibration was limited by diffusion of water into the head space of the vials and by slow diffusion of water into the 2 mL EGP reservoir. This slow two day equilibration time was significantly decreased to 100 minutes by flowing humid air over the sensor in the presence of minimal excess EGP as shown in Figure 4.4A. The equilibration time in flowing air is much faster but we observe a transient swelling event in the first 20 minutes before the pHEMA gel relaxes and returns to equilibrium.

This short time transient behaviour is observed both when water is absorbed from the air and when water is directly added to EGP as shown in Figure 4.4B. The initial swelling is driven by equilibration of the water concentration which causes the gel to swell because water diffuses in before the EGP can escape. The subsequent shrinking is due to slower diffusion of the bulky EGP as the system comes to equilibrium. This transient behaviour also occurs in the reverse direction when the water concentration is decreased. The network initially shrinks as water leaves the polymer network to mitigate the chemical potential difference across the membrane then subsequently swells as the polymer relaxes to equilibrium and EGP diffuse into the gel.

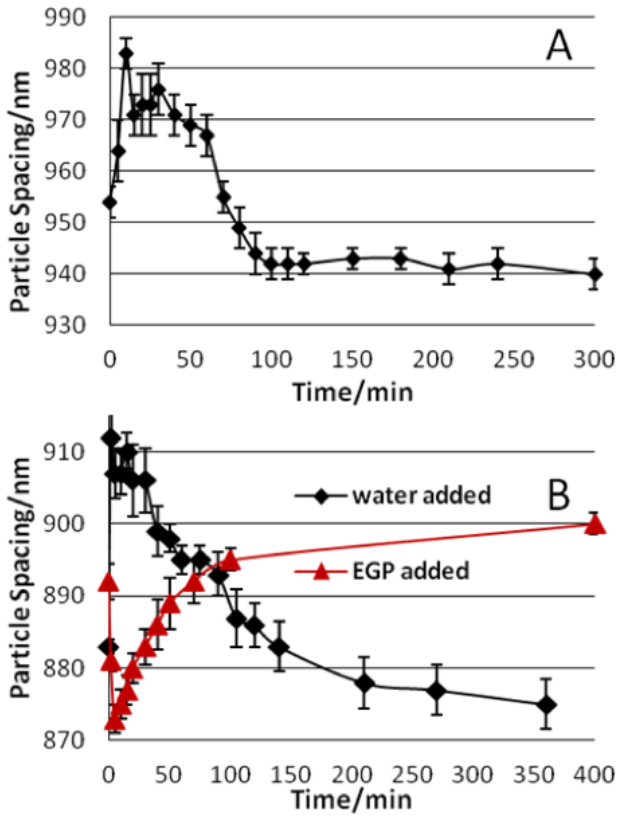

Figure 4.4 - Flowing air time dependence of IL2DPC particle spacing at small time intervals. (A) Swelling when gel is exposed to 70% RH. (B) Swelling when water is directly added to EGP (black diamonds) and when EGP is directly added to a EGP/water mixture (red triangles).

4.3.4 Ammonia Detection

The IPN-IL2PCS ammonia sensor utilizes a pH sensitive interpenetrating network (IPN) made by polymerizing acrylic acid. Ammonia absorbed by the ionic liquid deprotonates the acrylic acid carboxyl groups, localizing anionic carboxylates on the polymer. Ammonia selectively deprotonates the poly(acrylic acid).

In low ionic strength solutions, localization of charges on the polymer creates a Donnan potential that causes polymer swelling. However, these charges have little impact on polymer swelling in very high ionic strength solutions such as in ionic liquids. Thus, the VPT observed

due to polymer deprotonation by ammonia derives mainly from a change in the free energy of mixing. The localization of charges on the polymer increases favorable interactions between the polymer and ionic liquid therefore lowering the interaction parameter and swelling the polymer (Figure 4.5). This deprotonated polymer swelling that stems from a change in the free energy of mixing was previously described in our creatinine sensor designed for use in high ionic strength blood or serum samples.[27]

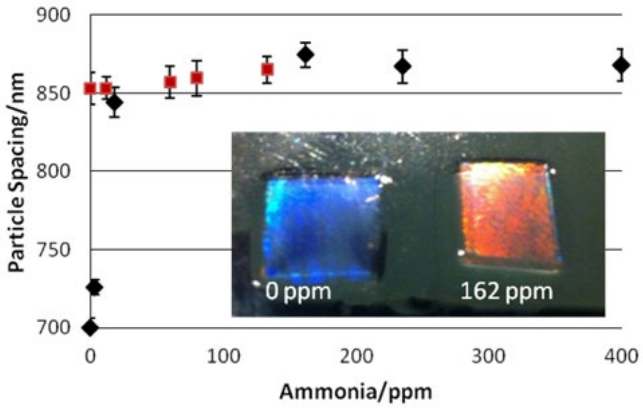

Figure 4.5 - Dependence of particle spacing of IPN-IL2DPC on air ammonia concentration. The black diamonds indicate the particle spacing as the ammonia concentration increases, while the red squares indicate the particle spacing as the ammonia concentration decreases. The inset shows the diffraction colors of IPN-IL2DPC ammonia sensors exposed to 0 ppm (left) and 162 ppm (right) ammonia. The IPN-IL2DPC were placed on a mirror so that the forward diffracted light reflects back to the camera.

The IPN-IL2DPC response to ammonia is irreversible; the sensor acts as a dosimeter. The IPN-IL2DPC response measured after 24 hr saturates when all the carboxyl groups are deprotonated by the absorbed ammonia. The sensor is irreversible since the equilibrium lies far towards NH_4^+ and carboxylates, neither of which have significant vapor pressures.

The IPN-IL2PCS is very sensitive to low ammonia concentrations. The particle spacing increases 25 nm for 3 ppm ammonia in stagnant air after 24 hours. The 24 hr observed red shift saturates above 18 ppm ammonia. The Figure 4.5 inset shows the visually evident color change associated with ammonia exposure.

The ammonia concentrations in air determine the rate of change of the particle spacings. The transport rate of NH_3 into the system depends on the NH_3 concentration at the sensor. Figure 4.6A shows the particle spacing change for an IPN-IL2DPC exposed to 10 ppm and 90 ppm NH_3. The particle spacing of the IPN-IL2DPC exposed to the higher NH_3 gas concentration increases faster than the IPN-IL2DPC exposed to 10 ppm NH_3. Figure 4.6B shows the particle spacing change that occurs during the first 15 minutes of exposure. The slope of the particle spacing change for the IPN-IL2DPC exposed to 10 ppm NH_3 is 0.9 nm/min. The slope increases to 1.8 nm/min when the IPN-IL2DPC is exposed to 90 ppm NH_3.

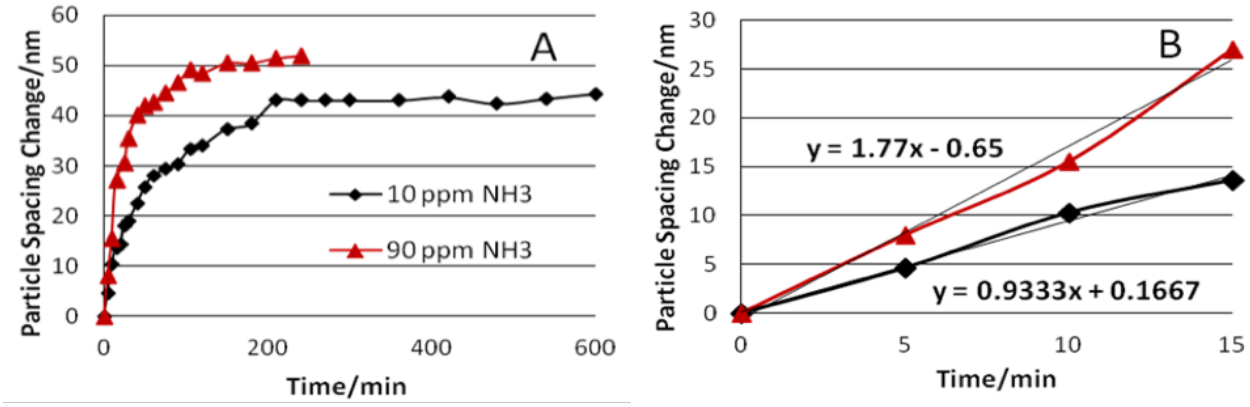

Figure 4.6 - (A) The particle spacing change, ($d-d_o$) over time for IPN-IL2DPC exposed to 10 ppm NH_3 (black diamonds) and 90 ppm NH_3 (red triangle). (B) Particle spacing change during the first 15 minutes. Equations for the linear trendlines are included for both 10 ppm and 90 ppm NH_3.

4.4 Conclusions

We developed a photonic crystal responsive material for the visual determination of gas phase analytes such as water vapor and ammonia. The ionic liquid ethylguanidine perchlorate (EGP) was utilized as the mobile phase for a poly(hydroxyethylmethacrylate) (pHEMA) organogel networks. The ionic liquid-polymer system undergoes a volume phase transition in response to changes in the Gibbs free energy of mixing. This volume change shifts the wavelength of light diffracted from the embedded photonic crystal. The humidity sensor blue shifts when water is absorbed by EGP due to the change in the solubility parameter of the mobile phase. A transient volume phase transition at small time scales is observed due to fast diffusion of water into the EGP-polymer network. The ammonia sensor red shifts when NH_3 is absorbed because the NH_3 deprotonates the polymer carboxylate groups, localizing charges on the polymer. The rate at which the particle spacing changes reports on the concentration of ammonia present.

This novel IL2DPC gas sensing demonstrates proof of concept for a new generation of 2DPC air sensors that use ionic liquids as their mobile phase. There is a great need for detecting airborne analytes such as environmental toxins, chemical warfare agents, etc. Our IL2DPC can provide visually evident determination of atmospheric chemical threats. The sensors demonstrated here are far from optimized in their sensitivity and optical response. These IL2DPC sensors are easily fabricated and should be inexpensive to manufacture.

4.5 References

1. Asher, J.-T. Z. N. S. S., Two Dimensional Photonic Crystal Surfactant Detection. *Analytical Chemistry.* **2012,** *84*, 6416-6420.

2. Zhang, J.-T.; Wang, L.; Luo, J.; Tikhonov, A.; Kornienko, N.; Asher, S. A., 2-D Array Photonic Crystal Sensing Motif. *Journal of the American Chemical Society.* **2011,** *133*, 9152-9155.

3. Zhang, J.-T.; Wang, L.; Chao, X.; Asher, S. A., Periodicity-Controlled Two-Dimensional Crystalline Colloidal Arrays. *Langmuir.* **2011,** *27*, 15230-15235.

4. Zhang, J.-T.; Wang, L.; Lamont, D. N.; Velankar, S. S.; Asher, S. A., Fabrication of Large-Area Two-Dimensional Colloidal Crystals. *Angewandte Chemie International Edition.* **2012,** *51*, 6117-6120.

5. Goponenko, A. V.; Asher, S. A., Modeling of Stimulated Hydrogel Volume Changes in Photonic Crystal Pb2+ Sensing Materials. *Journal of the American Chemical Society.* **2005,** *127*, 10753-10759.

6. Ben-Moshe, M.; Alexeev, V. L.; Asher, S. A., Fast Responsive Crystalline Colloidal Array Photonic Crystal Glucose Sensors. *Analytical Chemistry.* **2006,** *78*, 5149-5157.

7. Flory, P. J., *Principles of Polymer Chemistry*. Cornell University Press: 1953.

8. Susan, M. A. B. H.; Kaneko, T.; Noda, A.; Watanabe, M., Ion Gels Prepared by in Situ Radical Polymerization of Vinyl Monomers in an Ionic Liquid and Their Characterization as Polymer Electrolytes. *Journal of the American Chemical Society.* **2005,** *127*, 4976-4983.

9. Snedden, P.; Cooper, A. I.; Scott, K.; Winterton, N., Cross-Linked Polymer−Ionic Liquid Composite Materials. *Macromolecules.* **2003,** *36*, 4549-4556.

10. Furumi, S.; Kanai, T.; Sawada, T., Widely Tunable Lasing in a Colloidal Crystal Gel Film Permanently Stabilized by an Ionic Liquid. *Advanced Materials.* **2011,** *23*, 3815-3820.

11. Kanai, T.; Yamamoto, S.; Sawada, T., Swelling of Gel-Immobilized Colloidal Photonic Crystals in Ionic Liquids. *Macromolecules.* **2011,** *44*, 5865-5867.

12. Ueki, T.; Watanabe, M., Polymers in Ionic Liquids: Dawn of Neoteric Solvents and Innovative Materials. *Bulletin of the Chemical Society of Japan.* **2012,** *85*, 33-50.

13. Ueki, T.; Yamaguchi, A.; Watanabe, M., Unlocking of interlocked heteropolymer gel by light: photoinduced volume phase transition in an ionic liquid from a metastable state to an equilibrium phase. *Chemical Communications.* **2012,** *48*, 5133-5135.

14. Kamenjicki, M.; Lednev, I. K.; Asher, S. A., Photoresponsive Azobenzene Photonic Crystals. *The Journal of Physical Chemistry B.* **2004,** *108*, 12637-12639.

15. Kamenjicki, M.; Asher, S. A., Photochemically Controlled Cross-Linking in Polymerized Crystalline Colloidal Array Photonic Crystals. *Macromolecules.* **2004,** *37*, 8293-8296.

16. Benito-Lopez, F.; Byrne, R.; Raduta, A. M.; Vrana, N. E.; McGuinness, G.; Diamond, D., Ionogel-based light-actuated valves for controlling liquid flow in micro-fluidic manifolds. *Lab on a Chip.* **2010,** *10*, 195-201.

17. Kamenjicki Maurer, M.; Lednev, I. K.; Asher, S. A., Photoswitchable Spirobenzopyran-Based Photochemically Controlled Photonic Crystals. *Advanced Functional Materials.* **2005,** *15*, 1401-1406.

18. Huang, J.; Tao, C.-a.; An, Q.; Lin, C.; Li, X.; Xu, D.; Wu, Y.; Li, X.; Shen, D.; Li, G., Visual indication of enviromental humidity by using poly(ionic liquid) photonic crystals. *Chemical Communications.* **2010,** *46*, 4103-4105.

19. OSHA Occupational Chemical Database. Ammonia. https://www.osha.gov/dts/chemicalsampling/data/CH_218300.html. (accessed on May, 12 2014)

20. Center for Disease Control and Prevention. NIOSH. Ammonia. http://www.cdc.gov/niosh/ershdb/EmergencyResponseCard_29750013.html. (accessed on May, 15, 2014)

21. Timmer, B.; Olthuis, W.; Berg, A. v. d., Ammonia sensors and their applications—a review. *Sensors and Actuators B: Chemical.* **2005,** *107*, 666-677.

22. Kwok, A. Y.; Qiao, G. G.; Solomon, D. H., Synthetic hydrogels 3. Solvent effects on poly(2-hydroxyethyl methacrylate) networks. *Polymer.* **2004,** *45*, 4017-4027.

23. Muscatello, M. M. W.; Asher, S. A., Poly(vinyl alcohol) Rehydratable Photonic Crystal Sensor Materials. *Advanced Functional Materials.* **2008,** *18*, 1186-1193.

24. Hirotsu, S.; Hirokawa, Y.; Tanaka, T., Volume-phase transitions of ionized N-isopropylacrylamide gels. *The Journal of Chemical Physics.* **1987,** *87*, 1392-1395.

25. Alexander Tikhonov, N. K., Jian-Tao Zhang, Luling Wang, Sanford A. Asher, Relectivity Enhanced Two-Dimensional Dielectric Particle Array Monoloayer Diffraction. *Journal of Nanophotonics.* **2012,** *6*, 063509-1-063509-9.

26. Khan, I.; Kurnia, K. A.; Sintra, T. E.; Saraiva, J. A.; Pinho, S. P.; Coutinho, J. A. P., Assessing the activity coefficients of water in cholinium-based ionic liquids: Experimental measurements and COSMO-RS modeling. *Fluid Phase Equilibria.* **2014,** *361*, 16-22.

27. Sharma, A. C.; Jana, T.; Kesavamoorthy, R.; Shi, L.; Virji, M. A.; Finegold, D. N.; Asher, S. A., A General Photonic Crystal Sensing Motif: Creatinine in Bodily Fluids. *Journal of the American Chemical Society.* **2004,** *126*, 2971-2977.

28. Reese, C. E.; Asher, S. A., Emulsifier-Free Emulsion Polymerization Produces Highly Charged, Monodisperse Particles for Near Infrared Photonic Crystals. *Journal of Colloid and Interface Science.* **2002,** *248*, 41-46.

29. Prevo, B. G.; Velev, O. D., Controlled, Rapid Deposition of Structured Coatings from Micro- and Nanoparticle Suspensions. *Langmuir.* **2004,** *20*, 2099-2107.

30. Lumsdon, S. O.; Kaler, E. W.; Velev, O. D., Two-Dimensional Crystallization of Microspheres by a Coplanar AC Electric Field. *Langmuir.* **2004,** *20*, 2108-2116.

5.0 Revolutionary Pure Protein Organogel Sensors and Biocatalytic Materials

This chapter has been accepted upon condition of revisions for publication in the journal Applied Materials and Interfaces authored by Smith, N.L.; Coukouma, A.E.; Wilson, D.C.; Ho, B.; Gray, V.P.; Asher, S.A., Manuscript ID:am-2019-09785h, and is reprinted with permission.

Author Contributions: N.L.S. designed and performed experiments and oversaw organogel sensors and catalysts testing. OPH enzymes were recombinantly produced by D.C.W. at FLIR Systems Inc in Pittsburgh, PA. A.E.C assisted with the fabrication and testing of BSA organogels. B.H. and V.P.G. assisted with the fabrication and testing of OPH organogels. The manuscript was prepared by N.L.S with assistance from S.A.A.

Utilizing protein chemistry in organic solvents has important biotechnology applications. Typically, organic solvents negatively impact protein structure and function. Immobilizing proteins via crosslinks to a support matrix or to other proteins is a common strategy to preserve the native protein function. Recently we developed methods to fabricate macroscopic responsive pure protein hydrogels by lightly crosslinking the proteins with glutaraldehyde for chemical sensing and enzymatic catalysis applications. The water in the resulting protein hydrogel can be exchanged for organic solvents. The resulting organogel contains pure organic solvents as their mobile phases. The organogel proteins retain much of their native protein function i.e. protein-ligand binding and enzymatic activity. A step-wise ethylene glycol (EG) solvent exchange was performed to transform these hydrogels into organogels with a very low vapor pressure mobile phase. These responsive organogels are not limited by solvent/mobile phase evaporation. The

solvent exchange to pure EG is accompanied by a volume phase transition (VPT) that decreases the organogel volume compared to that of the hydrogel. Our organogel sensor systems utilize shifts in the particle spacing of an attached 2D Photonic Crystals (2DPC) to report on the volume changes induced by protein-ligand binding. Our 2DPC Bovine Serum Albumin (BSA) organogels exhibit VPT that swell the organogels in response to BSA binding of charged ligands like ibuprofen and fatty acids (Figure 5.1). To our knowledge, this is the first report of a pure protein organogel VPT induced by protein-ligand binding. Catalytic protein organogels were also fabricated that utilize the enzyme Organophosphorus Hydrolase (OPH) to hydrolyze toxic organophosphates (OP) nerve agents (Figure 5.1). Our OPH organogels retain significant enzymatic activity. The OPH organogel rate of OP hydrolysis is >160 times higher than that of uncrosslinked OPH monomers in a 1:1 ethylene glycol: water mixture.

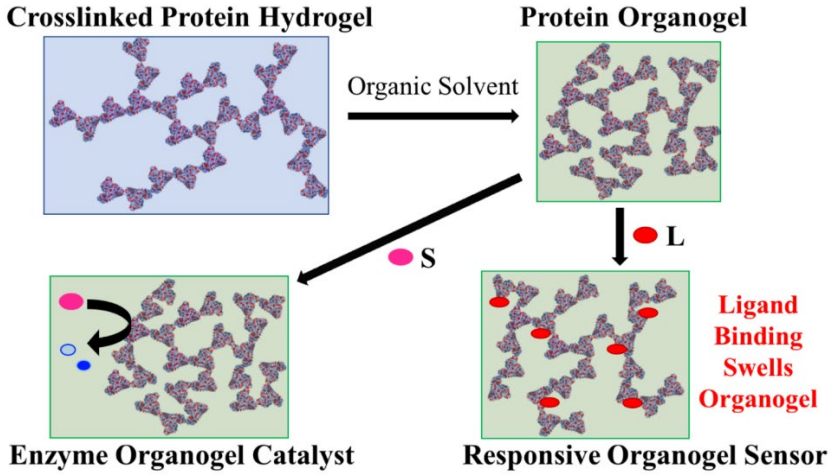

Figure 5.1 - Illustration summerizing the development of pure protein organogel sensors and catalysts. Protein organogel sensors that detect protein-ligand binding were fabricated using BSA. The crosslinked BSA proteins in the organogel retain their native protein-ligand binding affinity. Protein organogel catalysts were fabricated using the enzyme OPH that catalyzes the hydrolysis of organophosphates. This figure was used as the table of contents graphic for publication in Applied Materials and Interfaces.

5.1 Introduction

Hydrogels and organogels consist of three-dimensional polymer networks that utilize water or organic solvents as their mobile phases. Smart hydrogels and organogels contain functional groups, such that the materials are responsive to chemical or physical stimuli such as pH[1, 2], light[3, 4], temperature[5, 6] or to chemical species[7-9]. Responsive hydrogel materials have been designed for selective chemical sensing[10, 11], catalysis[12], and drug delivery systems[5, 13].

Chemoselective responsive hydrogels[14, 15] and organogels[16-18] often incorporate molecular recognition groups within the polymer networks that actuate selective chemical responses such as volume changes, color changes, or that trigger catalysis. We developed multiple hydrogel chemical sensors by attaching molecular recognition groups that induce hydrogel volume phase transitions (VPT) upon analyte binding.[15, 19, 20] This VPT response is understood in the context of Flory-Rehner-Tanaka Theory.[21-23] Chemical binding processes that induce Gibbs free energy changes in the system generate osmotic pressures that swell or shrink the hydrogel or organogel. Small perturbations in the chemical environment can lead to remarkably large VPT.[23] Ultra low limits of analyte detection have been achieved by utilizing molecular recognition groups with large analyte binding affinities.[7]

Proteins serve many roles in biology, including molecular recognition. Proteins evolved highly efficient molecular recognition processes such as having large binding affinities for specific analytes, and for carrying out highly selective enzymatic reactions. Highly chemoselective responsive hydrogels have been fabricated that utilize this protein molecular recognition.[7, 14, 24] For example, we fabricated organophosphate sensors with detection limits of ~4 fM by utilizing the extremely large binding affinity of organophosphates to acetylcholinesterase.[7]

More recently, pure protein hydrogels were developed that consist of physically[12, 25, 26] or chemically[27-30] crosslinked proteins. Each protein monomer acts as a molecular recognition group to maximize the density of hydrogel functional groups. We designed several chemically crosslinked protein hydrogels for chemoselective 2D Photonic Crystal (2DPC) sensor applications using Human and bovine serum albumin (HSA and BSA)[8], Concanavalin A[31], and glucose binding protein[32]. These protein hydrogels retain similar ligand affinities as the native protein monomers. Protein-ligand binding that changes the Gibbs free energy actuates the VPT, which shifts the particle spacing of an embedded 2DPC. Particle spacing changes shift the 2DPC light diffraction and report on the hydrogel volume changes.[33] These pure protein hydrogel sensors are biocompatible and biodegradable[34], making them an attractive sustainable alternative to organic polymer materials derived from petroleum.

The utilization of proteins in organic solvents has numerous applications such as for the synthesis of pharmaceuticals, specialty chemicals, and biofuels[35-37], as well as in the defense and environmental industries for sensing and degrading hazardous compounds.[38] Organic solvents generally deactivate protein function, i.e. ligand binding or catalysis. Organic solvents disrupt the protein-solvent interactions that drive polypeptide folding and control protein secondary and tertiary structures, causing denaturation of the native protein conformation.[39] Protein function is intimately linked to its highly specific 3D conformation, where even slight perturbations from its native structure can have a large impact on the protein's functionality.[40] The protein's conformational flexibility may also decrease in organic solvent by disrupting the solvation shell waters at the protein interface.[37, 39, 41-46] Numerous approaches have attempted to improve protein function in organic solvents; these methods include immobilizing proteins by

crosslinking[42, 43, 47-52] them to either other proteins or to other support materials such as silica or polymers, or by encapsulating the protein within other materials.[42, 49]

Immobilized proteins often show higher activities in harsh environments compared to proteins free in solution. The protein secondary and tertiary structures of immobilized proteins are stabilized due to the accompanying increase in activation barriers for protein denaturation.[53-55] The subunits of immobilized multimeric proteins are also less likely to dissociate.[56, 57] Additionally, proteins immobilized within hydrophilic polymers create favorable microenvironments containing the solvation shell waters that contribute to protein flexibility.[47, 48, 58, 59]

Numerous protein crosslinking stabilization methods have been investigated. For example, crosslinked Enzymes (CLE) were developed in the 1960s.[60] Subsequently, Crosslinked Enzyme Crystals (CLEC)[61] were commercialized by Altus Biologics.[56] Crosslinked Enzyme Aggregates (CLEA®) were developed decades later to overcome the need for enzyme crystallization prior to crosslinking.[47, 56] CLEAs are produced by adding a small concentration of a denaturant such as urea or organic solvent to force protein aggregation. Then a crosslinking agent, commonly glutaraldehyde, is added to crosslink the proteins within the aggregate. These crosslinked enzyme systems exhibit high protein activity in organic solvents.[54, 62] However, the resulting microscopic enzyme particulates (5-50 μm) still require time consuming separation processes that impede their recovery and reuse.

In the work here, we discuss our development of revolutionary responsive protein organogels. We demonstrate their utility for chemical sensing and for enzyme catalysis. Large protein organogel films were fabricated by a stepwise solvent exchange in pure protein hydrogels to replace the aqueous solvent with pure ethylene glycol, a low vapor pressure organic solvent

(0.06 mm Hg at 20° C). We show that our protein organogels retain substantial native protein functionalities such as selective ligand binding and enzymatic activity. The development of our 2DPC organogel sensors enable detection of protein-ligand binding in non-aqueous environments. To the best of our knowledge, this is the first report of a pure protein organogel that exhibits a chemoselective VPT. Our catalytic protein organogels that utilize the enzyme Organophosphorus Hydrolase (OPH) to hydrolyze organophosphate nerve agents exhibit higher enzymatic activity in organic solvents relative to that of the native uncrosslinked enzyme in organic solvent. A dispersion of these biocatalytic organogel films could be used for both personal and large-scale decontamination of environmental toxins.

5.2 Experimental

5.2.1 Materials

Proteins, such as bovine serum albumin (BSA) (>98%; lyophilized powder, essentially fatty acid free, CAS: 9048-46-8), was purchased from Sigma-Aldrich and dissolved in nanopure water at a concentration of 200 mg/mL prior to use. Ibuprofen sodium salt, Sigma-cote®, NaOH pellets, $Ca(NO_3)_2$, $Cu(NO_3)_2 \bullet 3H_2O$, and $CoCl_2$ were purchased from Sigma-Aldrich and used as received. Glutaraldehyde (50 wt % in water) was purchased from Sigma-Aldrich and diluted with nanopure water to make a 12.5 wt % glutaraldehyde solution. Ethylene glycol and glycerol were purchased from Fisher Scientific and used as received. The recombinant Organophosphorus Hydrolase (OPH) (EC 8.1.3.1; 72 kDa) mutant enzyme from *Pseudomonas diminuta* was produced in E. coli at FLIR Systems Inc. The OPH solution contained 5.6 mg OPH/mL in 0.01

M HEPES buffer with 100 μM $CoCl_2$ co-factor at pH 8. Ethyl-Paraoxon (99.9%) was purchased from Chem Service, Inc. and diluted with methanol to make a 152 mM Paraoxon solution and stored at 4° C. in Nanopure water. Paraoxon is a highly toxic chemical. Appendix D provides information on the safety protocols utilized to handle paraoxon.

5.2.2 Fabrication of Protein Organogels

Two pure protein organogels were fabricated for this study. One contained the transport protein BSA, while the other contained the enzyme OPH. Protein hydrogels were fabricated, followed by a stepwise solvent exchange procedure that transformed the protein hydrogels into protein organogels.

5.2.2.1 Fabrication of BSA Hydrogels and Organogels

BSA hydrogels were fabricated first by polymerizing 200 mg/mL BSA solutions, made by dissolving lyophilized BSA solid in nanopure water, between two glass slides using glutaraldehyde as the crosslinker, as described previously.[8] Glass slides were treated with Sigma-cote® so that the glass slide surface was hydrophobic. Scotch tape was layered along the 4 edges of the slide to create a 410 μm thick spacer (measured using a digital micrometer with 10 μm precision). 64 μL of a 12.5% glutaraldehyde solution was added to 1 mL of the 200 mg/mL BSA solution. This solution was polymerized between the slides for 3 hrs at room temperature. The resulting transparent yellow pure BSA hydrogel films contained 15 vol% BSA. The hydrogel films were cut into square pieces. The dimensions of each piece were measured using a digital micrometer before being washed with nanopure H_2O for 48 hr to remove unreacted glutaraldehyde and BSA.

The BSA hydrogels then underwent a stepwise solvent exchange that replaced the aqueous mobile phase with an organic solvent. We used EG as the organic solvent. EG is miscible with water and has a vapor pressure of 0.06 mm Hg at 20 ºC. The dimensions of the BSA hydrogel pieces, equilibrated in nanopure water, were measured before the solvent exchange process. Samples were then incubated in 250 mL of 30 vol% EG aqueous solution for 24 hr, followed by incubation in 250 mL of 50 vol% EG for 24 hr, then incubated in 250 mL of 70 vol% EG for 24 hr. Finally, the samples were equilibrated in pure EG solutions for 48-72 hr, during which the EG solvent was replaced twice a day to remove nearly all the water from the system.

The dimensions of the square BSA hydrogel films were measured using the digital micrometer after equilibrating at each EG concentration. The volume fraction of BSA in the organogel samples equilibrated in each solvent mixture was calculated using the volume swelling ratio, $Q = \left({A_f}/{A_i}\right)^{3/2}$, where A_i and A_f are the areas of the hydrogel/organogel square directly after polymerization and after equilibrating in the solvent mixture, respectively. The volume fraction of BSA in the hydrogel after polymerization is equal to that of the 200 mg/mL BSA solution, ~ 0.15 vol. fraction BSA. The vol. fraction of BSA in the organogel can thus be calculated as $volume\ fraction\ BSA_{organogel} = 0.15/Q$.

5.2.2.2 Fabrication of OPH Hydrogels and Organogels

The OPH enzyme, provided by FLIR Systems Inc., was received as a 5.6 mg/mL OPH solution in 0.01 M HEPES buffer with 100 μM $CoCl_2$ at pH 8. For fabricating OPH hydrogels, the dilute OPH solution was first concentrated to ~200 mg/mL using Millipore Amicon® 30 kDa centrifuge filters. The absorption at 280 nm was measured using a Cary 5000 UV-Vis

Spectrometer. We calculated the OPH concentration using the Beer-Lambert equation. The molar extinction coefficient for the OPH mutant was experimentally determined by FLIR Systems Inc, $\varepsilon_{280nm} = 28290\ M^{-1}\ cm^{-1}$.

Polymerization of the concentrated OPH solution was initiated by adding 24 µL of 5 wt% glutaraldehyde to 400 µL of the 200 mg OPH/mL solution. The OPH was polymerized between two glass slides separated by a spacer of 6 layers of tape for 2 hr at room temperature. The resulting 360 μm thick OPH hydrogel films were washed with pH 8, 100 µM $CoCl_2$, 0.01 M HEPES buffer for 48 hr to remove unreacted glutaraldehyde and OPH. The OPH concentration in the hydrogel was 200 mg/mL.

OPH organogels were fabricated using the same step-wise solvent exchange process as described for the BSA organogels. However, the OPH enzymes, as well as other metalloenzymes[63] require an excess of the co-factor, Co^{2+} for maximum activity.[64] The activity of OPH is maximized in basic solutions[24]; the solutions were adjusted to pH~ 8. Aqueous EG solutions containing 30%, 50% and 70% EG were made using a HEPES buffer that contained $CoCl_2$ mixed with pure EG such that the final concentration in the solution contained 100 µM $CoCl_2$ and 0.01 M HEPES buffer. The pH was adjusted to 8 by addition of solid NaOH. Solid $CoCl_2$ and NaOH were directly dissolved into EG for the 100% EG solutions such that the final pure EG solution contained 100 µM $CoCl_2$ at pH 8.

5.2.3 Fabrication of 2D Photonic Crystal Protein Hydrogels and Organogels

Anionic monodisperse polystyrene spheres (1150 nm diameter) were synthesized via a dispersion polymerization method.[65] The 2DPC are fabricated by self-assembly of the charged particles at the air-water interface using the needle tip-flow self-assembly method we

developed.[66-67] The needle tip-flow method forms a highly ordered close packed particle array at the air-water interface, which is easily transferred to a solid support such as a glass slide.[67] 2DPC BSA hydrogels were fabricated by polymerizing the BSA solution on top of a close packed 2DPC, which embeds the particles on the hydrogel surface, as previously described.[8] We attach 2DPC to the organogel surface after the solvent exchange to pure EG, because otherwise the VPT induced by solvent exchange would disorder the close packed 2DPC particles.

The 2DPC was attached to the surface of BSA organogels equilibrated in pure EG for 48 hrs, as shown in Figure 5.2. First, the organogel film was placed on a glass microscope slide. The organogel on the slide has a thick layer of EG surrounding it. Excess EG on the slide and organogel surface was removed by flushing the surface with a stream of nanopure water. A thick layer of EG surrounding the organogel impedes 2DPC attachment. Replacing the EG on the organogel surface with water creates a more hydrophilic interface for the 2DPC transfer from the air-water interface. A 2DPC transferred from an air-water interface to a hydrophobic substrate tends to roll off hydrophobic surfaces, similar to how droplets of pure water tend to roll off a hydrophobic surface. This results in a non-uniform coating of the 2DPC on the hydrophobic substrate. Additionally, removing the thick EG coating decreases the drying time after 2DPC transfer.

EG and water are miscible solvents, and inevitably some water will diffuse into the organogel when the EG is washed from its surface. The minor addition of water does not swell the organogel. Any water that diffuses into the organogel during the 2DPC attachment is removed in the final step when the 2DPC organogel is equilibrated in pure EG.

Flushing with water removes EG from the organogel surface and leaves a layer of water around the organogel interface, effectively creating a more hydrophilic surface for the 2DPC

transfer (Figure 5.2B). The 2DPC particle array at the air-water interface was subsequently transferred onto the organogel surface, shown in Figure 5.2C-D. The procedure to transfer the 2DPC from the air-water interface to the organogel surface was discussed in detail previously.[67]

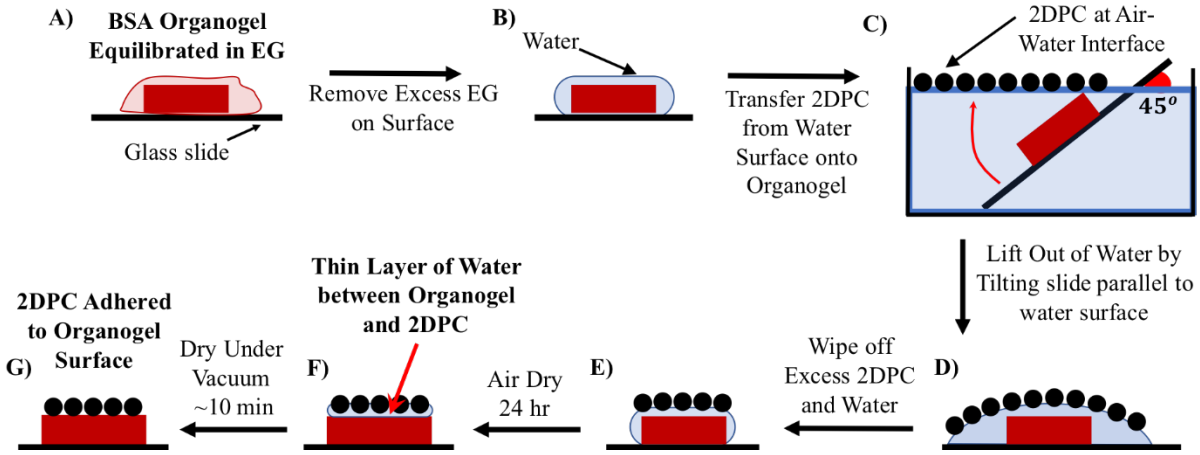

Figure 5.2 - Attachment of 2DPC to BSA organogels after EG solvent exchange. A) Organogel equilibrated in pure EG placed on a glass slide. B) Organogel rinsed with a stream of nanopure water to exchange EG on the surface with water. C) The 2DPC is transferred from the air-water interface onto the organogel, as previously described.[1] D) The slide and organogel are covered by a water layer with the 2DPC at the air-water interface. E) Excess 2DPC and water is removed from around the organogel with filter paper. F) Allow the wet organogel to dry in ambient conditions for 24 hr to evaporate most of the water layer. G) The organogel is further dried under decreased pressure (0.6 atm) for ~10 min, attaching the 2DPC to the organogel surface.

The EG inside the organogel has a low vapor pressure. The water layer between the 2DPC and the organogel, shown in Figure 5.2E, will preferentially evaporate before the EG solvating the organogel. The 2DPC BSA organogels are dried in air for 24 hr to allow most of the water to evaporate. Further drying is required to decrease the water content and promote adhesion of the 2DPC to the organogel. The remaining water is removed by drying the 2DPC organogels in a vacuum oven under reduced pressure (0.6 atm) for 10-15 mins at room

temperature. After additional drying under reduced pressure, the 2DPC particles adhere to the organogel surface. The 2DPC organogels are then re-equilibrated in 250 mL of pure EG for 24 hr.

5.2.4 2DPC Particle Spacing Changes Monitor BSA Organogel VPT

We monitored the volume response of the 2DPC BSA hydrogels and organogels to protein ligand binding by measuring the particle spacing of the attached 2DPC. The 2DPC particle spacing, a, was calculated from the Debye ring diffraction measurements as previously described.[67-68] The hydrogel and organogel volume response to ligand binding is plotted as the 2DPC particle spacing change. The 2DPC particle spacing change is calculated as $\Delta a = a_{ligand} - a_{initial}$, where $a_{initial}$ is the 2DPC particle spacing of the BSA gel in equilibrium with its respective mobile phase and a_{ligand} is the 2DPC particle spacing of the BSA gel after 24 hr exposure to solutions containing the ligand. The particle spacing of three 2DPC BSA gel samples were measured for each ligand concentration. The BSA ligands examined were ibuprofen and the two fatty acids (FA), sodium dodecanoate a C12 FA and sodium myristate a C14 FA.

For the Ibuprofen experiments, the BSA hydrogels were equilibrated in 50 mM phosphate buffer pH 7.2. BSA organogels were equilibrated in either pure EG or a 50 mM NaCl in EG solution. The particle spacing was measured after the hydrogels and organogels equilibrated in the appropriate mobile phase for 24 hr. BSA hydrogels were then incubated in 50 mM phosphate buffer containing 0, 1, 5, 10, 15, and 20 mM ibuprofen for 24 hr. BSA organogels were incubated in either pure EG or a 50 mM NaCl in EG solution containing 0, 1, 5, 10, 15, 20, and 25 mM ibuprofen. The 2DPC particle spacing was measured after the samples were incubated in ibuprofen solutions for 24 hr.

The pKa of fatty acids increase as the hydrocarbon tail length increases[69], therefore BSA hydrogels were equilibrated in 50 mM carbonate-bicarbonate buffer at pH 9 and BSA organogels were equilibrated in EG solutions containing 10^{-5} M NaOH (EG ~ pH 9) to ensure most FA molecules are ionized in solution. The C12 and C14 FA have very low solubilities in water. We could obtain 5 mM dodecanoate (C12) solutions in 50 mM pH 9 buffer, however the myristate (C14) FA was insoluble in buffer at 1 mM FA. Thus, the 2DPC particle spacing of BSA hydrogels were measured only for C12 FA solutions containing 0, 1, 2.5 and 5 mM C12 FA.

Both the C12 and C14 FA were readily soluble in pure EG and EG pH 9 solutions. The 2DPC particle spacing of BSA organogels were measured after 24 hr exposure to 0, 1, 5, 10, 15, 20, and 25 mM FA in EG pH 9 for both the C12 and C14 FA.

5.2.5 Enzyme Activity Measurements of OPH Hydrogels and Organogels

The organophosphate, paraoxon is used as the substrate to measure the OPH specific activity of OPH solutions, hydrogels, and organogels. Paraoxon is a highly toxic chemical and must be handled with extreme care. Appendix D provides more information on the proper paraoxon safety procedures. Hydrolysis of paraoxon by OPH was monitored through the production of p–nitrophenol (pNP), which absorbs at 405 nm. The time dependence of the increasing absorbance at 405 nm for the OPH-Paraoxon solutions was measured using a Cary 5000 UV-Vis spectrometer. A 2 mm path length quartz cuvette was used for OPH solution measurements and a 10 mm path length quartz cuvette was used for the hydrogel and organogel measurements.

The 5.6 mg/mL OPH solution from FLIR was diluted with either water or an EG/water mixture to a concentration of 2.8×10^{-4} mg/mL for the OPH monomer samples. The OPH gel

films were cut into roughly 0.5 mm × 0.5 mm pieces so that the OPH concentration in the 4 mL cuvette volume was ~2.8×10^{-4} mg/mL. The 0.036 mm thick OPH hydrogel and organogel films contain 200 mg OPH per mL of gel. Each piece of OPH gel was measured with a digital micrometer and the weight of OPH, mg_{OPH}, was calculated for each hydrogel or organogel sample. As a control, the supernatant buffer solution from OPH hydrogel samples was also measured. OPH hydrogels were separated from the buffer by centrifugation at 5000 rpm for 5 min. The specific activity of the supernatant was calculated to determine if any OPH monomer remained in the supernatant.

A stock solution of Paraoxon was added to each sample so that the final concentration was 1.5 mM Paraoxon. The 15 mM Paraoxon stock solution contained 10% ethanol in water to increase the OP solubility in water. 100 μL of the paraoxon stock solution was added to 1 mL of the OPH monomer solution and the hydrogel supernatant solution. 400 μL of the paraoxon stock solution was added to the 4 mL samples containing the OPH hydrogel and organogel samples. After the addition of paraoxon, the samples were very quickly moved to the spectrometer where the absorbance at 405 nm was measured every 30 sec for 5 min. The solutions were stirred between absorbance measurements to facilitate diffusion of paraoxon to the OPH gel, which rests at the bottom of the cuvette. Measurements were performed in triplicate.

We calculated OPH specific activity in units of the molarity of pNP produced per mg of OPH with time: (M_{pNP}) /(min*mg_{OPH}) from the evolution of the absorption at 405 nm over several minutes. The slope of the absorbance/time is determined for each sample and used in the specific activity equation (Equation 5.1). The molar extinction coefficient, ε of p-nitrophenol in alkaline conditions is 17,100 $M^{-1}cm^{-1}$. The path length, b was 0.2 cm for OPH solution measurements and 1 cm for OPH hydrogel and organogel measurements. The OPH

concentration, [OPH] in the hydrogel and organogel samples was calculated from the gel size as described in the previous paragraphs for each calculation.

Equation 5.1 $$Activity = \frac{slope}{\varepsilon * b * [OPH]}$$

5.3 Results and Discussion

5.3.1 Fabrication of Functional Pure Protein Organogels From Pure Protein Hydrogels

Pure protein hydrogels were fabricated by crosslinking the protein lysine groups using glutaraldehyde.[8, 27] We previously demonstrated this mild glutaraldehyde crosslinking method results in the formation of transparent hydrogels that undergo VPT in responses to protein-ligand binding for the proteins Bovine and Human Serum Albumin, Glucose Binding Protein, and Concanavalin A.[8, 31-32] These fabricated pure protein hydrogels are robust macroscopic films. We have fabricated pure protein hydrogels as large as 4 cm x 7 cm and believe this process can easily be scaled up much further.

Proteins evolved to function mainly in aqueous solvents, where interactions between amino acid sidechains and water are important for protein folding and dynamics.[39] Thus, we expected that these glutaraldehyde crosslinked hydrogel proteins would retain their native protein monomer structures and functions. Somewhat surprisingly, the organogel proteins also retain a significant portion of their native protein monomer function, enabling revolutionary applications of pure protein sensors and catalysts. An organic solvent mobile phase hinders the growth of microbes that would digest the proteins, therefore increasing the shelf life of the pure protein organogels compared to the protein hydrogels. We have observed significant degradation

of our pure protein hydrogels by microbes after a week at room temperature, whereas we do not observe such degradation in the organogels after more than 3 months. The solubility of hydrophobic analytes increases in organic solvents, enabling the use of protein organogel sensors and biocatalysts for detecting or catalyzing reactions of hydrophobic species, such as organophosphates, polychlorinated biphenyls, and many volatile organic compounds such as toluene. The utilization of enzyme chemistry in pure organic solvents is also highly important in the pharmaceutical industry. The organic mobile phases can promote enhanced enantioselectivity of the substrate and/or products and enable novel enzymatic transformations such as reverse hydrolysis of alcohols to esters because water dependent reactions are disabled.[36]

Our responsive pure protein organogels are fabricated by performing a stepwise solvent exchange on pure protein hydrogels, as shown in Figure 5.3A. The protein crosslinking that forms the hydrogel network effectively immobilizes the proteins prior to their exposure to organic solvent. Protein immobilization of proteins increases the protein stability against thermal and chemical denaturation.[53, 56] This method of fabricating protein organogels seems to be universal with respect to the protein identity, producing transparent and mechanically stable protein organogel films for each protein tested. We successfully fabricated many protein organogels, including bovine/human serum albumin (BSA/HSA), Organophosphorus Hydrolase (OPH), lysozyme, and myoglobin. Similar to protein immobilization onto a solid matrix, our macroscopic protein hydrogel and organogel films enhance the recovery and reuse of the proteins and enable their use in continuous operations such as fixed-bed reactors.[54, 70]

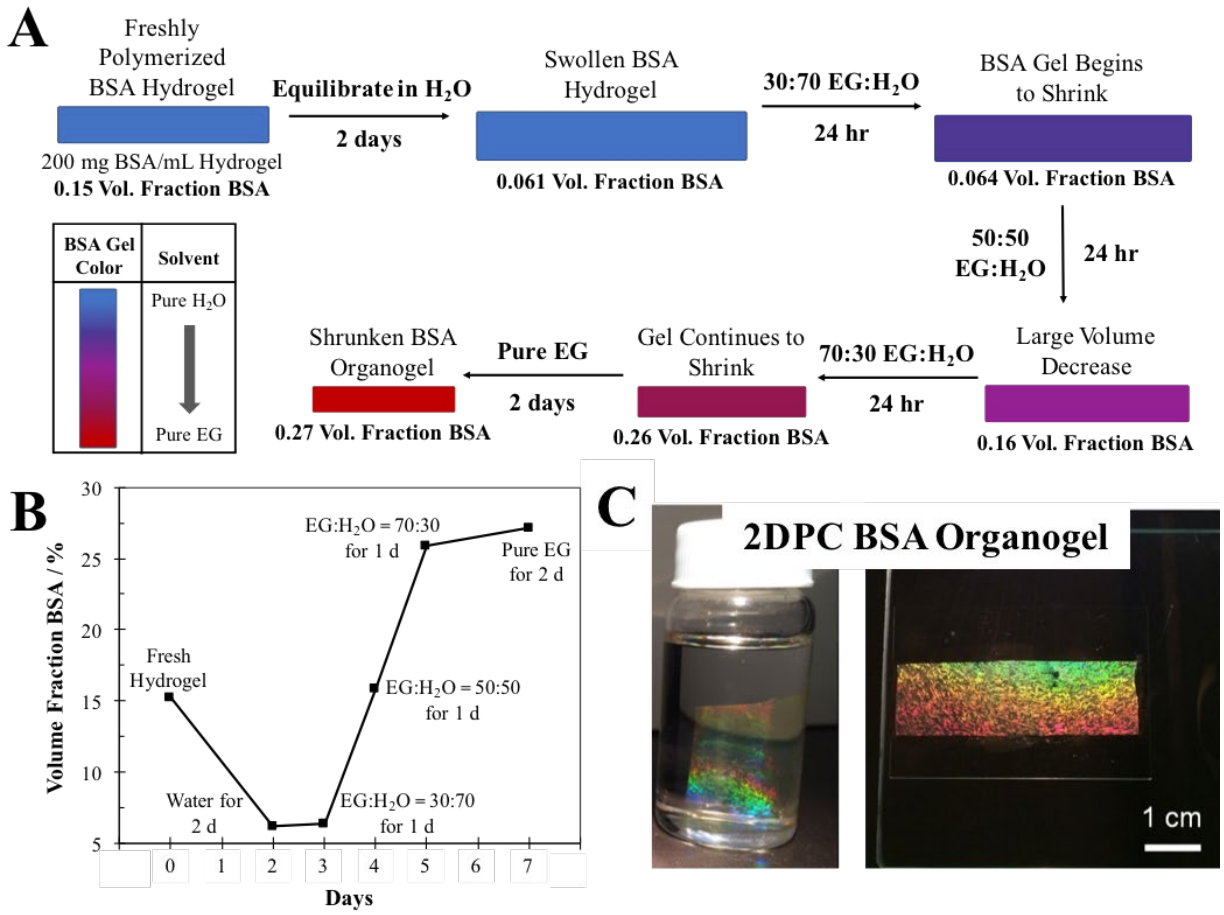

Figure 5.3 - (A) Schematic showing stepwise solvent exchange procedure that transforms BSA hydrogels into BSA organogels in pure EG. (B) The volume fraction of BSA in the gel is calculated from the swelling ratio after each stage of the step-wise solvent exchange process. (C) Photographs of 2DPC BSA organogels. A flashlight illuminates the samples so light diffraction from the 2DPC was observed. The left image shows the 2DPC BSA organogel in EG. The flashlight is placed beside the camera such that the backscattered diffraction is observed. The right image illustrates the bright diffraction that results from forward scattered light for a 2DPC BSA organogel lying flat on a glass slide. The flashlight was placed behind the sample such that the forward diffracted light is recorded.

By utilizing the low vapor pressure organic solvent, EG we create functional pure protein organogels that resist mobile phase evaporation. The mobile phase is essential for the 2DPC sensor VPT response to ligand binding; the VPT volume change is the result of an osmotic pressure within the protein polymer system that triggers mass transport of the mobile phase. For example, VPT swelling in response to an analyte is not possible in the absence of a mobile phase because swelling is caused by solvent repartitioning within the polymer network. A low vapor pressure mobile phase increases the sensor operational time and enhances their potential applications. Additionally, mobile phase evaporation can limit diffusion of species to the protein active sites, therefore decreasing the sensor and/or catalyst kinetics.

We first characterized the solvent exchange induced VPT that transforms our protein hydrogels into protein organogels. Much of our initial organogel work utilized the inexpensive and ubiquitous protein BSA. As shown in Figure 5.3A, the BSA hydrogels undergo a VPT that significantly shrinks the system as the EG concentration increases.

We quantitatively monitor this VPT by calculating the BSA volume fraction at each EG concentration using the swelling ratio, Q (Figure 5.3B). The BSA volume fractions in the hydrogel and organogel are proportional to the volume, increasing or decreasing when the protein polymer shrinks or swells. Calculating the BSA volume fraction from the swelling is possible because the initial BSA volume fraction is known; the freshly polymerized BSA hydrogel contains 200 mg/mL BSA which corresponds to a BSA volume fraction of 15%.

As shown in Figure 5.3A-B, the initially polymerized BSA hydrogels swell upon equilibration in nanopure water. The resulting BSA volume fraction decreases to 6.1 %. The BSA volume fraction increases during the step-wise EG exchange towards pure EG to a maximum volume fraction of 27% BSA upon equilibrating in pure EG after 2 days.

5.3.2 Fabrication of 2DPC Protein Organogels

We recently developed several 2DPC hydrogel sensors for multiple analytes.[9, 68, 71] The 2DPC consists of a well-ordered hexagonal array of nanoparticles with particle spacings comparable to the wavelength of visible light. The 2DPC diffracts visible light according to the 2D Bragg diffraction equation.[67] The 2DPC simultaneously diffracts these multiple wavelengths of light into multiple angles to produce the rainbow patterns observed in Figure 5.3C. When monochromatic incident light is normal to the 2DPC, the diffraction produces a Debye ring that has a diameter corresponding to the diffraction angle.[31, 67] These wavelength dependent diffraction angles are determined by the 2DPC particle spacings, and the intensity of this diffraction depends on the 2DPC particle ordering.[67] Hydrogel volume changes induced by analyte binding alter the 2DPC particle spacings and shift the diffraction angles. Thus, these shifts in the diffraction angle monitor the hydrogel VPT and report on the analyte concentration.

The 2DPC particles are close packed when fabricated.[67] For hydrogels, this close packed particle array is embedded in the hydrogel surface during polymerization. Generally, hydrogels swell upon exposure to aqueous solutions after they are polymerized, increasing the 2DPC particle spacing. The solvent exchange induced VPT, shown in Figure 5.3B, significantly shrinks the protein hydrogel/organogel. The organogel BSA volume fraction is roughly twice that of the initially polymerized protein hydrogel. Thus, the close packed 2DPC that was initially attached to the hydrogel during polymerization will disorder during the solvent exchange when it attempts to decrease the particle spacing to less than the close packed particle spacing.

To avoid 2DPC disordering, we attached the 2DPC to the organogel after EG solvent exchange. This enables the 2DPC diffraction measurements to monitor organogel swelling

induced by ligand binding. 2DPC diffraction measurements are a much more sensitive monitor of organogel volume changes than physically measuring the dimensions of the organogel film.

5.3.3 Functional Pure Protein Organogel Sensors and Enzymatic Catalysts

We fabricated pure protein organogels using two proteins with very different biological functions to demonstrate the versatility of our fabrication procedure and to highlight two different applications of these materials.

Our protein organogels retain a significant fraction of their native protein function because the proteins are immobilized during the protein hydrogel fabrication. Immobilization of the proteins is critical for the preservation of protein function in our organogels. The glutaraldehyde crosslinking immobilizes the proteins by forming multiple covalent bonds between lysine residues on the protein surface. This immobilization stabilizes the native protein structure by increasing the activation barrier for protein unfolding[54], creating a system where the proteins are more resistant to denaturation or deactivation by organic solvents. For multimeric proteins, such as the dimeric enzyme, OPH, discussed below, the immobilization also prevents subunit dissociation.

5.3.3.1 2DPC BSA Organogel Ligand Binding Sensor: Ibuprofen and Fatty Acids

Albumins are promiscuous proteins that bind many ligands and transport them throughout the body.[72-75] We previously developed 2DPC BSA hydrogel sensors that exhibit VPT in response to changes in the number of bound charges on the protein caused by pH changes and the binding of divalent metal ions, surfactants, fatty acids, and charged drug

molecules.[8] We discovered that our 2DPC BSA organogels also exhibit VPT in response to BSA-ligand binding.

Figure 5.4 compares the 2DPC particle spacing change of BSA hydrogels and organogels in response to binding an ibuprofen salt and two fatty acids, sodium dodecanoate (C12 FA) and sodium myristate (C14 FA). Ibuprofen and the two FA are more soluble in EG than in water, enabling the BSA organogels to sense larger ligand concentrations compared to that of the hydrogel. This increases the functional dynamic range of the sensor. This increase in dynamic range is most notable in the FA system, for example the solubility of the C14 FA in pH 9 buffer is less than 1 mM, whereas the solubility in EG is greater than 25 mM.

The particle spacing of both the 2DPC BSA hydrogels and organogels monotonically increase with increasing concentrations of ibuprofen (Figure 5.4A) and two FA (Figure 5.4B). The increasing particle spacing is caused by volume phase transitions (VPT) that swell the hydrogels and organogels in response to the charged ligands binding to the crosslinked BSA proteins.

Hydrogel and organogel VPT result from induced osmotic pressures, Π, that cause translocation of the mobile phase. According to Flory theory[21-22], these osmotic pressures are induced by changes in the total Gibbs free energy of the system, ΔG_{Total}. The resulting VPT causes the polymer network to either expel solvent, causing the system to shrink or to transport additional solvent into the polymer network, causing the system to swell until an equilibrium volume is reached where the osmotic pressure is zero, Equation 5.2.

$$\textbf{Equation 5.2} \quad \Pi_{Total} = {}^{\partial \Delta G_{Total}}/_{\partial V} = 0$$

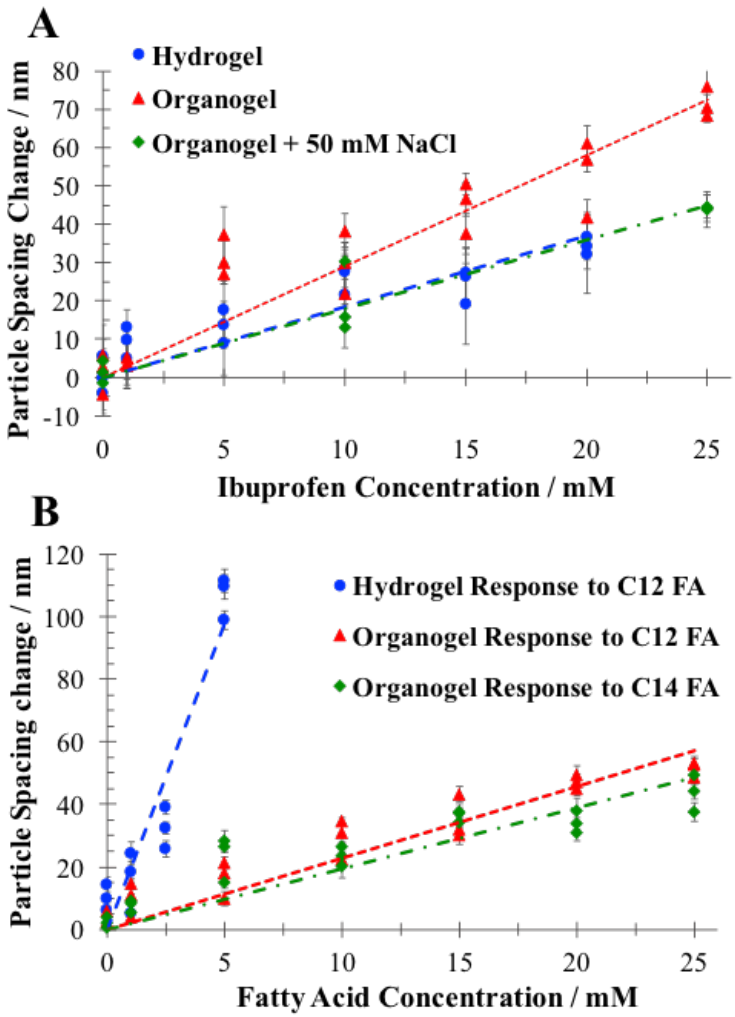

Figure 5.4 - Particle spacing changes of 2DPC BSA hydrogels and organogels as a function of ligand concentration. (A) Ligand: Ibuprofen sodium salt. For the hydrogels, ibuprofen was dissolved in 50 mM phosphate buffer at pH 7.2. For the organogels, ibuprofen was dissolved in either pure EG or EG containing 50 mM NaCl. (B) Ligands: C12 and C14 fatty acids (FA). For the hydrogels, C12 FA was dissolved in 50 mM carbonate-bicarbonate buffer at pH 9. For organogels, C12 and C14 FA were dissolved in EG pH 9. Error bars are one standard deviation.

The total Gibbs free energy change in an ionic polymer network such as our BSA polymer has contributions from changes in the free energy of mixing, ΔG_{Mix}, changes in the free energy of elasticity, $\Delta G_{Elastic}$, and changes in the ionic free energy, ΔG_{Ion}[15, 22]. At the equilibrium volume, the interactions between the polymer and solvent that contribute to the total Gibbs free energy are balanced. Thus, a reaction that disrupts this balance of interactions causes $\Delta G_{Total} \neq 0$, which subsequently actuates a volume change to relieve the osmotic pressure. The magnitude of the volume change is proportional to the magnitude of the change in the total Gibbs free energy.

The BSA hydrogel and organogel VPT are measured using the 2DPC particle spacing changes due to binding the charged ligands, shown in Figure 5.4. These changes are caused by ΔG_{Ion} and ΔG_{Mix}. The free energy of mixing depends on the interactions between the BSA polymer and the mobile phase solvating the polymer. The significant difference between the hydrogel volume and the organogel volume, shown in Figure 5.3, indicates there is a large difference in the polymer-solvent interactions. Assuming the degree of ligand ionization is constant, ΔG_{Ion} is directly correlated to the number of charges bound to the protein polymer network, the Donnan potential. ΔG_{Ion} is attenuated by increasing the mobile phase ionic strength.

We can directly observe this ionic strength attenuation in Figure 5.4A. The 2DPC organogel particle spacing change in response to ibuprofen in pure EG is larger than that of the hydrogel in 50 mM buffer. However, when 50 mM NaCl is added to EG such that the ionic strength of the EG is roughly equal to that of the buffer, the particle spacing change for the hydrogel and organogel become similar. These results indicate that the hydrogel and organogel VPT in response to ibuprofen binding is primarily driven by ΔG_{Ion}. Since ΔG_{Ion} is directly proportional to the number of bound charges, we can also conclude that the binding affinities of the 6 ibuprofen binding sites in BSA[76] are roughly the same for the hydrogel and organogel

systems. Our results also suggest that the ΔG_{Mix} caused by ibuprofen binding to the BSA polymer is similar for the hydrogel and organogel systems, due to the similar responses of the hydrogel in 50 mM buffer and the organogel in the 50 mM NaCl EG solution when the ionic strengths are roughly equal.

The 2DPC particle spacing change of BSA hydrogels and organogels in response to FA binding is shown in Figure 5.4B for the C12 FA, dodecanoate and the C14 FA, myristate. The BSA organogel has a much larger functional dynamic range because the FA have larger solubilities in EG. The 2DPC BSA hydrogel particle spacing change is much larger than that of the organogel at the same FA concentration despite the hydrogel system having a higher ionic strength. These results indicate that either the binding affinities of the 9 FA binding sites on BSA decreases when the protein polymer is solvated by EG or that ΔG_{Mix} has a more significant contribution to ΔG_{Total} for the FA-BSA binding VPT response compared to that of ibuprofen.

5.3.3.2 Catalytic OPH Hydrogels and Organogels

Organophosphates (OP) are a class of highly toxic organic molecules used as pesticides and chemical warfare agents that cause >200,000 deaths per year.[77] Despite a ban on chemical weapons, OP nerve agents are continually used in attacks, such as in Syria, and political assassinations. Current commercial products used by the military for OP decontamination are often caustic due to the use of strong inorganic oxidizers such as hypochlorite or require preparation prior to use, which complicates their use in the field.[38]

Some species of bacteria and fungi have evolved enzymes, like OPH, that hydrolyze the phosphoester bond of OP, creating less toxic products.[78] These enzymes are highly efficient catalysts that generally hydrolyze numerous OP compounds such as paraoxon, parathion, sarin, VX, and Soman. Enzymatic decontamination solutions generally operate under mild conditions

that are appropriate for personal and/or sensitive material decontamination, however the use of enzymes in harsher conditions are limited by their stability. Practical utilization of enzyme based decontamination solutions require stabilization of the enzymes to increase their shelf-life and operating time.

Our goal is to create simple decontamination systems that are appropriate for many potential applications such as personal decontamination for war-fighters and victims, large-scale decontamination of OP residues on surfaces, and for OP stockpile elimination. We envision a sprayable decontamination solution that can be easily and quickly applied to contaminated surfaces and skin. This would be accomplished by formulating a dispersion of small OPH hydrogel or organogel particles and flakes in appropriate mobile phases.

An aqueous dispersion of our OPH hydrogel system would function as a potentially non-toxic, biodegradable solution that could be used on the skin and for sensitive materials where evaporation of water is not a concern. The OPH enzymes are immobilized via crosslinking to form the hydrogel network. Immobilized enzymes generally have longer shelf lives compared to their monomers,[79] enhancing the usefulness of these materials. However, evaporation of the hydrogel aqueous mobile phase limits their application in hot, dry environments.

Our OPH organogels that utilize the low vapor pressure mobile phase, ethylene glycol, surmount some of the limitations of hydrogel materials such as evaporation. These low vapor pressure OPH organogel materials can be utilized for large-scale decontamination applications after a chemical weapons attack for example, because the mobile phase resists evaporation. This allows for a stand-off application of the OPH organogel dispersion, where it can be sprayed over large areas from long distances without risk to the user. Preserving the mobile phase for a longer time also enables diffusion of the OPH organogel flake dispersion into porous materials such as

soil and affords the materials a longer working time to ensure complete hydrolysis of the dangerous OP molecules residing on the surfaces of streets and buildings.

OPH organogels can also be utilized to neutralize stockpiles of bulk nerve agents. Stockpiles consist of concentrated OP solutions in organic solvents. OP nerve agents are stored in organic solvents because they limited solubility in water.[80-81] Uncrosslinked OPH monomers cannot be used to neutralize these stockpiles because the enzymes are inhibited by the presence of the organic solvents.[82] The immobilized OPH in the organogel retains much of its native enzyme activity in the organic solvent, enabling OPH organogel neutralization of OP stockpiles. An additional advantage of these macroscopic OPH organogel films are that they can easily be separated from the stockpile solutions after OP hydrolysis, and reused.

Biocatalytic pure protein hydrogels and organogels were fabricated using the enzyme Organophosphorus Hydrolase (OPH) provided by FLIR Systems Inc. OPH is a dimeric metalloenzyme that catalyzes hydrolysis of various OPs.[12,82] We examined the hydrolysis of the OP, ethyl-paraoxon, a commonly used nerve gas simulant. OPH is a remarkably efficient enzyme, having a nearly diffusion limited hydrolysis rate.[78] Ethyl-paraoxon is hydrolyzed by OPH in the presence of the cofactor, Co2+ to produce p-nitrophenol (pNP), diethylphosphate and two protons (Figure 5.5A). The rate of OP hydrolysis is easily measured from the increasing concentration of the hydrolysis product, pNP, which strongly absorbs 405 nm light under alkaline conditions.

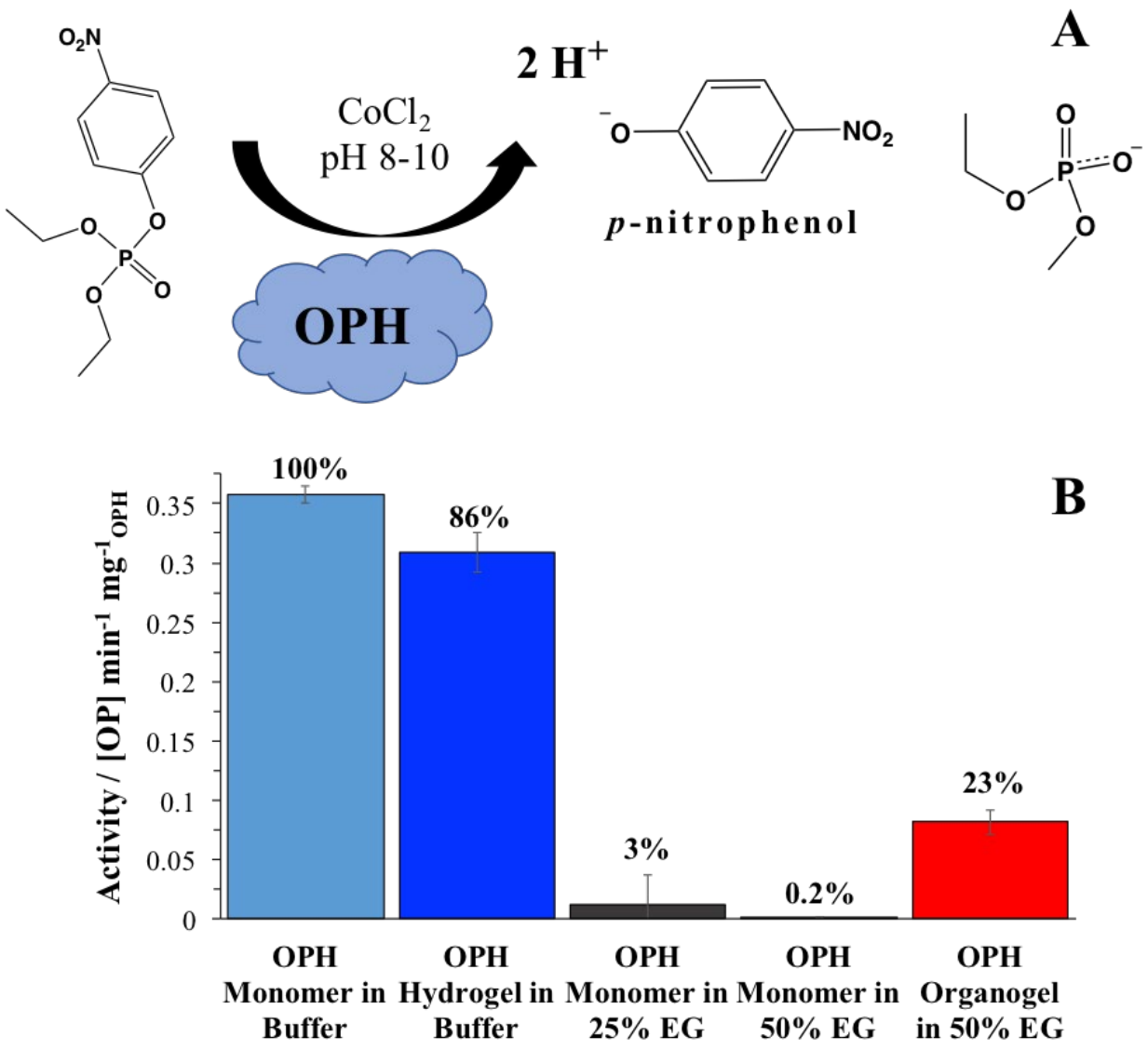

Figure 5.5 - (A) Hydrolysis of ethyl-paraoxon by OPH enzyme in pH 8 HEPES buffer solution containing the co-factor, 100 µM Co^{2+}. (B) Specific activities for OPH monomer in buffer solution and EG-buffer solutions, the OPH hydrogel in buffer, and the OPH organogel in 50% EG-buffer solution.

We used the methods described above to fabricate OPH hydrogels and organogels. The specific activities of OPH monomer solutions and OPH hydrogels are shown in Figure 5.5B. Glutaraldehyde crosslinked OPH hydrogels retain 86% of their native enzymatic activity. The modest reduction in activity compared to the OPH monomer is comparable to that of other crosslinked enzymes in aqueous solutions.[83] The supernatant buffer solution separated from the OPH hydrogel by centrifugation, exhibits insignificant OPH activity. This demonstrates that OPH irreversibly crosslinks into the protein polymer and does not leach from the hydrogel. The specific activity calculated for the OPH hydrogel stems solely from the crosslinked OPH hydrogel.

The OPH enzyme monomers are typically deactivated by organic solvents. The specific activity of the uncrosslinked OPH monomers drastically decreases with increasing concentrations of EG (Figure 5.5B). The negative effects of organic solvents on the OPH activity was documented for other water-organic solvent mixtures; OPH was inhibited by 50% in aqueous mixtures containing 0.5% of common organic solvents like ethanol and isopropanol.[82]

Our OPH organogels are less inhibited by the presence of a deactivating organic solvent. The enzymatic activity of OPH organogels is roughly 160 times larger than the OPH monomer activity in 50% EG-water, as shown in Figure 5.5B. The impressive activity of these OPH organogels in EG/water solutions most likely results from the enzyme crosslinking that stabilizes the OPH native structure and prevents dissociation of the 2 identical subunits. Glutaraldehyde crosslinking of OPH lysine residues potentially creates four covalent bonds at the four reactive lysine residues on the surface of OPH that immobilizes the dimeric enzyme.[78]

The continued utilization of OP as chemical weapons, assassination agents, and pesticides represents an extremely dangerous threat to our military, aid workers, and the public.

The development of our OPH hydrogels and revolutionary OPH organogels significantly advance efforts towards producing improved OP decontamination solutions that can be utilized under harsh conditions such as in an organic solvent or in hot, dry environments where either the OPH monomers or the OPH hydrogels would have limited functionality. Our crosslinked OPH hydrogel and organogel materials formulated as a dispersion of small particles or flakes represent a simple sprayable solution for OP decontamination. These OPH organogels improve existing inorganic-based OP decontamination solutions in that they would not be corrosive to coatings and sensitive equipment.[38] Furthermore, the pure OPH polymer of the organogels offers revolutionary catalytic capabilities compared to materials where OPH is immobilized on solid substrates because every monomer is a catalytic functional group. These macroscopic OPH organogel films also improve upon existing pure enzyme technologies such as OPH crosslinked enzyme crystals[84] that consist of small particulates having diameters of 5-50 μm because our large OPH organogel films are much easier to separate from the reaction medium and reused.

5.4 Conclusion

We developed a simple approach to fabricating responsive pure protein hydrogels and organogels and demonstrated valuable applications like sensing and catalysis. Our method for fabricating pure protein organogels can be extended to other enzymes and protein-ligand binding pairs. This approach is a general platform for developing pure protein functional organogels. The major advantage of the protein organogel system lies in its ability to utilize low vapor pressure organic liquids as a mobile phase that will not evaporate in ambient conditions. Furthermore,

organic solvent mobile phases increase the solubility of hydrophobic compounds, increasing the functional dynamic range of our 2DPC sensors.

The BSA organogels bind the same ligands as the native protein. This ligand binding induces macroscopic volume phase transitions. Our BSA organogels act as sensors for protein-ligand binding and represent a novel sensing motif for quantitating ligand binding in non-aqueous solvents. An important future application may include detection of fentanyl in drug samples, a dangerous opiate with limited water solubility.

Our OPH organogels act as catalysts for decontaminating toxic OP. OPH organogels retained significant activity towards hydrolysis of paraoxon compared to the OPH monomer in the presence of organic solvents. For field applications, the organogels could be formulated into a sprayable dispersion of OPH organogel flakes in EG. Important future applications could include developing these catalytic organogels using enzymes that degrade additional chemical weapon agents like mustard gas or agent orange.

5.5 References

1. Xu, X.; Goponenko, A. V.; Asher, S. A., Polymerized PolyHEMA Photonic Crystals: pH and Ethanol Sensor Materials. *Journal of the American Chemical Society*. **2008**, 130, 3113-3119.

2. Richter, A.; Bund, A.; Keller, M.; Arndt, K.-F., Characterization of a microgravimetric sensor based on pH sensitive hydrogels. *Sensors and Actuators B: Chemical*. **2004**, 99, 579-585.

3. Kamenjicki, M.; Lednev, I. K.; Asher, S. A., Photoresponsive Azobenzene Photonic Crystals. *The Journal of Physical Chemistry B*. **2004**, 108, 12637-12639.

4. Kamenjicki Maurer, M.; Lednev, I. K.; Asher, S. A., Photoswitchable Spirobenzopyran-Based Photochemically Controlled Photonic Crystals. *Advanced Functional Materials*. **2005**, 15, 1401-1406.

5. Guo, B.-L.; Gao, Q.-Y., Preparation and properties of a pH/temperature-responsive carboxymethyl chitosan/poly(N-isopropylacrylamide)semi-IPN hydrogel for oral delivery of drugs. *Carbohydrate Research*. **2007**, 342, 2416-2422.

6. Xu, F.-J.; Kang, E.-T.; Neoh, K.-G., pH- and temperature-responsive hydrogels from crosslinked triblock copolymers prepared via consecutive atom transfer radical polymerizations. *Biomaterials*. **2006**, 27, 2787-2797.

7. Walker, J. P.; Asher, S. A., Acetylcholinesterase-Based Organophosphate Nerve Agent Sensing Photonic Crystal. *Analytical Chemistry*. **2005**, 77, 1596-1600.

8. Cai, Z.; Zhang, J.-T.; Xue, F.; Hong, Z.; Punihaole, D.; Asher, S. A., 2D Photonic Crystal Protein Hydrogel Coulometer for Sensing Serum Albumin Ligand Binding. *Analytical Chemistry*. **2014**, 86, 4840-4847.

9. Cai, Z.; Smith, N. L.; Zhang, J.-T.; Asher, S. A., Two-Dimensional Photonic Crystal Chemical and Biomolecular Sensors. *Analytical Chemistry.* **2015**, 87, 5013-5025.

10. Lin, G.; Chang, S.; Kuo, C. H.; Magda, J.; Solzbacher, F., Free swelling and confined smart hydrogels for applications in chemomechanical sensors for physiological monitoring. *Sensors and Actuators B: Chemical.* **2009**, 136, 186-195.

11. Ben-Moshe, M.; Alexeev, V. L.; Asher, S. A., Fast Responsive Crystalline Colloidal Array Photonic Crystal Glucose Sensors. *Analytical Chemistry.* **2006**, 78, 5149-5157.

12. Lu, H. D.; Wheeldon, I. R.; Banta, S., Catalytic biomaterials: engineering organophosphate hydrolase to form self-assembling enzymatic hydrogels. *Protein Engineering, Design and Selection*. **2010**, 23, 559-566.

13. Gupta, P.; Vermani, K.; Garg, S., Hydrogels: from controlled release to pH-responsive drug delivery. *Drug Discovery Today*. **2002**, 7, 569-579.

14. Sharma, A. C.; Jana, T.; Kesavamoorthy, R.; Shi, L.; Virji, M. A.; Finegold, D. N.; Asher, S. A., A General Photonic Crystal Sensing Motif: Creatinine in Bodily Fluids. *Journal of the American Chemical Society*. **2004**, 126, 2971-2977.

15. Goponenko, A. V.; Asher, S. A., Modeling of Stimulated Hydrogel Volume Changes in Photonic Crystal Pb2+ Sensing Materials. *Journal of the American Chemical Society.* **2005**, 127, 10753-10759.

16. Dey, N.; Samanta, S. K.; Bhattacharya, S., Selective and Efficient Detection of Nitro-Aromatic Explosives in Multiple Media including Water, Micelles, Organogel, and Solid Support. *ACS Applied Materials & Interfaces.* **2013**, 5, 8394-8400.

17. Mukhopadhyay, P.; Iwashita, Y.; Shirakawa, M.; Kawano, S.-i.; Fujita, N.; Shinkai, S., Spontaneous Colorimetric Sensing of the Positional Isomers of Dihydroxynaphthalene in a 1D Organogel Matrix. *Angewandte Chemie.* **2006**, 118, 1622-1625.

18. Lin, Q.; Lu, T.-T.; Zhu, X.; Sun, B.; Yang, Q.-P.; Wei, T.-B.; Zhang, Y.-M., A novel supramolecular metallogel-based high-resolution anion sensor array. *Chemical Communications*. **2015**, 51, 1635-1638.

19. Holtz, J. H.; Asher, S. A., Polymerized colloidal crystal hydrogel films as intelligent chemical sensing materials. *Nature*. **1997**, 389, 829-830.

20. Ward Muscatello, M. M.; Stunja, L. E.; Asher, S. A., Polymerized Crystalline Colloidal Array Sensing of High Glucose Concentrations. *Analytical Chemistry*. **2009**, 81, 4978-4986.

21. Tanaka, T.; Fillmore, D.; Sun, S.-T.; Nishio, I.; Swislow, G.; Shah, A., Phase Transitions in Ionic Gels. *Physical Review Letters.* **1980**, 45, 1636-1639.

22. Flory, P. J., Principles of Polymer Chemistry. Cornell University Press: 1953.

23. Shibayama, M.; Tanaka, T., Volume phase transition and related phenomena of polymer gels. In Responsive Gels: Volume Transitions I, Dušek, K., Ed. Springer Berlin Heidelberg: Berlin, Heidelberg, 1993; pp 1-62.

24. Walker, J.; Kimble, K.; Asher, S., Photonic crystal sensor for organophosphate nerve agents utilizing the organophosphorus hydrolase enzyme. *Anal Bioanal Chem*. **2007**, 389, 2115-2124.

25. Baler, K.; Michael, R.; Szleifer, I.; Ameer, G. A., Albumin Hydrogels Formed by Electrostatically Triggered Self-Assembly and Their Drug Delivery Capability. *Biomacromolecules*. **2014**, 15, 3625-3633.

26. Xu, X.; Xu, Z.; Yang, X.; He, Y.; Lin, R., Construction and characterization of a pure protein hydrogel for drug delivery application. *International Journal of Biological Macromolecules*. **2017**, 95, 294-298.

27. Caillard, R.; Remondetto, G. E.; Mateescu, M. A.; Subirade, M., Characterization of Amino Cross-Linked Soy Protein Hydrogels. *Journal of Food Science*. **2008**, 73, C283-C291.

28. Kaehr, B.; Shear, J. B., Multiphoton fabrication of chemically responsive protein hydrogels for microactuation. *Proceedings of the National Academy of Sciences.* **2008**, 105, 8850-8854.

29. Heck, T.; Faccio, G.; Richter, M.; Thöny-Meyer, L., Enzyme-catalyzed protein crosslinking. *Applied microbiology and biotechnology*. **2013**, 97, 461-475.

30. Gao, X.; Fang, J.; Xue, B.; Fu, L.; Li, H., Engineering Protein Hydrogels Using SpyCatcher-SpyTag Chemistry. *Biomacromolecules*. **2016**, 17, 2812-2819.

31. Zhongyu, C.; H., K. D.; David, P.; Zhenmin, H.; S., V. S.; Xinyu, L.; A., A. S., A Photonic Crystal Protein Hydrogel Sensor for Candida albicans. *Angewandte Chemie.* **2015**, 127, 13228-13232.

32. Cai, Z.; Luck, L. A.; Punihaole, D.; Madura, J. D.; Asher, S. A., Photonic crystal protein hydrogel sensor materials enabled by conformationally induced volume phase transition. *Chemical Science*. **2016**, 7, 4557-4562.

33. Zhang, J.-T.; Wang, L.; Luo, J.; Tikhonov, A.; Kornienko, N.; Asher, S. A., 2-D Array Photonic Crystal Sensing Motif. *Journal of the American Chemical Society.* **2011**, 133, 9152-9155.

34. Ma, X.; Sun, X.; Hargrove, D.; Chen, J.; Song, D.; Dong, Q.; Lu, X.; Fan, T.-H.; Fu, Y.; Lei, Y., A Biocompatible and Biodegradable Protein Hydrogel with Green and Red Autofluorescence: Preparation, Characterization and In Vivo Biodegradation Tracking and Modeling. *Scientific Reports*. **2016**, 6, 19370.

35. Fjerbaek, L.; Christensen, K. V.; Norddahl, B., A review of the current state of biodiesel production using enzymatic transesterification. *Biotechnology and Bioengineering*. **2009**, 102, 1298-1315.

36. Carrea, G.; Riva, S., Properties and Synthetic Applications of Enzymes in Organic Solvents. *Angewandte Chemie International Edition*. **2000**, 39, 2226-2254.

37. Klibanov, A. M., Improving enzymes by using them in organic solvents. *Nature*. **2001**, 409, 241-246.

38. Jacquet, P.; Daudé, D.; Bzdrenga, J.; Masson, P.; Elias, M.; Chabrière, E., Current and emerging strategies for organophosphate decontamination: special focus on hyperstable enzymes. *Environmental Science and Pollution Research*. **2016**, 23, 8200-8218.

39. Mattos, C.; Ringe, D., Proteins in organic solvents. *Current Opinion in Structural Biology*. **2001**, 11, 761-764.

40. Bhattacharya, R.; Rose, P. W.; Burley, S. K.; Prlić, A., Impact of genetic variation on three dimensional structure and function of proteins. *PloS one*. **2017**, 12, e0171355-e0171355.

41. Verma, R.; Mitchell-Koch, K., In Silico Studies of Small Molecule Interactions with Enzymes Reveal Aspects of Catalytic Function. *Catalysts*. **2017**, 7, 212.

42. Stepankova, V.; Bidmanova, S.; Koudelakova, T.; Prokop, Z.; Chaloupkova, R.; Damborsky, J., Strategies for Stabilization of Enzymes in Organic Solvents. *ACS Catalysis*. **2013**, 3, 2823-2836.

43. Huang, C.; Bai, H.; Li, C.; Shi, G., A graphene oxide/hemoglobin composite hydrogel for enzymatic catalysis in organic solvents. *Chemical Communications*. **2011**, 47, 4962-4964.

44. Schmitke, J. L.; Wescott, C. R.; Klibanov, A. M., The Mechanistic Dissection of the Plunge in Enzymatic Activity upon Transition from Water to Anhydrous Solvents. *Journal of the American Chemical Society*. **1996**, 118, 3360-3365.

45. Levy, Y.; Jortner, J.; Becker, O. M., Solvent effects on the energy landscapes and folding kinetics of polyalanine. *Proceedings of the National Academy of Sciences of the United States of America*. **2001**, 98, 2188-2193.

46. Rupley, J. A.; Careri, G., Protein Hydration and Function. In Advances in Protein Chemistry, Anfinsen, C. B.; Richards, F. M.; Edsall, J. T.; Eisenberg, D. S., Eds. Academic Press: 1991; Vol. 41, pp 37-172.

47. Cui, J. D.; Jia, S. R., Optimization protocols and improved strategies of cross-linked enzyme aggregates technology: current development and future challenges. *Critical Reviews in Biotechnology*. **2015**, 35, 15-28.

48. Iyer, P. V.; Ananthanarayan, L., Enzyme stability and stabilization—Aqueous and non-aqueous environment. *Process Biochemistry*. **2008**, 43, 1019-1032.

49. Mateo, C.; Palomo, J. M.; Fernandez-Lorente, G.; Guisan, J. M.; Fernandez-Lafuente, R., Improvement of enzyme activity, stability and selectivity via immobilization techniques. *Enzyme and Microbial Technology*. **2007**, 40, 1451-1463.

50. Zdarta, J.; Meyer, A.; Jesionowski, T.; Pinelo, M., A General Overview of Support Materials for Enzyme Immobilization: Characteristics, Properties, Practical Utility. *Catalysts*. **2018**, 8, 92.

51. Cao, L., Immobilised enzymes: science or art? *Current Opinion in Chemical Biology*. **2005**, 9, 217-226.

52. Kisley, L.; Serrano, K. A.; Guin, D.; Kong, X.; Gruebele, M.; Leckband, D. E., Direct Imaging of Protein Stability and Folding Kinetics in Hydrogels. *ACS Applied Materials & Interfaces*. **2017**, 9, 21606-21617.

53. Burton, S. G.; Cowan, D. A.; Woodley, J. M., The search for the ideal biocatalyst. *Nature Biotechnology*. **2002**, 20, 37.

54. Sheldon, R. A., Characteristic features and biotechnological applications of cross-linked enzyme aggregates (CLEAs). *Applied Microbiology and Biotechnology*. **2011**, 92, 467-477.

55. Rodrigues, R. C.; Ortiz, C.; Berenguer-Murcia, Á.; Torres, R.; Fernández-Lafuente, R., Modifying enzyme activity and selectivity by immobilization. *Chemical Society Reviews*. **2013**, 42, 6290-6307.

56. Sheldon, R. A.; Schoevaart, R.; Van Langen, L. M., Cross-linked enzyme aggregates (CLEAs): A novel and versatile method for enzyme immobilization (a review). *Biocatalysis & Biotransformation*. **2005**, 23, 141-147.

57. Fernandez-Lafuente, R., Stabilization of multimeric enzymes: Strategies to prevent subunit dissociation. *Enzyme and Microbial Technology*. **2009**, 45, 405-418.

58. Pires-Cabral, P.; da Fonseca, M. M. R.; Ferreira-Dias, S., Esterification activity and operational stability of Candida rugosa lipase immobilized in polyurethane foams in the production of ethyl butyrate. *Biochemical Engineering Journal*. **2010**, 48, 246-252.

59. Vitola, G.; Büning, D.; Schumacher, J.; Mazzei, R.; Giorno, L.; Ulbricht, M., Development of a Novel Immobilization Method by Using Microgels to Keep Enzyme in Hydrated Microenvironment in Porous Hydrophobic Membranes. *Macromolecular Bioscience*. **2017**, 17, 1600381.

60. Doscher, M. S.; Richards, F. M., The Activity of an Enzyme in the Crystalline State: Ribonuclease S. *Journal of Biological Chemistry*. **1963**, 238, 2399-2406.

61. Quiocho, F. A.; Richards, F. M., Intermolecular Cross Linking Of A Protein In The Crystalline State: Carboxypeptidase-A. *Proceedings of the National Academy of Sciences of the United States of America*. **1964**, 52, 833-839.

62. Kartal, F.; Janssen, M. H. A.; Hollmann, F.; Sheldon, R. A.; Kılınc, A., Improved esterification activity of Candida rugosa lipase in organic solvent by immobilization as Cross-linked enzyme aggregates (CLEAs). *Journal of Molecular Catalysis B: Enzymatic*. **2011**, 71, 85-89.

63. Pallares, I. G.; Moore, T. C.; Escalante-Semerena, J. C.; Brunold, T. C., Spectroscopic Studies of the EutT Adenosyltransferase from Salmonella enterica: Evidence of a Tetrahedrally Coordinated Divalent Transition Metal Cofactor with Cysteine Ligation. *Biochemistry*. **2017**, 56, 364-375.

64. Lai, K.; Dave, K. I.; Wild, J. R., Bimetallic binding motifs in organophosphorus hydrolase are important for catalysis and structural organization. *Journal of Biological Chemistry*. **1994**, 269, 16579-84.

65. Zhang, F.; Cao, L.; Yang, W., Preparation of Monodisperse and Anion-Charged Polystyrene Microspheres Stabilized with Polymerizable Sodium Styrene Sulfonate by Dispersion Polymerization. *Macromolecular Chemistry and Physics.* **2010**, 211, 744-751.

66. Zhang, J.-T.; Wang, L.; Lamont, D. N.; Velankar, S. S.; Asher, S. A., Fabrication of Large-Area Two-Dimensional Colloidal Crystals. *Angewandte Chemie International Edition*. **2012**, 51, 6117-6120.

67. Smith, N. L.; Coukouma, A.; Dubnik, S.; Asher, S. A., Debye ring diffraction elucidation of 2D photonic crystal self-assembly and ordering at the air-water interface. *Physical Chemistry Chemical Physics*. **2017**, 19, 31813-31822.

68. Smith, N. L.; Hong, Z.; Asher, S. A., Responsive ionic liquid-polymer 2D photonic crystal gas sensors. *Analyst.* **2014**, *139*, 6379-6386.

69. Kanicky, J. R.; Shah, D. O., Effect of Premicellar Aggregation on the pKa of Fatty Acid Soap Solutions. *Langmuir.* **2003**, 19, 2034-2038.

70. Mohamad, N. R.; Marzuki, N. H. C.; Buang, N. A.; Huyop, F.; Wahab, R. A., An overview of technologies for immobilization of enzymes and surface analysis techniques for immobilized enzymes. *Biotechnology, Biotechnological Equipment.* **2015**, 29, 205-220.

71. Zhang, J.-T.; Smith, N.; Asher, S. A., Two-Dimensional Photonic Crystal Surfactant Detection. *Analytical Chemistry*. **2012**, 84, 6416-6420.

72. Bal, W.; Sokołowska, M.; Kurowska, E.; Faller, P., Binding of transition metal ions to albumin: Sites, affinities and rates. *Biochimica et Biophysica Acta - General Subjects*. **2013**, 1830, 5444-5455.

73. Fasano, M.; Curry, S.; Terreno, E.; Galliano, M.; Fanali, G.; Narciso, P.; Notari, S.; Ascenzi, P., The extraordinary ligand binding properties of human serum albumin. *IUBMB Life*. **2005**, 57, 787-796.

74. Ghuman, J.; Zunszain, P. A.; Petitpas, I.; Bhattacharya, A. A.; Otagiri, M.; Curry, S., Structural Basis of the Drug-binding Specificity of Human Serum Albumin. *Journal of Molecular Biology*. **2005**, 353, 38-52.

75. Sułkowska, A., Interaction of drugs with bovine and human serum albumin. *Journal of Molecular Structure*. **2002**, 614, 227-232.

76. Evoli, S.; Mobley, D. L.; Guzzi, R.; Rizzuti, B., Multiple binding modes of ibuprofen in human serum albumin identified by absolute binding free energy calculations. *Physical Chemistry Chemical Physics*. **2016**, 18, 32358-32368.

77. Mew, E. J.; Padmanathan, P.; Konradsen, F.; Eddleston, M.; Chang, S.-S.; Phillips, M. R.; Gunnell, D., The global burden of fatal self-poisoning with pesticides 2006-15: Systematic review. *Journal of Affective Disorders*. **2017**, 219, 93-104.

78. Gotthard, G.; Hiblot, J.; Gonzalez, D.; Elias, M.; Chabriere, E., Structural and Enzymatic Characterization of the Phosphotriesterase OPHC2 from Pseudomonas pseudoalcaligenes. *PLOS ONE*. **2013**, 8, e77995.

79. DiCosimo, R.; McAuliffe, J.; Poulose, A. J.; Bohlmann, G., Industrial use of immobilized enzymes. *Chemical Society Reviews*. **2013**, 42, 6437-6474.

80. O'Neil, M. J., The Merck index : an encyclopedia of chemicals, drugs, and biologicals. Merck: Whitehouse Station, N.J., 2001.

81. Grimsley, J. K.; Scholtz, J. M.; Pace, C. N.; Wild, J. R., Organophosphorus Hydrolase Is a Remarkably Stable Enzyme That Unfolds through a Homodimeric Intermediate. *Biochemistry*. **1997**, 36, 14366-14374.

82. Rastogi, V. K.; Defrank, J. J.; Cheng, T.-c.; Wild, J. R., Enzymatic Hydrolysis of Russian-VX by Organophosphorus Hydrolase. *Biochemical and Biophysical Research Communications*. **1997**, 241, 294-296.

83. Li, X.-D.; Wu, J.; Jia, D.-C.; Wan, Y.-H.; Yang, N.; Qiao, M., Preparation of Cross-Linked Glucoamylase Aggregates Immobilization by Using Dextrin and Xanthan Gum as Protecting Agents. *Catalysts.* **2016**, 6, 77.

84. Laothanachareon, T.; Champreda, V.; Sritongkham, P.; Somasundrum, M.; Surareungchai, W., Cross-linked enzyme crystals of organophosphate hydrolase for electrochemical detection of organophosphorus compounds. *World Journal of Microbiology and Biotechnology*. **2008**, 24, 3049.

6.0 Mechanisms by which Organic Solvent Exchange Transforms Responsive Pure Protein Hydrogels into Responsive Organogels

This chapter is being prepared for submission to the journal ACS Biomacromolecules, authored by Smith, N. L.; Coukouma, A.E.; Jakubek, R.S.; Asher, S. A.

Author Contributions: N.L.S performed Cryo-SEM imaging at the University of Minnesota Characterization Facility with assistance from Chris Frethem and Hanseung Lee. N.L.S. measured the organogel NIR absorbance and calculated the solvation shell waters. N.L.S. fabricated samples and measured swelling ratios with assistance from A.E.C. R.S.J. performed the UVRR experiments and calculations of protein secondary structure. A.E.C. performed titration experiments. N.L.S determined VPT mechanisms with assistance from S.A.A. The manuscript was prepared by N.L.S with assistance from S.A.A.

Recently, we demonstrated the fabrication of responsive pure protein organogel sensors and catalysts. Our Bovine Serum Albumin (BSA) organogel sensors undergo volume changes in response to protein-ligand binding. These responsive protein organogels are fabricated using a step-wise solvent exchange that replaces the aqueous mobile phase of protein hydrogels with pure ethylene glycol (EG). The exchange to EG that transforms the protein hydrogels into protein organogels causes a Volume Phase Transition (VPT) that dramatically decreases the gel volume. We demonstrate herein that this VPT is irreversible, i.e. incubating this organogel in water does not result in reswelling. This work examines the protein secondary structure, protein hydration, and protein polymer morphology in the BSA hydrogels, BSA organogels, and in the

water incubated BSA organogels by using UV Resonance Raman (UVRR) and NIR absorption spectroscopies, Cryo-SEM imaging, and titration of the amino acid carboxyl groups. We discuss the mechanisms involved in the BSA hydrogel to organogel transformation that give rise to this irreversible VPT.

The native BSA secondary structure and solvation shell water layers are mostly retained in the BSA organogel. The BSA organogel UVRR spectrum reveals that a ~4% increase in the α-helix population occurs upon exchange to EG. This secondary structure change is reversible; the UVRR of the BSA hydrogel and water incubated BSA organogel are identical. In contrast, the EG exchange irreversibly changes the BSA polymer morphology. The BSA hydrogel morphology consisting of interconnected thin BSA polymer strands is transformed into a dense amorphous protein polymer phase in the water incubated BSA organogel. These results indicate the VPT is driven by the free energy of mixing changes between the BSA protein polymer and mobile phase during the EG exchange. The change in solvent quality causes BSA polymer phase separation, which minimizes the BSA polymer surface area exposed to EG. This phase separation proceeds as a kinetic two-stage process that decreases the distances between BSA polymer strands, enabling inter-protein interactions between BSA polymer strands. These additional protein polymer interactions increase the effective polymer crosslink density, preventing organogel swelling as the mobile phase is exchanged back to water.

6.1 Introduction

Hydrogels and organogels are versatile materials with numerous applications as sensors[2-8], catalysts[9], drug delivery materials[10-13], tissue engineering scaffolds[14], wound dressings[15-16], membranes[17], and mechanical actuators[18-19]. These responsive materials consist of two primary components; a stationary phase made up of a 3-dimensional chemically or physically crosslinked polymer network and a liquid mobile phase that facilitates diffusion and mass transport within the polymer network. Hydrogels contain an aqueous mobile phase, whereas organogels contain an organic solvent mobile phase.

Our group pioneered the development of photonic crystal-based[20-21] colorimetric chemical sensors that utilize the hydrogel volume phase transitions (VPT) responses to external stimuli such as pH, light, temperature, and chemical analytes.[6, 21-26] Hydrogels or organogels that have molecular recognition groups attached to the polymer network selectively undergo VPT in response to a specific analyte.[25-27] This sensing mechanism relies on an analyte induced VPT that shifts the embedded photonic crystal diffraction.[21-22] This VPT involves a sharp change in the hydrogel/organogel volume in response to small changes in the hydrogel/organogel chemical environment.[28] These volume changes are caused by osmotic pressures, $\prod$ which derive from changes in the Gibbs free energy, ΔG_{Total}.[29,30] Osmotic pressures in the system induce mass transfer of the mobile phase; either partitioning the mobile phase into the polymer network to cause swelling, or expelling the mobile phase to cause shrinking. When the polymer and mobile phase are at equilibrium, $\prod_{Total} = \partial \Delta G_{Total}/\partial V = 0$. In general, analyte recognition must induce a change in the Gibbs free energy to actuate a VPT.

Recently, we developed several stimuli responsive pure protein hydrogels that sense pH, glucose, yeast cells, drugs, surfactants, and fatty acids.[5, 7-8] These protein hydrogels have

selective chemical responses because the constituent proteins show specific molecular recognition. There exists a large body of research developing functional pure protein hydrogels using a variety of fabrication methods, such as glutaraldehyde crosslinking, or enzyme catalyzed crosslinking of proteins, and self-assembly of engineered proteins.[9, 13, 31-35]

There are very few studies of pure protein organogels,[36-37] despite the intense interests in utilizing protein chemistry in organic solvents for enzymatic synthesis of pharmaceuticals and biofuels[38-40], as well as for sensing and degrading toxic compounds important to the defense industry.[41-42] Organic solvents typically denature proteins and significantly decrease protein reactivity.[43] This has led to the development of several techniques to stabilize proteins against denaturation or deactivation by organic solvents.[44-47]

We very recently developed methods to fabricate stimuli responsive pure protein organogels for sensing and catalysis applications.[48] The pure protein organogels are fabricated from pure protein hydrogels by using a stepwise solvent exchange that replaces the aqueous mobile phase of pure protein hydrogels with ethylene glycol (EG). Chemically crosslinked pure protein polymer hydrogels are fabricated by polymerizing protein monomers in solution using glutaraldehyde. The proteins are immobilized by this protein polymerization such that the proteins retain their native reactivity after the aqueous mobile phase is replaced with pure EG. Protein immobilization is a widely used strategy to stabilize proteins against denaturation. Immobilization typically enhances protein activity in organic solvents.[44-45, 49-55]

We believe that our photonic crystal BSA organogel sensor[48] is the first reported responsive pure protein organogel to show a VPT in response to ligand binding. The polymerized BSA in the organogels bind the same ligands as do the BSA hydrogels[5] and the

native protein monomers.[56-57] Both, the BSA hydrogels and organogels swell in response to BSA binding of charged ligands like ibuprofen and fatty acids, for example.

The solvent exchange that transforms responsive BSA hydrogels into responsive BSA organogels also induces a large VPT that decreases the organogel volume as the concentration of EG in the mobile phase increases. As shown below, this solvent exchange induced VPT is irreversible; rehydrating the BSA organogel by exchanging the EG mobile phase back to water does not result in reswelling.

In this work, we characterize the changes in the protein secondary structure, protein hydration, and the protein polymer morphology in the BSA hydrogels and organogels in order to elucidate the mechanisms involved in this irreversible VPT. The BSA secondary structure in the hydrogel, organogel, and water incubated organogel is determined using the UVRR $AmIII_3$ band frequencies that are sensitive to changes in the peptide secondary structure.[58] The protein solvation shell water layer in the BSA organogel is estimated using the strong NIR absorbance of water. Cryo-SEM is used to image the morphology[59] of the BSA hydrogels and water incubated organogels; elucidating the supermolecular structure of the protein polymer networks. The change in the protein polymer surface area exposed to the mobile phase is determined by titrating the BSA amino acid carboxyl groups.

We discuss the mechanisms of the BSA hydrogel to organogel transformation that result in a very large VPT. VPT that dramatically decrease the volume of crosslinked polymer networks are often driven by polymer phase separations.[60-61] We also posit that the origin of the irreversible VPT stems from inter-protein interactions formed in the phase separated polymer. These inter-protein interactions act as effective polymer crosslinks that prevent BSA polymer swelling of the water incubated organogel.

6.2 Experimental

6.2.1 Materials

BSA (>98%; lyophilized powder, essentially fatty acid free) and Sigmacote™, were purchased from Sigma Aldrich and used as received. 50 wt% glutaraldehyde in water was purchased from Sigma Aldrich and diluted to 12.5 wt% glutaraldehyde with nanopure water. Ethylene glycol (certified, 0.05% water) was purchased from Fisher Chemical and used as received. Nanopure water was produced using a Barnstead NANOpure infinity system. Type A Brass Planchets were purchased from Ted Pella.

6.2.2 Fabrication of BSA Hydrogels, Organogels, and Water Incubated Organogels

BSA hydrogels were fabricated by polymerizing BSA monomers in solution using glutaraldehyde to form covalent linkages between BSA lysine residues, as described in our previous publications.[5] Glass microscope slides were treated with Sigmacote™ to make their surfaces hydrophobic. A ~410 μm thick spacer was created by adhering layers of 3M Scotch® Magic™ Greener tape along the four edges of the slide. The spacer ensures that the polymerized hydrogel film has a uniform thickness.

A 200 mg/ml BSA stock solution was prepared by dissolving lyophilized BSA powder in nanopure water. BSA hydrogel polymerization was initiated by adding 64 μL of a 12.5 wt% glutaraldehyde solution to 1.0 mL of the BSA stock solution. The solution was shaken to mix the components, then poured onto the glass slide within the spacer. A second glass slide was placed on top and pressed firmly into the spacer to expel excess solution. The BSA/glutaraldehyde

solution was polymerized for 3 hr at room temperature. After polymerization, the slides were separated, releasing the BSA hydrogel films. BSA hydrogels were washed with large amounts of nanopure water for 2 days to remove unreacted BSA and glutaraldehyde.

BSA organogels were fabricated by using a stepwise solvent exchange process that replaces the aqueous mobile phase with EG.[48] BSA hydrogels were incubated in aqueous solutions containing increasing concentrations of EG for 24 hr during which the solvent was replaced 3 times with ~250 mL of fresh solution. The samples were placed on a shaker to mix the BSA gels and solution during the exchange. The BSA hydrogels were transferred from nanopure water to 30% (v/v) EG in water, then to 50% (v/v) EG in water, then to 70% (v/v) EG in water. Finally, the BSA gels were equilibrated with pure EG for 2 days to complete the solvent exchange. ~250 mL of pure EG was replaced 6 times over those 2 days to ensure excess water was removed from the mobile phase.

Water incubated BSA organogels were fabricated by exchanging the mobile phase of BSA organogels from pure EG back to pure water. The step wise solvent exchange described above was reversed, BSA organogels were incubated in 70% (v/v) EG, followed by 50% (v/v) EG, then 30% (v/v) EG for 24 hr each on the shaker where the solvent (~250 mL) was replaced 3 times each day. Finally, the organogels were incubated in nanopure water for 3 days where ~250 mL of fresh water was replaced 4 times daily to ensure that all the EG was removed from the mobile phase.

6.2.3 Volume Phase Transition Measurements

Directly after BSA polymerization, before washing the hydrogels in water, the hydrogel films were cut into smaller square pieces using a razor blade. The dimensions of each piece were

measured using a digital micrometer. The precisely measured hydrogel samples were washed in nanopure water followed by the stepwise solvent exchange described above. The dimensions of the hydrogel samples were measured after equilibration at each solvent composition.

The BSA hydrogel pieces exist as free-floating films that appear to swell isotropically. Therefore, the hydrogel and organogel volumes can be calculated from the measured gel areas using the swelling ratio, $\left(\frac{A}{A_i}\right)^{3/2} = \frac{V}{V_i}$, where A_i and V_i are the initial area and volume of the BSA hydrogel pieces directly after polymerization, while A and V are the area and volume of the BSA hydrogel or organogel equilibrated in a particular EG/water solution.

The initial BSA concentration in the hydrogel directly after polymerization is 200 mg/mL, which corresponds to an initial BSA polymer volume fraction of $\phi_i = 15\%$, given the specific volume of BSA in water is 0.734 cm^{-3}/g.[62-63] The BSA polymer volume fraction in the hydrogel or organogel after swelling or shrinking in solvent is calculated using the volume swelling ratio (Equation 6.1).

$$\textbf{Equation 6.1} \quad \boldsymbol{\phi = \phi_i(15\%) * \frac{V}{V_i}}$$

6.2.4 UV Resonance Raman Spectroscopy of BSA Hydrogels, Organogels, and Water Incubated Organogels

UV resonance Raman (UVRR) spectroscopy was used to investigate the secondary structure of BSA monomers free in solution and polymerized BSA in the hydrogel, organogel, and organogel incubated in water.

The instrumentation used was previously described in detail by Bykov et al.[64] We generated ~204 nm excitation light by first frequency tripling the fundamental of a Nd:YAG

laser to ~355 nm. The ~355 nm light was then Raman shifted to ~204 nm using the 5th anti-Stokes harmonic of hydrogen gas (30 psi). The 204 nm light was focused onto a spinning Suprasil quartz NMR tube containing the sample, and a ~165° backscattering geometry was used to collect the scattered light. The scattered light was dispersed using a home-built double spectrometer in a subtractive configuration. The dispersed light was imaged using a liquid nitrogen cooled back-thinned CCD camera (Princeton Instruments) with a Lumogen E coating.

6.2.5 NIR Absorbance Measurements of BSA Organogels

The strong water absorption band at 1915 nm was used to calculate the water content in BSA organogels using a protocol similar to that of our previous publication.[65] The NIR absorption between 1400-2000nm was measured for solutions containing 1.6 mL of EG and 0, 5, 10, 15, 20, and 25 μL water in a 5 mm path length quartz cuvette. The absorption of 1 and 2 layers of the BSA organogel film was measured. Excess EG on the surface of the organogel films was removed by blotting the films with filter paper until the surface appeared dry.

The 420 μm thick organogel film was cut to the size of the cuvette inner wall (~1 cm x 4 cm). The film was then placed on the wall of the quartz cuvette. Experimental details of these measurements are provided in Appendix C. Appendix C also includes the absorbance of EG/water solutions, the calibration curve for water absorption in EG at 1915 nm and the calculation of the water concentration in the organogel.

6.2.6 Cryo-SEM of BSA Hydrogels and Water Incubated Organogels

Cryo-SEM imaging was performed at the University of Minnesota Characterization Facility in collaboration with Chris Fretham and Hanseung Lee.

6.2.6.1 Preparation of BSA Solution, Hydrogel and Water Incubated Organogel Samples for Cryo-SEM

BSA was dissolved in nanopure water to make 200 mg/mL BSA solutions. The BSA solution samples were prepared for Cryo-SEM by sandwiching a 3 μL aliquot of the 200 mg/mL BSA solution between two brass planchets. The Ted Pella Type A planchets were 3 mm in diameter. They contained a 2 mm diameter 100 μm deep well in the center. The cylindrical cavity between the planchets that contained the samples was 200 μm thick.

The BSA hydrogel samples were prepared by polymerizing the BSA/glutaraldehyde solution between two Type A brass planchets, in the 2 mm diameter, 200 μm thick cavity. The surface of the brass planchets was abraded prior to hydrogel polymerization to promote adhesion between the hydrogel and planchet so that the hydrogel fractured after freezing.

Cryo-SEM imaging requires sublimation of the water mobile phase to reveal the polymer stationary phase. Protocols to flash freeze pure EG and subsequently sublimate the EG mobile phase do not currently exist. Therefore, the EG mobile phase was exchanged back to water to form the water incubated organogel as described above. The thickness of the water incubated organogel film was between 0.18-0.2 mm after the solvent exchange process was completed. A specialized die was fabricated by the University of Pittsburgh machine shop and used to cut 1.8 mm diameter discs from the BSA organogel films. These organogel discs fit snuggly into the 2 mm diameter/ 0.2 mm thick cavity between the two Type A brass planchets.

High pressure flash freezing of the samples between brass planchets was done using a BAL-TEC HPM 010 high pressure freezing machine at 2100 bar with liquid nitrogen (LN_2). High pressure freezing promotes formation of vitreous ice and prevents the formation of ice crystals that can destroy the delicate network structure.[66] Samples were stored under constant cryogenic temperatures.

The planchets containing frozen samples were affixed to a sample holder while still immersed in a LN_2 bath. A photograph of the sample holder is shown in Appendix C. The sample holder was then transferred to the Leica EM ACE600 high vacuum sputter coater using the Leica VCT100 shuttle. The Leica VCT100 shuttle and the Leica EM ACE600 were cooled with LN_2 prior to transferring the samples. It is important that the sample remains at cryogenic temperatures to avoid ice crystal formation. The pressure and temperature inside the chambers were maintained at 1.5×10^{-5} mbar and at –166 °C. A cold knife was used to remove the top planchet, fracturing the sample to reveal the inner hydrogel and organogel polymer networks.

Vitrified ice in the interstitial spaces of the protein polymer network was removed by sublimation, a process sometimes referred to as Cryo-etching[66]. The temperature inside the chamber was increased from -166 °C to -100 °C at a rate of 3 °C/min. The sample was held at -100 °C for 40 minutes to allow significant sublimation of vitreous ice at the surface. This reveals the protein polymer network. A cold trap kept at -160 °C was placed over the sample to prevent sublimated water vapor from condensing back onto the sample.

After 40 min, the temperature was decreased to -115 °C, halting the sublimation of water. After sublimation, samples were sputter coated, depositing a 2.5 ± 0.03 nm layer of platinum on the sample. The thickness of the Pt coating was determined by the frequency shift of a quartz crystal oscillator, calibrated for the density of the Pt deposited.

6.2.6.2 Cryo-SEM of Frozen Hydrated BSA Hydrogels and Water Incubated Organogels

The samples were transferred to the Hitachi SU8230 Field Emission Gun Scanning Electron Microscope under vacuum in the Leica VCT100 shuttle. The Leica VCT100 Cryo-stage temperature was maintained at -115 °C throughout imaging. Samples were examined using low accelerating voltages (0.8 - 2 kV) to avoid charging and subsequent damage to the sample. Samples were left in the SEM chamber overnight under vacuum after Cryo-SEM imaging was complete. As the temperature inside the vacuum chamber slowly increased throughout the night, the samples became freeze dried. The freeze-dried samples were imaged the next day before the SEM was cooled with liquid nitrogen. The stage temperature was ~10 °C during SEM imaging of the freeze-dried samples.

We used the NIH software ImageJ[67] to analyze the BSA polymer networks in the Cryo-SEM micrographs. The BSA polymer strand diameters, pore diameters, and the length of the protein polymer strands were measured in several Cryo-SEM images and averaged.

6.2.7 Titration of BSA Hydrogels and Water Incubated Organogels

BSA hydrogels were prepared as described above and cut to various sizes directly after polymerization before incubating in water. The concentration of BSA in these BSA hydrogels are 200 mg/mL. The area of each freshly prepared 420 μm thick BSA hydrogel piece is measured using a Vernier micrometer. The moles of protein contained in each BSA hydrogel piece was calculated from its volume. The hydrogel samples were then equilibrated in nanopure water.

Half of the BSA hydrogel samples were transformed to BSA organogels using the step-wise EG exchange process. These organogel samples were then rehydrated with nanopure water

by reversing the step-wise solvent exchange process. These samples were then incubated in water for 3 days, during which the water was replaced twice daily with fresh nanopure water.

The BSA hydrogels and water incubated organogels were placed in 2 mL of pH 7.5 nanopure water. The pH was monitored using a Hanna Instruments HI5522 pH meter with a Hanna Instruments HI 1083 microelectrode as 5-20 μL aliquots of 0.1 M HCl titrant were added to solutions containing the gels. After each addition of HCL, the solution was mixed for 15 minutes before the pH was recorded. The pH was then plotted against (moles HCl added / mole BSA). 6 replicate measurements were performed for both the BSA hydrogels and water incubated organogels.

6.3 Results and Discussion

Responsive pure protein hydrogels are fabricated by polymerizing BSA protein monomers using glutaraldehyde to form covalent linkages between BSA lysine residues (Figure 6.1). Glutaraldehyde is a commonly used protein crosslinker and fixative that has little impact on the native protein structure and the native protein reactivity.[50, 68] We use the term '**inter-protein** crosslinks' to specifically describe the short glutaraldehyde linkages between BSA proteins in the pure protein polymer chains. This is distinct from the **polymer** crosslinks that define points where the protein polymer chains interconnect to form the 3-dimensional hydrogel polymer network.

Glutaraldehyde is most reactive towards lysine residues on the protein surface.[68] BSA contains 60 lysine residues, 34 of which are located on the BSA surface (Figure 6.1A) and are available for glutaraldehyde inter-protein crosslinking.[69] The BSA surface lysine residues are up

to 20-24 Å apart.[69] Glutaraldehyde reacts in aqueous solutions to form a mixture of glutaraldehyde monomers and glutaraldehyde polymers of various lengths.[68] Thus, both inter-protein and intra-protein crosslinking can occur.

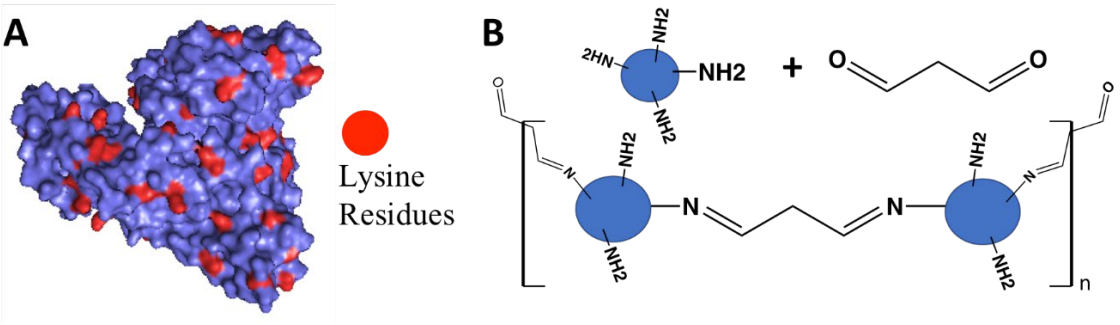

Figure 6.1 - A. BSA protein structure showing lysine residues highlighted in red. Structure obtained from Protein Data Bank, 3V03.[1] Image made using PyMol software. B. One possible glutaraldehyde inter-protein crosslinking reaction; the aldehyde and lysine amine form a Schiff base that covalently links the two proteins.

Intra-protein crosslinking is favored at low protein and glutaraldehyde concentrations.[68, 70] At high protein concentrations and at higher glutaraldehyde/protein ratios (typically >25), inter-protein crosslinking is favored.[68] The 27 glutaraldehyde/BSA ratio that was used to polymerize the 200 mg/mL BSA solution should favor inter-protein crosslinking over intra-protein crosslinking, forming a polymer of covalently linked protein monomers. One possible inter-protein crosslinking reaction is shown in Figure 6.1B, where monomeric glutaraldehyde reacts with two lysine residues to form a Schiff base. The formation of inter-protein crosslinks is evident from the formation of the insoluble protein polymer network that makes up the hydrogel. These elastic BSA hydrogels are sufficiently robust to be easily handled.

6.3.1 Cryo-SEM Imaging of BSA Hydrogel Morphology and Topology

We utilized Cryo-SEM to image the BSA hydrogel morphology in the hydrated state.[66,71-73] The hydrogel morphology is defined as the supermolecular structure of the 3D polymer network that gives rise to the polymer strand diameters, polymer strand lengths, and the network pore sizes.[74-75] Polymer morphology impacts hydrogel properties, such as their swelling behavior, which effects hydrogel sensing and drug release behaviors, and their mechanical properties.[17, 76] For example, hydrogel networks with increased crosslink density form increasingly robust materials that exhibit smaller VPT in response to analyte recognition.

Macroscopically, our BSA hydrogels are transparent and appear to be homogeneous films. These BSA hydrogel films also exhibit homogeneous VPT swelling in response to hydrogel protein-ligand binding.[5, 48] At the nano and/or micro scale, the BSA hydrogel supermolecular structure appears relatively heterogeneous, as shown in Figure 6.2. The BSA hydrogel network pore sizes have a large distribution of diameters, ranging from ~50 nm to ~200 nm.

The Cryo-SEM micrographs show a discernible BSA polymer network once the vitreous ice is sublimed from the sample (Figure 6.2A-D). The 40 min sublimation time removes most of the sample bulk water, revealing the protein polymer network morphology of our frozen hydrated BSA hydrogel. Figure 6.2B shows an area with many patches of vitreous ice remaining on the sample. The red arrow in Figure 6.2B points to one of these remaining vitreous ice patches. BSA is a hydrophilic, water soluble protein. Thus, solvation shell waters will be difficult to sublimate and will tend to remain bound to the polymerized BSA.

Shown in Figure 6.2A-D, the hydrogel consists of a dense network of interconnected thin BSA polymer strands. The BSA polymer strand diameters were measured in areas where

vitreous ice had mostly sublimated, as shown in Figure 6.2D. The BSA hydrogel is primarily composed of BSA polymer strands having diameters of ~15 ± 5 nm.

These ~15 nm BSA polymer strand diameters are roughly the width of a single hydrated BSA protein monomer. X-ray diffraction measurements of BSA crystals determined that BSA proteins have dimensions of ~4 × 6.5 × 7.5 nm^3.[1] We expect the measured dimensions of a single BSA in our samples will be larger than the crystal structure dimensions due to its bound water layers and its Pt coating. Terahertz spectroscopy has shown that the water solvation shell can extend up to ~0.8 – 1.5 nm from the protein surface.[77-78] The 2.5 nm Pt sputter coating will also increase the dimensions of the hydrated BSA polymer strands. These measured BSA polymer strand diameters (Figure 6.2) are roughly similar to the expected dimension of a single, Pt coated, hydrated BSA protein.

From these high resolution Cryo-SEM images of hydrated BSA hydrogels, we can detect the polymerized BSA hydrogel topology, i.e. how the BSA protein monomers are interconnected by glutaraldehyde inter-protein crosslinking to form the polymer network.[79] The ~single BSA diameter of the protein polymer strands indicates that most of the globular proteins are bound together into roughly linear BSA chains, reminiscent of a pearl necklace like-structure. Polymer crosslinks in the BSA hydrogel network are created by a protein that forms ≥3 inter-protein crosslinks that connect two or more of these BSA polymer strands, as illustrated in Figure 6.3.

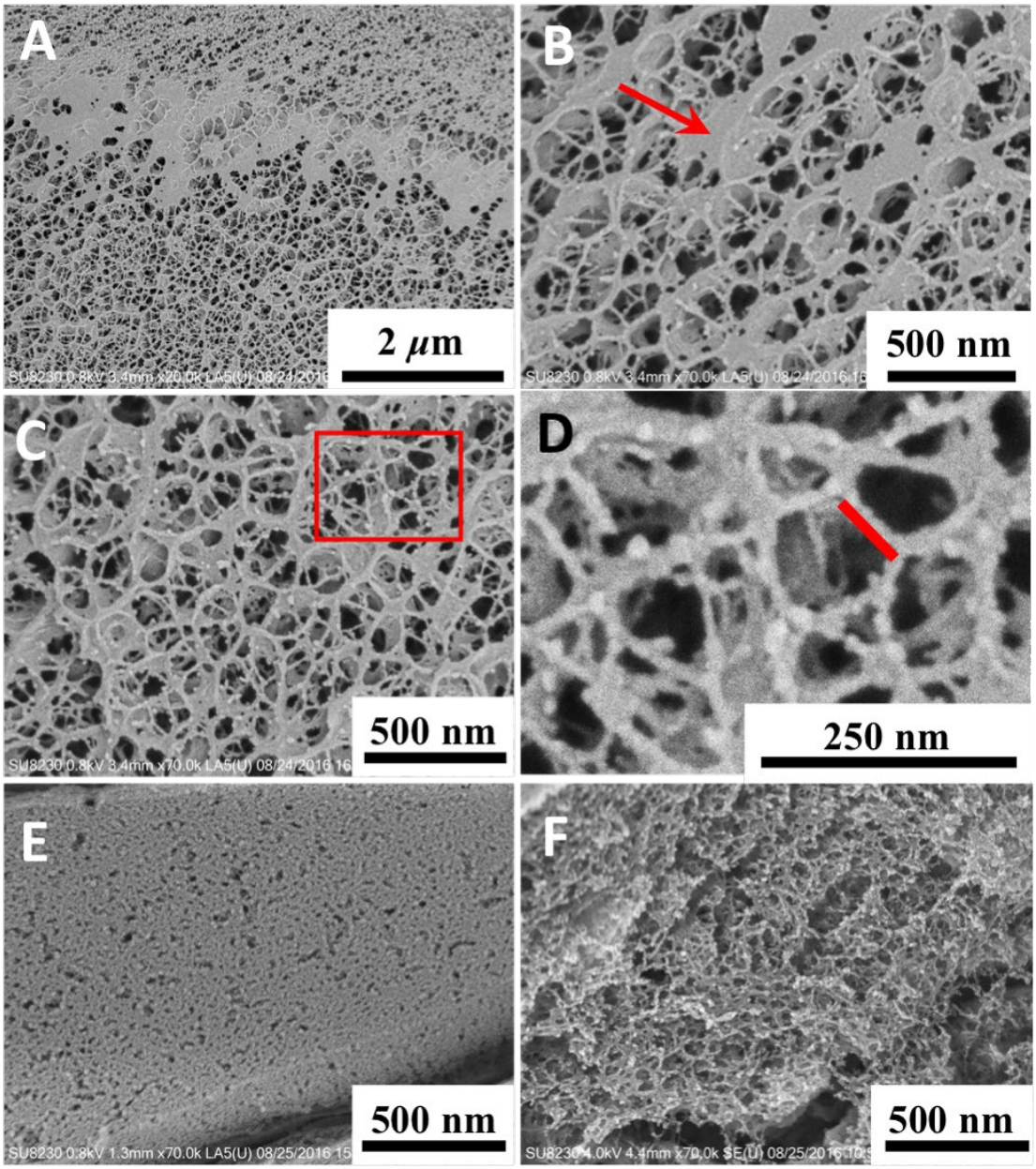

Figure 6.2 - Cryo-SEM of frozen hydrated BSA hydrogels (A-D), and of a BSA monomer solutions prior to polymerization (E), and a non-Cryo SEM of a BSA hydrogel that was freeze dried (F). Frozen hydrated BSA hydrogels are shown at (A) 20K magnification; (B) 70K magnification, red arrow points to vitreous ice remaining in the sample; (C) 70K magnification, red box indicates the area that is enlarged in image D. Image D is an enlarged section of image C where the thin BSA polymer strands are clearly visible. The red line highlights one of the measured protein polymer strand lengths. (E) Cryo-SEM of BSA monomer solutions before glutaraldehyde polymerization; 70K magnification. (F) Non-Cryo SEM of freeze dried BSA hydrogel; 70K magnification.

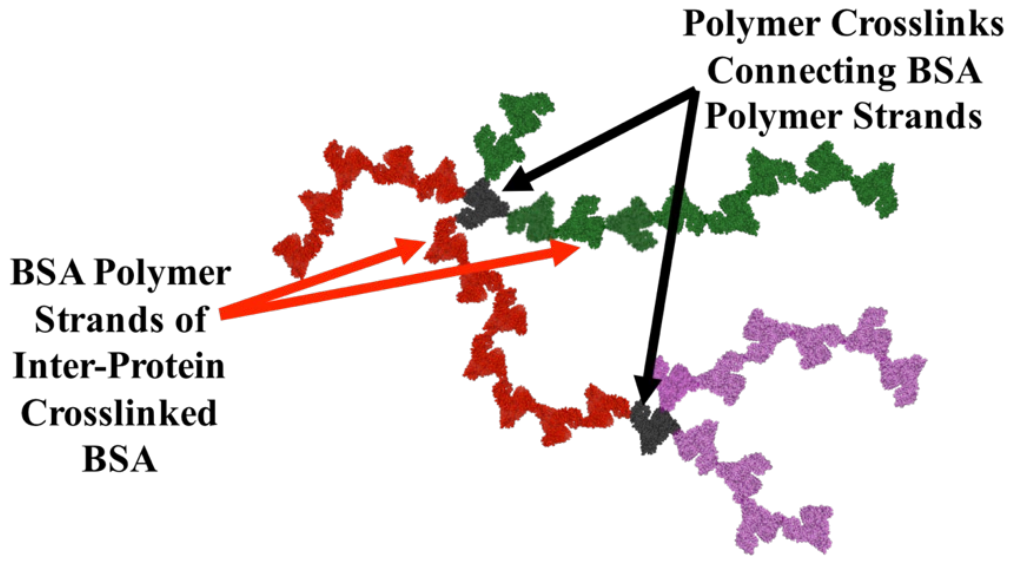

Figure 6.3 - Proposed BSA hydrogel topology based on the Figure 6.2 Cryo-SEM images. Black arrows point to polymer crosslinks, where a BSA forms inter-protein crosslinks that connect two polymer strands. Red arrows point to different BSA protein polymer strands that are colored red, green, and pink.

We can approximate the molecular weight between crosslinks in the BSA hydrogel network by estimating the number of proteins (MW: 66,463 g/mol BSA) in the polymer strands between polymer crosslinks. The red line in Figure 6.2D highlights a measured polymer strand length. The BSA polymer strand lengths correspond to ~5-30 BSA proteins, i.e. the molecular weight between crosslinks in the BSA polymer network is between ~$3 \times 10^5 - 2 \times 10^6$ g/mol.

The polymer crosslink density is the dominant factor determining the elastic free energy storage of the responsive BSA hydrogel.[29, 80] Increasing the polymer crosslink density limits VPT swelling and shrinking. The crosslink density is inversely proportional to the average molecular weight between crosslinks.

There are clear differences between the BSA hydrogel morphology (Figure 6.2A-D) and the morphology of the BSA monomer solution before glutaraldehyde polymerization (Figure 6.2E). Cryo-SEM images of the BSA monomer solution lack the characteristic interconnected

polymer network observed for the BSA hydrogels. This difference between the glutaraldehyde polymerized BSA hydrogel and the BSA monomer solution confirms that predominantly inter-protein crosslinks are formed by the polymerization of a 200 mg/mL BSA solutions at a glutaraldehyde/BSA protein ratio of 27.

Cryo-SEM is uniquely able to probe hydrated samples like hydrogels without significantly altering the protein polymer morphology.[71, 73, 81] In contrast, non-Cryo/traditional SEM techniques require sample drying prior to SEM imaging. Drying the hydrogel results in the collapse of the polymer network. It is much more difficult to observe and measure the individual polymer strands in Non-Cryo SEM images where BSA hydrogel samples are freeze dried (Figure 6.2F). Freeze dried BSA hydrogel samples also appear to have smaller pores compared to those of the frozen hydrated samples (Figure 6.2A-D).

6.3.2 EG Solvent Exchange Causes Irreversible VPT

The stepwise solvent exchange from water to EG transforms responsive BSA hydrogels into responsive BSA organogels that sense protein-ligand binding in the pure organic solvent environment.[48] This EG exchange causes a large VPT that decreases the organogel volume. This VPT is irreversible with respect to the mobile phase composition. Attempting to rehydrate the BSA organogel by reversing the stepwise solvent exchange back to water does not cause organogel swelling. The volume swelling ratios, V/V_o, (red circles) and the resulting BSA polymer volume fractions, ϕ, (black squares) are shown in Figure 6.4, beginning with the initial BSA hydrogel directly after glutaraldehyde polymerization (ϕ = 15 vol%), and for each subsequent solvent exchange step in the hydrogel to organogel transformation.

The BSA hydrogel initially swells in water after polymerization until the system comes to equilibrium; $\prod_{Total} = \partial \Delta G_{Total}/\partial V = 0$. BSA hydrogel swelling in nanopure water decreases the BSA polymer volume fraction from ϕ = 15 vol% to ϕ = 6 vol% BSA.

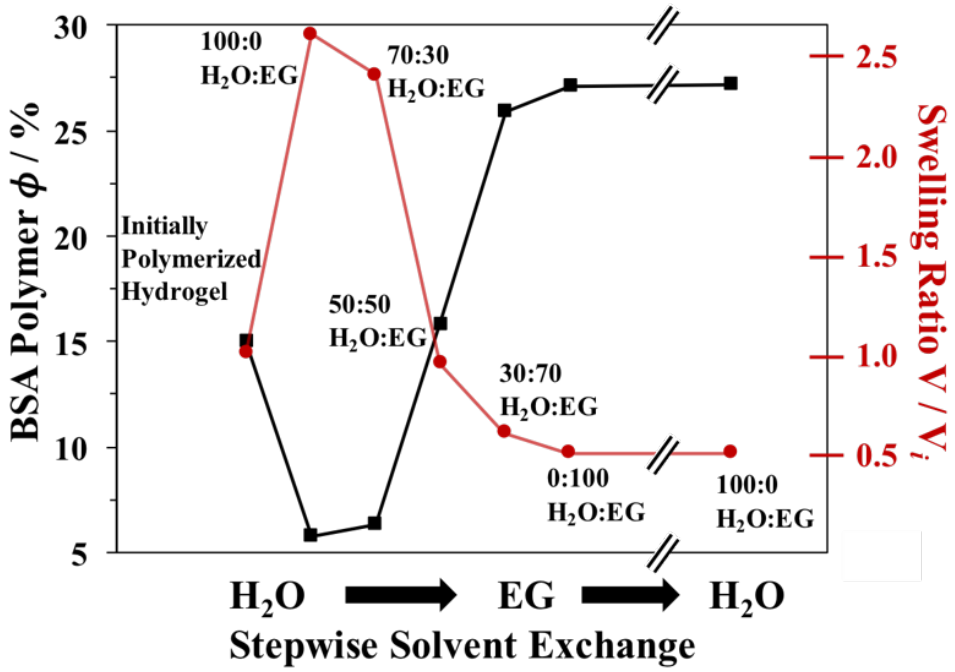

Figure 6.4 - The dependence of the BSA polymer volume fraction, ϕ (left axis;black squares) and the swelling ratio, V/V_i (right axis;red circles) as a function of mobile phase composition during the stepwise water to EG exchange. The breaks in the graph illustrate the stepwise solvent exchange from pure EG back to pure water.

Rehydrating the organogel by exchanging the EG mobile phase back to water does not cause organogel swelling. The BSA organogel does not reswell after incubating in water for over 7 days, nor does it swell when the solution is mildly heated to 45 ºC. This temperature is below the 57 ºC temperature that induces BSA conformational changes.[82] Above 57 ºC, swelling may result from protein unfolding. The BSA polymer volume fraction of these water incubated BSA organogels is equal to that of the BSA organogel in EG, ϕ = 27 vol% BSA.

Flory polymer solution theory is often used to describe the VPT phenomenon,[29] which describes the VPT in terms of osmotic pressures in the system that drive the volume change. These osmotic pressures derive from Gibbs free energy changes in the polymer-mobile phase system. The change in the total Gibbs free energy, ΔG_{Total}, has contributions from free energy of mixing changes, ΔG_{Mix}, elastic free energy changes, ΔG_{El}, and ionic free energy changes, ΔG_{Ion}.[83-84] Changes in the mobile phase composition often induces ΔG_{Mix}. Typically, ΔG_{El} and ΔG_{Ion} are expected to be small for a simple solvent exchange.

The VPT that results in a dramatic decrease in volume suggests phase separation of the BSA polymer and mobile phase occurs during the water to EG exchange. The irreversibility very generally indicates there is a hysteresis in the total Gibbs free energy between the BSA hydrogel and water incubated BSA organogel. The mechanisms of this phase separation and the origin of this irreversible VPT are discussed below.

6.3.3 BSA Hydrogel, Organogel, and Water Incubated Organogel Secondary Structures

The secondary structures of BSA hydrogels, organogels, and water incubated organogels were investigated using UV Resonance Raman (UVRR) spectroscopy. UVRR spectroscopy is a powerful tool for investigating the hydrogen bonding[85-86], solvation environment[87-89], and secondary structure[58, 90-91] in proteins.[92-93] UVRR measurements were performed with an excitation wavelength of ~204 nm that is in resonance with the secondary amide $\pi \rightarrow \pi^*$ transitions of the polypeptide backbone.[93] This enhances the Raman scattering of vibrations that couple to the backbone amide electronic transitions.[93]

The UVRR enhanced amide III_3 band is highly sensitive to protein secondary structure.[58, 91] The $AmIII_3$ band, found in the ~1200-1300 cm^{-1} spectral region, consists primarily of C-N

stretching and NH bending of the peptide bond.[93] The frequency of the $AmIII_3^s$ band sinusoidally depends on the Ramachandran Ψ torsion angle of the peptide bond.[58, 91] Mikhonin et al. developed equations to calculate the Ramachandran Ψ angles from the measured $AmIII_3^s$ frequencies.[58]

The distribution of secondary structure populations in proteins give rise to a particular set of Ψ angles. The secondary structure distribution inhomogeneously broadens the $AmIII_3$ band. The secondary structures in our BSA proteins are determined from the broadened $AmIII_3$ Raman bands. The $AmIII_3$ band shape is fit to a series of Lorentzians whose sum fits the $AmIII_3$ Raman band shapes. Each Lorentzian band correlates to a particular Ψ angle frequency. The details of the calculated distribution of protein secondary structures in the BSA hydrogels, organogels and water incubated organogels is provided in Appendix C.

We reproduced UVRR measurements of the BSA hydrogel and BSA monomers in aqueous solution. The reproduced UVRR spectra, shown in Appendix C Figure C.2, agree with previous measurements.[5] The $AmIII_3$ band shape of the polymerized BSA hydrogel and BSA monomer are essentially identical, indicating that the protein secondary structure is not perturbed by the glutaraldehyde inter-protein crosslinking that forms the BSA polymer network.

In both the BSA monomer and the BSA hydrogel, the fit of the $AmIII_3$ band shape produces a dominant Lorentzian band at ~1263 cm^{-1}; this $AmIII_3^s$ frequency correlates to a Ψ angle of ~-47°.[58, 91] This Ψ angle derives from an α-helical secondary structure. The area under the Lorentzian band at 1263 cm^{-1} accounts for ~65% of the total $AmIII_3$ band intensity, indicating that BSA is predominantly α-helical. Other investigations on native BSA monomers also found the BSA secondary structure to be ~67% α-helical.[94-96]

The BSA organogel $AmIII_3$ band is shifted to a higher frequency from that of the BSA hydrogel (Figure 6.5). The negative peak in the hydrogel – organogel difference spectrum at ~1265 cm^{-1} (green spectrum in Figure 6.5) highlights the differences in the two $AmIII_3$ bands. This indicates that the α-helix type $AmIII_3$ band has an increased intensity in the organogel compared to the hydrogel. The BSA proteins in the organogel show a roughly 4% increase in α-helical secondary structures compared to that of the BSA hydrogels.

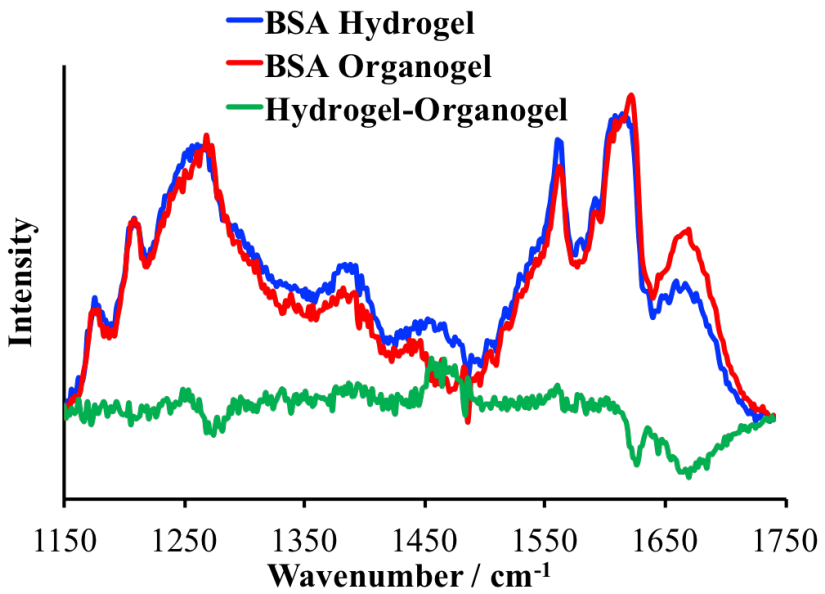

Figure 6.5 - UVRR spectra of BSA hydrogel (blue), BSA organogel (red), and BSA hydrogel-organogel difference spectrum (green). The broad AmIII3 band at ~1240-1270 cm^{-1} results from the distribution of peptide backbone Ψ angles used to calculate the protein secondary structure. Spectral differences around 1460 cm^{-1} result from the subtraction of an EG peak in the BSA organogel.

This result is consistent with previously reported data for immobilized albumins in the presence of EG.[97-98] For example, Wasacz et al. used IR/ATR spectroscopy to investigate the structure of Human Serum Albumin (HSA) that was adsorbed onto a substrate in water, EG, and methanol.[97] They observed an increased intensity of the α-helix $AmIII_3$ band when HSA was

exposed to EG. Organic mobile phases generally decrease the solvent's ability to compete for hydrogen bonds compared to water. As a result, the proteins form more intra-peptide hydrogen bonding which increases the propensity for α-helix and β-sheet secondary structure formation.

The UVRR spectra of water incubated BSA organogels reveals that the ~4% increase in the BSA organogel α-helical conformations is reversible when EG is exchanged back to water. The $AmIII_3$ band for the water incubated organogel is essentially identical to that of the BSA hydrogel (Figure 6.6), indicating the BSA hydrogel and water incubated organogel have similar secondary structures.

The EG appears to be completely washed out of the organogel during the EG to water exchange. The intense EG Raman peak at ~1460 cm^{-1} in the UVRR BSA organogel spectrum does not appear in the water incubated BSA organogel spectrum.

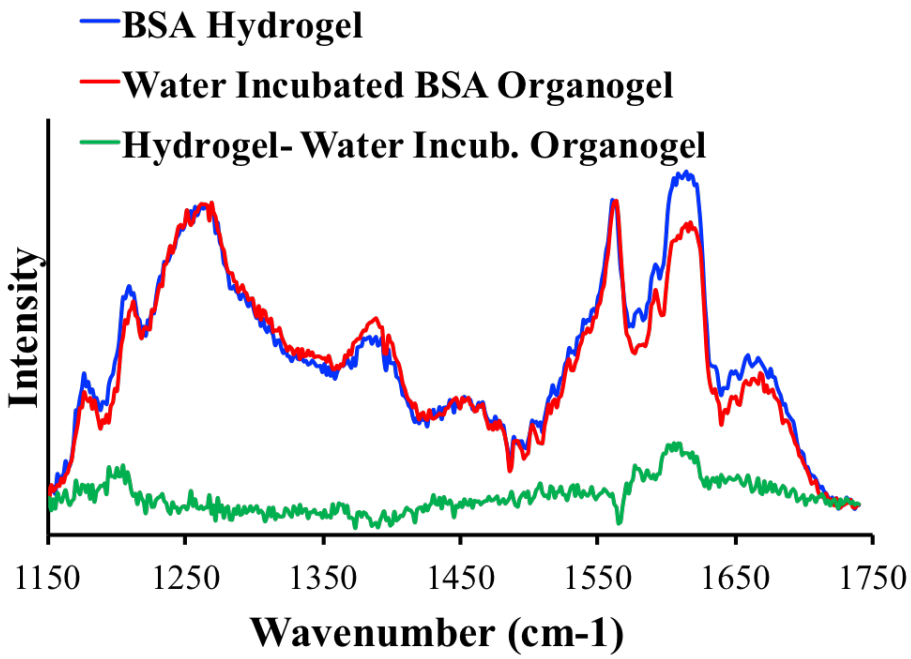

Figure 6.6 - UVRR spectra of (blue) BSA hydrogel, (red) water incubated BSA organogel, and (green) (BSA hydrogel - water incubated organogel) difference spectrum.

We also examined the frequency of the AmI band of the BSA hydrogel, BSA organogel, and rehydrated BSA organogel. The AmI band in the ~1650-1700 cm^{-1} spectral region consists predominantly of the C=O stretching motion of the peptide backbone.[93] The BSA hydrogel, BSA organogel, and water incubated BSA organogel all have AmI bands at about 1665 cm^{-1} The constant AmI band frequency in the BSA hydrogel and organogel spectra indicates that the hydrogen bonding, and dielectric environments of the protein backbone amides are similar for the polymerized BSA proteins in the water and EG mobile phases.[85-86, 92] This is unexpected since the dielectric constant of EG is significantly lower than that of water. This frequency would shift if the lower dielectric EG mobile phase caused disruptions to the protein H-bonding environment. AmI band frequency shifts in FT-IR spectra have been observed for HSA when bound water layers are stripped from the protein surface by the addition of EG.[98]

6.3.4 Water Content in BSA Organogels

NIR absorption spectroscopy was used to measure the water content in our BSA organogels to elucidate the microenvironment around the proteins of the organogel. Water strongly absorbs between 1900-1950 nm, whereas the EG has minimal absorption at these wavelengths.[99] Details on our calculation of the organogel water content is provided in Appendix C. In Appendix C, we include the 1400-2000 nm NIR absorbance of BSA organogels, the absorbance of EG-water mixtures, and the dependence of the 1915 nm absorbance as a function of water concentration. Details on the calculations of the water molar absorptivity at 1915 nm, the water concentration in bulk EG and the calculation of the water concentration in our BSA organogels are also included in Appendix C.

The BSA organogels are in equilibrium with an EG mobile phase that contains ~0.08 M water. The 1850-2000 nm absorbance spectra of the BSA organogel films is shown in Figure 6.7. The strong absorption in this region stems from water that is partitioned into the organogel films. From these absorbance measurements, we calculate that the maximum BSA organogel water concentration is 8.0 ± 0.2 M.

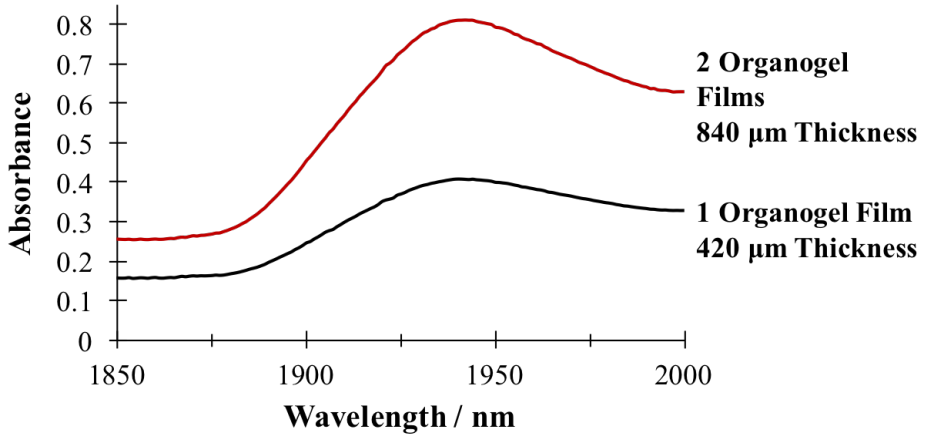

Figure 6.7 - NIR absorbance of a single and double layer of a 420 µm thick BSA organogel film. The strong absorption between 1900 and 1950 nm stems from water bound to the BSA polymer network in the organogel film.

To account for the small EG absorbance contributions to the total organogel absorbance, the absorbance of a 420 µm and 820 µm thick pure EG film was subtracted from the total BSA organogel absorbance. This subtraction over estimates the EG absorption since the EG content in the organogel is less than that of a pure EG film. The minimum BSA organogel water concentration is calculated using this EG subtracted absorbance. Our BSA organogels contain at least 6.5 ±0.2 M water. We assume that the increased water content in the BSA organogels relative to the bulk EG stems from a solvation shell water layer that is bound to the polymerized BSA proteins.

These BSA organogel water concentrations correspond to 1182 to 1475 water molecules per BSA protein. Small-angle neutron scattering experiments and theoretical calculations of a single water layer based on the BSA surface area have shown that the first solvation shell of BSA contains ~1070 water molecules.[78, 100] Terahertz spectroscopy studies of albumin proteins in aqueous solutions found the bound solvation shell waters, which have slower water relaxation times relative to bulk water, can extend ~0.85 nm[78] to ~1.5 nm[77] from the protein surface. Shiraga et al. estimated that the ~0.85 nm solvation shell contains ~3400 waters per BSA (3 – 4 hydration layers).[78]

The polymerized BSA proteins in pure EG retain more than one hydration layer. The 1182 – 1475 waters per BSA calculated in our BSA organogels correspond to 1.1-1.4 solvation shells. The retained BSA solvation shell waters most likely account for the constant UVRR AmI frequency measured in the BSA hydrogels and organogels.

This protein hydration layer is important for protein folding and the dynamics necessary for protein ligand binding and catalysis.[101-107] For example, it has been experimentally observed that there is a critical hydration level required for enzymatic activity (~ a single monolayer of water).[78, 102, 107] Our pure protein organogel sensors and catalysts[48] retain much of their native protein activity in EG, at least in part, due to the retained hydration layers.

6.3.5 Water Incubated BSA Organogel Morphology

Only the water incubated BSA organogels could be investigated using Cryo-SEM. The BSA organogels could not be imaged because the EG mobile phase could not be sublimed from the BSA polymer structure. We hypothesize that the BSA organogel and water incubated BSA organogel morphologies are roughly similar. The irreversibility of the VPT indicates that the

polymer morphology changes occur during the water to EG exchange. We believe that additional significant morphology changes during the solvent exchange back to water are unlikely.

The mobile phase exchange induces significant irreversible changes in the morphology of the BSA polymer network. As a result, there is an obvious difference between the BSA protein polymer structure observed in Cryo-SEM images of the water incubated BSA organogel (Figure 6.8C-D) compared to that of the BSA hydrogel (Figure 6.8A-B). The water to EG exchange changes the BSA polymer morphology from an interconnected network of thin BSA polymer strands to a dense amorphous BSA polymer phase in the water incubated BSA organogel. This is accompanied by a decrease in the polymer pore diameters compared to that of the BSA hydrogel. The water incubated BSA organogel pore diameters range from ~5 nm to ~30 nm.

We could not resolve the individual BSA polymer strands in the dense amorphous BSA polymer phase. Thus, the topological properties of the organogel network, such as the number of inter-protein crosslinked BSA in the protein polymer chains between polymer crosslinks cannot be estimated in the water incubated organogels, as we did for the BSA hydrogels. Thus, changes in the BSA polymer crosslink density cannot be determined from these Cryo-SEM images.

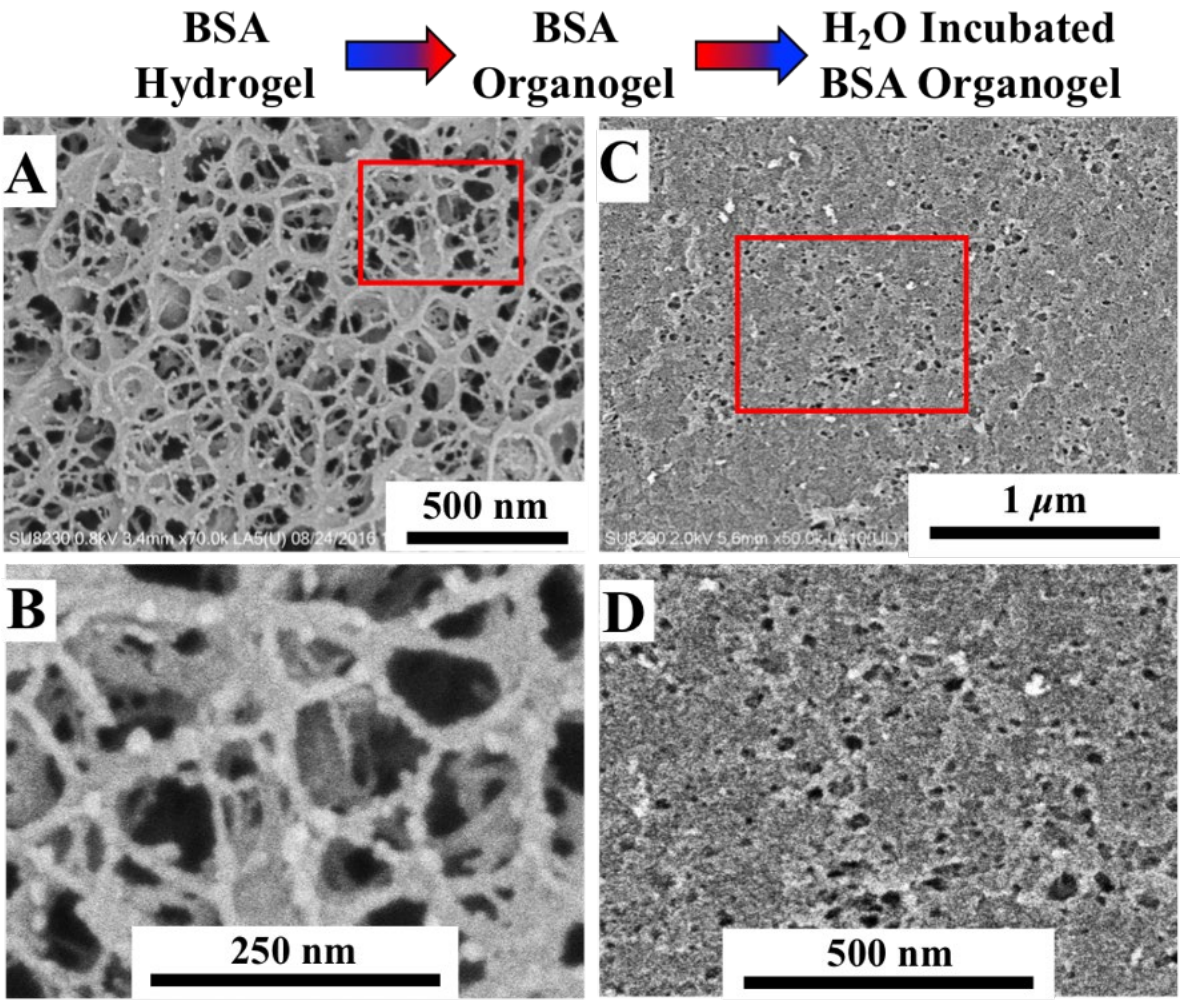

Figure 6.8 - Cryo-SEM images comparing the morphology of BSA hydrogels (A-B) to that of the water incubated BSA organogels (C-D) after 40 min. of sublimation and the application of a 2.5 nm Pt sputter coat. (A) BSA hydrogel; 70K magnification. (B) Enlarged area of BSA hydrogel, indicated by the red box in Figure 6.8A. (C) Water incubated BSA organogel; 50K magnification. (D) Enlarged area of water incubated BSA organogel, indicated by the red box in Figure 6.8C.

From titration studies, we found that these morphology changes are accompanied by a decrease in the BSA polymer surface area that is accessible to the mobile phase. The change in the mobile phase exposed BSA polymer surface area was examined by titrating the pH sensitive amino acid carboxyl groups in the BSA hydrogels and in the water incubated organogels.

BSA contains 39 aspartic acid residues (pKa 3.71) and 59 glutamic acid residues (pKa 4.15).[1] The H^+ concentration required to titrate aqueous solutions containing BSA hydrogels or water incubated organogels from pH 6 to pH ~3.35 is directly proportional to the number of BSA carboxyl groups protonated. Only mobile phase accessible carboxyl groups on the BSA polymer surface are titratable. Carboxyl groups buried by the BSA polymer morphology change are not titrated because mobile phase diffusion to the buried polymer surface area is significantly slowed.

As shown in Figure 6.9, the water incubated BSA organogel titration curve is shifted to lower acid concentrations relative to that of the BSA hydrogel. The titration curves of the hydrogels and water incubated organogels can be directly compared because the titration is normalized to the number of moles of H^+ added per mole of BSA in the hydrogel or water incubated organogel.

The water incubated BSA organogels require ~2-fold less acid to protonate all titratable aspartic and glutamic acid residues compared to that of the BSA hydrogels. These titration results directly demonstrate that the VPT phase separation irreversibly changes the BSA polymer surface area exposed to the mobile phase. The VPT buries about half the polymer surface area inaccessible to the mobile phase.

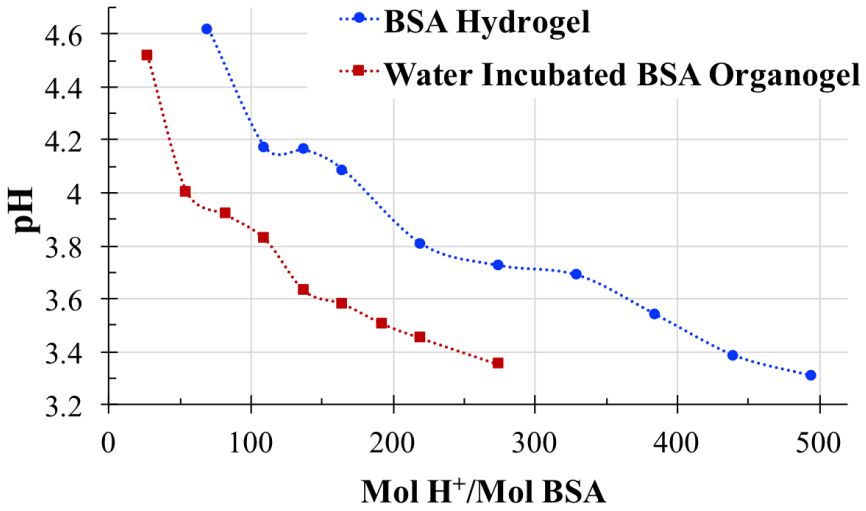

Figure 6.9 - Titration Curve of the BSA hydrogel before water to EG exchange (blue), and the water incubated BSA organogel after water to EG exchange and EG to water exchange (red). The titration is normalized to the number of moles of H+ added to solution per mole of BSA.

It should also be noted that formation of amino acid sidechain interactions that occur in the phase separated BSA organogel may also contribute to the decrease in titratable carboxyl groups. Interactions between carboxylates and other amino acids may decrease the effective pKa of those carboxylates. For example, salt bridges could form between the carboxylates and positively charged amino acids to stabilize the charged species.

6.3.6 The Mechanisms of the Irreversible VPT Caused by EG Exchange

From these results, we are able to make certain conclusions on the mechanisms that actuate the VPT during the water to EG exchange. The large VPT that decreases the BSA organogel volume as a result of the EG exchange suggests a phase separation of the BSA polymer from the EG mobile phase occurs. This BSA polymer phase separation is primarily driven by free energy of mixing changes, ΔG_{Mix}. The hydrogel/organogel free energy of mixing

is determined by the Flory-Huggins polymer-solvent interaction parameter, χ.[29, 80] Polymers in a good solvent are highly swollen and have small χ values because polymer-solvent interactions are favorable. In contrast, polymers in a poor solvent have larger χ values, and contain little solvent because polymer-polymer interactions are more favorable than polymer-mobile phase interactions.[108]

Flory theory predicts that when $\chi \geq 0.5$, phase separation of the polymer from the mobile phase will occur due to enthalpic and/or entropic penalties resulting from the poor solvent interacting with the polymer chains.[29, 108-109] The large swelling ratio of the BSA hydrogel in water indicates $\chi_{BSA\text{-}Water} << 0.5$. The continuous decrease in BSA hydrogel volume that occurs upon EG exchange indicates that χ increases with increasing EG concentrations. When χ exceeds the critical value of 0.5 and phase separation occurs. However, we cannot determine the EG concentration that initiates the phase separation from these existing data. A more careful investigation of the BSA hydrogel VPT generated with smaller incremental increases in the EG concentration is necessary. The critical EG concentration that induces phase separation could be determined through titration of the BSA polymer carboxyl groups after equilibration in each EG/water solution. A large decrease in the solvent accessible polymer surface area would elucidate the EG concentration at which phase separation occurs.

This mobile phase exchange induced phase separation causes a collapse of the water swollen 3D protein polymer network. During phase separation, the polymer attempts to minimize its free energy, thus initiating conformational changes in the polymer strands that minimize its surface area in contact with the mobile phase.[110-111]

Polymer phase separation in a poor solvent is thought to occur as a (at least) two-stage process; a fast polymer strand collapse that induces a coil-to-globule like transition in the polymer strands, followed by a slower stage that involves knotting of those globules and entanglement of the polymer strands.[112-114] We postulate that the BSA hydrogel to organogel transformation via the exchange from water to EG generates a similar kinetic two-stage phase separation, resulting in the dense amorphous BSA polymer phase observed in the water incubated organogel Cryo-SEM images, as illustrated in Figure 6.10.

The first stage of the phase separation involves a coil-to-globule transition of the BSA polymer strands (Figure 6.10 Stage 1a-1b). The thin BSA polymer strands in the water swollen hydrogel have an extended coil-like conformation. These extended polymer strand conformations collapse into a globule-like conformation to minimize the polymer surface area in contact with the EG mobile phase. As depicted in Figure 6.10 Stage 2a, this fast coil-to-globule transition creates localized high polymer density globules throughout the crosslinked network connected by stretched bridging BSA polymer strands.[113]

The coil-to-globule transition is followed by globule knotting, where these localized globules coalesce into a very high density BSA polymer phase.[112] Entanglement of the polymer strands within the dense BSA polymer phase also occurs in this second stage and increases over time.[115] This kinetic two-stage phase separation that occurs during the BSA hydrogel to organogel transformation results in the amorphous, very dense BSA polymer phase observed in water incubated BSA organogels (Figure 6.10 Stage 2b).

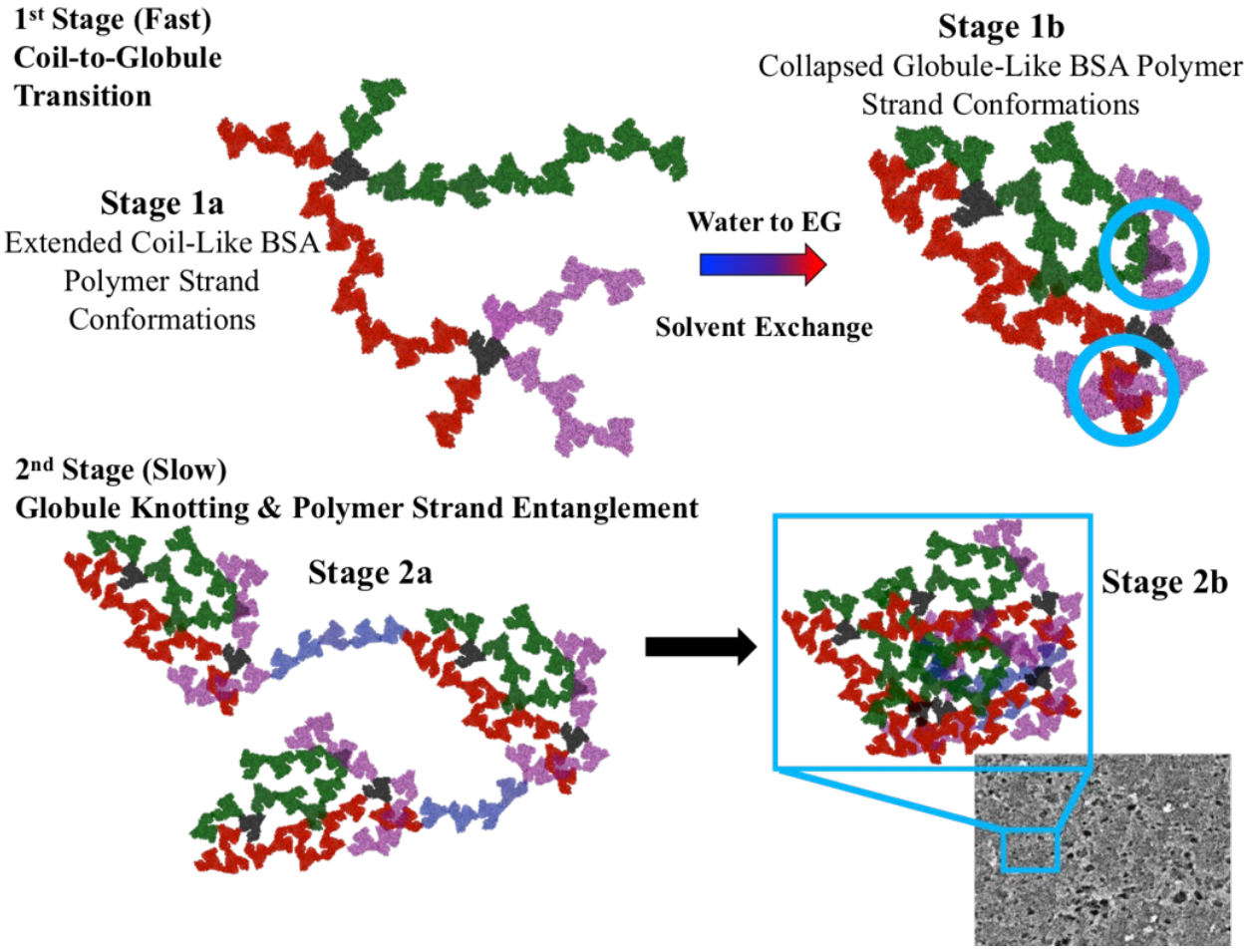

Figure 6.10 - Illustration of the proposed kinetic two-stage phase separation of the BSA polymer that occurs during the water to EG exchange. The first stage (1a-1b) involves a fast coil-to-globule transition of the BSA polymer strands. This coil-to-globule transition decreases the distance between BSA polymer strands. Polymerized BSA on different protein polymer strands can form inter-protein interactions where the BSA polymer strands are in close proximity, highlighted by the blue circles in Stage 1b.These additional inter-protein polymer strand interactions formed during phase separation increase the polymer crosslink density through physical polymer crosslinking. Thus, prevents organogel reswelling. The second slower stage (2a-2b) of the phase separation involves knotting of the localized globules in the network and entanglement of the BSA polymer strands. This second stage further increases the BSA polymer density, resulting in the very dense BSA polymer phase observed in the Cryo-SEM.

The phase separation mechanisms of thermoresponsive polymers have extensively been studied, for linear poly(N-isopropylacrylamide),[108, 116-117] polystyrene,[118] and poly(methylmethacrylate)[114] polymer chains in solution. The phase separation of crosslinked poly(N-isopropylacrylamide) hydrogel networks has also been investigate in polymer microparticles.[61] The rate of both stages of the phase separation is significantly slowed in a crosslinked polymer network due to the topological constraints compared to the linear polymer chains in solution.

The VPT after phase separation in these synthetic organic polymers is typically reversible. Entanglement of the polymer strands slows globule swelling in a good solvent.[115] Hysteresis in the globule-to-coil transition of poly(N-isopropylacrylamide) polymers has been observed, where melting of the globule is slowed by physical entanglements formed in the globule state.[119]

In contrast, our BSA polymer system exhibits a completely irreversible VPT, where negligible swelling is measured upon the exchange back to a good solvent, water. We hypothesize that this irreversible VPT phenomenon of the pure protein polymer is caused by the formation of additional physical or chemical crosslinks in the phase separated BSA polymer. The initial coil-to-globule transition and subsequent globule knotting decreases the distances between BSA polymer strands in the network. This allows formation of inter-protein strand interactions between different BSA polymer strands that can act as polymer crosslinks, indicated by the blue circles in Figure 6.10 Stage 1b.

Additional inter-protein strand interactions may include the formation of salt bridges or hydrogen bonds between AA sidechains that act as physical polymer crosslinks. Chemical polymer crosslinks could also form if dangling glutaraldehyde groups are present. Polymer

strand entanglement also creates physical polymer crosslinks in the BSA polymer network. Thus, the elastic free energy of the BSA polymer network increases during the BSA hydrogel to organogel transition. The elastic free energy is an entropically derived restoring force that resists polymer strand conformational changes which are intrinsic to hydro/organogel swelling or shrinking. Therefore, incubating the BSA organogel in water does not result in swelling due to a significant increase in the crosslink density of the BSA polymer network.

Finally, it must be noted that attempting to fabricate the BSA organogels using a single step solvent exchange where the BSA hydrogels are directly incubated in pure EG creates a material that is in a kinetically trapped state far from the thermodynamic equilibrium. The stepwise solvent exchange to EG allows the BSA polymer network to homogeneously shrink with increasing EG concentration prior to the phase separation event, that we believe occurs at higher EG concentrations. This creates a material much closer to the thermodynamic equilibrium state.

An interfacial skin layer can form in hydrogels when exposed to drastic changes in solvent quality that cause a phase separation induced VPT.[120] Skin layer formation has been utilized for drug release applications, where the drug is not released from the hydrogel material until the VPT of the skin layer is reversed.[121] However, formation of a skin layer in our photonic crystal organogel sensing materials may confound the sensor response. The BSA organogels fabricated using the stepwise solvent exchange swell in response to BSA-ligand binding.[48] In contrast, the single step solvent exchanged BSA organogels shrink in response to the ligand binding (unpublished data). The magnitude of this volume changes varies in the kinetically trapped BSA organogels depending on the time the BSA hydrogel was equilibrated in pure EG

prior to ligand addition. This results in an unreliable sensor response for the single step solvent exchanged BSA organogels.

6.4 Conclusions

Using UVRR and IR spectroscopy, Cryo-SEM, and physical measurements of the gel volume and concentration of titratable amino acids, we characterized changes to the BSA secondary structure and BSA polymer morphology that accompanies the stepwise solvent exchange to EG that transforms BSA hydrogels into BSA organogels. We determined the following:

(1) The BSA hydrogel is an interconnected network of thin BSA polymer strands with diameters roughly that of a single BSA protein. BSA hydrogel pores have diameters ranging from 50-200 nm. The molecular weight between polymer crosslinks was approximated from the polymer strand lengths, which equal ~5-30 BSA or $3 \times 10^5 - 2 \times 10^6$ g/mol.

(2) The solvent exchange from the water mobile phase of the hydrogel to the EG mobile phase of the organogel causes a VPT that increases the BSA polymer volume fraction from $\phi_{Hydrogel}$ = 6% to $\phi_{Organogel}$ = 27%. The VPT is irreversible; $\phi_{Water\ Incubated\ Organogel}$ = 27%after exchanging the EG mobile phase back to water.

(3) There is a ~4% increase in the population of α-helix secondary structure in the BSA organogel compared to that of the BSA hydrogel and native BSA monomers. These

secondary structure changes are reversible; the UVRR $AmIII_3$ bands of water incubated BSA organogels are identical to those of the BSA hydrogels.

(4) The water incubated organogel UVRR spectrum does not contain contributions from EG, indicating the EG mobile phase is qualitatively removed during exchange back to water.

(5) The NIR absorbance of water in the BSA organogels demonstrate there is a higher water content in the BSA organogels compared to the bulk EG mobile phase. There are roughly 1200-1500 water molecules per BSA protein in the organogel, meaning 1.1-1.4 hydrations layers remain bound to the proteins.

(6) Irreversible BSA polymer morphology changes occur during EG exchange. The water incubated BSA organogel morphology drastically differs from that of the BSA hydrogel. The water incubated organogel morphology is a dense amorphous polymer phase with significantly smaller pore diameters (5-30 nm) compared to the BSA hydrogel pore diameters (50-200 nm).

(7) The hydrogel to organogel morphology change results in a decrease in the solvent exposed surface area. There are approximately 50% fewer titratable amino acid carboxyl groups in the BSA organogel than in the BSA hydrogel.

We determined that a phase separation of the BSA polymer and mobile phase causes the VPT that accompanies the hydrogel to organogel transformation. This phase separation is driven by free energy of mixing changes where the Flory-Huggins interaction parameter increases with increasing EG concentrations. This phase separation proceeds in two stages, a fast coil-to-globule transition followed by globule knotting and BSA polymer strand entanglement, that results in a dense amorphous BSA polymer morphology. Additional inter-protein strand

interactions that are formed in the phase separated BSA polymer state are the most likely source of the irreversible VPT phenomenon. Physical or chemical polymer crosslinks increase the polymer crosslink density. Thus, the elastic free energy increases, resisting BSA polymer swelling when the mobile phase is exchanged back to water.

The irreversible VPT phenomena of our BSA polymer is advantageous for our photonic crystal sensing motif where BSA organogels sense BSA-ligand binding through an organogel swelling response. EG is a hydroscopic organic solvent and absorbs water vapor proportional to the relative humidity of the air. Water absorption by EG in the BSA organogel does not impact the sensor response because the addition of water will not reswell the organogel. This is in contrast to our previously fabricated evaporation resistant sensing materials that contain an ionic liquid mobile phase[24] which undergo a VPT in response to humidity changes.

6.5 References

1. Majorek, K. A.; Porebski, P. J.; Dayal, A.; Zimmerman, M. D.; Jablonska, K.; Stewart, A. J.; Chruszcz, M.; Minor, W., Structural and immunologic characterization of bovine, horse, and rabbit serum albumins. *Molecular Immunology.* **2012**, 52, 174-182.

2. Elliott, J. E.; Macdonald, M.; Nie, J.; Bowman, C. N., Structure and swelling of poly (acrylic acid) hydrogels: effect of pH, ionic strength, and dilution on the crosslinked polymer structure. *Polymer*. **2004**, 45, 1503-1510.

3. Lee, Y.-J.; Pruzinsky, S. A.; Braun, P. V., Glucose-sensitive inverse opal hydrogels: analysis of optical diffraction response. *Langmuir*. **2004**, 20, 3096-3106.

4. Zhang, J.-T.; Chao, X.; Liu, X.; Asher, S. A., Two-dimensional array Debye ring diffraction protein recognition sensing. *Chemical Communications.* **2013**, 49, 6337-6339.

5. Cai, Z.; Zhang, J.-T.; Xue, F.; Hong, Z.; Punihaole, D.; Asher, S. A., 2D Photonic Crystal Protein Hydrogel Coulometer for Sensing Serum Albumin Ligand Binding. *Analytical Chemistry*. **2014**, 86, 4840-4847.

6. Cai, Z.; Smith, N. L.; Zhang, J.-T.; Asher, S. A., Two-Dimensional Photonic Crystal Chemical and Biomolecular Sensors. *Analytical Chemistry.* **2015**, 87, 5013-5025.

7. Cai, Z.; Kwak, D. H.; Punihaole, D.; Hong, Z.; Velankar, S. S.; Liu, X.; Asher, S. A., A Photonic Crystal Protein Hydrogel Sensor for Candida albicans. *Angewandte Chemie International Edition*. **2015**, 54, 13036-13040.

8. Cai, Z.; Luck, L. A.; Punihaole, D.; Madura, J. D.; Asher, S. A., Photonic crystal protein hydrogel sensor materials enabled by conformationally induced volume phase transition. *Chemical Science.* **2016**, 7, 4557-4562.

9. Lu, H. D.; Wheeldon, I. R.; Banta, S., Catalytic biomaterials: engineering organophosphate hydrolase to form self-assembling enzymatic hydrogels. *Protein Engineering, Design and Selection*. **2010**, 23, 559-566.

10. Qiu, Y.; Park, K., Environment-sensitive hydrogels for drug delivery. *Advanced drug delivery reviews*. **2001**, 53, 321-339.

11. Jeong, B.; Kim, S. W.; Bae, Y. H., Thermosensitive sol–gel reversible hydrogels. *Advanced drug delivery reviews*. **2002**, 54, 37-51.

12. Hoffman, A. S., Hydrogels for biomedical applications. *Advanced drug delivery reviews*. **2012**, 64, 18-23.

13. Baler, K.; Michael, R.; Szleifer, I.; Ameer, G. A., Albumin Hydrogels Formed by Electrostatically Triggered Self-Assembly and Their Drug Delivery Capability. *Biomacromolecules*. **2014**, 15, 3625-3633.

14. Leach, J. B.; Schmidt, C. E., Characterization of protein release from photocrosslinkable hyaluronic acid-polyethylene glycol hydrogel tissue engineering scaffolds. *Biomaterials*. **2005**, 26, 125-135.

15. Kamoun, E. A.; Kenawy, E.-R. S.; Chen, X., A review on polymeric hydrogel membranes for wound dressing applications: PVA-based hydrogel dressings. *Journal of Advanced Research*. **2017**, 8, 217-233.

16. Teramoto, H.; Kameda, T.; Tamada, Y., Preparation of Gel Film from Bombyx mori Silk Sericin and Its Characterization as a Wound Dressing. *Bioscience, Biotechnology, and Biochemistry*. **2008**, 72, 3189-3196.

17. Idris, A.; Man, Z.; Maulud, A.; Khan, M., Effects of phase separation behavior on morphology and performance of polycarbonate membranes. *Membranes*. **2017**, 7, 21.

18. Liu, Z.; Calvert, P., Multilayer hydrogels as muscle-like actuators. *Advanced Materials*. **2000**, 12, 288-291.

19. Gerlach, G.; Arndt, K.-F., *Hydrogel sensors and actuators: engineering and technology*. Springer Science & Business Media: 2009; Vol. 6.

20. Smith, N. L.; Coukouma, A.; Dubnik, S.; Asher, S. A., Debye ring diffraction elucidation of 2D photonic crystal self-assembly and ordering at the air-water interface. *Physical Chemistry Chemical Physics*. **2017**, 19, 31813-31822.

21. Asher, S. A.; Holtz, J.; Liu, L.; Wu, Z., Self-Assembly Motif for Creating Submicron Periodic Materials. Polymerized Crystalline Colloidal Arrays. *Journal of the American Chemical Society*. **1994**, 116, 4997-4998.

22. Zhang, J.-T.; Wang, L.; Luo, J.; Tikhonov, A.; Kornienko, N.; Asher, S. A., 2-D Array Photonic Crystal Sensing Motif. *Journal of the American Chemical Society*. **2011**, 133, 9152-9155.

23. Holtz, J. H.; Asher, S. A., Polymerized colloidal crystal hydrogel films as intelligent chemical sensing materials. *Nature*. **1997**, 389, 829.

24. Smith, N. L.; Hong, Z.; Asher, S. A., Responsive ionic liquid-polymer 2D photonic crystal gas sensors. *Analyst*. **2014**, 139, 6379-6386.

25. Walker, J.; Kimble, K.; Asher, S., Photonic crystal sensor for organophosphate nerve agents utilizing the organophosphorus hydrolase enzyme. *Anal Bioanal Chem.* **2007**, 389, 2115-2124.

26. Walker, J. P.; Asher, S. A., Acetylcholinesterase-Based Organophosphate Nerve Agent Sensing Photonic Crystal. *Analytical Chemistry*. **2005**, 77, 1596-1600.

27. Sharma, A. C.; Jana, T.; Kesavamoorthy, R.; Shi, L.; Virji, M. A.; Finegold, D. N.; Asher, S. A., A General Photonic Crystal Sensing Motif: Creatinine in Bodily Fluids. *Journal of the American Chemical Society*. **2004**, 126, 2971-2977.

28. Wu, C.; Zhou, S., Volume Phase Transition of Swollen Gels: Discontinuous or Continuous? *Macromolecules*. **1997**, 30, 574-576.

29. Flory, P. J., *Principles of Polymer Chemistry*. Cornell University Press: 1953.

30. Hirotsu, S.; Hirokawa, Y.; Tanaka, T., Volume-phase transitions of ionized N-isopropylacrylamide gels. *The Journal of Chemical Physics*. **1987**, 87, 1392-1395.

31. Kim, Y. H.; Campbell, E.; Yu, J.; Minteer, S. D.; Banta, S., Complete Oxidation of Methanol in Biobattery Devices Using a Hydrogel Created from Three Modified Dehydrogenases. *Angewandte Chemie International Edition*. **2013**, 52, 1437-1440.

32. Gao, X.; Lyu, S.; Li, H., Decorating a Blank Slate Protein Hydrogel: A General and Robust Approach for Functionalizing Protein Hydrogels. *Biomacromolecules*. **2017**, 18, 3726-3732.

33. Xu, X.; Xu, Z.; Yang, X.; He, Y.; Lin, R., Construction and characterization of a pure protein hydrogel for drug delivery application. *International Journal of Biological Macromolecules*. **2017**, 95, 294-298.

34. Heck, T.; Faccio, G.; Richter, M.; Thöny-Meyer, L., Enzyme-catalyzed protein crosslinking. *Applied microbiology and biotechnology*. **2013**, 97, 461-475.

35. Kaehr, B.; Shear, J. B., Multiphoton fabrication of chemically responsive protein hydrogels for microactuation. *Proceedings of the National Academy of Sciences*. **2008**, 105, 8850-8854.

36. de Vries, A.; Hendriks, J.; van der Linden, E.; Scholten, E., Protein Oleogels from Protein Hydrogels via a Stepwise Solvent Exchange Route. *Langmuir*. **2015**, 31, 13850-13859.

37. Scholten, E., Chapter 12 - Protein Oleogels: Network Formation of Proteins in Hydrophobic Conditions. *In Edible Oleogels* (Second Edition), Marangoni, A. G.; Garti, N., Eds. AOCS Press: 2018; pp 285-305.

38. Fjerbaek, L.; Christensen, K. V.; Norddahl, B., A review of the current state of biodiesel production using enzymatic transesterification. *Biotechnology and Bioengineering*. **2009**, 102, 1298-1315.

39. Carrea, G.; Riva, S., Properties and Synthetic Applications of Enzymes in Organic Solvents. *Angewandte Chemie International Edition*. **2000**, 39, 2226-2254.

40. Klibanov, A. M., Improving enzymes by using them in organic solvents. *Nature*. **2001**, 409, 241.

41. Jacquet, P.; Daudé, D.; Bzdrenga, J.; Masson, P.; Elias, M.; Chabrière, E., Current and emerging strategies for organophosphate decontamination: special focus on hyperstable enzymes. *Environmental Science and Pollution Research*. **2016**, 23, 8200-8218.

42. Yang, F.; Wild, J. R.; Russell, A. J., Nonaqueous Biocatalytic Degradation of a Nerve Gas Mimic. *Biotechnology Progress*. **1995**, 11, 471-474.

43. Mattos, C.; Ringe, D., Proteins in organic solvents. *Current Opinion in Structural Biology*. **2001**, 11, 761-764.

44. Stepankova, V.; Bidmanova, S.; Koudelakova, T.; Prokop, Z.; Chaloupkova, R.; Damborsky, J., Strategies for Stabilization of Enzymes in Organic Solvents. *ACS Catalysis*. **2013**, 3, 2823-2836.

45. Iyer, P. V.; Ananthanarayan, L., Enzyme stability and stabilization—Aqueous and non-aqueous environment. *Process Biochemistry*. **2008**, 43, 1019-1032.

46. Zdarta, J.; Meyer, A.; Jesionowski, T.; Pinelo, M., A General Overview of Support Materials for Enzyme Immobilization: Characteristics, Properties, Practical Utility. *Catalysts*. **2018**, 8, 92.

47. Huang, C.; Bai, H.; Li, C.; Shi, G., A graphene oxide/hemoglobin composite hydrogel for enzymatic catalysis in organic solvents. *Chemical Communications*. **2011**, 47, 4962-4964.

48. N.L. Smith, A. E. C., D.C. Wilson, B. Ho, V.P. Gray, and S.A. Asher, Revolutionary Pure Protein Organogel Sensors and Biocatalytic Materials. *Applied Materials and Interfaces*. **2019**, In Review.

49. Cui, J. D.; Jia, S. R., Optimization protocols and improved strategies of cross-linked enzyme aggregates technology: current development and future challenges. Critical *Reviews in Biotechnology*. **2015**, 35, 15-28.

50. López-Gallego, F.; Betancor, L.; Mateo, C.; Hidalgo, A.; Alonso-Morales, N.; Dellamora-Ortiz, G.; Guisán, J. M.; Fernández-Lafuente, R., Enzyme stabilization by glutaraldehyde crosslinking of adsorbed proteins on aminated supports. *Journal of Biotechnology*. **2005**, 119, 70-75.

51. Mateo, C.; Palomo, J. M.; Fernandez-Lorente, G.; Guisan, J. M.; Fernandez-Lafuente, R., Improvement of enzyme activity, stability and selectivity via immobilization techniques. *Enzyme and Microbial Technology*. **2007**, 40, 1451-1463.

52. Kartal, F.; Janssen, M. H. A.; Hollmann, F.; Sheldon, R. A.; Kılınc, A., Improved esterification activity of Candida rugosa lipase in organic solvent by immobilization as Cross-linked enzyme aggregates (CLEAs). *Journal of Molecular Catalysis B: Enzymatic*. **2011**, 71, 85-89.

53. Park, J.-M.; Kim, M.; Park, H.-S.; Jang, A.; Min, J.; Kim, Y.-H., Immobilization of lysozyme-CLEA onto electrospun chitosan nanofiber for effective antibacterial applications. *International Journal of Biological Macromolecules*. **2013**, 54, 37-43.

54. Sheldon, R. A.; Schoevaart, R.; Van Langen, L. M., Cross-linked enzyme aggregates (CLEAs): A novel and versatile method for enzyme immobilization (a review). *Biocatalysis & Biotransformation*. **2005**, 23, 141-147.

55. Homaei, A. A.; Sariri, R.; Vianello, F.; Stevanato, R., Enzyme immobilization: an update. *J Chem Biol*. **2013**, 6, 185-205.

56. Curry, S.; Brick, P.; Franks, N. P., Fatty acid binding to human serum albumin: new insights from crystallographic studies. *Biochimica et Biophysica Acta (BBA) - Molecular and Cell Biology of Lipids*. **1999**, 1441, 131-140.

57. Evoli, S.; Mobley, D. L.; Guzzi, R.; Rizzuti, B., Multiple binding modes of ibuprofen in human serum albumin identified by absolute binding free energy calculations. *Physical Chemistry Chemical Physics*. **2016**, 18, 32358-32368.

58. Mikhonin, A. V.; Bykov, S. V.; Myshakina, N. S.; Asher, S. A., Peptide Secondary Structure Folding Reaction Coordinate: Correlation between UV Raman Amide III

Frequency, Ψ Ramachandran Angle, and Hydrogen Bonding. *The Journal of Physical Chemistry B*. **2006**, 110, 1928-1943.

59. Introduction to Polymer Morphology. *In Polymer Microscopy*, Springer New York: New York, NY, 2008; pp 1-25.

60. Kobayashi, T.; Horinaka, J.-i.; Takigawa, T., Volume phase transition of a polymer gel induced by phase separation of mixed solvents of water and 2-butoxyethanol. *Journal of Applied Polymer Science*. **2018**, 135, 46366.

61. Wu, C., A comparison between the `coil-to-globule' transition of linear chains and the "volume phase transition" of spherical microgels1Dedicated to the 80th birthday of Professor Renyuan Qian. *Polymer*. **1998**, 39, 4609-4619.

62. Erickson, H. P., Size and shape of protein molecules at the nanometer level determined by sedimentation, gel filtration, and electron microscopy. *Biol Proced Online*. **2009**, 11, 32-51.

63. Chalikian, T. V.; Totrov, M.; Abagyan, R.; Breslauer, K. J., The Hydration of Globular Proteins as Derived from Volume and Compressibility Measurements: Cross Correlating Thermodynamic and Structural Data. *Journal of Molecular Biology*. **1996**, 260, 588-603.

64. Bykov, S.; Lednev, I.; Ianoul, A.; Mikhonin, A.; Munro, C.; Asher, S. A., Steady-State and Transient Ultraviolet Resonance Raman Spectrometer for the 193–270 nm Spectral Region. *Appl. Spectrosc*. **2005**, 59, 1541-1552.

65. Smith, N. L.; Hong, Z.; Asher, S. A., Responsive ionic liquid-polymer 2D photonic crystal gas sensors. *Analyst.* **2014,** 139, 6379-6386.

66. Heuser, J. E., The origins and evolution of freeze-etch electron microscopy. *Journal of electron microscopy*. **2011**, 60, S3-S29.

67. Schneider, C. A.; Rasband, W. S.; Eliceiri, K. W., NIH Image to ImageJ: 25 years of image analysis. *Nature Methods.* **2012**, 9, 671.

68. Migneault, I.; Dartiguenave, C.; Bertrand, M. J.; Waldron, K. C., Glutaraldehyde: behavior in aqueous solution, reaction with proteins, and application to enzyme crosslinking. *BioTechniques*. **2004**, 37, 790-802.

69. Huang, B. X.; Kim, H.-Y.; Dass, C., Probing three-dimensional structure of bovine serum albumin by chemical cross-linking and mass spectrometry. *Journal of the American Society for Mass Spectrometry*. **2004**, 15, 1237-1247.

70. Cheung, D. T.; Nimni, M. E., Mechanism of Crosslinking of Proteins by Glutaraldehyde II. Reaction with Monomeric and Polymeric Collagen. *Connective Tissue Research*. **1982**, 10, 201-216.

71. Apkarian, R. P.; Wright, E. R.; Seredyuk, V. A.; Eustis, S.; Lyon, L. A.; Conticello, V. P.; Menger, F. M., In-lens cryo-high resolution scanning electron microscopy: methodologies for molecular imaging of self-assembled organic hydrogels. *Microscopy and Microanalysis*. **2003**, 9, 286-295.

72. Walther, P., High-resolution cryo-SEM allows direct identification of F-actin at the inner nuclear membrane of Xenopus oocytes by virtue of its structural features. *Journal of Microscopy*. **2008**, 232, 379-385.

73. Wright, E. R.; Conticello, V. P.; Apkarian, R. P., Morphological Characterization of Elastin-Mimetic Block Copolymers Utilizing Cryo- and Cryoetch-HRSEM. *Microscopy and Microanalysis*. **2003**, 9, 171-182.

74. Vezie, D. L.; Thomas, E. L.; Adams, W. W., Low-voltage, high-resolution scanning electron microscopy: a new characterization technique for polymer morphology. *Polymer*. **1995**, 36, 1761-1779.

75. Guo, Q., *Polymer Morphology : Principles, Characterization, and Processing*. John Wiley & Sons, Incorporated: New York, UNITED STATES, 2016.

76. Lou, X.; Munro, S.; Wang, S., Drug release characteristics of phase separation pHEMA sponge materials. *Biomaterials*. **2004**, 25, 5071-5080.

77. Bye, J. W.; Meliga, S.; Ferachou, D.; Cinque, G.; Zeitler, J. A.; Falconer, R. J., Analysis of the Hydration Water around Bovine Serum Albumin Using Terahertz Coherent Synchrotron Radiation. *The Journal of Physical Chemistry A*. **2014**, 118, 83-88.

78. Shiraga, K.; Ogawa, Y.; Kondo, N., Hydrogen Bond Network of Water around Protein Investigated with Terahertz and Infrared Spectroscopy. *Biophysical journal*. **2016**, 111, 2629-2641.

79. Gu, Y.; Zhao, J.; Johnson, J. A., A (Macro)Molecular-Level Understanding of Polymer Network Topology. *Trends in Chemistry*. **2019**, 1, 318-334.

80. White, E. M.; Yatvin, J.; Grubbs III, J. B.; Bilbrey, J. A.; Locklin, J., Advances in smart materials: Stimuli-responsive hydrogel thin films. *Journal of Polymer Science Part B: Polymer Physics*. **2013**, 51, 1084-1099.

81. Marmorat, C.; Arinstein, A.; Koifman, N.; Talmon, Y.; Zussman, E.; Rafailovich, M., Cryo-Imaging of Hydrogels Supermolecular Structure. *Scientific Reports*. **2016**, 6, 25495.

82. Murayama, K.; Tomida, M., Heat-Induced Secondary Structure and Conformation Change of Bovine Serum Albumin Investigated by Fourier Transform Infrared Spectroscopy. *Biochemistry*. **2004**, 43, 11526-11532.

83. Goponenko, A. V.; Asher, S. A., Modeling of Stimulated Hydrogel Volume Changes in Photonic Crystal Pb2+ Sensing Materials. *Journal of the American Chemical Society*. **2005**, 127, 10753-10759.

84. Tanaka, T.; Fillmore, D.; Sun, S.-T.; Nishio, I.; Swislow, G.; Shah, A., Phase Transitions in Ionic Gels. *Physical Review Letters*. **1980**, 45, 1636-1639.

85. Punihaole, D.; Jakubek, R. S.; Workman, R. J.; Asher, S. A., Interaction Enthalpy of Side Chain and Backbone Amides in Polyglutamine Solution Monomers and Fibrils. The *Journal of Physical Chemistry Letters*. **2018**, 9, 1944-1950.

86. Wang, Y.; Purrello, R.; Georgiou, S.; Spiro, T. G., UVRR spectroscopy of the peptide bond. 2. Carbonyl H-bond effects on the ground- and excited-state structures of N-methylacetamide. *Journal of the American Chemical Society*. **1991**, 113, 6368-6377.

87. Jakubek, R. S.; White, S. E.; Asher, S. A., UV Resonance Raman Structural Characterization of an (In)soluble Polyglutamine Peptide. *The Journal of Physical Chemistry B*. **2019**, 123, 1749-1763.

88. Punihaole, D.; Jakubek, R. S.; Dahlburg, E. M.; Hong, Z.; Myshakina, N. S.; Geib, S.; Asher, S. A., UV Resonance Raman Investigation of the Aqueous Solvation Dependence of Primary Amide Vibrations. *The Journal of Physical Chemistry B*. **2015**, 119, 3931-3939.

89. Mayne, L. C.; Hudson, B., Resonance Raman spectroscopy of N-methylacetamide: overtones and combinations of the carbon-nitrogen stretch (amide II') and effect of solvation on the carbon-oxygen double-bond stretch (amide I) intensity. *The Journal of Physical Chemistry*. **1991**, 95, 2962-2967.

90. Jakubek, R. S.; Workman, R. J.; White, S. E.; Asher, S. A., Polyglutamine Solution-State Structural Propensity Is Repeat Length Dependent. *The Journal of Physical Chemistry B*. **2019**, 123, 4193-4203.

91. Asher, S. A.; Ianoul, A.; Mix, G.; Boyden, M. N.; Karnoup, A.; Diem, M.; Schweitzer-Stenner, R., Dihedral ψ Angle Dependence of the Amide III Vibration: A Uniquely Sensitive UV Resonance Raman Secondary Structural Probe. *Journal of the American Chemical Society*. **2001**, 123, 11775-11781.

92. Jakubek, R. S.; Handen, J.; White, S. E.; Asher, S. A.; Lednev, I. K., Ultraviolet resonance Raman spectroscopic markers for protein structure and dynamics. *TrAC Trends in Analytical Chemistry*. **2018**, 103, 223-229.

93. Oladepo, S. A.; Xiong, K.; Hong, Z.; Asher, S. A.; Handen, J.; Lednev, I. K., UV Resonance Raman Investigations of Peptide and Protein Structure and Dynamics. *Chemical Reviews*. **2012**, 112, 2604-2628.

94. Reed, R. G.; Feldhoff, R. C.; Clute, O. L.; Peters, T., Fragments of bovine serum albumin produced by limited proteolysis. Conformation and ligand binding. *Biochemistry*. **1975**, 14, 4578-4583.

95. Takeda, K.; Shigeta, M.; Aoki, K., Secondary structures of bovine serum albumin in anionic and cationic surfactant solutions. *Journal of Colloid and Interface Science*. **1987**, 117, 120-126.

96. Moriyama, Y.; Watanabe, E.; Kobayashi, K.; Harano, H.; Inui, E.; Takeda, K., Secondary Structural Change of Bovine Serum Albumin in Thermal Denaturation up to 130 °C and Protective Effect of Sodium Dodecyl Sulfate on the Change. *The Journal of Physical Chemistry B*. **2008**, 112, 16585-16589.

97. Wasacz, F. M.; Olinger, J. M.; Jakobsen, R. J., Fourier transform infrared studies of proteins using nonaqueous solvents. Effects of methanol and ethylene glycol on albumin and immunoglobulin G. *Biochemistry*. **1987**, 26, 1464-1470.

98. Jakobsen, R. J.; Wasacz, F. M.; Brasch, J. W.; Smith, K. B., The relationship of bound water to the IR amide I bandwidth of albumin. *Biopolymers*. **1986**, 25, 639-654.

99. GuidedWave An Introduction to Online NIR Water Measurements in Liquid Samples. (accessed May, 27, 2019).

100. Rejou-Michel, A.; Henry, F.; Villardi, M. d.; Delmotte, M., Protein and ion hydration variation in fixed aqueous solutions: measurement by dielectric decrement. *Physics in Medicine and Biology*. **1985**, 30, 831-837.

101. Bellissent-Funel, M. C., Hydration in protein dynamics and function. *Journal of Molecular Liquids*. **2000**, 84, 39-52.

102. Rupley, J. A.; Careri, G., Protein Hydration and Function. *In Advances in Protein Chemistry*, Anfinsen, C. B.; Richards, F. M.; Edsall, J. T.; Eisenberg, D. S., Eds. Academic Press: 1991; Vol. 41, pp 37-172.

103. Klibanov, A. M., Why are enzymes less active in organic solvents than in water? *Trends in Biotechnology*. **1997**, 15, 97-101.

104. Schmitke, J. L.; Wescott, C. R.; Klibanov, A. M., The Mechanistic Dissection of the Plunge in Enzymatic Activity upon Transition from Water to Anhydrous Solvents. *Journal of the American Chemical Society*. **1996**, 118, 3360-3365.

105. Balcão, V. M.; Vila, M. M. D. C., Structural and functional stabilization of protein entities: state-of-the-art. *Advanced Drug Delivery Reviews*. **2015**, 93, 25-41.

106. Laage, D.; Elsaesser, T.; Hynes, J. T., Water Dynamics in the Hydration Shells of Biomolecules. *Chemical reviews*. **2017**, 117, 10694-10725.

107. Brovchenko, I.; Oleinikova, A., Which Properties of a Spanning Network of Hydration Water Enable Biological Functions? *Chem Phys Chem*. **2008**, 9, 2695-2702.

108. Wang, R.; Wang, Z.-G., Theory of Polymer Chains in Poor Solvent: Single-Chain Structure, Solution Thermodynamics, and Θ Point. *Macromolecules*. **2014**, 47, 4094-4102.

109. Shibayama, M.; Tanaka, T., Volume phase transition and related phenomena of polymer gels. *In Responsive Gels: Volume Transitions* I, Dušek, K., Ed. Springer Berlin Heidelberg: Berlin, Heidelberg, 1993; pp 1-62.

110. De Gennes, P. G., Collapse of a polymer chain in poor solvents. *J. Physique Lett.* **1975**, 36, 55-57.

111. Raos, G.; Allegra, G., Chain collapse and phase separation in poor-solvent polymer solutions: A unified molecular description. *The Journal of Chemical Physics*. **1996**, 104, 1626-1645.

112. Grosberg, A. Y.; Kuznetsov, D. V., Single-chain collapse or precipitation? Kinetic diagram of the states of a polymer solution. *Macromolecules*. **1993**, 26, 4249-4251.

113. Halperin, A.; Goldbart, P. M., Early stages of homopolymer collapse. *Physical Review E*. **2000**, 61, 565-573.

114. Maki, Y., Chain collapse and aggregation in dilute solutions of poly(methyl methacrylate) below the theta temperature. *Polymer Journal*. **2014**, 46, 641.

115. Lee, N.-K.; Abrams, C. F.; Johner, A.; Obukhov, S., Arrested Swelling of Highly Entangled Polymer Globules. *Physical Review Letters*. **2003**, 90, 225504.

116. Wu, T.-Y.; Zrimsek, A. B.; Bykov, S. V.; Jakubek, R. S.; Asher, S. A., Hydrophobic Collapse Initiates the Poly(N-isopropylacrylamide) Volume Phase Transition Reaction Coordinate. *The Journal of Physical Chemistry B*. **2018**, 122, 3008-3014.

117. Wang, X.; Qiu, X.; Wu, C., Comparison of the Coil-to-Globule and the Globule-to-Coil Transitions of a Single Poly(N-isopropylacrylamide) Homopolymer Chain in Water. *Macromolecules*. **1998**, 31, 2972-2976.

118. Chu, B.; Ying, Q.; Grosberg, A. Y., Two-Stage Kinetics of Single-Chain Collapse. Polystyrene in Cyclohexane. *Macromolecules*. **1995**, 28, 180-189.

119. Wu, C.; Wang, X., Globule-to-Coil Transition of a Single Homopolymer Chain in Solution. *Physical Review Letters*. **1998**, 80, 4092-4094.

120. Matsuo, E. S.; Tanaka, T., Patterns in shrinking gels. *Nature*. **1992**, 358, 482-485.

121. Yoshida, R.; Sakai, K.; Okano, T.; Sakurai, Y., Surface-modulated skin layers of thermal responsive hydrogels as on-off switches: II. Drug permeation. *Journal of Biomaterials Science, Polymer Edition*. **1992**, *3*, 243-252.

7.0 Summary of Significant Results and Future Investigations

This dissertation demonstrates the design, fabrication, and utilization of several 2D Photonic Crystal (2DPC) sensing materials, including revolutionary low vapor pressure pure protein organogel sensors. We also demonstrate that our pure protein organogels can be utilized as catalysts by using enzymes to create the pure protein polymer network. Below is a summary of the most significant results.

Chapter 2 shows that the Debye ring diffraction can be utilized as a non-destructive and quantitative monitor of the 2DPC ordering. We demonstrate our needle tip flow method of self-assembling anionic polystyrene (PS) particles at the air-water interface produces close packed hexagonal particle arrays. Additionally, we show the transfer of the PS particle array to a substrate followed by drying does not disrupt the particle spacing or ordering. This is significant because previously proposed mechanisms for the formation of close packed hexagonal arrays assumed the particles were non-close packed at the air-water interface. These mechanisms suggested that immersion capillary forces create attractive interactions between particles in order to form close packed hexagonal array as the water under the particle monolayer evaporates. We have shown that these attractive forces, that occur after the particle array is transferred to a substrate and dried, do not play a significant role in the formation of the close packed structure. The close packed particle array structure is present at the air-water interface.

Another significant result shown in Chapter 2 is related to the electrostatic repulsive interactions between highly charged PS colloids at the air-water interface. Strong repulsive particle interactions are necessary to form highly ordered hexagonal arrays. The strengths of these repulsive forces decrease monotonically with increasing salt concentration because the salt

ions screen the colloidal particle charge, decreasing the charged particle Debye length in solution. Thus, we expected the 2DPC ordering to decrease monotonically with increasing salt solution. However, this is not the case for the 2DPC ordering from arrays fabricated on NaCl solutions, nor for the measured Zeta-potentials of the anionic PS particles in NaCl solutions. We discovered that Cl^- ion absorption onto the PS surface increases the total particle charge. The increase in particle charge counteracts the decreasing Debye length, therefore increasing the electrostatic repulsive interaction energy between particles

Chapters 4-6 discuss the development of evaporation resistant materials that utilize low vapor pressure mobile phases. We demonstrate these low vapor pressure materials can be utilized for sensing gases and for decontaminating organophosphate (OP) nerve agents. These responsive polymer and bio-polymer materials that utilized an ionic liquid or low vapor pressure organic solvent as the mobile phase are novel and significantly extend the sensing capabilities of our photonic crystal sensor technology.

The 2DPC pHEMA ionogels, presented in Chapter 4, are among the first photonic crystal ionogel chemical sensors reported. This system served as a proof-of-concept sensor for detecting gas phase analytes using the 2DPC sensing motif. These 2DPC ionogel gas sensors utilized a newly discovered ionic liquid, Ethylguanidine perchlorate (EGP). EGP was fortuitously discovered by Zhenmin Hong in our lab while he was trying to lyophilize a peptide solution. We discovered EGP could replace traditional glycol co-solvents, that are required to prevent polymerization induced phase separation during pHEMA hydrogel fabrication. Transparent 2DPC pHEMA hydrogel films were polymerized from a 20 wt% HEMA aqueous solution containing 23 vol% EGP. The 2DPC PHEMA ionogels were sensitive to humidity, and the 2DPC P(HEMA-co-AA) ionogels were sensitive to ammonia gas. These ionogels demonstrated

that the absorption of gases by the mobile phase can interact with the polymer network to actuate VPT.

The pure protein organogel sensors and catalysts, described in Chapters 5 and 6, represent a new class (or at least subclass) of responsive materials. These pure protein organogels retain most of their native protein reactivity in the presence of an ethylene glycol mobile phase. As shown in Chapter 6, the proteins mostly retain their native protein secondary structure and their solvation shell of water, which, at least in part, leads to the retention of the protein ligand binding affinities and enzymatic activity. These organogel sensors and catalysts resist mobile phase evaporation, enabling organogel utilization in applications where the sensing material is exposed to air, such as in a wearable sensor badge.

The BSA organogels are the first reported pure protein organogel materials that exhibit VPT in response ligand binding. BSA is a highly promiscuous binding protein; numerous analytes act as ligands for BSA to produce the sensor response. This BSA organogel sensor demonstrates proof-of-concept sensing of protein-ligand binding. This pure protein organogel sensing motif that was demonstrated in the BSA organogels is being extended to proteins that selectively bind hazardous species such as organophosphate (OP) nerve agents. Below, we show preliminary data for a 2DPC Acetylcholinesterase (AchE) hydrogel OP sensor. Based on our BSA organogel sensor work, we believe that AchE organogels will exhibit a similar VPT response to paraoxon as do the AchE hydrogels.

Our OPH organogels catalyze the hydrolysis of OP in organic solvent solutions at significantly higher rates than OPH monomers in organic solvents. These results demonstrate that the glutaraldehyde polymerization of the proteins stabilizes the protein such that enzymatic activity is retained in the presence of a denaturing agent, such as ethylene glycol. The OPH

organogel catalysts are novel in that a macroscopic pure enzyme polymer film is created. This is in contrast to the small micron size particulates that form during production of crosslinked enzyme crystals or aggregates. Our films are more easily separated from solution after catalysis is complete. This improves the utility of these stabilized enzymes materials.

In Chapter 6, we show that the solvent exchange induced VPT that occurs during the BSA hydrogel to organogel transformation is irreversible. This is an important result because it demonstrates that these sensors would be insensitive to humidity variation. This is in contrast to the pHEMA ionogel sensors presented in Chapter 4, which are sensitive to humidity changes. A selective chemical sensing material that responds to humidity changes will yield false positive or false negative results for the analyte of interest.

Additionally, we carefully characterized the protein secondary structures, the protein hydration, and the protein polymer morphology in BSA hydrogels, BSA organogels and in water incubated BSA organogels. These results show that the proteins mostly retained their native secondary structures and solvation shell water layers after the exchange to pure organic solvent. Retention of the protein structure and hydration likely accounts for the similar protein-ligand binding affinities observed in our BSA organogels and for the increased enzymatic activity of our OPH organogels compared to the OPH monomers.

We were able to determine the mechanism(s) that cause the large irreversible VPT in BSA hydrogels upon the mobile phase exchange from water to EG. The mobile phase exchange that transforms BSA hydrogels into BSA organogels induces irreversible changes in the pure protein polymer morphology. The change in morphology is accompanied by a decrease in the BSA polymer surface area that is accessible to the mobile phase. These results indicate the BSA polymer phase separates from the EG mobile phase.

This phase separation is driven by free energy of mixing changes where the Flory-Huggins interaction parameter increases with increasing EG concentrations. To minimize its free energy in EG, the BSA polymer undergoes a two-stage phase separation that results in a very dense protein polymer phase. Inter-protein interactions between BSA polymer strands can occur in the collapsed BSA polymer state. These additional inter-protein interactions increase the effective polymer crosslink density of the BSA polymer network. Thus, the likely origin of the irreversible VPT phenomenon stems from an increase in the polymer's elastic restoring force that resist gel shrinking and swelling.

7.1 Intriguing Results and Future Investigations

7.1.1 Optimization of Pure Protein Organogels and Development of Pure Acetylcholinesterase OP Sensors

This final thesis section includes preliminary results from an Acetylcholinesterase (AchE) hydrogel organophosphate (OP) sensor study. It discusses the future work that is necessary to optimize the AchE hydrogel response and to develop a sensitive AchE organogel OP sensor. The AchE organogel OP sensor would utilize a low vapor pressure mobile phase similar to our BSA and OPH organogels, creating a material that could easily be integrated into a wearable sensor. This work represents the final phase of our DTRA funded project to develop super responsive materials for sensing chemical warfare agents. This work will require acquisition of additional expensive AchE protein.

We fabricated 2DPC pure Acetylcholinesterase (AchE) hydrogels using the same glutaraldehyde inter-protein crosslinking as our BSA and OPH hydrogels in Chapters 5 and 6. Paraoxon binds to the AchE active site with very high affinity (Figure 7.1A). Paraoxon binding attaches additional charges to the AchE polymer, causing changes in the ionic free energy and free energy of mixing.[1] As shown in Figure 7.1A, initial paraoxon binding induces ionic free energy changes by attaching charged groups to the protein polymer. Subsequently, hydrolysis and aging removes the nitrophenol group from the bound paraoxon, leaving a charged phosphate group attached to the AchE serine residue in the enzyme's active site. Removing the hydrophobic nitrophenol groups causes a change in the free energy of mixing that results in additional hydrogel swelling.

The AchE hydrogel response to 1 μM Paraoxon is shown in Figure 7.1B, where the particle spacing of the embedded 2DPC is used to monitor hydrogel swelling. We are able to resolve the binding and subsequent aging events. The particle spacing increases ~300 nm in response to 1 μM Paraoxon after 2 hr. Over 24 hr, the particle spacing increases another ~100 nm from hydrolysis of the bound paraoxon.

The large 300 nm 2DPC particle spacing change that was measured 2 hr after the addition of paraoxon indicates a visually evident color change should occur in only a few minutes. The 2DPC particle spacing of AchE hydrogel must be monitored at smaller time scales to determine the kinetics of the AchE hydrogel response to paraoxon and to determine the visually evident response time.

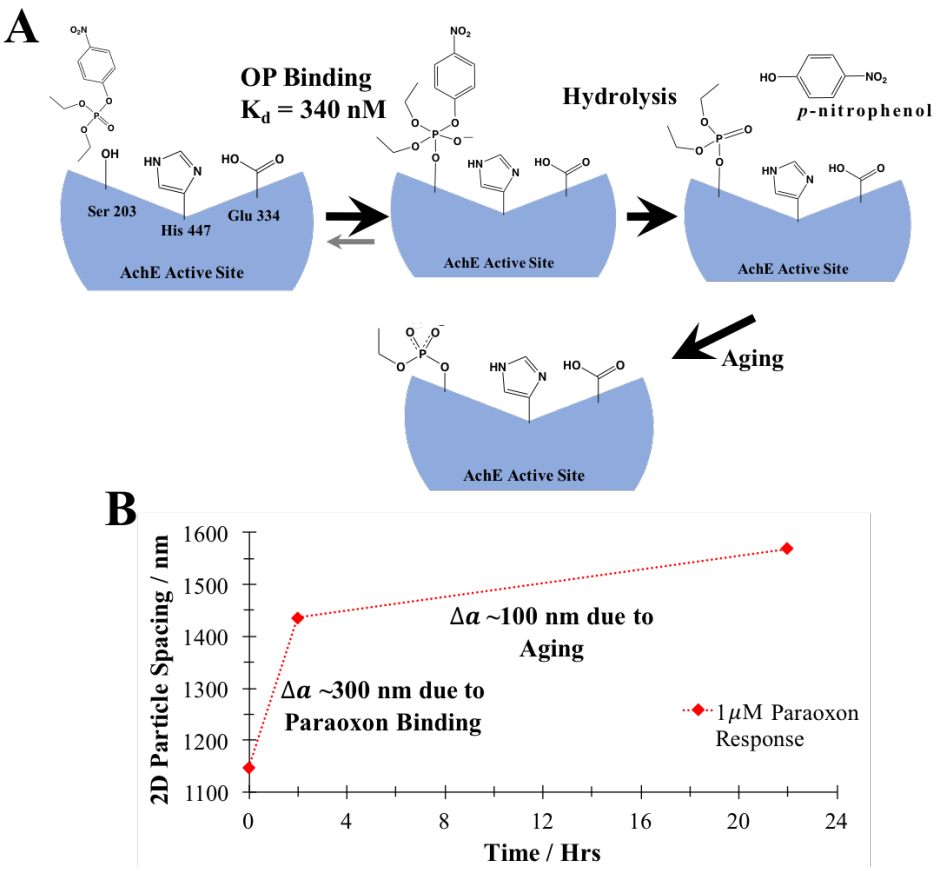

Figure 7.1 – (A) Paraoxon binding mechanism in the AchE active site. (B) 2DPC particle spacing change over time for a pure AchE hydrogel exposed to 1µM Paraoxon.

From the results in Figure 7.1B, we estimated the limit of detection at 2 hr is 150 nM Paraoxon. The AchE hydrogel response must be optimized to decrease the sensor response time and decrease the limit of detection. Fabricating ultra thin AchE hydrogel films may decrease the sensor response by decreasing the distances the analyte diffuses in the AchE hydrogel network. Generally, lower polymer crosslink densities result in larger VPT. Fabricating AchE hydrogels with a lower crosslink density would increase their VPT response. Thus, optimization of the sensor response time and limit of detection could be achieved by fabricating ultra thin AchE hydrogel films with very low polymer crosslink densities.

The goal of the program that funded this work is to create sensing materials that detect the presence of threat agents such as nerve gases in the atmosphere. Creating sensing materials that have long operating times in ambient conditions require utilizing low vapor pressure mobile phases. Therefore, the next step in this project would involve transforming AchE hydrogels into AchE organogels by exchanging the water mobile phase of AchE hydrogels to a low vapor pressure mobile phase like ethylene glycol. Glycerol is another low vapor pressure mobile phase that should be investigated. Glycerol is non-toxic, whereas ethylene glycol is toxic if ingested.

We expect paraoxon binding in the 2DPC AchE organogels will induce swelling similar to that of the AchE hydrogels. This expectation is based on the similar volume changes exhibited by our BSA hydrogels and BSA organogels in response to protein-ligand binding of charged ligands. Protein-ligand binding of charged ligands like ibuprofen induce changes in the ionic free energy and free energy of mixing for both the BSA hydrogels and organogels. Analogously, we hypothesize that paraoxon binding to an AchE organogel will generate similar VPT responses as the AchE hydrogels.

7.2 References

1. Walker, J. P.; Asher, S. A., Acetylcholinesterase-Based Organophosphate Nerve Agent Sensing Photonic Crystal. *Analytical Chemistry.* **2005**, 77, 1596-1600.

Appendix A Debye Ring Diffraction Elucidation of 2D Photonic Crystal Self-Assembly and Ordering at the Air-Water Interface Supporting Information

Adapted from the Supporting Information of the published work presented in Chapter 2. Smith, N. L.; Coukouma, A.; Dubnik, S.; Asher, S. A., *Physical Chemistry Chemical Physics* **2017,** *19* (47), 31813-31822 **DOI: 10.1039/c7cp07130b**

A.1 Video of 2DPC Self-Assembly at the Air-Water Interface and MATLAB Programs

The video illustrating the self-assembly of colloidal particles at the air-water interface using the needle tip flow is provided in the link below. The MATLAB scripts used to calculate the 2D pair correlation function, g(r), the FFT (g(r)-1), and the order parameter are also provided in this link. The file downloads are located on the right hand side of the RSC Analyst webpage. **https://pubs.rsc.org/en/content/articlelanding/2017/cp/c7cp07130b#!divAbstract**

A.2 Representative SEM Images of 2DPC for 915, 570, and 409nm Diameter Particles for All Salt Concentration

2D Photonic Crystals (2DPC) were made using highly charged polystyrene particles that have diameters of 915, 570, and 409 nm. 2DPC were fabricated by self-assembly of particles at the air-water interface using the needle tip flow method described in Chapter 2. The self-assembly of charged particles at the air-water interface produces monolayers of particles. The

2DPC particle monolayer was transferred to glass slides and dried under ambient conditions. After the Debye rings were measured, the 2DPC samples were sputter coated with a thin layer of gold using a PELCO SC-7 sputter coater. The gold coated samples were then imaged by Scanning Electron Microscopy using a JEOL 6390LV SEM.

For each particle diameter, 2DPC were made such that the ordering of the particle array varied from a highly ordered hexagonal crystal structure to highly disordered. 2DPC disorder was induced by fabricating 2DPC on water surfaces that contain salt. 2DPC were self-assembled on water surfaces that contain 0, 0.001, 0.01, 0.1, and 1 M NaCl. Salt ions in the water subphase screen the charge on the polystyrene particles, reducing the Debye length and therefore the repulsive force between particles at the interface.

Appendix Figure A.1, Appendix Figure A.2, and Appendix Figure A.3 show 2DPC fabricated at the air-water interface of solutions containing NaCl for each particle diameter.

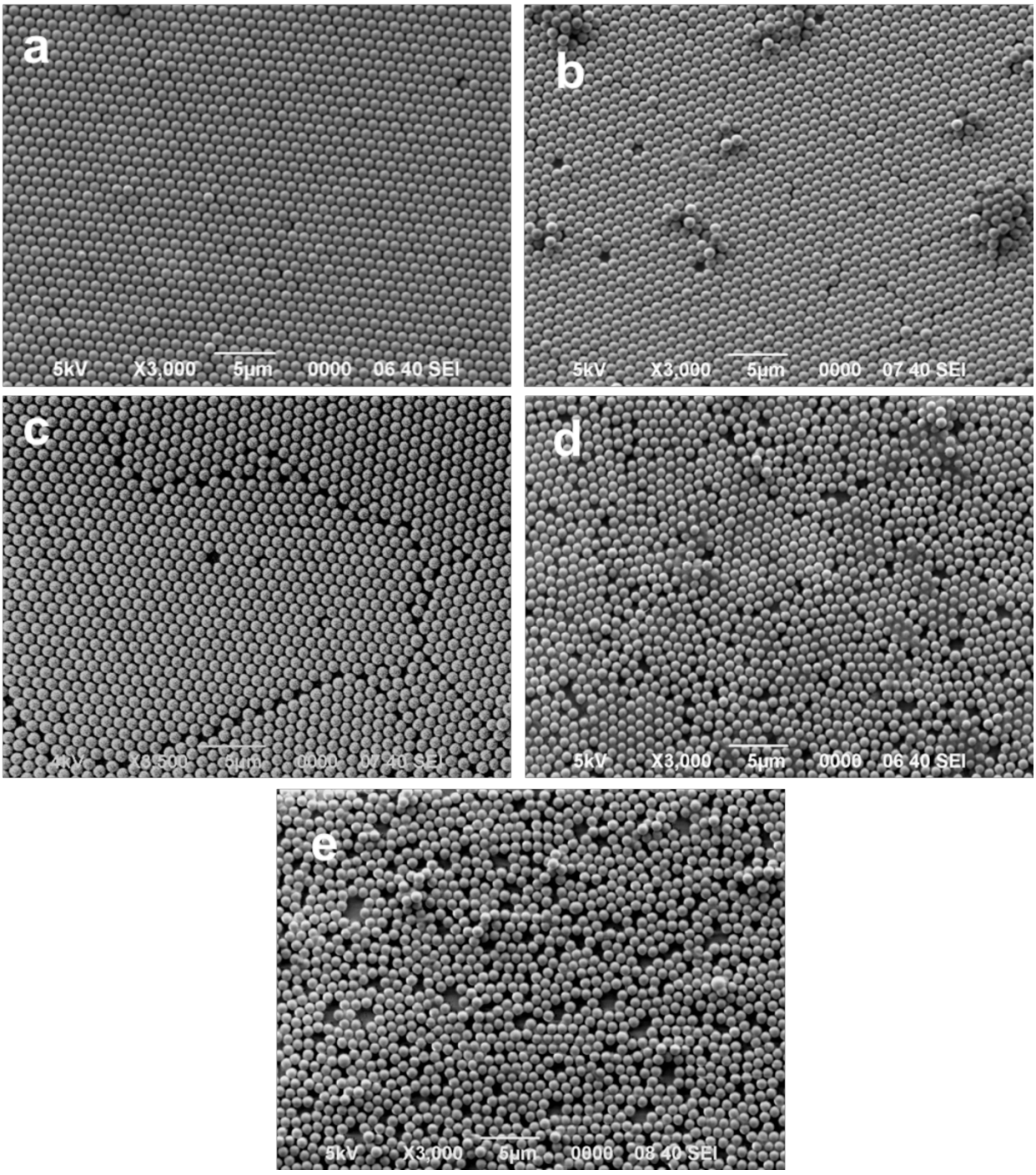

Appendix Figure A.1 - SEM micrographs of 2DPC fabricated by self-assembly of 915 nm diameter charged polystyrene particles at the air-water interface of electrolyte solutions containing NaCl. (A) Pure Water (B) 0.001 M NaCl (C) 0.01 M NaCl (D) 0.1 M NaCl (E) 1 M NaCl.

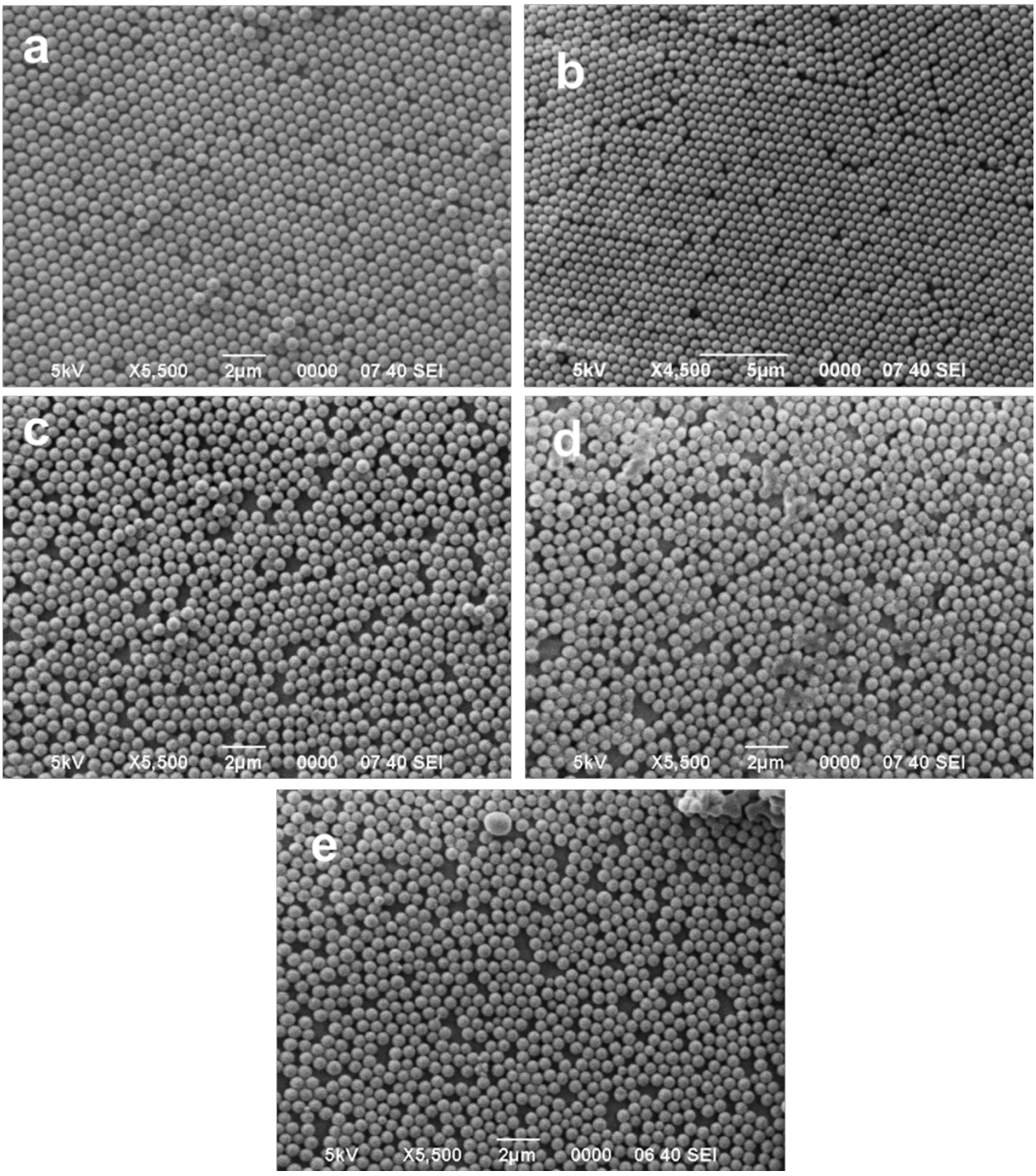

Appendix Figure A.2 - SEM micrographs of 2DPC fabricated by self-assembly of 570 nm diameter charged polystyrene particles at the air-water interface of electrolyte solutions containing NaCl. (A) Pure Water (B) 0.001 M NaCl (C) 0.01 M NaCl (D) 0.1 M NaCl (E) 1 M NaCl.

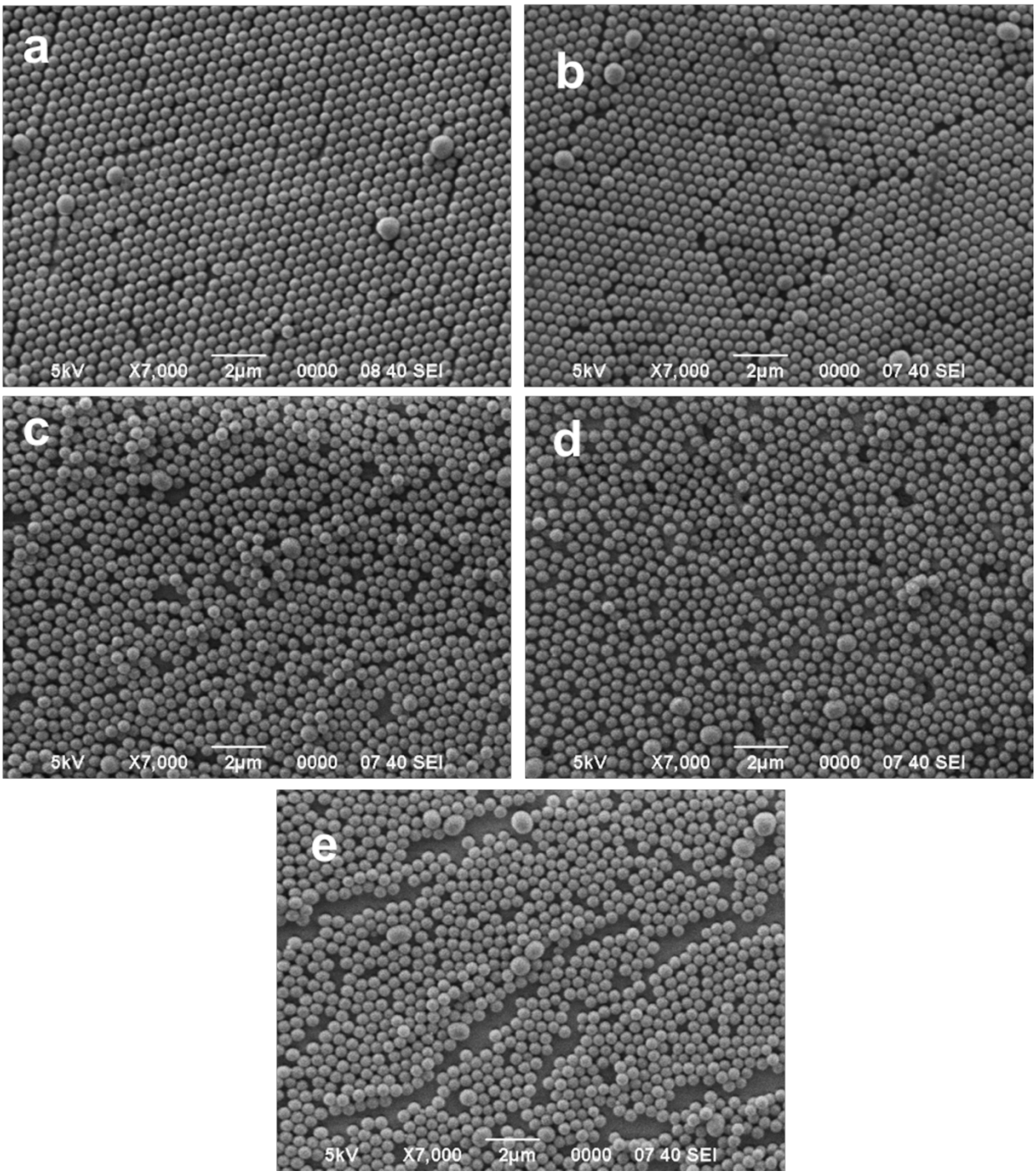

Appendix Figure A.3 - SEM micrographs of 2DPC fabricated by self-assembly of 409 nm diameter charged polystyrene particles at the air-water interface of electrolyte solutions containing NaCl. . (A) Pure Water (B) 0.001 M NaCl (C) 0.01 M NaCl (D) 0.1 M NaCl (E) 1 M NaCl.

A.3 2DPC Order Analysis

First, each image was transformed into a black and white binary image using the GNU Image Manipulation Program (GIMP) using a difference between Gaussians edge-detection filter. The particles in each image were then found using the circle Hough transform algorithm included in the MATLAB scripting package (MathWorks). The centers of the detected particles were passed into a function to calculate the pair correlation function (Equation 2.4). The program counts the number of particles, dn, in the area of the shell, da having an inner diameter, r, and outer diameter, r + dr.

$$\textbf{Equation 2.4} \quad g(r) = \frac{1}{\langle p \rangle} \frac{dn(r, r+dr)}{da(r, r+dr)}$$

This was done for increasing shell radii, r = 0 to 14, increasing by, dr = 0.016R_o, where R_o is the particle radius.[1] A plot of g(r) with respect to the normalized distance R/2Ro from 15 SEM images was produced for each particle size and salt concentration. The MATLAB script utilized is appended as ArrayOrdering and automated using the MATLAB script 2DOrderingProc.

The g(r) plots were further analyzed utilizing a discrete Fast Fourier Transform (FFT). The FFTs of the average g(r) spectra were taken using the FFTW library included in the MATLAB software. The Full Width Half Maximum (FWHM) bandwidth of the first peak of the FFT of g(r)-1 can be used to quantify 2DPC ordering.[1-3] The width of the first peak is directly related to the decay in g(r). As the 2DPC long range order decreases, the width the first FFT peak increases. The dimensionless ordering parameter (κ / κ_o) is the ratio of the FWHM of the FFT peak for a fabricated 2DPC, κ and the FWHM of the FFT peak for a perfect array, κ_o.[1] κ / κ_o was

averaged over all 15 data sets for each salt concentration and particle size with the appended MATLAB script, KAve.

A Gaussian baseline was observed in the FFTs of 2DPCs of poor ordering. A Gaussian peak in the g(r) spectrum appears as a Gaussian peak in the FFT of g(r)-1.[4] The baseline was nearly eliminated by removing the first Gaussian peak in the g(r) spectrum. Removal of the first Gaussian peak in g(r) does not affect the rate of decay in g(r) peaks, the source of the line width, therefore the FFT bandwidth is not affected.[4]

A.4 2D Pair Correlation Function g(r) and FFT g(r)-1 Plots

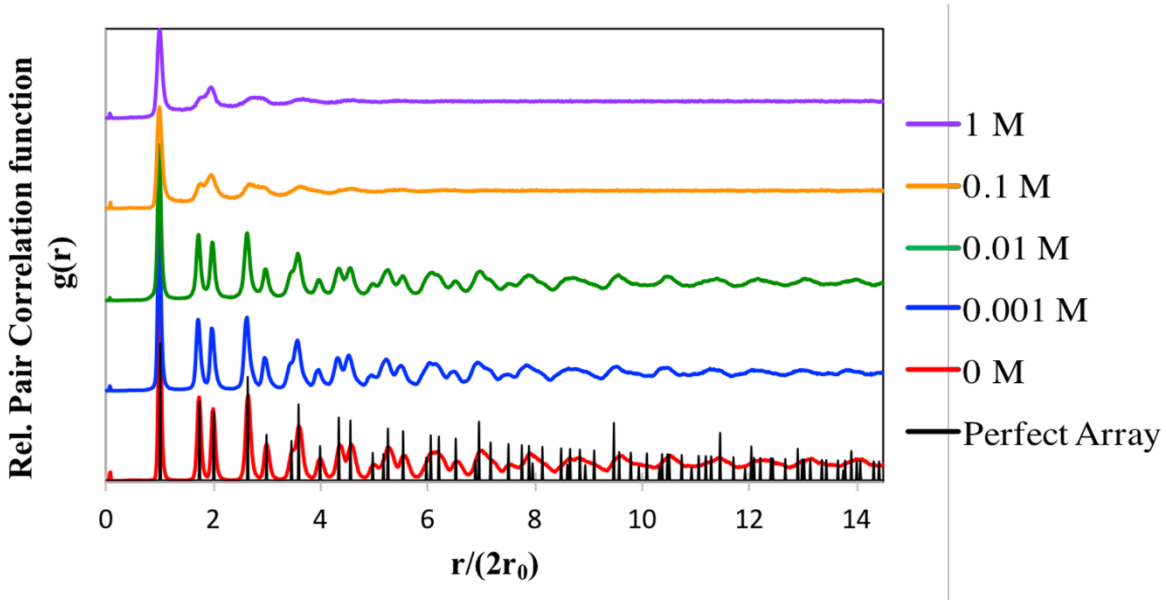

Appendix Figure A.4 - 2D Pair Correlation function for a perfect close-packed 2D array of circles with 915 nm diameters and 2DPC of 915 nm particles fabricated on pure water and on 0.001, 0.01, 0.1, and 1M NaCl solutions.

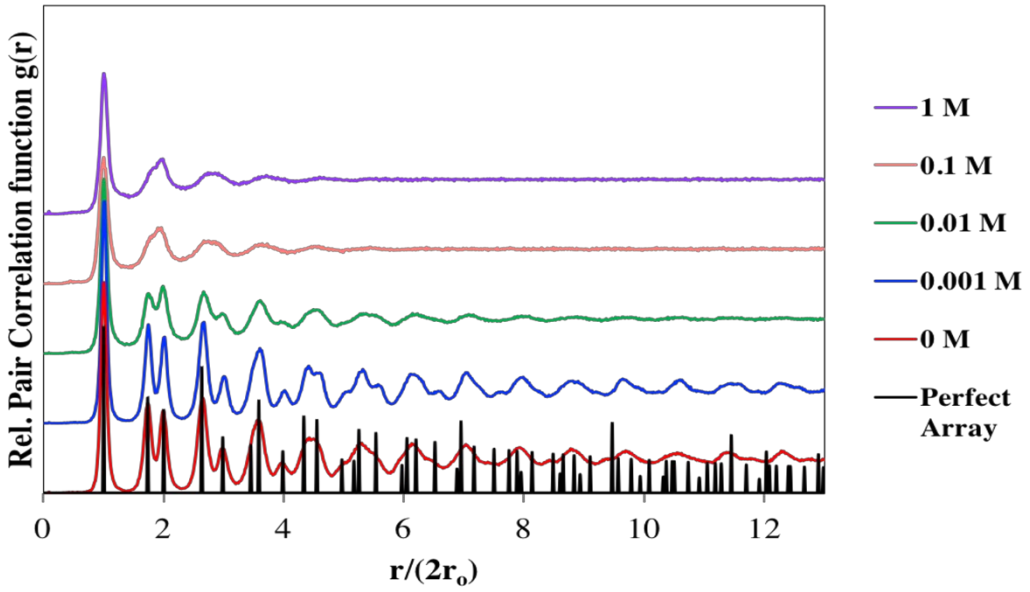

Appendix Figure A.5 - 2D Pair Correlation function for a perfect close-packed 2D array of circles with 570 nm diameters and 2DPC of 570 nm particles fabricated on pure water and on 0.001, 0.01, 0.1, and 1M NaCl solutions.

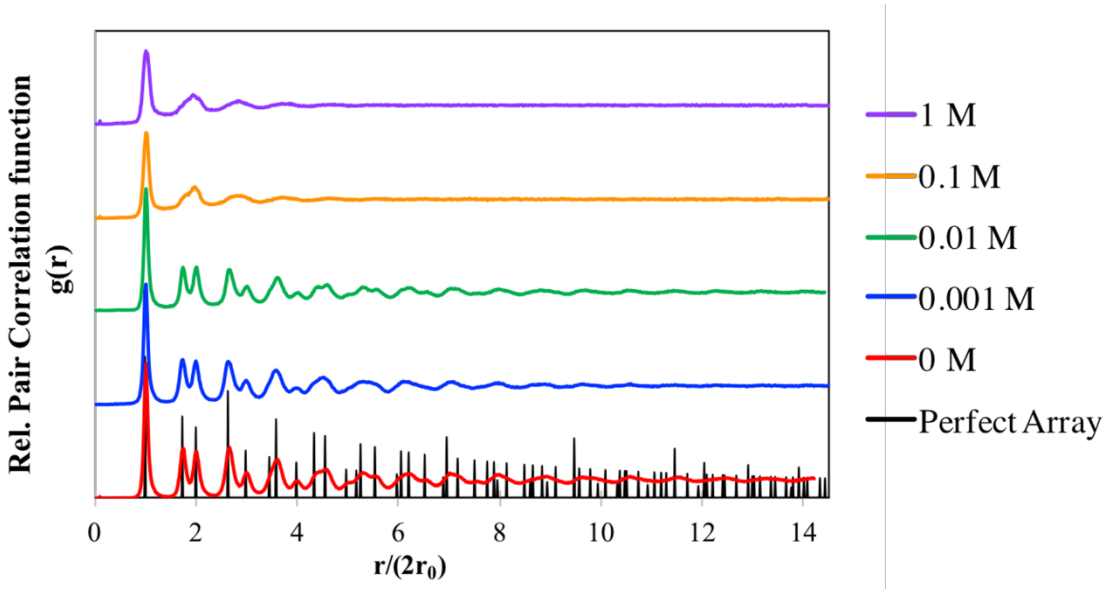

Appendix Figure A.6 - 2D Pair Correlation function for a perfect close-packed 2D array of circles with 409 nm diameters and 2DPC of 409 nm particles fabricated on pure water and on 0.001, 0.01, 0.1, and 1M NaCl solutions.

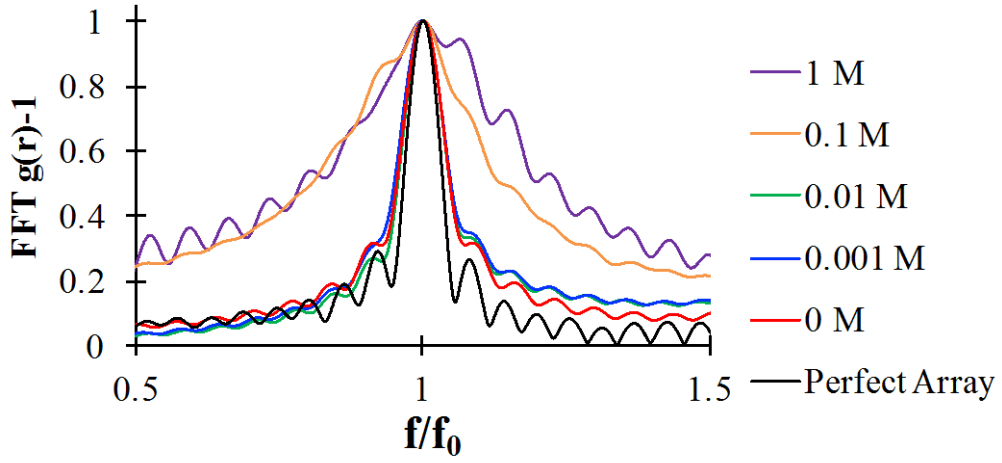

Appendix Figure A.7 - The first peak of the FFT of g(r)-1 plots for 2DPC of 915 nm particles self-assembled on water and aqueous solutions containing increasing concentrations of NaCl.

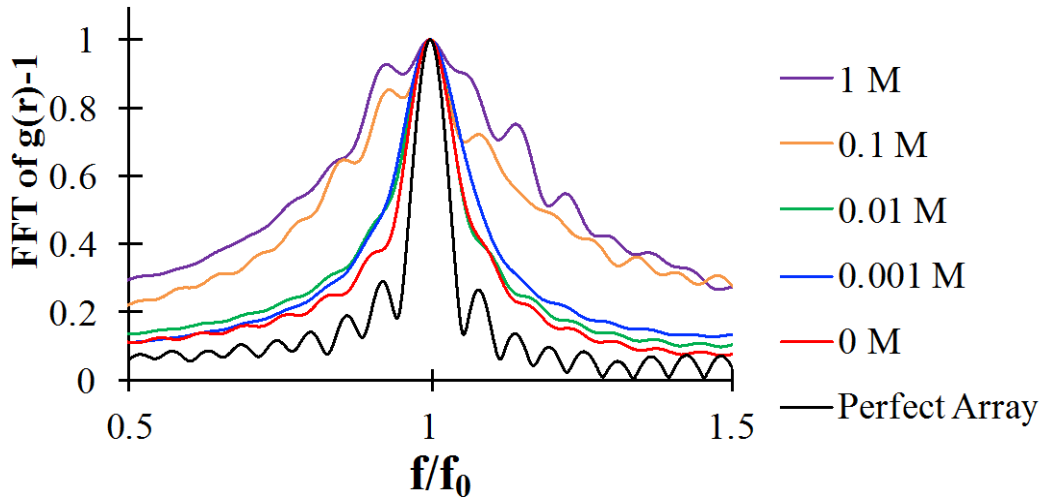

Appendix Figure A.8 - The first peak of the FFT of g(r)-1 plots for 2DPC of 570 nm particles self-assembled on water and aqueous solutions containing increasing concentrations of NaCl.

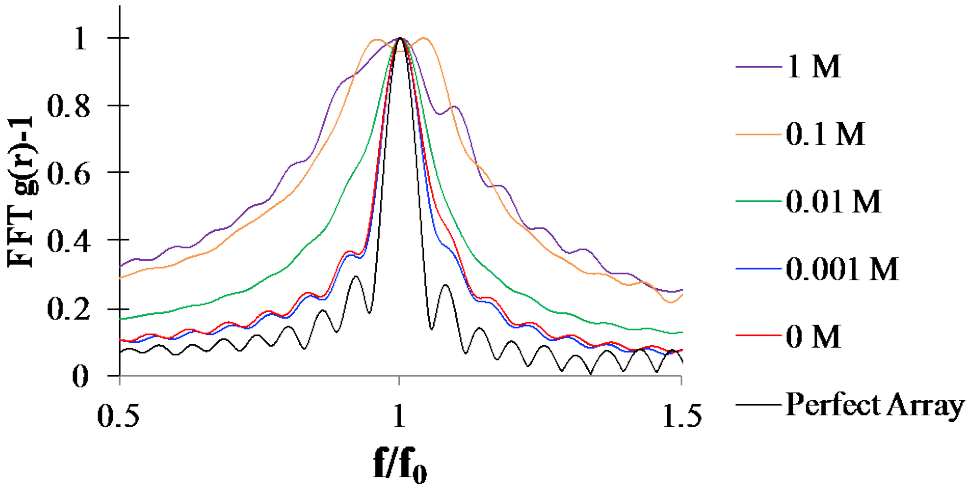

Appendix Figure A.9 - The first peak of the FFT of g(r)-1 plots for 2DPC of 409 nm particles self-assembled on water and aqueous solutions containing increasing concentrations of NaCl.

A.5 References

1. Zhang, J.-T.; Wang, L.; Lamont, D. N.; Velankar, S. S.; Asher, S. A., Fabrication of Large-Area Two-Dimensional Colloidal Crystals. *Angew. Chem. Int. Ed*. **2012**, 51, 6117-6120.

2. Bohn, J. J.; Ben-Moshe, M.; Tikhonov, A.; Qu, D.; Lamont, D. N.; Asher, S. A., Charge stabilized crystalline colloidal arrays as templates for fabrication of non-close-packed inverted photonic crystals. *J. Colloid Interface Sci.* **2010**, 344, 298-307.

3. Rengarajan, R.; Mittleman, D.; Rich, C.; Colvin, V., Effect of disorder on the optical properties of colloidal crystals. *Physical Review E.* **2005**, 71, 016615.

4. Bracewell, R. N., The Fourier transform and its applications. McGraw Hill: Boston, 2000; Vol. 3rd.

Appendix B Responsive Ionic Liquid-Polymer 2D Photonic Crystal Gas Sensors Supporting Information

Adapted from the Supporting Information of the published work presented in Chapter 4. Smith, N. L.; Hong, Z.; Asher, S. A., *Analyst* 2014, *139* (24), 6379-6386.

The supporting information for Chapter 4 contains details on the near infrared absorption measurements used to determine the concentration of water in ethylguanidine perchlorate solutions. We focus on the water absorptions bands at 1420 nm and 1915nm.

B.1 Near Infrared Absorption of Water in EGP

The absorption of water in EGP was measured using a Varian CARY5000 UV-vis-IR spectrometer, scanning over the range of 1200-2200 nm at a rate of 500nm/min. A 1 mm path length quartz cuvette was used and it was rinsed with water several times followed by acetone between samples. EGP/water mixtures were made with 0, 0.1, 0.25, 0.5, 0.75, and 0.9 mole fractions water in EGP. The NIR spectra of defined concentrations of water in EGP are shown in Appendix Figure B.1. Figure S2 shows the absorption at 1915 nm and 1420 nm, plotted as a function of the mole fraction of water in EGP. Equations generated from the best fit lines were used to calculate the mole fraction of water present in EGP from the absorbance data.

A small amount of EGP was taken from the vials containing the IL2DPC films after equilibrating in 0.5, 13, 22, 52, 80, and 97% Relative Humidity. The NIR spectra for these

samples are shown in Figure S3. The absorbance at 1420 nm and 1915 nm were used to calculate the mole fraction of water absorbed by EGP for each relative humidity.

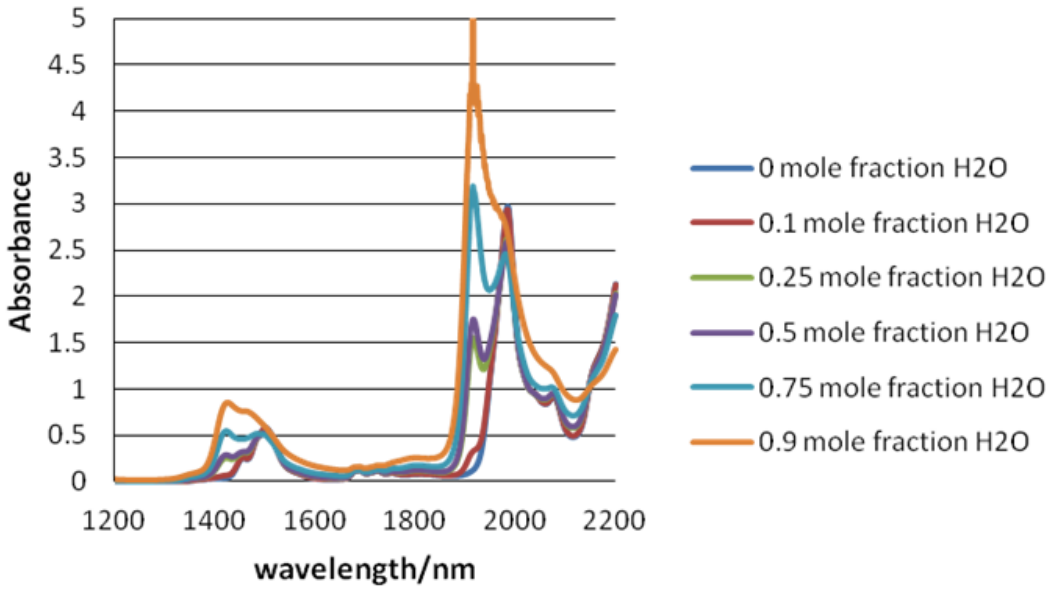

Appendix Figure B.1 - NIR Spectra of defined water concentrations in EGP.

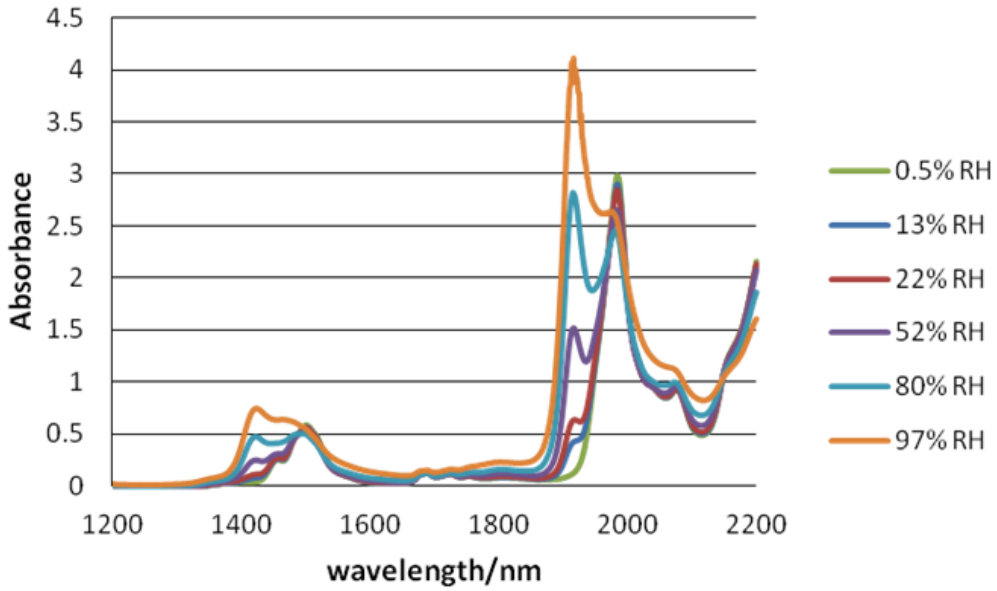

Appendix Figure B.2 - NIR spectra of water absorbed by EGP after equilibrating for 48 hr.

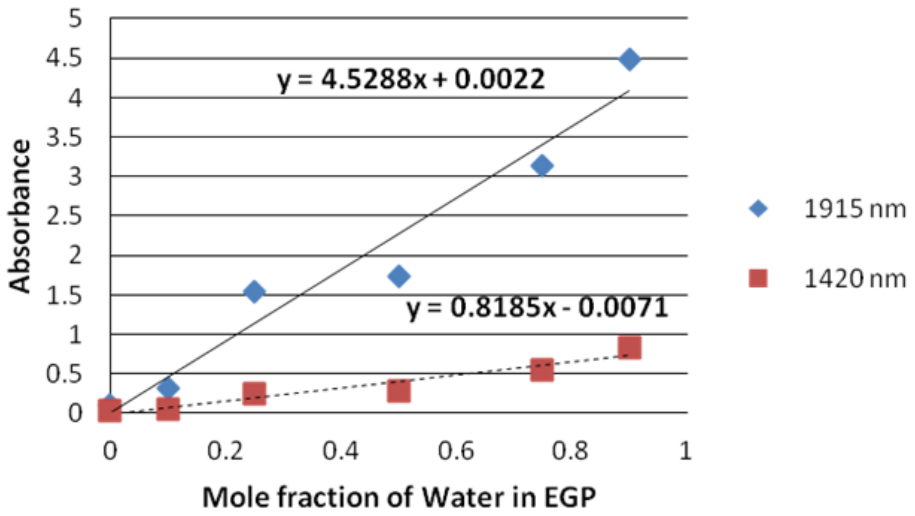

Appendix Figure B.3 - Optical densities of water absorption overtones at 1915 nm (blue diamonds) and 1420 nm (red squares).

Appendix C Mechanisms by which Organic Solvent Exchange Transforms Responsive Pure Protein Hydrogels into Responsive Organogels Supporting Information

Appendix C is the Supporting information for Chapter 6, which will be submitted to the journal ACS Biomacromolecules, authored by: Natasha L. Smith, Andrew E. Coukouma, Ryan S. Jakubek, [+]Sanford A. Asher

C.1 Cryo-SEM Sample Holder Frozen Hydrated BSA Hydrogel and Water Incubated Organogel Samples

Appendix Figure C.1 - Cryo-SEM sample holder. The sample cavity on the right contains a Ted Pella brass planchet. The sample cavity on the left is empty.

C.2 UVRR Spectra of BSA Hydrogels and BSA Monomers in Water

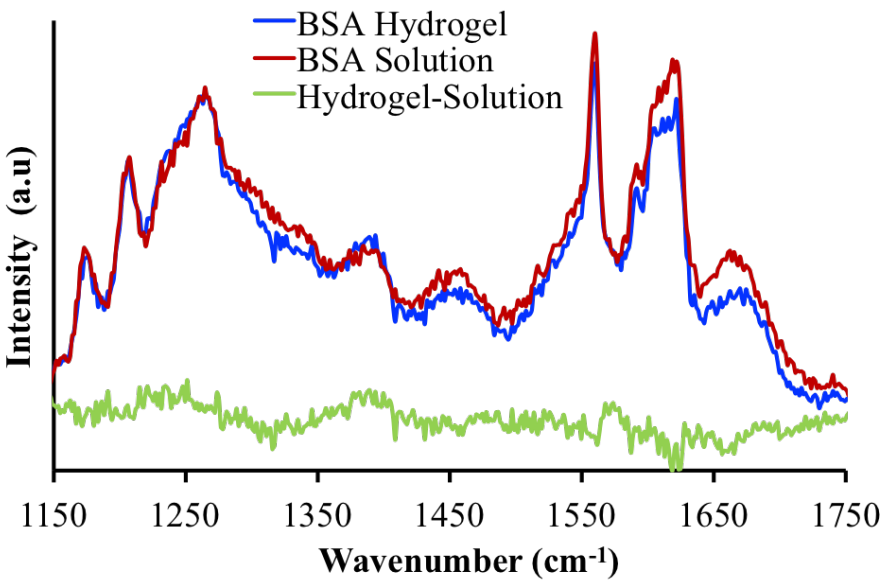

Appendix Figure C.2 - UVRR spectra of BSA hydrogel (blue), BSA protein monomer solution (red), and BSA hydrogel-monomer difference spectrum (green).

C.3 UVRR Measurement Details

We used Grams software (version 8.0, Thermo Fisher Scientific, Inc. Waltham, Mass., USA) to model our UVRR spectra as a sum of Gaussian and Lorentzian bands:

Equation C.3.1 $$f(x) = \sum_i (1 - M)\, Hv^{(-\frac{x - x_0}{w})^2 (4\ln(2))} + (M)\left(\frac{H}{4(\frac{x - x_0}{w})^2 + 1}\right)$$

where H is the peak height, X_0 is the peak frequency, w is the full width at half height, M=1 if the band is Lorentzian, and M=0 if the band is Gaussian for the i^{th} UVRR band. The $AmIII_3{}^S$

fitted bands were modeled as Gaussian bands because they are inhomogenously broadened due to the peptide Ψ angle distribution.[1]

The procedure below outlines the Ψ Ramachandran angle calculations used to determine protein secondary structures. Details describing the methodologies for calculating Ψ angles are reported by Mikhonin et al.[1-2] We use the following equation to calculate the Ψ angle for the α-helix $AmIII_3^S$ bands:

Equation C.3.2 $\upsilon_i = 1244\ cm^{-1} - 54\ cm^{-1} \sin(\Psi+26)$

where υ_i is the $AmIII_3^S$ frequency and Ψ is the backbone Ramachandran Ψ angle. As discussed by Mikhonin et al.,[1] this equation is used to calculate the Ψ angles for the peptide backbones involved in backbone-backbone hydrogen bonding.[1]

To estimate the change in protein secondary structure in the BSA organogel, we divided the total intensity of the $AmIII_3$ bands in BSA by the intensity of the hydrogel-organogel difference spectrum. We find that the intensity of the hydrogel-organogel difference spectrum is ~4% that of the total intensity of the $AmIII_3$ band. Therefore, we estimate that the organogel contains ~4% more α-helical peptide bonds compared to that of the hydrogel.

C.4 NIR Absorbance Measurements of EG-Water Solutions and BSA Organogels

Small volumes of water were added to 1.6 mL aliquots of EG, taken from the EG solution in which the organogels were equilibrated. During the solvent exchange, the organogels were placed on a shaker to mix the solutions. The exchange to pure EG took place over 2 days, in which ~250 mL of pure EG was replaced 3 times daily to remove bulk water in the samples.

The 1400-2000 nm NIR absorption spectra of ethylene glycol (EG) solutions containing 0, 5, 10, 15, 20, and 25 μL water are shown in Appendix Figure C.3a. EG-water solutions were measured in a 5 mm path length quartz cuvette. Water has strong absorption peaks at ~1400 and ~1900 nm that are used to monitor the samples water content.[3,4-5] These absorption bands derive from the first overtone of the OH-stretching band (~1400 nm) and the combination of the OH-stretching band and the O-H bending band (~1900 nm).[6]

We utilize the ~1900 nm peak to monitor the EG water content because EG absorbs around 1400 nm due to its O-H stretching mode. EG has minimal absorption at ~1900 nm.[7] Pure EG in a 5 mm pathlength cuvette shows an absorbance of 0.7.[7] We measure an absorbance of 0.74 at 1915 nm for the EG extracted from the bottle containing the organogels, corresponding to 0.08 M water in the bulk EG.

The difference spectrum of the EG/water solutions with the pure EG spectrum subtracted is shown in Appendix Figure C.3b. The increasing absorbance from the increasing water concentration at ~1400 and ~1900 nm is clearly evident. The 1915 nm absorbance of the EG/water solutions from this difference spectrum (Appendix Figure C.4) was used to calculate the molar absorptivity, ε, of water using the Beer-Lambert equation. The 1915 nm molar absorptivity coefficient of water was calculated to be $\varepsilon = 0.95\ M^{-1}\ cm^{-1}$.

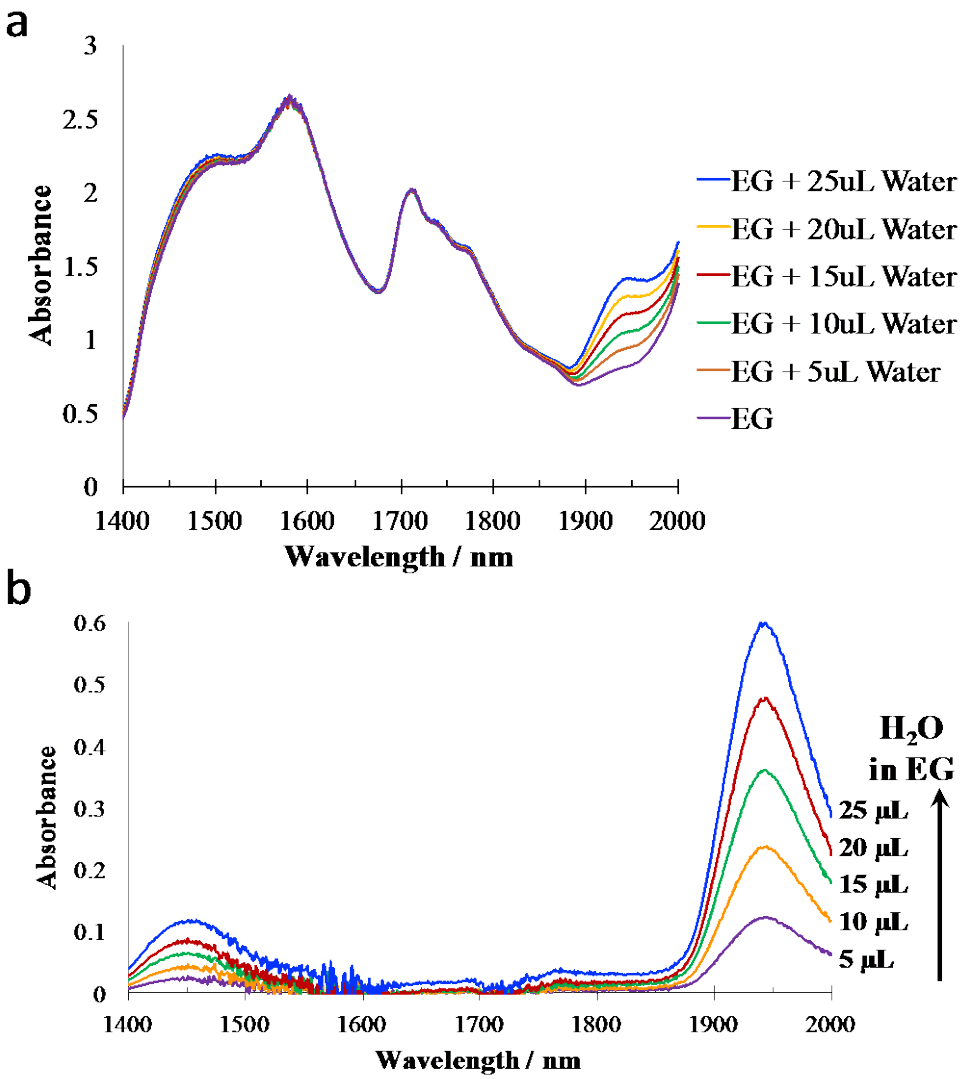

Appendix Figure C.3 - NIR absorbance of EG and its water solutions in a 5 mm path length quartz cuvette from 1400 nm to 2000 nm. (a) Spectra of pure EG with 0, 5, 10, 15, 20, and 25 µL water added (b) Difference Spectrum of (EG/water solution) – EG spectra.

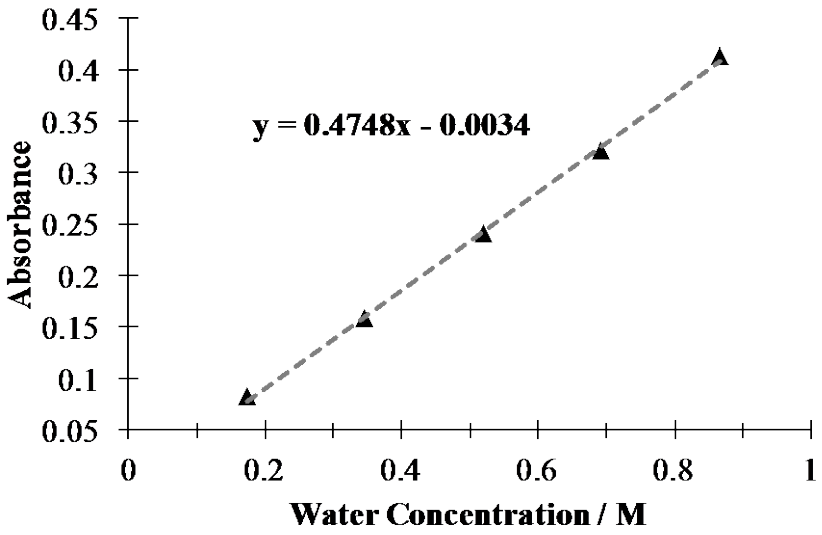

Appendix Figure C.4 - (EG+water)-EG difference spectrum absorbance at 1915 nm as a function of water concentration. The slope of the best fit line is 0.4748 A.U. M^{-1}.

The 1400 – 2000 nm NIR absorbance of our BSA organogels is shown in Appendix Figure C.5. The organogel films are 420 µm thick such that the double film layer is 840 µm thick. The 1915 nm absorbance of these organogels are 0.32 for the single film layer and 0.63 for two film layers. These absorbance values yield organogel water concentrations of 8.1 M for a single organogel film and 7.9 M for two organogel films (average 8.0 ± 0.2 M water).

To account for the small EG absorbance at 1915 nm in the organogel, we subtracted the absorbance of a pure EG film having a thickness of either 420 µm or 840 µm. A pure EG film of 420 µm thickness has a theoretical absorbance of 0.065 and a 840 µm thick EG film has an absorbance of 0.13. The 1915 nm absorbance of the organogel films decrease to 0.26 (420 µm) and 0.50 (840 µm) when the pure EG film absorbance is subtracted. The water concentration calculated from the EG subtracted organogel absorbance is now 6.5 M for a single organogel film and 6.3 M for two organogel films (average 6.4 ± 0.2 M water). This subtraction overestimates the absorbance from EG in the BSA organogels because the organogels contain

less EG than a pure EG film. Thus, the water concentration calculated from the subtracted organogel absorbance underestimates the water content.

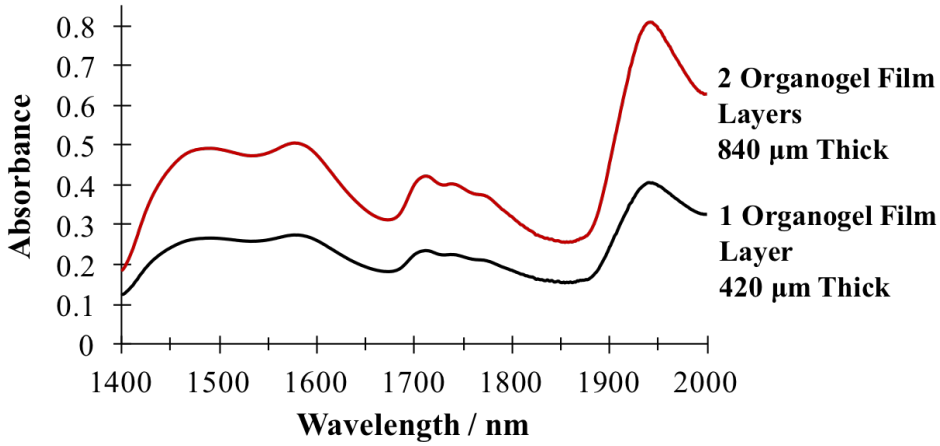

Appendix Figure C.5- NIR absorption of BSA organogels between 1400 – 2000 nm. The strong absorption peak between 1900 and 2000 nm stems from water in the organogel.

Based on these measurements, we calculate the number of water molecules per BSA protein in a 1 mL BSA organogel sample. The organogel has a BSA polymer volume fraction of $\phi = 0.27$. The organogel protein concentration is 360 mg/mL BSA (BSA MW: 66430 g/mol). Thus, a 1 mL sample of the BSA organogel contains 3.3 x 10^{18} molecules of BSA. A 1 mL BSA organogel sample that contains 6.5 – 8 M water has 3.9 x 10^{21} to 4.8 x 10^{21} molecules of water. Therefore, the ratio of water molecules per BSA protein in the organogel is calculated to be 1182-1477 Waters/BSA.

C.5 References

1. Mikhonin, A. V.; Bykov, S. V.; Myshakina, N. S.; Asher, S. A., Peptide Secondary Structure Folding Reaction Coordinate: Correlation between UV Raman Amide III Frequency, Ψ Ramachandran Angle, and Hydrogen Bonding. *The Journal of Physical Chemistry B*. **2006**, 110, 1928-1943.

2. Asher, S. A.; Mikhonin, A. V.; Bykov, S., UV Raman Demonstrates that α-Helical Polyalanine Peptides Melt to Polyproline II Conformations. *Journal of the American Chemical Society*. **2004**, 126, 8433-8440.

3. Büning-Pfaue, H., Analysis of water in food by near infrared spectroscopy. *Food Chemistry*. **2003**, 82, 107-115.

4. Tran, C. D.; De Paoli Lacerda, S. H.; Oliveira, D., Absorption of Water by Room-Temperature Ionic Liquids: Effect of Anions on Concentration and State of Water. *Appl. Spectrosc.* **2003**, 57, 152-157.

5. Smith, N. L.; Hong, Z.; Asher, S. A., Responsive ionic liquid-polymer 2D photonic crystal gas sensors. *Analyst.* **2014**, *139*, 6379-6386.

6. Luck, W. A. P.; Schiöberg, D., Spectroscopic investigations of the structure of liquid water and aqueous solutions. *Advances in Molecular Relaxation and Interaction Processes*. **1979**, 14, 277-296.

7. Guided Wave, An Introduction to Online NIR Water Measurements in Liquid Samples. *AZO Materials*. [Online]. January 2019.

Appendix D Organophosphate Safety

We worked with the hazardous compound 99.9% Ethyl-Paraoxon (Chem Service, Inc.).

Organophosphates are a class of highly toxic compounds used as pesticides and nerve agents. We utilize ethyl-paraoxon as a nerve agent simulant to test our enzyme activity. In addition to reading this safety document, you should review the safety data sheet fully before working with this hazardous chemical.

The paraoxon has a lower vapor pressure (1.1×10^{-6} mm Hg at 25 °C) compared to common nerve agents such as Sarin (2.9 mm Hg at 25 °C) or VX (7×10^{-4} mm Hg at 20 °C).[1] Paraoxon is ~70% the potency of Sarin with respect to acetylcholinesterase inhibition[2] and still presents a significant hazard and strict safety procedures must be taken when working with this substance. The LD_{50} of >98% paraoxon is 1.8 mg/kg (rat) through oral exposure and 5 mg/kg (rabbit) through dermal exposure.[2-3]

Acute exposure to low doses of paraoxon may cause[4]:

- nausea or vomiting (most commonly the first symptom)
- abdominal cramps
- diarrhea
- abnormal pupils (pinpoint pupils most commonly but dilated pupils have also been observed)
- excessive salivation
- headaches
- vertigo
- weakness

Acute Exposure to higher doses may cause[4]:

- difficulty breathing
- Cyanosis- bluish discoloration of the skin particularly the hands and feet
- an irregular heart beat (both slowed, Bradycardia, and elevated, tachycardia, heart rates have been observed)
- loss of muscle coordination, muscle twitching or spasms (particularly in tongue and eyelids)
- slurred speech
- profound weakness
- mental confusion or disorientation
- frothing at nose and mouth from excessive salivation and mucus secretion
- convulsions
- coma
- death often due to respiratory arrest

D.1 Personal Protective Equipment (PPE)

- Paraoxon should always be handled in a well-ventilated hood
- Lab goggles (not glasses)

- Lab coat- preferably with elastic cuffs, or use rubber bands to tighten the sleeves over your gloves to prevent splashes into sleeve cuff and prevent the wide cuffs from touching surfaces or bumping vials over.
- Nitrile 5.9 mil thick, preferably extra-long so they easily reach beyond the lab coat sleeve. When cleaning: Double layer gloves; 1 layer nitrile and 1 layer latex (at least 5.9 mil nitrile and 5.1 mil latex). Remove top latex glove layer in between solvent wipes
- N-100 mask, ensure mask fits well by testing for leaks with ethanol. If you can smell ethanol with the mask on, it does not fit.

D.2 Storage and Waste Management

Glass vials of 99.9% Ethyl-Paraoxon and any diluted stock solutions are stored in the refrigerator at 4 °C in a metal container that is clearly labeled Paraoxon/Organophosphate. After using paraoxon in the hood, place opened vials and any stock solutions in a plastic ziplock and label with the date it was opened or made. Place the bags in the metal container, make sure the container lid is tightly sealed, and wrap with parafilm. Ensure the container has been cleaned by wiping it down with bleach followed by ethanol several times before returning to the fridge. More details on the paraoxon cleaning procedure is provided in section D.3 Handling Paraoxon.

When performing experiments with paraoxon, coordinate with group members to dedicate a fume hood for this work and ensure everyone knows not to conduct work in that hood during the course of your experiments without proper PPE. Remove all chemicals or equipment in the hood that is not related to the paraoxon experiments. Put signage on the hood indicating

the hazard. Never place contaminated (or possibly contaminated) items such as beakers, scintillation vials, pipets outside of the hood before they have been properly cleaned.

A separate liquid waste container with proper waste labeling should be placed in the designated paraoxon hood for sample disposal and disposal of liquids used to clean non-disposable items. DO NOT throw disposable items in trash cans, such as gloves, Pasteur pipets, pipet tips, and the paper towels used for wiping down equipment. Disposable items should be placed in 1 gallon ziplock bags labeled solid paraoxon waste. When a bag is ¾ full, wipe the bag down with bleach then ethanol (at least 2 times with clean gloves and towels) to remove any residue and place in a clean secondary containment bag with a new label. The solid waste bags should be kept in the designated paraoxon hood until they are taken to the waste room.

DO NOT let waste pile up in the designated paraoxon hood. Take the waste out regularly if you are working over several days/weeks. Before paraoxon waste bottle and bags are removed from the hood and taken to the waste room, thoroughly clean the outside of the bottles and bags by wiping with bleach soaked towels followed by ethanol soaked towels. Do not forget to wipe down the bottom of the waste bottles. Replace waste labels that are damaged or unclear. Place all the double bagged solid paraoxon waste containers is a larger thick plastic bag (I used the broken glass disposal bags) and place in a cardboard box. Put a waste label on the outside of the box.

It will feel as if you are generating a lot of waste, particularly the solid waste because you need to use new paper towels between cleaning steps, replace your gloves regularly and replace the outside latex layer of glove even more regularly between each bleach or ethanol wipe to prevent cross contamination. Just remember, it is better to make sure paraoxon residue is fully removed from surface and to take waste out regularly than to accidentally expose yourself or others to the hazardous chemical.

D.3 Handling Paraoxon

In general, be overly cautious when working with paraoxon. Alert other group members on days you are working with paraoxon so they are aware and can be cautious around the area as well. Assume everything you touch with gloved hands has been contaminated. Thoroughly clean all containers, pipets, and equipment that may have come in contact with paraoxon. Don't forget to clean hood sashes/doors, light switches, etc. at the end of each day when you have finished.

Use ≥5.9 mil nitrile gloves when working with paraoxon. Replace your gloves frequently, at least every 0.5 hr. Double glove when cleaning, or when moving a cuvette to the UV-Vis spectrometer so that the outer glove layer can be removed easily to prevent cross-contamination of equipment.

Below, the decontamination of Paraoxon solutions or residues on the surface of non-disposable items and equipment is detailed.

Alkaline solutions catalyze the hydrolysis of paraoxon to p-nitrophenol.[5] Decontamination of paraoxon solutions can be accomplished by adding bleach to the solution then disposing of the solution in the liquid waste container. To clean paraoxon residue off surfaces, first wipe the item with a bleach soaked towel at least 2 times to decontaminate the paraoxon. Wipe with an ethanol soaked towel several times to remove the p-nitrophenol hydrolysis product from the surface.

To prevent cross-contamination, double glove while cleaning up and change the outer latex glove layer in between cleaning steps. Clean all items or equipment that may have come in contact with paraoxon thoroughly. Once all paraoxon experiments are complete, thoroughly

clean the paraoxon designated fume hood with bleach, followed by ethanol, and finally soapy water. Clean monkey bars and all surfaces in the hood before letting others know the hood to is safe to use. Dispose of all towels and gloves used for cleaning as solid paraoxon waste. DO NOT let liquids go down the sink in the hood when cleaning the fume hood bench top.

When performing experiments involving Paraoxon the following precautions should be taken.

A stock solution of 152 mM Ethyl-Paraoxon in methanol is prepared in a 1 dram vial from 99.9% Ethyl-Paraoxon. Aqueous paraoxon solutions containing 15.2 mM paraoxon/10% methanol in water are prepared in 1 dram vials from the 152 mM paraoxon stock solution and used in enzyme activity experiments. These 1 dram vials and the vials received from Chem. Service Inc. containing 99.9% Paraoxon are small and can be knocked over easily, particularly during pipetting. To prevent spills, secure the vials by placing them in a vial rack. Alternatively, if a vial rack is not available, the vials can be secured to the monkey bars in the hood with a clamp.

The UV-Vis spectrometer is used to measure enzyme activity with paraoxon. This instrument is located outside of the hood so increased safety protocols must be taken. Inform all group members of the hazard prior to performing the experiments. All group members must wear a N-100 respirator/mask if working near the experimenter during enzyme activity experiments. Do not conduct these experiments when no one else is in the building. You must ensure someone is in the office in case an accident occurs.

Double glove for these experiments. You should put on a clean top and bottom pair of gloves for each UV-Vis absorption measurement. Typically, 100 μL of 15.2 mM Paraoxon/10% methanol solution is added to 900 μL of an enzyme solution in a quartz cuvette that has a

matching lid. Once paraoxon is added to the enzyme solution, cap the cuvette and carefully transport the cuvette to the spectrometer. Remove outer glove layer, then close the spectrometer cover and run the experiment. It is helpful to have a partner for these experiments that can initiate the experiment on the computer after the lid is closed so the paraoxon handler does not touch the computer mouse or keyboard.

Once the absorption measurement is finished, carefully remove the capped cuvette from the spectrometer and return to the fume hood. Poor liquid into a bleach solution to decontaminate. Clean the spectrometer sample holder, cover, and any other item you touched during the experiments with bleach and ethanol. Cuvette and lid should be cleaned with bleach, followed by several ethanol washes, and finally soap and water. Again, be overly cautious, wipe down equipment several times and make sure the paper towels are soaked in bleach or ethanol to thoroughly decontaminate the paraoxon and remove the hazards from surfaces.

D.4 References

1. Bennett, S. R., *Environmental hazards of chemical agent simulants*. Aberdeen Proving Ground, MD, 1984.

2. National Center for Biotechnology Information, PubChem Database. Paraoxon, CID=9395. https://pubchem.ncbi.nlm.nih.gov/compound/Paraoxon (accessed Aug. 19, 2019).

3. O'Neil, M. J., *The Merck Index : an encyclopedia of chemicals, drugs, and biologicals*. Merck: Whitehouse Station, N.J., 2001.

4. Gosselin, R. E. S., R.P.; and Hodge, H.C., *Clinical Toxicology of Commercial Products*. 5th ed. ed.; Williams & Wilkins: Baltimore, 1984.

5. Larranaga, M. D. L., R.J. Sr.; Lewis, R.A., P. *In Hawley's Condensed Chemical Dictionary*, Sixteenth Edition, 16th ed.; Lewis, R. J. S., Ed. Van Nostrand Rheinhold Co.: New York, 2016; pp 1025-1158.